Graphene quantum dots and their metallophthalocyanines nanoconjugates as novel photoluminescent nanosensors

A thesis submitted in fulfilment of the requirements for the degree of

DOCTOR OF PHILOSOPHY (PhD)

Of

RHODES UNIVERSITY

By

OJODOMO JOHN ACHADU

SEPTEMBER 2017

DEDICATION

To my family and most specially my dad

(Mr John Reuben Achadu)

ACKNOWLEDMENTS

My grateful thanks go to God for his gift of life and sustenance during the time of this study.

My utmost appreciation and in-depth gratitude goes to my supervisor, Distinguished Prof. Tebello Nyokong for her mentorship and relentless guidance leading up to the completion of this PhD research. Also, your drive towards developing the African continent via the training of young scientists like myself, afforded me the opportunity to study under your supervision. Thank you Prof.

I wish to thankfully appreciate my family for all their supports during my sojourn in South Africa. Special thanks to my dad, Mr J. R. Achadu for the prayers and encouragements.

I also express my sincere gratitude to Ms Gail Cobus, Dr Jonathan Britton, Dr John Mack and Mr Francis Chindeka for their supports and help in the course of this research.

I would be remiss not to gratefully thank and appreciate my colleagues and the S22 family for the wonderful time and experience we shared. You guys rock!

To the entire member of staff of Chemistry department of Rhodes University, I say thank you.

Financial support from the Department of Science and Technology (DST)/MINTEK Nanotechnology Innovation and National Research Foundation (NRF), South Africa, is gratefully acknowledged.

ABSTRACT

The fabrication and application of graphene quantum dots (GQDs)-based photoluminescent probes for the detection of analytes is presented. GQDs were functionalized with complexes such as metallophthalocyanines (MPcs), metal nanoparticles (Au@Ag NPs), 2,2,6,6-tetramethyl(piperidin-1-yl)oxyl (TEMPO), maleimide and thymine for the sensing of target analytes such as ascorbic acid (AA), biothiols (cysteine, homocysteine and glutathione) and mercury ion (Hg^{2+}). The design strategy and approach was based on the quenching of the fluorescence of the GQDs upon functionalization with the above-mentioned complexes, which could be restored in the presence of the target analytes (due to their specific interaction affinity with the complexes). For the detection of AA, GQDs were covalently and/or non-covalently conjugated to TEMPO-bearing complexes to form GQDs-4A-TEMPO and GQDs-TEMPO-MPc systems with nanomolar limits of detection. For the detection of biothiols, Au@Ag NPs and maleimide-bearing complexes (MPc), which have specific affinity to interact with biothiols, were deployed. Hg^{2+} detection involved the use of GQDs and/or MPcs with thiol and thymine groups, respectively. In addition, a smart sensing platform was designed for the dual detection of biothiols and Hg^{2+} using supramolecular hybrid of polyethyleneimine functionalized-GQDs and MPc-Au@Ag conjugate. The probe could detect, in a sequential manner, Hg^{2+} and biothiols with high sensitivity. Results obtained from the LODs of the probes showed that GQDs sensing performances could be enhanced in the presence of MPcs. The probes designed in this work were successfully deployed in the assays of the target analytes in real samples and the recoveries obtained confirmed the analytical applicability of the probes.

CONTENT

CHAPTER ONE

1. INTRODUCTION

LIST OF ABRREVIATIONS

4AC-TEMPO = 4-Acetamido-2,2,6,6-tetramethyl(piperidin-1-yl)oxyl

4A-TEMPO = 4-Amino-2,2,6,6-tetramethyl(piperidin-1-yl)oxyl

AA = Ascorbic acid

AFM = Atomic force microscopy

Au@Ag NPs = Gold-silver core-shell nanoparticles

BSA = Bovine serum albumin

CV = Coefficient of variation

Cys = Cysteine

DAMN = Diaminomaleonitrile

DCM = Dichloromethane

DLS = Dynamic light scattering

DMF = Dimethyl formamide

DMSO = Dimethyl sulfoxide

EDC = 1-Ethyl-3-(3-dimethylaminopropyl)-carbodiimide

EDTA = Ethylenediaminotetraacetic acid

EDX = Energy dispersive X-ray spectroscopy

Eff = FRET efficiency

EPR = electron paramagnetic resonance

FRET = Förster resonance energy transfer

gCNQDs = Graphitic carbon nitride quantum dots

GO = Graphene oxide

GQDs = Graphene quantum dots

GSH = Glutathione

HSA = Human serum albumin

Hcy = Homocysteine

HMDS = hexamethyldisilazane

ICT = Intramolecular charge transfer

LOD = Limit of detection

MP = Metalloporphyrin

MPc = Metallophthalocyanine

NHS = N-hydroxysuccinimide

PBS = Phosphate buffered solution

Pc = phthalocyanine

PEI = Polyethyleneimine

PET = Photo-induced electron transfer

ROS = Reactive oxygen specie

RSD = Relative standard deviation

TEM = Transmission electron microscopy

TEMPO = 2,2,6,6-tetramethyl(piperidin-1-yl)oxyl

TGA = Thermo-gravimetric analysis

XPS = X-ray photoemission spectroscopy

XRD = X-ray powder diffraction

LIST OF SYMBOLS

Φ_F = Fluorescence quantum yield

τ_F = Fluorescence lifetime

α = Non-peripheral position

β = Peripheral position

F = Fluorescence intensity

A = Absorbance

eV = Electron volt

K_{SV} = Stern Volmer quenching constant

k_q = Bimolecular quenching constant

δ = Standard deviation

1. INTRODUCTION

This chapter presents a general overview of graphene quantum dots with discussions on their compositions, synthesis routes, optical properties, structural characterization and their reported applications in fluorescence-based nanosensor design.

The general properties and synthesis of metallophthalocyanines and their conjugates with various quantum dots and reported applications is presented.

1.1. Graphene quantum dots

Graphene quantum dots (GQD) are zero-dimensional (0D) materials regarded as fragmented pieces of larger and multi-layered graphene sheets [1–3]. The cutting of the two-dimensional graphene sheets into smaller pieces results in materials which exhibit the phenomena of quantum confinement and edge effects [4]. These phenomena bestow excellent optical and photoluminescence (PL) properties on GQDs. GQDs possess sizes typically within the range of 1-20 nm [5], and are highly fluorescent carbon-based nanoparticles which have sparked huge interest within the research community due to their potential for a plethora of applications [6]. They combine the advantages of excellent water dispersibility, biocompatibility, ease of surface functionalization, green synthesis and are a low toxicity alternative to the conventional semiconductor quantum dots (SQDs) [7,8]. They also share similar excellent characteristics with semiconductors QDs such as high photostability, size and wavelength tunable photoluminescence (PL) [2, 7, 8].

The uniqueness of GQDs amongst other QDs stems from the fact that they clearly possess graphene-like structure irrespective of the diameter of the GQDs core, which bestows on them some of the peculiarly unique properties of graphene [9]. Recently, efforts have been devoted towards finding various methods for GQDs synthesis. Due to their attractive properties, nanoprobes based on GQDs and their derivatives are envisaged to achieve high levels of performance.

1.1.1. General applications of GQDs

GQDs have been potentially found useful in several areas such as in fluorescence sensing [1, 5], electrochemiluminescence and electrochemical sensing [10, 11]; in photocatalysis [12], photovoltaics [13-15], drug delivery [16, 17], bioimaging [18-20] and photodynamic therapy (PDT) [20]. Other emerging applications include GQDs light-emitting diodes (LEDs) [21, 22], and plasmonics [23] for electronic devices. A schematic representation of the applications of GQDs in different fields of science and technology is given in Fig. 1.1.

1.1.2. Synthesis of GQDs

Table 1.1 shows the list of the various precursor materials and methods for GQDs synthesis reported thus far in the literature [8, 12, 19, 20, 24-46].

1.1.2.1. Top-down route

The top-down approach for GQDs synthesis involves the cutting or breaking down of large materials with graphene-like structures into nanosized (<100 nm) structures to yield GQDs as shown in Fig. 1.2. As such, GQDs have been fabricated from large sized carbon nanomaterials such as fullerenes (C_{60}) [24], graphene [25], graphene oxide [26-29], carbon nanotubes (single or multi-walled) [30, 31], graphite nanoparticles (NPs) [32], carbon fibres [33], natural coals [34], carbon black [35], block co-polymer graphite electrodes [36], and recently using metal organic frameworks (MOFs)-derived carbon [37]. The carbon-based materials employed as precursors for GQDs preparation are

subjected to different physical and chemical treatments under specialized and optimized conditions to obtain fluorescent GQDs of different sizes (Table 1.1).

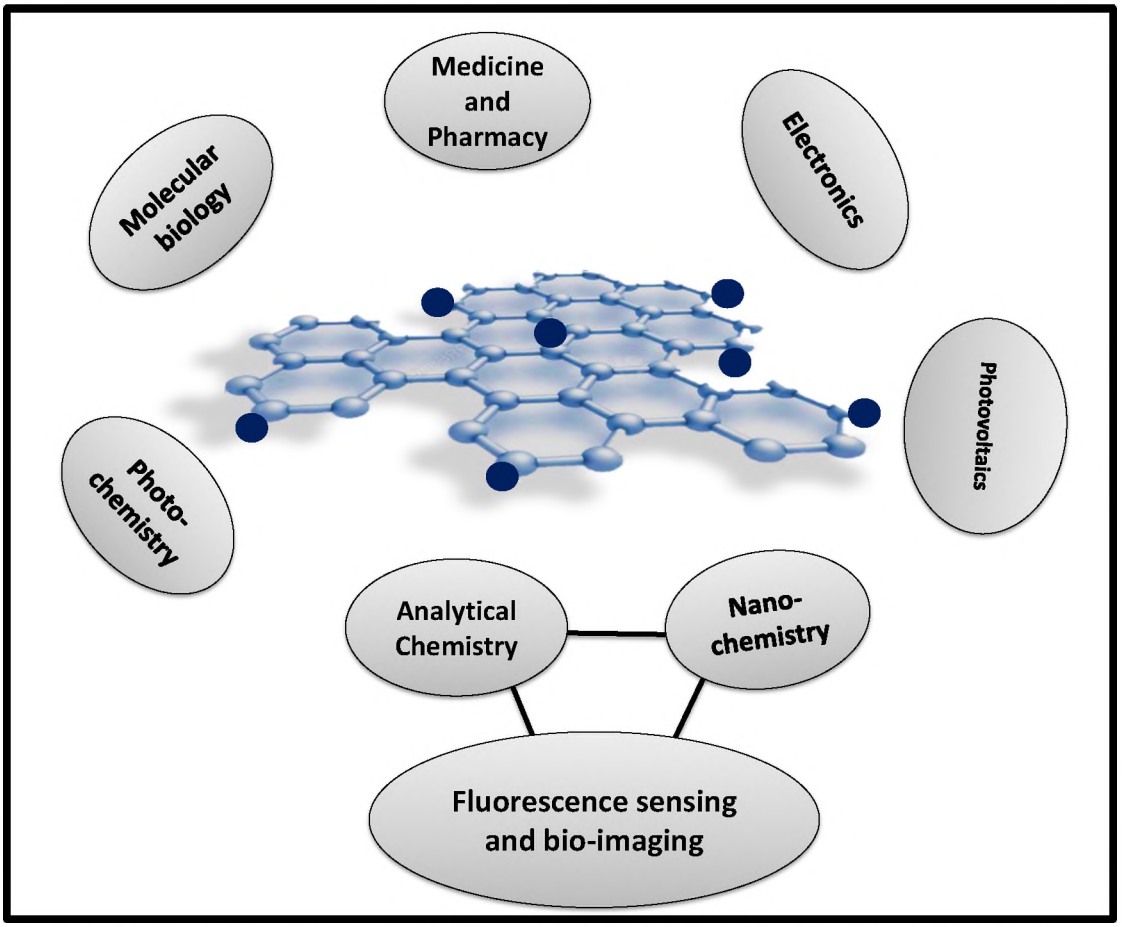

Fig. 1.1. Summary of the various fields of applications of graphene quantum dots [1].

The processes reported so far in the literature for the top-down approach of GQDs synthesis include: surface catalyzed decomposition reaction; acidic oxidation and exfoliation; electrochemical oxidation; hydrothermal and solvothermal processes, fast ultrasonic and microwave scissoring reactions [5, 6]. Other sparsely reported methods include controlled chemical oxidation and air (oxygen)-plasma treatment of multi-layered graphene based materials [6].

1.1.2.2. Bottom-up route

Many organic compounds which are rich in carbon have been employed as precursors for GQDs synthesis in processes typically involving hydrothermal or solvothermal reactions using high pressure reactors (autoclaves) or via microwave assisted hydrothermal methods. Direct pyrolysis (carbonization) and controlled heating of precursor materials have been reportedly employed for GQDs synthesis as well [38]. The various carbon source precursors employed for the bottom-up GQDs synthesis and conditions are shown in Table 1.1 [12, 20, 38-46]. The bottom-up synthetic route for GQDs using citric acid as the carbon source precursor is illustrated in Fig. 1.3. This method was employed in this work, but with some modifications.

1.1.2.3. Doping and surface functionalization

The *in situ* one-pot functionalization of GQDs with molecules or heteroatoms has resulted in the modulation of their optical and photoluminescence properties due to the introduction of different functionalities with a consequent surface or edge defects leading to band gap and electronic density perturbation [47, 48]. The discussed surface modification strategies have been proved theoretically and experimentally with observed enhanced optical activities (fluorescence quantum yield and PL emission) of GQDs and their derivatives [47].

Even though the PL origin of GQDs is not yet completely understood, it has been clearly argued that the presence of oxygen rich groups (hydroxyl, carbonyls and carboxyls) on the layers or intercalated within the lattice structure of the

graphene sheets provide GQDs with surface states and emissive traps which are responsible for their photoluminescence (PL) properties [49].

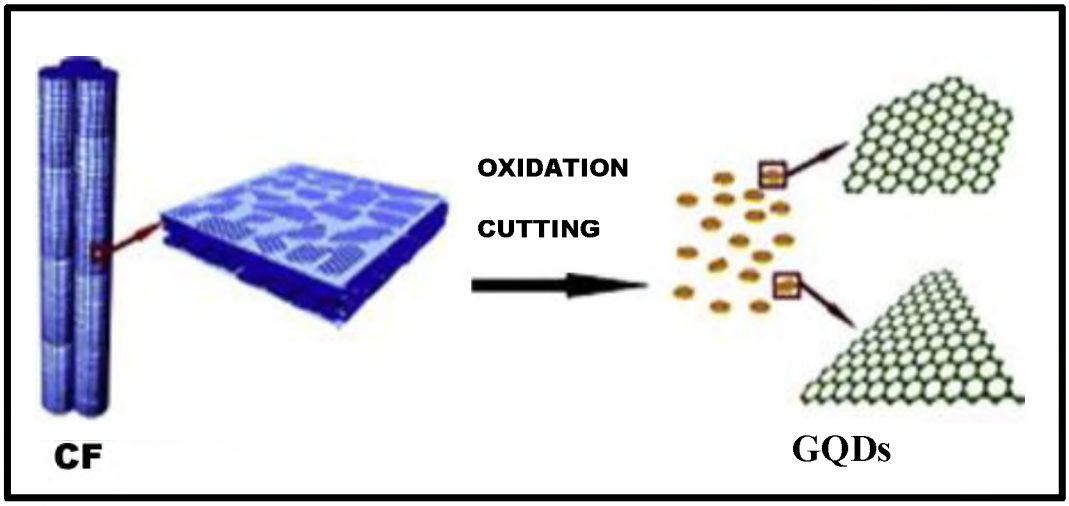

Fig. 1.2. Top-down route for GQDs synthesis using carbon fibres (CF) as an example [33].

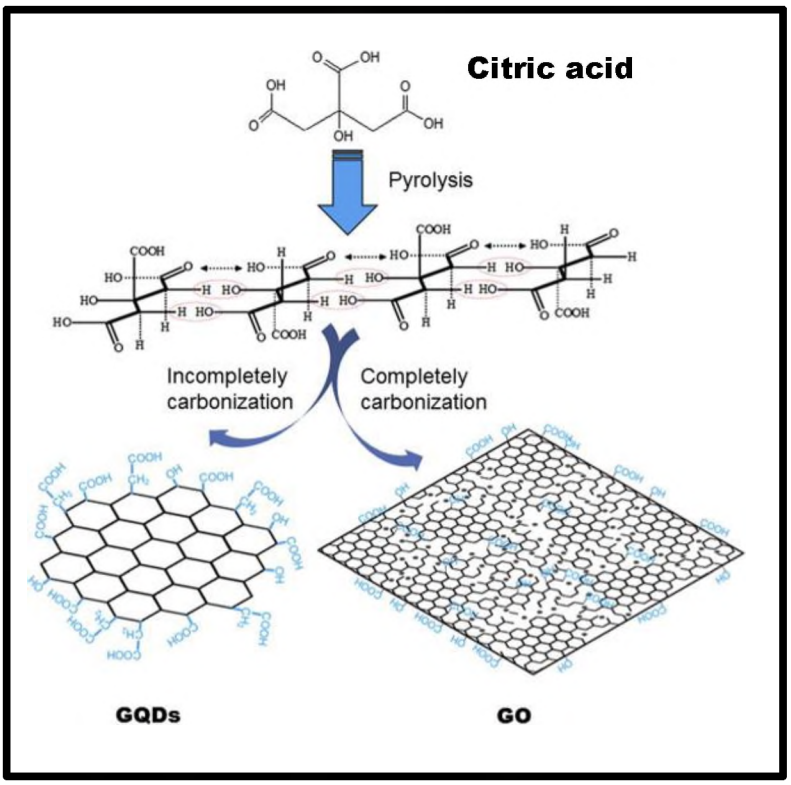

Fig. 1.3. Bottom-up route for GQDs synthesis from citric acid (CA) as an example [38].

Table 1.1. Summary of the various synthetic routes for GQDs preparations

Top-down Process	Precursor	Size(nm)	REF
Acid oxidation	Carbon fibres, coal and carbon black	15-18, 1-4 and 3	[33-35]
Hydrothermal	GO	1.5-5	[26]
Solvothermal	GO	3-5	[27]
Microwave-assisted hydrothermal	GO	2-7 and ~3	[28, 29]
Ultrasonication	Graphene	3-5	[8]
Electrochemistry	Graphite rod Graphene	5-10 ~3	[19] [25]
Chemical exfoliation	MWCNTs SWCNTs Graphite NPs Fullerenes (C_{60}) Graphite co-polymer MOF-carbon	20 ~8 ~4	[24, 30-32, 36, 37]
Bottom-up Process			
Hydrothermal	Pyrene Polythiophenes Citric acid	3.6±1.2 2-6 2.69±0.42	[39] [20] [12]
Microwave assisted pyrolysis	Glycerol	1-5	[40]
Precursor pyrolysis	L-glutamic acid Citric acid Glucose HBC Alginate Ethylene glycol Turbostic carbon (neem leaves)	4.66±1.24 15 1.6-21 ~60 (disc-like) 10-20 3-5 5-6	[41] [38] [42] [43] [44] [45] [46]

GO = Graphene oxide, SWCNTs = Single walled carbon nanotubes, MWCNTs = Multi walled carbon nanotubes, NPs = Nanoparticles, HBC = Hexabenzocoronene. MOF = Metal organic frameworks.

The enhancement in PL properties of GQDs resulting from doping and/or surface functionalization has been attributed to the introduction of new kinds of surface states. Specifically, N, S or S/N-doping of GQDs, where N and or S atoms are intercalated into the graphitic core, results in the introduction of new surface states (denoted as the N and or S-states) [12, 50]. These new states have emissive traps that are able to promote a high yield of radiative recombination [49]. Notably, it was reported that the quantum and edge effects phenomena in GQDs expedite the penetration of heteroatoms deeply into the carbon lattice structure of GQDs [5]. GQDs have been doped with heteroatoms such as N, S, B, F, Ag, P and Cl [5, 12, 51-55]. N-doped and S,N co-doped GQDs were employed in this thesis.

Surface functionalization with organic and inorganic molecules such as glutathione (GSH), hemin, cytochrome C, horseradish peroxidase (HRP), peptides, rhodamine, dopamine, diamines, polyethyleneimine (PEI), thiols, ionic liquids and aryl groups [56-67], have been found to be effective pathways to tuning the PL properties of GQDs (improvement in optical performance) by the introduction of groups with specific functionalities for desired applications. These strategies are quite promising since tailored designed materials can be obtained with GQDs as the core materials. However, the underlying formation mechanisms have not been fully elucidated.

1.1.2.4 . Conjugation

Post-synthesis modifications or treatments of GQDs have also been shown to be effective in terms of optical properties modulation. GQDs' planar structure

consisting of delocalized π-electrons of graphene enables strong π-π interactions with other π-conjugated aromatic molecules **[68]**. The presence of carboxyl and hydroxyl groups on GQDs surface and edges enable covalent attachment, electrostatic interactions and hydrogen bonding with other suitable moieties. The controlled post-synthesis functionalization of GQDs with biomolecule and macrocycles such as porphyrins has resulted in changes in their photophysical and chemical properties, leading to various applications of GQDs such as in nanoprobe fabrication (mostly as "turn ON" sensors) and fluorescence imaging microscopy **[63]**.

In this work, thymine-functionalized GQDs (T-GQDs) were synthesized for the first time to allow for the specific detection of analyte of interest. Thymine (a biomolecule) is known to possess the specific affinity to bind selectively and strongly with Hg^{2+} **[69]**, hence T-GQDs are employed in this work for the facile recognition of Hg^{2+} due to the known specific interaction between thymine and Hg^{2+} to form the T-Hg^{2+}-T pairs [**70-72**]. The incorporation of thymine onto the GQDs surface was aimed at creating functional probe material which is advantageous in terms of selectivity and sensitivity towards Hg^{2+} detection.

GQDs were also functionalized with 4-amino-2,2,6,6-tetramethyl(piperidin-1-yl)oxyl (4A-TEMPO), a known fluorescence quencher for the first time in this work. TEMPO moieties are known to possess specific interaction affinity for ascorbic acid (AA) **[73]**, hence 4A-TEMPO functionalized GQDs was deployed for the fluorescence "turn ON" detection of AA. The probes combined the

advantage of AA detection in aqueous media and low limits of detection (LODs) in the nanomolar range.

Also, metallic alloyed (core-shell) nanoparticles of Au and Ag (Au@Ag NPs) were blended with polyethyleneimine-functionalized GQDs (PEI-GQDs) for the first time in this work. The interaction between PEI-GQDs and Au@Ag NPs was via electrostatic interaction. The Au@Ag NPs possess negatively charged surface due to the tyrosine capping, whereas PEI-GQDs possess positively charged surface introduced by the polycationic PEI **[64]**. The blend was deployed for the sensitive recognition of target analytes (biothiols) following the restoration of the fluorescence of PEI-GQDs that had been initially quenched by Au@Ag NPs. The use of Au@Ag NPs as the fluorescence switching moiety (similar to 4A-TEMPO) has the advantage of easy and synergistic binding with sulfur atom of the target analytes to form Au-S and Ag-S bond **[53, 74]**, hence allowing the sensitive detection of the target analytes (biothiols).

GQDs directly functionalized with maleimide units (M-GQDs) were also deployed for biothiols recognition following the principle of Michael addition (thiol-maleimide reaction) of biothiols to the maleimide-appended GQDs **[75]**. This reaction is selective and rapid with the formation of stable thiol-maleimide products. The fabrication of maleimide-derivatized GQDs (M-GQDs) as a novel probe is reported for the first time in this thesis. The M-GQDs probe was found to be highly sensitive and selective towards biothiols detection in the nanomolar range in aqueous solution and at physiological pH.

1.1.3. GQDs/functionalized GQDs employed in this work

The GQDs employed in this work were synthesized using both top-down and bottom-up approaches and were all found to exhibit excellent water solubility and high PL properties. Heteroatoms doped GQDs such as N-doped and S, N co-doped were used in the design of sensor probes in this work. This work reports for the first time the post-synthesis conjugation and functionalization of GQDs with metallophthalocyanines (MPcs), 4A-TEMPO, Au@Ag NPs and maleimide leading to the "turn-OFF" of the fluorescence of the GQDs which was then recovered ("turn ON") by specific analytes of interest. Table 1.2 shows a list of GQDs synthesized and employed in this work. Novel hybrid conjugates of GQDs with macrocycles such as metalloporphyrin (MP) were also synthesized in this work for the first time. The resulting conjugates (GQDs-MPcs/GQDs-MP) were further deployed as fluorescent sensors for various analytes.

Table 1.2. List of GQDs/functionalized GQDs employed in this work

GQDs	Analyte	Detection method
Pristine GQDs	AA, Biothiols and Hg^{2+}	FL "turn ON"
N-doped GQDs	-	-
S, N co-doped GQDs	AA	FL "turn ON"
PEI-GQDs	Biothiols and Hg^{2+}	FL "turn ON"
T-GQDs	Hg^{2+}	FL "turn ON" and "turn OFF"
GQDs-4A-TEMPO	AA	FL "turn ON"
SN-GQDs-4A-TEMPO	AA	FL "turn ON"
M-GQDs	Biothiols	FL "turn ON"

TEMPO = 2,2,6,6-tetramethyl(piperidin-1-yl)oxyl, PEI = Polyethyleneimine.

T = Thymine, M = Maleimide, AA = Ascorbic acid.

1.1.4. Optical and fluorescence properties of GQDs

1.1.4.1. UV-Vis absorption

A typical UV-Vis absorption and emission spectra of GQDs are shown in Fig. 1.4 [76]. The ground-state absorption characteristics of GQDs typically show a broad peak observed around 300-350 nm which is attributed to the n-π^* transition of the C=O bonds of the surface carboxylic groups of GQDs [77-80]. Other peaks reported below 300 nm are rarely recorded due to solvent absorption in the region.

1.1.4.2. Fluorescence properties

GQDs with deep ultraviolet, bright blue, red, yellow and green emissions have been reported in the literature [18, 19, 42, 81, 82]. GQDs intrinsic emissive sites and defect state emissions due to quantum confinement effect, excitons of carbon atoms, aromatic π-electrons, edge effects and free zigzag sites of the graphitic domain have been reported [1-4, 47, 48, 82]. GQDs may exhibit excitation-wavelength dependent PL (where there is a change in emission wavelength with changes in excitation wavelength) or excitation-wavelength independent PL (where there is no change in emission wavelength, but there may be a change in intensity) [12, 77, 83]. The excitation-wavelength dependent emission PL is proposed to reflect the differences in sizes of GQDs and also the presence of a mixture of different emissive sites [1, 12]. Conversely, excitation-wavelength independent emissions in GQDs have been ascribed to the uniformity in both size and surface states [33]. Additionally, the fluorescence emissions of GQDs exhibit pH dependent behaviour where emissions are

strongest in neutral to alkaline pH, but completely quenched in acidic pH [84, 85].

1.1.4.3. Fluorescence quantum yields (Φ_F) and lifetimes (τ_F)

The fluorescence quantum yields (Φ_F) of GQDs are largely dependent on the synthesis routes and the extent of surface passivation or chemical modifications involved. When compared with their doped or functionalized derivatives, pristine GQDs exhibit lower fluorescence quantum yields (Φ_F).

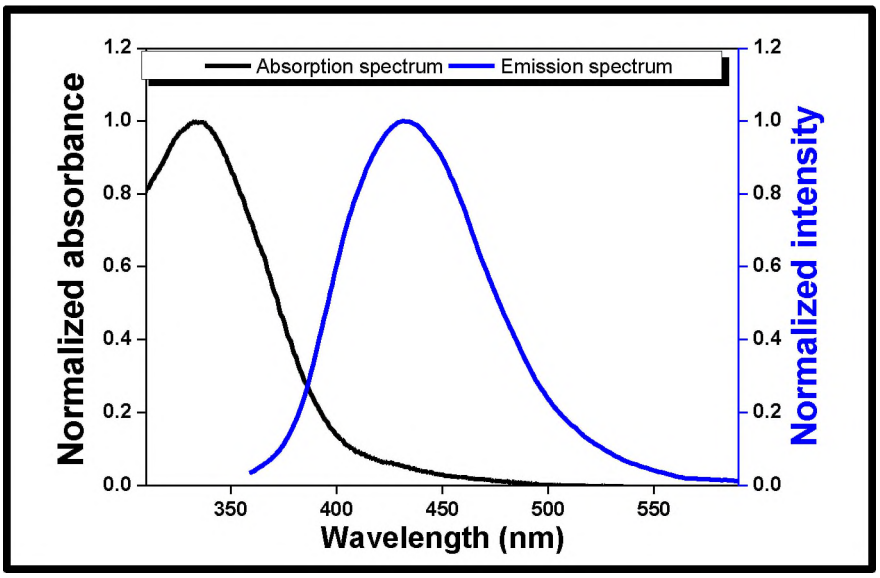

Fig. 1.4. Ground state absorption and emission spectra of GQDs recorded in PBS (10 mM) [76].

This has been ascribed to the fact that pristine GQDs usually contain rich oxygen groups such as carboxylics and hydroxyls that could act as non-radiative centres for electron-hole recombination [1, 2, 5, 6, 12]. As a result, Φ_F of GQDs has been improved by surface passivation or reduction strategies which involve the removal of the oxygen groups. This strategy was employed by Qian and co-

workers to obtain high PL from GQDs functionalized using diamines [63]. Amino-functionalized GQDs were reportedly prepared by Tetsuka and co-workers to derive GQDs with improved Φ_F ranging between 19-29% [48]. Zhu et al reported a 205% increase in the Φ_F of alkylamine functionalized GQDs with respect to the pristine GQDs [86]. GQDs functionalized with polyethyleneimine (PEI) and polyethylene glycol (PEG) were reported by Liu et al [64] and Shen et al [13] with improved Φ_F by 15% and 62.1%, respectively. In this work, the Φ_F of GQDs was improved by functionalization with thymine. The latter is employed for the first time in this work.

The fluorescence lifetimes (τ_F) of GQDs may exhibit single exponential decay typically within the range of 5-20 ns [1, 2]. τ_F values for the doped and/or surface functionalized GQDs are usually longer compared to pristine GQDs, which corresponds to higher Φ_F as a result of surface passivation [1, 2, 5, 6, 86, 87].

1.1.5. GQDs as optical sensors

A plethora of GQDs-based nanoprobes have been designed based on fluorescence "*off-on*" process as shown in Table 1.3 [51, 56, 58, 83, 88-99]. Compared to the conventional semi-conductor QDs, GQDs are better as sensors since they are non-toxic (biocompatibility) and exhibit excellent water solubility. Thus, maybe used for *in vivo* applications.

Wu *et al* proposed a "turn ON" probe for biothiols detection using GQDs in the presence of Hg^{2+} [88].

Table 1.3. A selection of GQDs-based fluorescent sensor probes for the detection of various analytes.

GQDs derivative	Analyte	Detected method	REF
GQDs-Hg^{2+}	Cys, Hcys and GSH	FL "turn ON"	[88]
GQDs-Cytochrome c	Trypsin	FL "turn ON"	[58]
GQDs-Cu^{2+}	Ascorbic acid	FL "turn ON"	[89]
N-doped(dicyanamide)-GQDs	pH	FL "turn ON"	[83]
GQDs-Europium (Eu^{3+})	Phosphate	FL "turn ON"	[90]
GQDs@Ag core-shell NCs	PSA	FL "turn ON"	[91]
Boron-doped GQDs (B-GQDs)	Glucose	FL "turn ON"	[51]
GQDs-BBV	Glucose	FL "turn ON"	[92]
GQDs@GSH-Fe^{3+}	ATP	FL "turn ON"	[56]
B-GQDs	Al^{3+}	FL "turn OFF"	[93]
aptamer/GQDs/GO	Pb^{2+}	FL "turn ON"	[94]
ssDNA-rGQDs/GO	tDNA	FL "turn ON"	[95]
GQDs- Europium (II)	Glutamic/Aspartic acid	FL "turn ON"	[96]
Europium-GQDs	Cu^{2+} and L-Cys	FL "turn ON"	[97]
GQDs- FeTMPyP	H_2O_2, Glucose	FL "turn ON"	[98]
N-GQDs-H_2TMPyP	Cd^{2+}	-	[99]

NCs = Nanoclusters, PSA = Prostate-specific antigen, BBV = N,N' -4,4-bis(benzyl-2-boronic acid)bi-pyridinium dibromide, ATP = Adenosine triphosphate, GO = graphene oxide, tDNA= Transfer deoxyribonucleic acid, Cys = L-cysteine, GSH = Glutathione, Hcy = Homocysteine, rGQDs = Reduced graphene quantum dots, TMPyP = 5,10,15,20-Tetrakis(N-methyl-4'-pyridyl)porphinato.

The interaction between GQDs and Hg^{2+} resulted in the efficient quenching of GQDs fluorescence. Conversely, the quenched fluorescence was recovered in the presence of biothiols. The selective binding of Hg^{2+} by the biothiols through the formation of Hg–S bond resulted in the recovery of the fluorescence of the GQDs. Liu et al **[89]** designed an ascorbic acid (AA) sensor based on GQDs-Cu^{2+} complex. The fluorescence of GQDs was quenched by Cu^{2+} ion via electron transfer process, the addition of AA led to the reduction of Cu^{2+} ion to Cu^{+} ion. Thus, the interaction between GQDs and Cu^{2+} was perturbed which resulted in the fluorescence recovery of GQDs **[89]**.

As Table 1.3 shows, porphyrins have been linked to GQDs for sensing, but not metallophthalocyanines (MPcs). MPcs are more stable than porphyrins hence employed in this work for the first time. This thesis reports on the use of GQDs conjugates with MPcs designed with specific ligands for the selective dual detection of Hg^{2+} and biothiols using "turn OFF-turn ON" system. This is the first time that an ***off/on/off*** system is used for dual detection of analytes.

In this work, GQDs-based probes were largely designed based on fluorescence "turn ON" mechanism due to the sensitive and reliable nature of "turn ON detection systems.

Sub-aim of this section of the thesis

1. The deployment of GQDs/functionalized GQDs for the fluorescence detection of target analytes and the comparative assessment of their performances with respect to sensitivity and selectivity.

2. Coordination of the as-synthesized GQDs to metallophthalocyanines (MPcs) and related molecules. Investigation of the fluorescence behaviour of GQDs when MPcs are coordinated to their surface and the deployment of the conjugates as fluorescent sensor probes.

1.2. Graphitic carbon nitride quantum dots (gCNQDs)

Graphitic carbon nitride-based nanomaterials have experienced resurgence lately, due to the discovery of facile synthetic routes for their preparation from rich nitrogen and carbon sources [100-102]. Fluorescent graphitic carbon nitride quantum dots (gCNQDs) possess layered structures similar to GQDs, but exhibit predominately π-conjugated framework of covalently joined C-N layers [103, 104], Fig. 1.5.

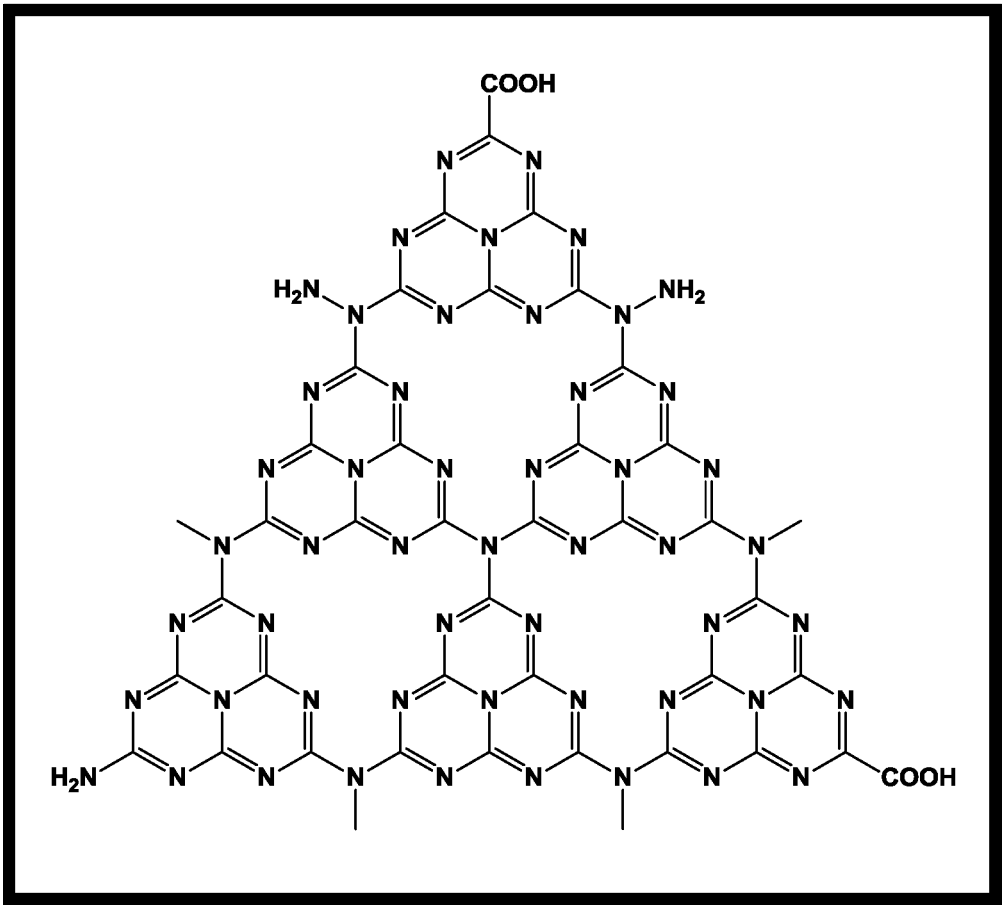

Fig. 1.5. General structure of gCNQDs showing their planar structure with C-N frame.

The presence of N atoms in the planar sheets of gCNQDs introduces another kind of intrinsic quantization effects, which makes them different (from GQDs) from a compositional point of view, thus receiving great attention.

gCNQDs possess similar admirable properties as other carbon-based QDs, such as aqueous solubility, excellent photoluminescence, chemical stability and biocompatibility [104-107]. The aforementioned characteristics have in general placed gCNQDs as fluorophores of choice for the design of probes for biological and environmental molecular species detection in recent times [107, 108].

1.2.1 Synthesis

The preparation of gCNQDs via the "bottom-up" approach has resulted in their scale-up synthesis from the condensation and/or pyrolysis of small organic molecules which are particularly nitrogen-rich such as formamide, N,N-dimethyl formamide (DMF), melamine, guanidine hydrochloride, urea and organic amines [104, 107, 108-113]. Diaminomaleonitrile (DAMN) was employed as a novel precursor for the synthesis of gCNQDs for the first time in this thesis. This precursor is better than most precursors reported in the literature since it has higher nitrogen content. In addition, TEMPO functionalized gCNQDs were synthesized for the first time in this work. The resulting TEMPO-functionalized gCNQDs was deployed for analyte detection.

1.2.2. UV-Vis absorption and fluorescence properties

gCNQDs exhibit typical absorptions in ultraviolet (UV) region which has been ascribed to the electronic transition (π-π^*) of the s-triazine units of the carbon

nitride family [104, 107]. Absorptions which are ascribed to n-π^* transition have also been reported and are attributed to the characteristic absorptions of carbon nanomaterials [110].

The fluorescence emission of gCNQDs appears to be quite similar to that of GQDs, with excitation-wavelength dependent properties [104, 107, 110], and this is a reflection of the different sizes and trap sites on the planar surface of gCNQDs [107]. The high relative fluorescence quantum yields (Φ_F) of gCNQDs are an indication of their suitability for use in fluorescence-based applications.

1.2.3. gCNQDs as optical sensors

Due to the excellent PL of gCNQDs, fluorescent probes based on their PL switching ("*off/on*") have been fabricated for the detection of various analytes such as dopamine, biothiols and ascorbic acid. Metal ions and anions such as Hg^{2+}, Cu^{2+}, Fe^{3+}, Cr^{3+}, I^- and Cl^- have also been detected using gCNQDs as shown in Table 1.4. [104, 114-118].

The sensing mechanisms reported are largely based on the interaction between the analytes and the N-groups within the layers of gCNQDs via coordination (with the metal ions) or charge complex formation with biomolecules [104]. No reports in the literature exist where gCNQDs have been surface passivated or intercalated with TEMPO for specific and selective interactions with target analyte. Hence, reported for the first time in this thesis.

Table 1.4. List of fluorescence "turn ON" detection of various analytes using gCNQDs as sensor probes.

gCNQDs derivative	Analyte	Detection method	REF
gC_3N_4-Cu^{2+}-PPi	ALP	FL "turn ON"	[114]
gC_3N_4-Cu^{2+}	CN	FL "turn ON"	[115]
gC_3N_4-Hg^{2+}	I^-	FL "turn ON"	[104]
gC_3N_4-Ag^+	Cys, Hcy and GSH	FL "turn ON"	[116]
gC_3N_4-Cr^{6+}	AA	FL "turn ON"	[117]
gC_3N_4-MnO_2	GSH	FL "turn ON"	[118]

ALP = Alkaline phosphatase, PPi = Pyrophosphate, CN = Cyanide, Cys = Cysteine, GSH = Glutathione, Hcy = Homocysteine, AA = Ascorbic acid.

Sub-aim of this section of the thesis

1. To assess the sensing efficiency and performances of gCNQDs in comparison with that of GQDs.

2. To further demonstrate the proof-of-concept of "turn ON" sensing.

1.3. Metallophthalocyanines (MPcs)

Metallophthalocyanines (MPcs) are two-dimensional 18 π-electron aromatic porphyrin synthetic analogues which are made up of four iso-indole subunits linked together through nitrogen atoms (Fig. 1.6), with central metals located within the cavity of the rings for metallated derivatives [119]. Phthalocyanines (Pcs) and porphyrins (Ps) are structurally similar macrocyclic compounds with unique electronic features such as high molar absorption coefficients, robust redox chemistry and ability to transfer and accept energy/electrons [120-122]. Over the years, Pcs and Ps have been deployed for various applications such as in organic photovoltaic devices, electrocatalysis, photocatalysis, photodynamic therapy (PDT), and non-linear optical (NLO) materials [123].

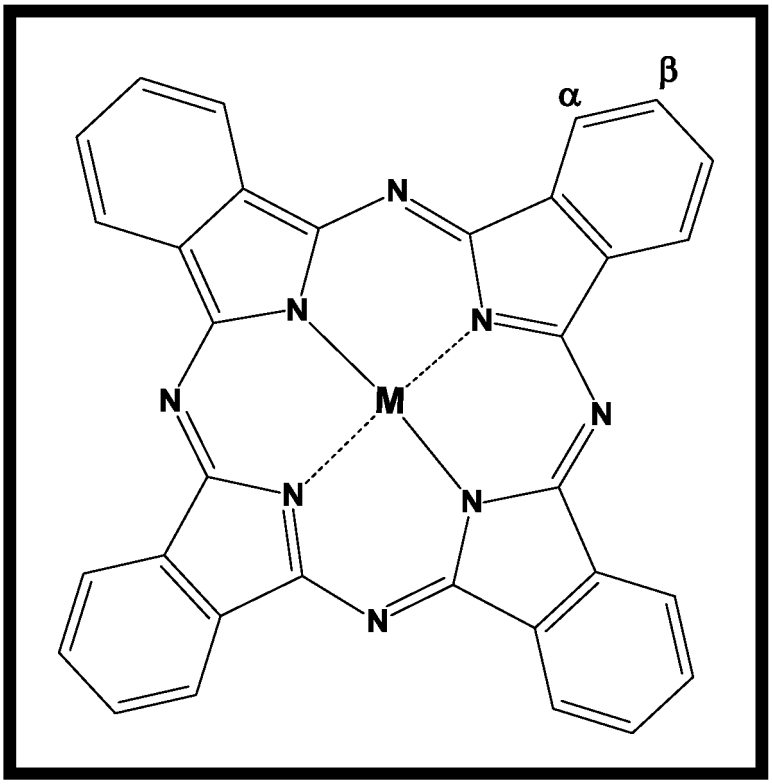

Fig. 1.6. General structure of MPcs (M= metal ion, Zn, Co and Al in this work). α = non-peripheral, β = peripheral.

The versatility of these compounds is rooted in their excellent optical and electronic properties which make them appealing tools for the construction of supramolecular ensembles and functional hybrid materials **[124-126]**.

1.3.1. UV-Vis spectra behaviour of MPcs

A typical UV/Vis absorption spectrum of MPc is shown in Fig. 1.7, and is characterized by the presence of a single intense Q-band corresponding to D_{4h} symmetry. The Q-band is due to the excitation between the ground state a_{1u} highest occupied molecular orbital (HOMO) to e_g lowest unoccupied molecular orbital (LUMO) as described by Gouterman's four orbital model **[127-129]**.

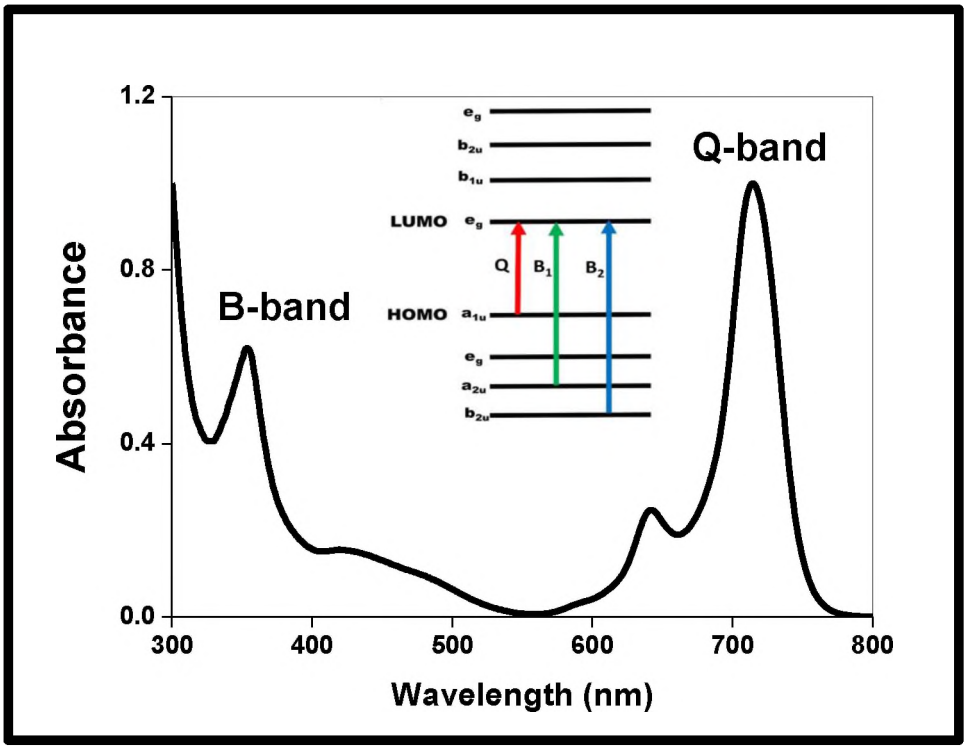

Fig. 1.7. Optical and electronic absorption spectrum of one of the MPcs (Unpublished work).

The less intense B-band appears at around 350 nm in the ultraviolet (UV) region (Fig. 1.7) which originates from two transitions; B_1 and B_2 corresponding to $a_{2u} \rightarrow e_g$ and $b_{2u} \rightarrow e_g$, respectively, inset in Fig. 1.7. The position of Q-band absorption in MPc complexes can be influenced by certain conditions which include; nature of central metal, peripheral or non-peripheral positions of substituents, number and nature of substituents and solvents effects [123, 130].

1.3.2. General synthetic methods for symmetrical MPcs

The symmetrical tetra-substituted MPcs may be synthesized as illustrated in Scheme 1.1.

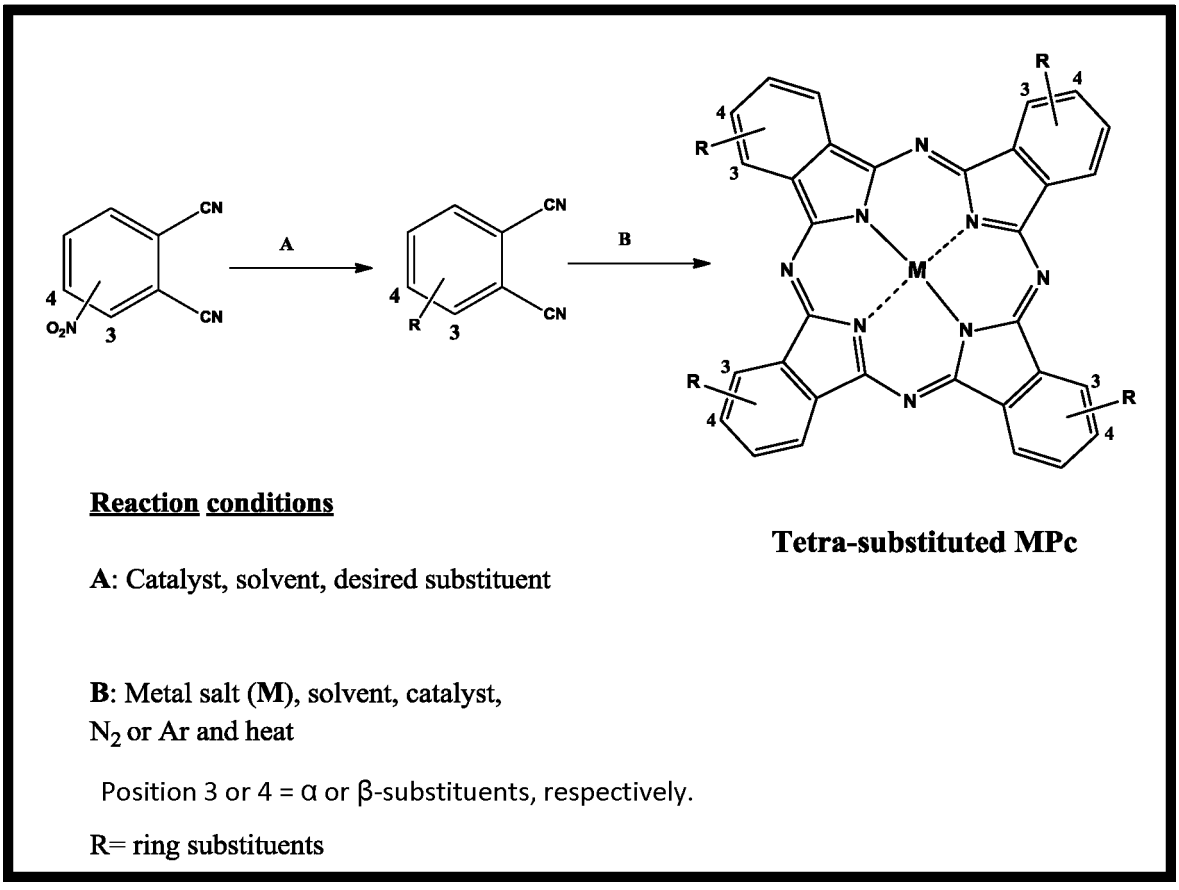

Scheme 1.1. Synthesis of peripheral and non-peripheral tetra-substituted MPcs from differently positioned (3 or 4) phthalonitriles.

Generally, the synthesis of symmetrically substituted MPcs involves the introduction of desired substituent(s) during the phthalonitriles preparation stage followed by the condensation of the resulting mono- or di-substituted phthalonitriles to form the corresponding symmetrical tetra- or octa-substituted MPc according to the reaction conditions outlined in Scheme 1.1. Positions of the ring substituents (peripheral and non-peripheral) on the MPcs may be controlled from the starting phthalonitriles according to Scheme 1.1 **[131]**. Only symmetrical MPcs were employed in this work.

1.3.3. MPcs and MPcs/QDs used for optical sensing

MPcs have been used as optical sensors due to their excellent optical and electronic properties **[120-122]**. MPcs have been fabricated widely for the detection of various gases by modifying the ring substituents and axial coordinating abilities **[132, 133]**. Molecular oxygen sensor has been reportedly fabricated using hybrids of AlPc-polystyrene thin films **[134]**. A highly sensitive room-temperature NO_2 sensor based on an n-type phthalocyanine semiconductor was fabricated **[135]**. Pentachlorophenol and simazine sensors were designed using films of NiPc derivatives via spin coating by total internal reflection ellipsometry (TIRE) technique **[136]**. Ammonia (NH_3) gas sensing properties of phthalocyanines were reported in liquid crystalline or thin film media **[137, 138]**. Thymine functionalized ZnPc and Zn porphyrin have been reportedly deployed for the fluorimetric detection of mercury ion (Hg^{2+}) **[139, 140]**. Also, volatile organic compounds (VOCs) were monitored using (OH)CuPc thin films **[141]**. Nitric oxide (NO) was reportedly detected via surface plasmonic

resonance technique using CoPc as an active added layer **[142]**. A hybrid of phthalocyanine-porphyrin was employed for alcohol vapours sensing using spin-coated films **[143]**.

The controlled functionalization of GQDs with biomolecules and macrocycles has resulted in their improved photophysical and chemical properties, leading to various applications of GQDs conjugates **[144]**. In this work, the syntheses of nanoconjugates of GQDs and macrocycles with extended π-conjugated systems such as MPcs were carried out for the first time. It was envisaged that GQDs-based nanosensor fabrication could be considerably extended when MPcs are coordinated to GQDs. The synthetic versatility and excellent optical properties of MPcs have motivated their deployment in the fabrication of multifunctional hybrid materials in 'donor–acceptor' supramolecular ensembles, which includes various carbon-based nanomaterials and semiconductor quantum dots (SQDs) for sensor probes fabrication **[145-149]**. As shown in Table 1.5, optical sensors for the detection of H_2O_2, reactive oxygen species (ROS), Br^-, F^-, Hg^{2+}, Zn^{2+}, NO and O_2 have been reported in the literature based on the conjugates of semiconductor QDs-MPcs and related macrocycles **[148-156]**. The only existing report in literature where GQDs and macrocycles hybrid was used for sensing is that involving GQDs assembled with a metalloporphyrin (MP) (similar in structure to MPcs). The hybrid was deployed for H_2O_2 and glucose sensing via a fluorescence "turn ON" process **[98]**. The fluorescence of GQDs was quenched by the MP and was 'switched ON' in the presence of H_2O_2.

The first ever hybrid conjugates of MPcs-GQDs/gCNQDs are reported in this thesis. The deployment of the MPcs-GQDs (MPcs-gCNQDs) nanoconjugates as fluorescence "turn ON" sensors for analytes detection is a key focus of this thesis.

Table 1.5. Summary of MPcs/MPs-semiconductor QDs conjugates for sensing applications

QDs-Macrocycle conjugate	Analyte	Detected method	REF
MPA-CdTe@ZnS-ClAlTAPc	H_2O_2	FL "turn ON"	[148]
GSH-CdTe@ZnS-CoTAPc	Cysteamine, GSH, TBHP, ClO_4^- and $HO^\bullet$	FL "turn ON"	[149]
MPA-CdTe@ZnS-CoTAPc	$O_2^{-\bullet}$	FL "turn ON"	[150]
GSH-CdTe@ZnS-NiTAPc	Br^-	FL "turn ON"	[151]
MPA-CdSe@ZnS-ClAlMAPc	F^-	FL "turn ON"	[152]
GSH-CdSe@ZnS-ClAlMAPPc	F^-	FL "turn ON"	[152]
GSH-CdSe@ZnS-NiMMSATBC	Hg^{2+}	FL "turn ON"	[153]
GSH-CdSe@ZnS-NiMMSAPc	Hg^{2+}	FL "turn ON"	[153]
CdSe@ZnS-Pyridyl-porphyrin	Zn^{2+}	FL "turn ON"	[154]
CdSe-tetraphenyl-porphyrins (Mn, Fe and Co)	Nitric oxide	FL "turn OFF"	[155]
QDs-Pd-pyridyl porphyrins	O_2	FL "turn ON"	[156]

MPA = Mercapto propionic acid, TBHP = t-butylhydroperoxide, TAPc = Tetraamino Pc, MAPc = Monoamino Pc, MAPPc = Monoaminophenoxy Pc, MMSATBC = Mono-mercaptosuccinic acid triazatetra-benzocorrole, MMSAPc = Mono-mercaptosuccinic acid Pc. GSH = Glutathione.

The π-π stacking interaction of GQDs/gCNQDs and MPcs was employed since no structural modification or defects could result from non-covalent interactions, hence the preservation of the optical and electronic properties of the interacting GQDs/gCNQDs and the macrocycles (MPcs) [157].

In this work, tetra-substituted maleimido-ZnPc and pyrene-derivatized ZnPc were synthesized for the first time and the resulting hybrid conjugates deployed as fluorimetric sensors for various target analytes detection in the presence of GQDs. Fluorescence behaviour of GQDs in the presence of the pyrene-substituted MPc was compared to that in the presence of pyrene-metalloporphyrin (MP) in this work.

1.3.4. MPcs and related macrocycles employed in this work

MPcs synthesized and employed in this work are shown in Table 1.6. The following MPcs were synthesized according to procedures well-documented in literature: ZnTAPc (**1**) [158], ZnTCPPc (**2**) [159], ZnTPPc (**3**) [160], ZnTMPPc (**4**), ZnTMPPcQ (**5**) [161], ClAlTMPPcQ (**6**) [162, 163], ZnOMPPcQ (**7**) [161], TEMPO-ZnPc (**8**) [164] and ZnTTPc (**9**) [139]. Complex **13** (ZnTPyP) was synthesized according to reported procedures [165]. MPc complex **1** (covalently conjugated to semiconductor quantum dots) and complex **9** (alone) have been used in the optical recognition of desired analytes in literature [139, 148]. Complex **8** was employed in electrochemical detection of AA [164]. MPcs have been extensively studied with semiconductor QDs or other nanoparticles for various studies and applications [148, 166-169].

Table 1.6. List of MPcs /MP used in this work

Molecular structure and Name	Studies done	Complex number
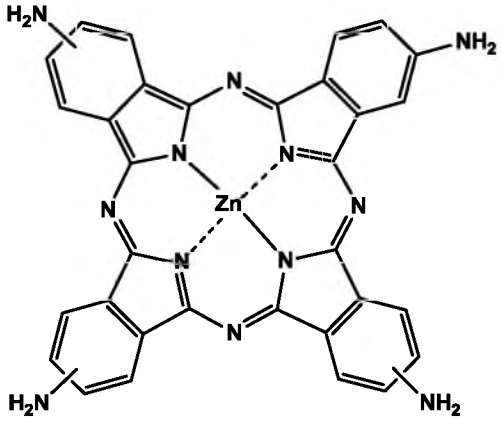 Zinc tetraamino phthalocyanine (ZnTAPc) [158]	Covalently linked to pristine GQDs Photophysics and Förster resonance energy transfer (FRET) studies	1
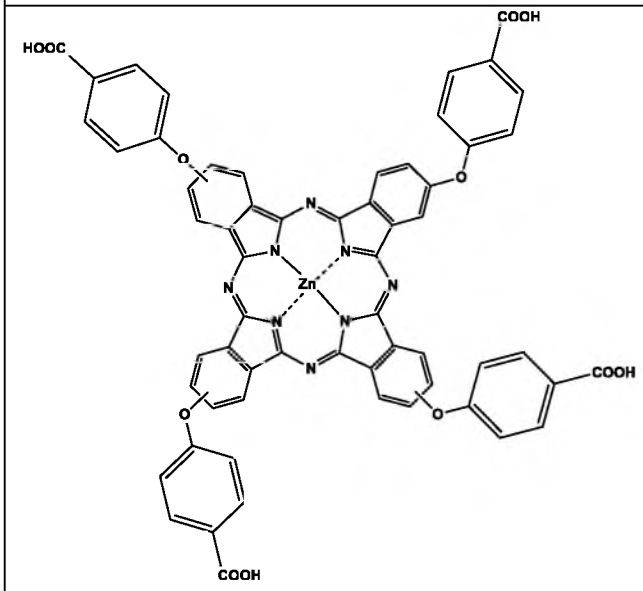 Zinc tetracarboxyphenoxy phthalocyanine (ZnTCPPc) [159]	Coordinated to pristine GQDs (π-π stacking) Photophysics and FRET	2

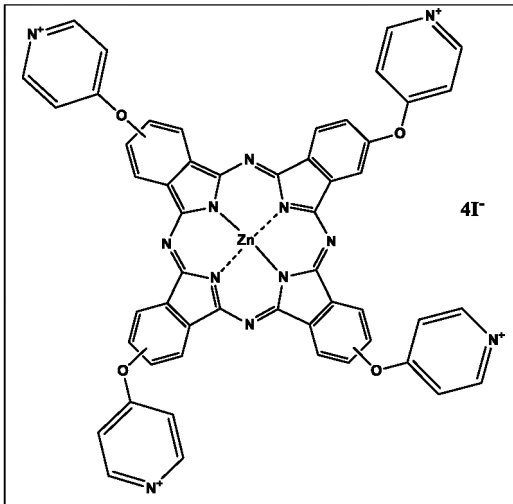 Zinc tetrapyridiloxy phthalocyanine [ZnTPPc (Q)] [160]	Coordinated to pristine GQDs (π-π stacking and electrostatic interaction) Photophysics and FRET	3
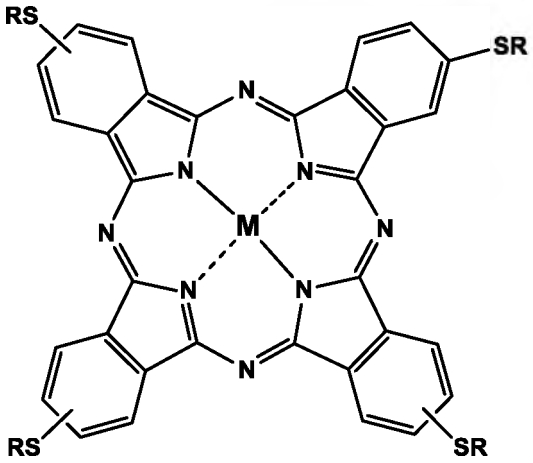 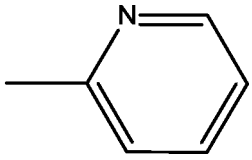 Zinc tetramercaptopyridine phthalocyanine (ZnTMPPc) [161]	Coordinated to pristine GQDs (π-π stacking) Photophysics and FRET Hg ion sensing	4

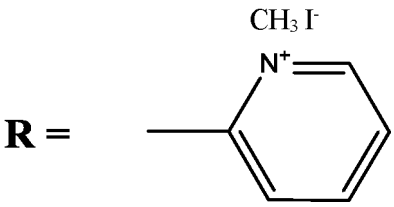 Quaternized zinc tetramercaptopyridine phthalocyanine [ZnTMPPc(Q)] [161] Quaternized chloroaluminium tetramercaptopyridine phthalocyanine [ClAlTMPPc(Q)] [162, 163]	Coordinated to pristine GQDs (π-π stacking), PEI-GQDs and Au@Ag NPs Photophysics and FRET Hg ion sensing *Dual sensing of Hg ion and biothiols	5(Zn) 6(Al)
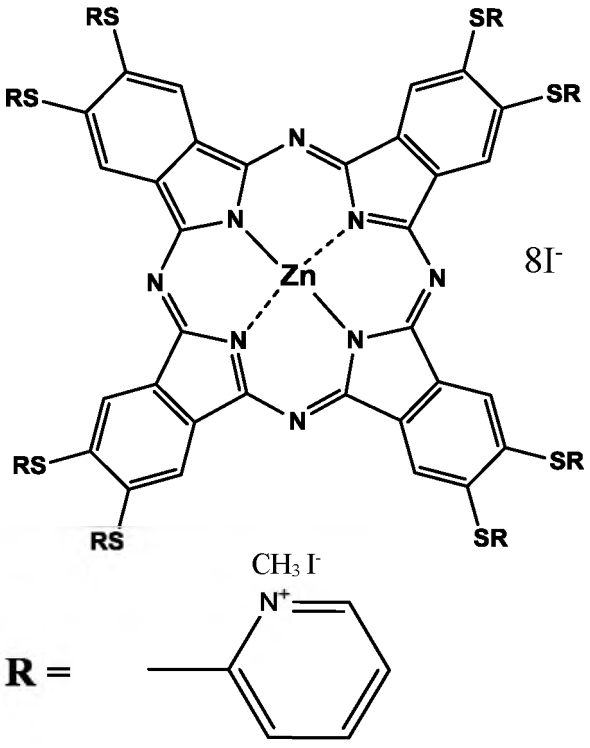 Quaternized zinc octamercaptopyridine phthalocyanine [ZnOMPPc (Q)] [161]	Coordinated to pristine GQDs (π-π stacking) Photophysics and FRET Hg ion sensing	7

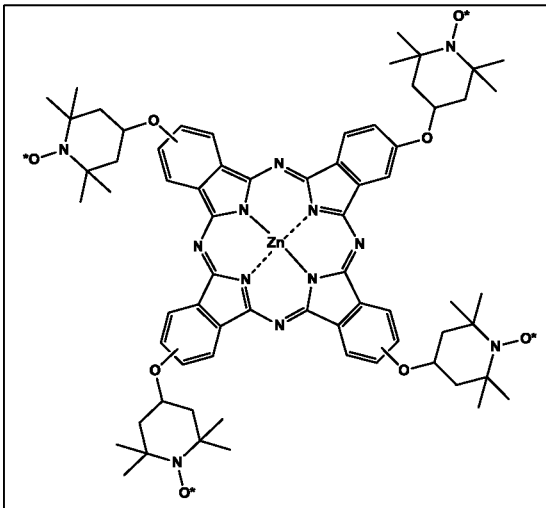 Zinc tetra (2,2,6,6-tetramethyl(piperidin-1-yl)oxyl) phthalocyanine (TEMPO-ZnPc) [164]	Coordinated to pristine GQDs/gCNQDs (π-π stacking) Photophysics and FRET Ascorbic acid sensing	8
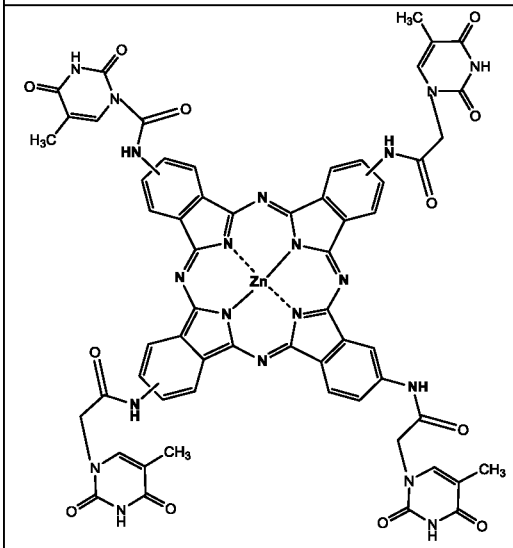 Zinc tetrathymino phthalocyanine (ZnTTPc) [139]	Coordinated to pristine GQDs and T-GQDs (π-π stacking) Photophysics and FRET Hg ion sensing	9

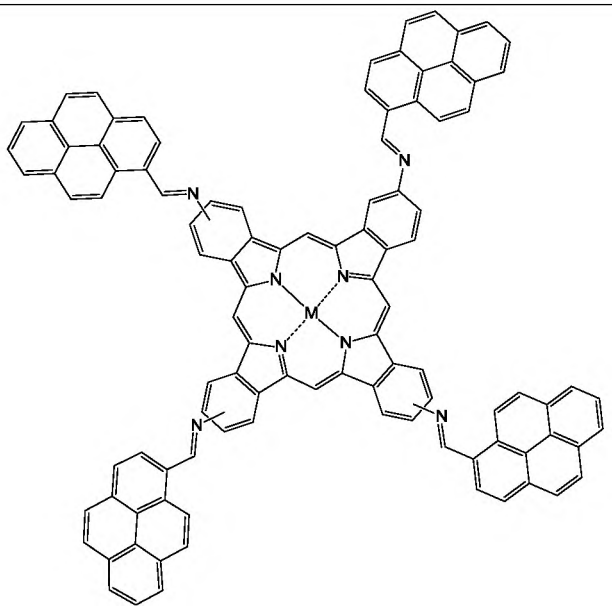 Tetrapyrenyl phthalocyanine (TPyPc) (ZnTPyPc) (CoTPyPc)	Coordinated to pristine GQDs (π-π stacking) Photophysics and FRET	10 (Zn) (New) 11 (Co) (New)
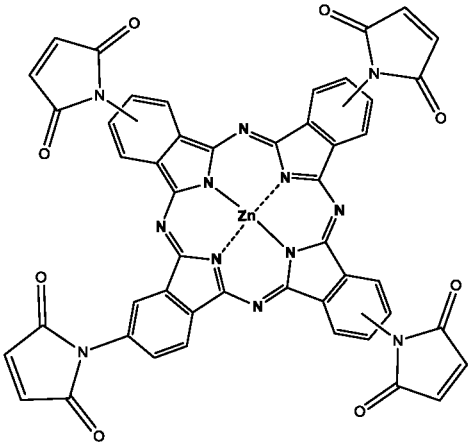 Zinc tetramaleimido phthalocyanine (ZnTMPc)	Coordinated to pristine GQDs (π-π stacking) Photophysics and FRET Biothiols sensing	12 (New)

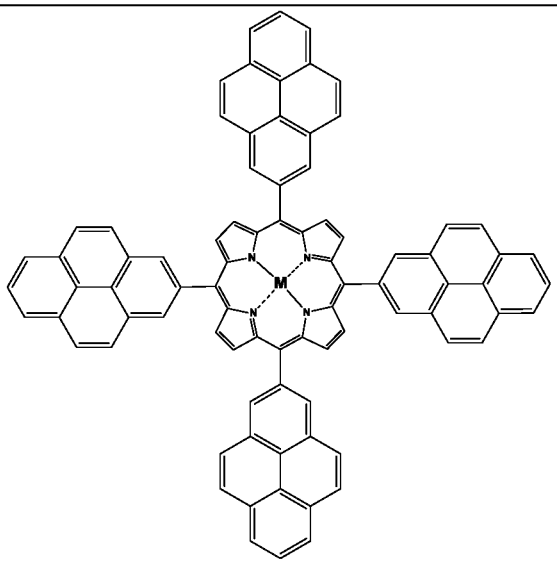 Tetrapyrenyl porphyrin (ZnTPyP) [165]	Coordinated to pristine GQDs (π-π stacking) Photophysics and FRET	**13 (Zn)**

FRET = Förster resonance energy transfer

However, their hybrids with GQDs or gCNQDs are reported for the first time in this thesis, as well as their application for the fluorescence detection of analytes.

Novel MPcs were synthesized and non-covalently coordinated to GQDs such as ZnTPyPc (**10**), CoTPyPc (**11**) and ZnTMPc (**12**). The photophysical properties of the MPcs **10**, **11** and **12** were elucidated upon non-covalent coordination to GQDs. ZnTMPc (**12**) hybrid with GQDs was further deployed for biothiols detection for the first time.

Also in this work, attempts were made to elucidate the mechanism of the electronic and/or energy transfer relationship between GQDs and MPcs upon interaction. To understand the observed changes in the optical behaviour of GQDs or MPcs in the presence of each other, Forster resonance energy transfer (FRET) phenomenon was studied. FRET is a study of the molecular dynamics of

the interaction between donor and acceptor molecules that are within certain distance from each other leading to radiative energy transfer due to excited state interactions [170].

In addition, another macrocycle with structure similar to MPcs such as tetra-substituted pyrene derivatized porphyrin (MP)-ZnTPyP (**13**) was coordinated to GQDs for the first time. An investigation of the photophysical properties of the MP were carried out upon coordination to GQDs so as to compare with those of the MPcs.

Pristine gCNQDs were separately coordinated to 4A-TEMPO molecules and TEMPO-derivatized MPc (complex **8**) for the first time to give gCNQDs-4A-TEMPO (linked) and **8**-gCNQDs via covalent and non-covalent routes, respectively. The TEMPO-functionalized gCNQDs were found to be highly sensitive and selective fluorescent probes for AA detection with limits of detection (LODs) in the nanomolar range. Hence, TEMPO functionality introduced into the gCNQDs afforded the derivation of selective and sensitive probes for AA detection.

1.3.5. Studies done using MPcs-GQDs conjugates

(1) Complexes **1**, **2**, **3** (conjugates with GQDs) were compared for the different charges and the effect on the photophysics in the presence of GQDs.

(2) Complexes **4** and **5** (conjugates with GQDs) were compared to complex **7** for the effects of tetra versus octa substitution for Hg ion detection.

(3) Complexes **5** and **6** (conjugates with GQDs) were compared for the effect of central metal for Hg ion detection.

(4) Complexes **8**, **9** and **12** have specific affinity to interact with AA, Hg and biothiols, respectively. Complex **8** was then employed to compare the sensing performances of GQDs and gCNQDs.

(5) Complexes **10** and **11** were compared with **13** for the effects of macrocycles on the fluorescence behaviour of GQDs using MPcs and an MP (with the same ring substituent).

Sub-aim of thesis

It is important to note that the MPcs used in this work have never been coordinated to GQDs. In this work, MPcs with ring substituents which have specific affinities for the target analytes were utilized, so as to increase the interaction chances between the target analytes and MPcs within the hybrid conjugates with GQDs. Hence, this thesis reports for the first time, the fabrication and applications of MPcs coordinated to GQDs (via π-π stacking) as novel photoluminescent nanosensor probes for analyte detection. Also, an attempt was made for the first time to interact MPcs with other carbon-based QDs (gCNQDs) via π-π stacking to prepare supramolecular hybrids capable of analyte detection and their performances compared with that of GQDs.

1.4. Metallic nanoparticles

The most widely utilized and reported metallic nanoparticles (NPs) contain the noble metals NPs (Au and Ag NPs) [171, 172]. The excellent electronic properties of nanoparticles compared to bulk materials are attributed to increased ratio of surface area-to-volume of the nanostructures and have been found useful in many state-of-the-art technological applications such as in the development of electronic devices, in bioimaging and optical sensing [173-176].

1.4.1. Gold (Au) and Silver (Ag) nanoparticles (NPs)

Au and Ag nanoparticles are peculiarly different from other metallic nanoparticles due to the presence of intense surface plasmon bands caused by the interaction of the "free electrons" within the conduction band (Fig. 1.8) [177,178]. The surface plasmon of AuNPs and AgNPs exhibit interesting scattering and absorbance properties which make them ideal candidates for molecular labelling, surfaced-enhanced Raman spectroscopy (SERS) and as optical sensors [172]. Recent advances in nanosensor development have resulted in the interaction of these noble metallic NPs with fluorophores, resulting in fluorescence quenching. AuNPs and AgNPs have recently emerged as an important fluorescence switching moieties in energy transfer/quenching-based fluorescence sensors [179-181]. However, attention has been diverted towards the synthesis and application of bimetallic core-shell hybrid of Au@Ag NPs, due to the envisaged synergistic properties of the alloyed NPs, which are different from the individual NPs since their combination could evolve new surface characteristics [182-186].

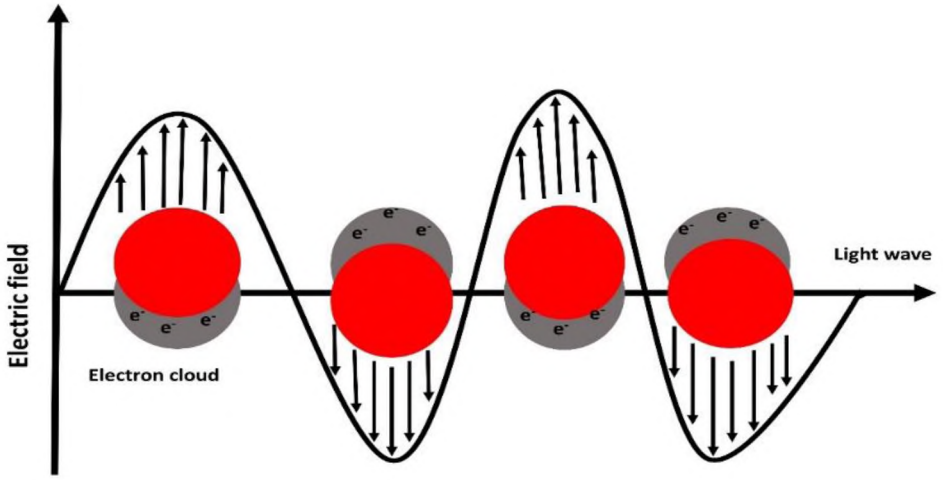

Fig. 1.8. Localized surface plasmon resonance of AuNPs' collective oscillations of free electrons due to applied electric field.

Hence, intensive studies have been focused on the variation of the compositions and ratios of the individual NPs in the core-shell architecture [182].

The quenching of the fluorescence of GQDs by individual Au NPs [179] or Ag NPs [53] has been explored for fluorescence nanosensor design in literature. However, the interaction of GQDs with bimetallic core-shell Au@Ag NPs is described for the first time in this thesis. Hence, the application of Au@Ag NPs as sensors component with MPcs and GQDs is a key part of this thesis. As such, a smart sensing platform was designed using the supramolecular hybrid of Au@Ag NPs when conjugated to GQDs in the presence of MPc (complex 5).

1.4.2. MPc-Au@Ag and GQDs supramolecular hybrid

Supramolecular hybrids containing multi-functional materials are interesting due to the unique functionality introduced by the constituent materials and the fine tuning of the nanoparticles hybrids for desired applications. Carbon nanomaterials have been surface and/or edge functionalized with various

biomolecules, metallic nanoparticles, and macrocycles (such as phthalocyanines and porphyrins) to derive functional hybrids [55, 187, 188]. As such, a multi-component hybrid was fabricated in this thesis for application as sensor materials using MPcs, Au@Ag NPs and polyethyleneimine-GQDs (PEI-GQDs). Complex **5** was conjugated to Au@Ag NPs via the interaction between the NPs and the bridging sulfur of complex **5**. The resulting conjugate (**5**-Au@Ag NPs) was coordinated to PEI-GQDs via electrostatic and/or π-π stacking interaction by taking advantage of the π-electronic structures of complex **5** and PEI-GQDs as well as the presence of negatively charged **5**-Au@Ag hybrid surface (due to the negatively charged surface of the Au@Ag NPs, which is larger in size compared to the MPc) and the positively charged PEI-GQDs (due to the presence of PEI, a polycationic polymer). The supramolecular hybrid was further deployed as dual sensor for the detection of Hg^{2+} and biothiols. This dual sensing system is reported for the first time in this thesis.

1.5. Target analytes in this work

The target analytes detected in this work are biomolecules with significant roles in human health and metabolism, and also the highly toxic metal ion of mercury. The importance and effects of the analytes are summarized below.

1.5.1. Ascorbic acid (AA)

Ascorbic acid is a well-known antioxidant and has been deployed for the prevention of free-radicals induced diseases and has attracted immense attention in modern cancer therapy and Parkinson's disease [189]. It was reported by Cameron and co-workers [190], that the administration of AA to cancer patients

improved their conditions for close to a year. Also, the intravenous use of ascorbate in pharmacological concentrations has been shown to lead to aptosis of cancer cells and exhibiting tremendous cure of several diseases **[191]**, hence rapid and sensitive assays for AA are needed. The conventional techniques for AA detection involve high-performance liquid chromatography (HPLC) and absorption spectrophotometry. However, the design of fluorescence nanoprobes for AA assays in clinical samples such as blood and urine is significantly desired since fluorescent-based probes are rapid, low cost, convenient and highly sensitive.

In this work, novel nanoprobes based on TEMPO-functionalized GQDs/gCNQDs and MPcs for the fluorescence detection of AA in nanomolar LODs are reported. TEMPO has a specific affinity to interact with AA. The TEMPO functionalized Pc employed in this work turned "OFF" the fluorescence of GQDs/gCNQDs which is restored in the presence of AA upon converting the TEMPO moiety to its hydroxylamines **[191, 192]**.

1.5.2. Biothiols (Cysteine, Homocysteine and Glutathione)

The design and synthesis of nanoensembles or nanoprobes capable of binding and sensing biological molecules (biomolecules) selectively has attracted much attention in recent years because of the fundamental roles played by biomolecules in human systems and in chemical and environmental processes **[193]**. Among the biologically important molecules, biothiols are of particular interest due to the fact that biothiols (such as L-cysteine (Cys), DL-homocysteine (Hcys) and glutathione (GSH)) (which are analytes of interest in this work) are

key players in cellular functions and take part in various redox reactions reversibly. Reactive oxygen species (ROS) are known to be constantly attacked by biothiols (GSH) in spontaneous and catalytic reactions **[194]**. Thus, biothiols play definitive roles in cell signalling proceedings as well as in human disease diagnosis and treatment. Biothiols monitoring and consequent observed imbalance could imply the presence of certain health related circumstances. As such, biothiols (especially GSH) metabolisms are usually implicated in diseases such as neurological disorders, cancer, human immune virus (HIV) and aging **[193]**.

Numerous sensor probes have been reported in literature for biothiols detection, several of these probes are based on fluorescence "turn OFF" process which is less reliable (since other factors may be responsible for the quenching of the fluorescence apart from the test analytes) as compared to the fluorescence "turn ON" process. Hence, novel and highly sensitive GQDs-based sensor probes for the fluorescence "turn ON" detection of biothiols reported in this thesis.

1.5.3. Mercury ion (Hg^{2+})

Mercury ion (Hg^{2+}) and its compounds are toxic and hazardous in the environment and food chains, and as such, a matter of global disturbance. Even low levels of mercury and its ion (Hg^{2+}) are toxic and have deleterious effects to human health and aquatic organisms **[195]**, since they can bioaccumulate/bio-magnify in human and animals' fatty tissues. Hence, novel probes with high sensitivity, rapidity and selectivity for its detection are desired. Fluorescence techniques ("turn ON") satisfy these criteria. The fluorescence nanoprobes

designed in this work demonstrated the detection of Hg^{2+} in the nanomolar range upon analysis of simulated spiked samples.

1.5.4. Summary of aims of this work

The aims and objectives of the work in this thesis are summarized below:

1. Synthesis and characterization of graphene quantum dots (GQDs) and graphitic carbon nitride quantum dots (gCNQDs) functionalized with target analyte specific groups.
2. Synthesis and spectroscopic characterization of novel analyte specific substituted MPc complexes.
3. Synthesis and spectroscopic characterization of Au@Ag core-shell NPs and their GQDs and MPc supramolecular hybrids: Applications as sensor probe for dual analytes detection.
4. Non-covalent (π-π stacking) and covalent coordination of MPc complexes to GQDs and characterization of the prepared conjugate hybrids.
5. Investigation of the fluorescence behaviour of novel GQDs and MPcs conjugate hybrids.
6. The application of MPcs-GQDs conjugates hybrids as fluorescence sensor probes for analyte detection.
7. Comparative Investigation of the fluorescence behaviours of MPs with respect to MPcs when coordinated to GQDs.
8. Elucidation of the interaction and detection mechanisms of functionalized GQDs and GQDs-MPc probes for analytes detection.

9. Comparison of the analytical performances of target analytes specific molecules functionalized GQDs with that of the MPcs-GQDs (with target analytes specific substituents) as fluorescence "turn ON" sensors probes.
10. Comparison of the sensing efficiency of GQDs with that of gCNQDs.
11. Deployment of the fabricated sensors probes for real samples analyses as a demonstration of their analytical applicability.

2. EXPERIMENTAL

This chapter contains detailed information on the materials, instrumentation and synthesis routes employed in this research study.

2.1. Materials

2.1.1. Nanomaterials preparation and conjugation

Graphene oxide (GO), citric acid, branched polyethyleneimine (PEI), chloroacetic acid, diaminomaleonitrile (DAMN), thymine, 4-amino-TEMPO (4A-TEMPO), ethylenediaminotetraacetic acid (EDTA), 4-maleimidobenzoic acid, dialysis membrane tubing (MWCO 1.5kDa), 1-ethyl-3-(3-dimethylaminopropyl)-carbodiimide (EDC), N-hydroxysuccinimide (NHS), $HAuCl_4.3H_2O$, 99.9%, silver nitrate and tyrosine were obtained from Sigma–Aldrich. Urea and sodium hydroxide pellets were obtained from Merck. Thiourea was obtained from Fluka.

2.1.2. MPcs and MP synthesis

Zinc acetate, 1-pyrene-carboxyaldehyde, anhydrous potassium carbonate, zinc bromide, hexamethyldisilazane (HMDS) and magnesium sulphate were obtained from Sigma-Aldrich. Sodium hydrogen carbonate and maleic anhydride were obtained from Merck. Column chromatography was performed using silica gel.

2.1.3. Analytes and other reagents

Ascorbic acid (AA), mercuric acetate, cysteine (Cys), homocysteine (Hcy), glutathione (GSH), 4-acetamido-2,2,6,6-tetramethylpiperidine-oxyl (4-AC-TEMPO), lysine, dopamine, folic acid, glucose, alanine, cystine, cytochrome c, human serum albumin (HSA), DL- tyrosine, quinine sulphate, sodium borohydride, zinc tetraphenyl porphyrin (ZnTPP) and zinc phthalocyanine (ZnPc) were purchased from Sigma-Aldrich. Histidine, lactic acid, bovine serum

albumin (BSA), lysozyme, trypsin, tryptophan, oxalic acid, potassium hydroxide were purchased from Fluka. Glycine (Gly) and salts of metal ions and anions such as Fe^{3+}, Ni^{2+}, Cu^{2+}, Fe^{2+}, Zn^{2+}, Ca^{2+}, Co^{2+}, Mg^{2+}, Pb^{2+}, Al^{3+}, Na^{+}, K^{+}, Ag^{+} and Cl^{-}, NO_3^{-}, CO_3^{2-}, SO_4^{2} were purchased from SAARCHEM (South Africa). Tris-HCl was obtained from Serva-Feinbiochemica GmbH (Germany).

2.1.4. Solvents

Benzene was obtained from Sigma-Aldrich. Dimethyl formamide (DMF), dichloromethane (DCM), dimethyl sulfoxide (DMSO), deuterated DMSO-d_6 and DMF-d_7 were obtained from Merck. Absolute ethanol, ethyl acetate, chloroform and methanol were obtained from SAARCHEM. All chemicals obtained were of analytical grade and employed directly without further purification. All aqueous solutions and mixtures were prepared using ultra-pure water obtained from a Mili-Q Water system (Millipore Corp. Bedford, MA, USA). Phosphate buffer solutions (PBS) employed in this work include: 10 mM, pH 4.0, 7.0, 7.4 and 10.0 or 50 mM pH 7.2, 8.0, 9.0 and 9.2. The PBS pH was adjusted using 0.1 M HCl or NaOH as the case maybe. Tris-HCl (10 mM, pH 7.4) was also employed in this work.

2.2. Instrumentation

Excitation and emission spectra were recorded on a Varian Eclipse spectrofluorimeter.

Ground state electronic absorption was performed on a Shimadzu UV-2550 spectrophotometer in the range of 300-800 nm.

X-ray photoelectron spectroscopy (XPS) analysis was done using an AXIS Ultra DLD (supplied by Kratos Analytical) using Al (monochromatic) anode equipped with a charge neutralizer, the following parameters were used: the emission was 10 mA, the anode (HT) was 15 kV and the operating pressure below 5 x 10^{-9} Torr. A hybrid lens was used and resolution to acquire scans was at 160 eV pass energy in slot mode. The centre used for the scans was at 520 eV (width of 1205 eV) with steps at 1 eV and dwell time at 100 ms. The high resolution scans were acquired using 80 eV pass energy in slot mode. Non-linear least squares curve fitting procedure was employed using Origin Pro version 8.0. The core level binding energies (BEs) were aligned with respect to the adventitious carbon C1s binding energy of 284.5 eV.

X-ray powder diffraction patterns were recorded on a Bruker D8 Discover equipped with a Lynx Eye detector, using Cu-K_α radiation (= 1.5405 A°, nickel filter). Data were collected in the range from 2θ = 10° to 100°, scanning at 1° min^{-1} with a filter time-constant of 2.5 s per step and a slit width of 6.0 mm. Samples were placed on a silicon wafer slide. The X-ray diffraction data were treated using the freely available Eva (evaluation curve fitting) software. Baseline correction was performed on each diffraction pattern by subtracting a spline fitted to the curved background.

A Bruker Vertex 70-Ram II Raman spectrometer (equipped with a 1064 nm Nd:YAG laser and liquid nitrogen cooled germanium detector) was used to collect Raman data. Samples for Raman spectroscopy were pressed into Raman aluminium sample disc using aluminium funnel set-up with a pestle and placed

into the internal sample compartment of the Raman spectrometer for measurement.

Atomic force microscopy (AFM) measurement in tapping mode was carried out with MFP-3D Origin supplied by Asylum research (Oxford instruments company, USA). Samples for AFM analysis were prepared by drop casting and room temperature drying of the analyte solution on freshly cleaved mica surface.

Transmission electron microscope (TEM) micrographs were obtained using a Zeiss Libra 120 TEM operating at 80kV.

^{1}H NMR spectra were obtained using a Bruker AVANCE 600 MHz NMR spectrometer in DMF-d_7 and DMSO-d_6.

Elemental analyses were done using a Vario-Elementar Microcube ELIII.

Mass spectra data were collected on a Bruker Auto-FLEX III Smart-beam TOF/TOF mass spectrometer using dithranol and α-cyano-4-hydroxycinnamic acid as MALDI matrices in the positive ion mode, using a 354 nm nitrogen laser.

Infra-red spectra were collected on a Bruker Alpha model FT-IR Spectrometer with platinum-ATR and Perkin Elmer Spectrum 100 FT-IR Spectrometer.

Fluorescence lifetimes were measured using a time correlated single photon counting setup (TCSPC) (FluoTime 300, Picoquant GmbH). The QDs excitation source was a diode laser LDH-P-C-485 with 10 MHz repetition rate, 88 ps pulse width. For MPcs, the excitation source was a diode laser LDH-P-670 driven by PDL 800-B, 670 nm, 20 MHz repetition rate, 44 ps pulse width, Picoquant GmbH. A monochromator with a spectral width of about 8 nm was used to

select the required emission wavelength band. The response function of the system, which was measured with a scattering LUDOX (HS-40) colloidal silica (DuPont), had a full width at half-maximum (FWHM) of 300 ps. All luminescence decay curves were measured at the maximum of the emission peak and lifetimes were obtained by deconvolution of the decay curves using the FluorFit Software program (PicoQuant GmbH, Germany). The support plane approach was used to estimate the errors of the decay times.

A Metrohm Swiss 827 pH meter was used for pH measurements.

Dynamic light scattering (DLS) and zeta potential experiments were done on a Malvern Zetasizer nanoseries, Nano-ZS90.

Electron paramagnetic resonance (EPR) measurements were carried out using a Bruker EMX Plus EPR spectrometer, model number: EMP-9.5/12B/P. EPR settings were 0.632 mW for the microwave power, frequency 9.714 GHz, resolution 2048 points, centre field 3460 G and 100 G sweep width.

Energy dispersive X-ray spectroscopy (EDX) analysis was carried out using an INCA PENTA FET coupled to VAGA TESCAN using a 20kV accelerating voltage.

Thermo-gravimetric analysis (TGA) was performed using a Perkin Elmer TGA 4000 analyzer. The analysis was carried out under nitrogen flow rate of 120 cm^{-3} min^{-1}. The weighed samples were heated from 50 to 800 ^{o}C at a rate of 10 ^{o}C min^{-1}.

Hydrothermal syntheses were carried out using a Berghof (Germany) High Pressure Laboratory Reactor *(highpreactor)* BR-300, V.3.0 equipped with PT-100

temperature and pressure sensors, BTC-300 Temperature regulator and manometer and PTFE lining.

2.3. Synthesis of GQDs

The hydrothermal process for the preparation of all the GQDs employed in this work was carried out using the high pressure reactor shown in Fig. 2.1.

2.3.1 Pristine GQDs

Pristine GQDs were synthesized following bottom-up methods discussed in the literature **[12, 196]**, but with some modifications as follows:

Citric acid (4.2 g, 1 mmol) and NaOH (2.4 g, 3 mmol) were dissolved in 100 mL water, and stirred to form a clear solution. Then the solution was transferred to a 400 mL Teflon-lined hydrothermal reactor. The sealed autoclave was heated to 160 ^{o}C for 4 h. The final product was collected by adding ethanol into the solution and centrifuged at 5000 rpm for 15 min. The solid was re-dispersed in water and dialyzed for two days using a dialysis membrane (MW 1.5 kDa) to remove excess salts.

Fig. 2.1. Berghof high pressure reactor employed for the hydrothermal syntheses of the GQDs/gCNQDs used in this work.

2.3.2 Nitrogen or Sulfur/Nitrogen doped GQDs (N-GQDs/SN-GQDs).

N-GQDs or SN-GQDs were prepared as described above for pristine GQDs, using urea (3.6 g, 3 mmol) or thiourea (4.6 g, 3 mmol), respectively, instead of NaOH.

2.3.3. GQDs/SN-GQDs-4A-TEMPO (Scheme 3.1)

The method employed in this work for the covalent conjugation of GQDs to 4A-TEMPO was adopted from the literature [197], but with some slight

modifications. Briefly: Chloroacetic acid (0.2 g) and NaOH (0.15 g) were added to the GQDs (representing both pristine GQDs and SN-GQDs) (2 mg/mL in aqueous solutions), followed by ultrasonication for 3 h to convert the surface –OH groups of the respective GQDs to $–OCH_2COO-$. After neutralization by 1 M HCl, the –COOH covered GQDs (carboxylated GQDs) were obtained. This was followed by the incubation of the carboxylated GQDs with 0.025 g (0.13 mmol) EDC and 0.013 g (0.11 mmol) NHS in PBS (50 mM, pH 9.0) at room temperature for 2 h (under gentle stirring) to activate the carboxylic groups. After this time, 4A-TEMPO (0.0172 g, 0.1 mmol) was added and the mixture further stirred for 24 h. The resulting conjugates (GQDs-4A-TEMPO and SNGQDs-4A-TEMPO) were precipitated out from solution to remove the unreacted 4A-TEMPO and other molecules (NHS and EDC) using a mixture of ethanol and water (1:1) followed by high speed centrifugation at 15000 rpm for 10 min. The products were dried *in vacuo* (at 60 °C) overnight to give GQDs and 4A-TEMPO covalent conjugates.

2.3.4. PEI-GQDs and M-GQDs (Scheme 3.2)

PEI-GQDs were synthesized by the top-down hydrothermal method adopted from the literature with some modifications **[64]**. Briefly: GO (0.5g) was oxidized in concentrated H_2SO_4 (10 mL) and HNO_3 (30 mL) for 4 h under ultrasonication. The mixture was then diluted with Millipore water (100 mL) and filtered through a 0.22 µm microporous membrane. The pH of the oxidized GO was adjusted to 8.0 using 10% NaOH. Aqueous solution of PEI (10 mL, 2.5 mg/mL) was added to the obtained GO suspension in a glass beaker, followed

by vigorous stirring for 2 h after which the mixture was transferred to a 400 mL Teflon-lined hydrothermal reactor and heated up to 160 ^{0}C for 8 h. The product was left to cool to room temperature and filtered using a 0.22 μm membrane. The collected solution was further dialyzed for 2 days using a dialysis membrane (MW 1.5 kDa) to remove unreacted PEI, acids and salts.

M-GQDs were then synthesized by the covalent amidation reaction between the -NH_2 groups of PEI-GQDs and the carboxylic groups (-COOH) of 4-maleimidobenzoic acid compound via EDC/NHS chemistry. In a typical experiment, the carboxylic groups of 4-maleimidobenzoic acid (0.1 g, 0.46 mmol) were activated with 0.025 g (0.13 mmol) of EDC and 0.013 g (0.11 mmol) of NHS in phosphate buffered solution (PBS) (10 mM, pH 7.0) under gentle stirring for 24 h. Then 5 mL PEI-GQDs (2 mg/mL) was added. The resulting mixture was left to further stir for another 24 h at room temperature. After this time, 10 mL of ethanol was added to the product and the resulting precipitate was collected by centrifugation and further purified by washing with a mixture of methanol and water (2:1) so as to dispel the unconjugated molecules and GQDs.

2.3.5. T-GQDs

Thymine-functionalized GQDs (T-GQDs) were synthesized according to similarly reported procedures in the literature with modifications **[69]**, via *in situ* one-step hydrothermal process using graphene oxide (GO) and thymine as follows: GO (0.5 g) was weighed into a beaker followed by the addition of thymine (1 g, 7.9 mmol). Ultra-pure Millipore water (100 mL) was added to the beaker and the

resulting mixture was vigorously stirred at room temperature for 2 h. The pH of the obtained suspension was adjusted to 8.0 using dilute solution of ammonia and further stirred for 30 min followed by ultrasonication for about 1 h. The suspension was then transferred to a 400 mL Teflon-lined hydrothermal reactor and heated up to 180 °C for 12 h. The product was left to cool to room temperature and filtered using a 0.22 µm membrane. The collected solution was boiled for 30 min on a hotplate to remove the ammonia and was further dialyzed for 2 days using a dialysis tubing membrane (MW 1.5 kDa).

2.4. Synthesis of gCNQDs

2.4.1. Pristine gCNQDs

Pristine graphitic carbon nitride quantum dots (gCNQDs) were prepared by employing the nitrogen rich diaminomaleonitrile (DAMN) following similarly described hydrothermal condensation process **[104, 106, 107]**. In a typical experiment, diaminomaleonitrile (1.0 g, 9.25 mmol), EDTA (0.5 g, 1.34 mmol) and NaOH (5mL, 1 M) were added to 100 mL of Millipore water and stirred for 1 h to ensure complete dispersion of the compounds. The resulting mixture was then transferred to a 400 mL capacity Teflon-lined hydrothermal reactor and was heated at 200 °C for 6 h. After cooling to room temperature, the resulting brown-green product was filtered through a 0.22 μm cellulose membrane, followed by the addition of ethanol. The product was centrifuged at 15000 rpm for 15 min. The collected solid was re-dispersed in Millipore water and further dialysed against ultrapure Millipore water for 2 days to get rid of excess starting

materials and by-products. The obtained solution was stored under refrigeration before further characterization and use.

2.4.2. TEMPO-functionalized gCNQDs (embedded)(Scheme 3.3A)

The synthesis of gCNQDs functionalized with TEMPO (gCNQDs-4A-TEMPO (embedded)) was achieved following a one-pot synthesis **[111, 112]**, as outline above for pristine gCNQDs, but in the presence of 4A-TEMPO (0.5 g, 2.92 mmol). All purification procedures are as described above in the case of pristine gCNQDs.

2.4.3. TEMPO-functionalized gCNQDs (linked) (Scheme 3.3B)

The covalent linkage of gCNQDs to 4A-TEMPO was achieved by utilizing the –COOH of gCNQDs and the NH_2 groups of 4A-TEMPO. Briefly: gCNQDs (5 mg) was firstly dissolved in 5 mL Millipore water and then incubated with 0.025 g (0.13 mmol) EDC and 0.013 g (0.11 mmol) NHS at room temperature for 24 h under gentle stirring to activate the carboxylic groups. After this time, 4A-TEMPO (0.0172 g, 0.1 mmol) was added and the mixture further stirred for 24 h. The resulting product was precipitated out from solution to remove the unreacted 4A-TEMPO and other molecules (NHS and EDC) using a mixture of ethanol and water (1:1), followed by high speed centrifugation at 15000 rpm for 10 min. The product was dried *in vacuo* (at 60 °C) overnight to give the covalently linked conjugate denoted as gCNQDs-4A-TEMPO (linked).

2.5. Synthesis of Au@Ag NPs

Au@Ag core-shell NPs were synthesized following procedures previously described with some modifications **[198]**. Briefly: Sodium borohydride ($NaBH_4$) (0.01 g) was added to a 100 mL $HAuCl_4$ (10^{-4} M) followed by vigorous stirring. This reaction was accompanied by the immediate appearance of deep ruby red colour characteristic of Au NPs. The solution was allowed to stand for a period of 24 h before further use. The Au NPs solution was heated in order to remove the excess sodium borohydride. The as-synthesized Au NPs were capped with tyrosine by the addition of 10 mL aqueous solution of 10^{-3} M tyrosine to 90 mL of the Au NPs solution. This solution was also allowed to stand for a period of 24 h before further use. For the synthesis of Au@Ag core-shell NPs, 90 mL tyrosine-capped Au NPs solution was mixed with 10 mL, 10^{-3} M $AgNO_3$ and 1 mL, 10^{-1} M KOH solution. Au@Ag NPs were formed following the reduction of Ag^+ ion by the tyrosine capping on the Au NPs (which is pH dependent and occurs in alkaline medium, hence the use of KOH). The solution was boiled until its colour changed to brownish yellow. The Au@Ag core-shell nanoparticles were thus obtained.

2.6. Synthesis of metallophthalocyanines (MPcs)

Some of the symmetrical MPcs employed in this work have been reported in the literature, hence detailed synthetic procedures are not provided. However, the synthetic methods for the novel MPcs of this thesis are presented.

2.6.1. Synthesis of zinc tetra-substituted pyrene phthalocyanine, ZnTPyPc (10), Scheme 3.4.

The synthesis of complex **10** (ZnTPyPc) was achieved by the Schiff base reaction between ZnTAPc (**1**) and 1-pyrene-1-carboxyaldehyde **[199]**. In a typical experiment, a mixture of zinc tetraamino phthalocyanine (ZnTAPc) (**1**) (0.10 g, 0.092 mmol) and 1-pyrene-1-carboxaldehyde (0.094 g, 0.41 mmol) was refluxed in 5 mL dry ethanol at 80-85 °C under an inert atmosphere for 2 days. The crude product was cooled to room temperature and washed successively with ethanol, methanol, acetone and n-hexane by centrifugation and was allowed to dry in air. The product was thereafter purified over a silica gel column using a DMF/ethanol mixture (2:1). Complex **10** yield: (40.5%). UV–vis (DMF): λ_{max}/nm (log ε): 724 (5.02), 648 (2.74), 396 (2.81), 360 (5.19). Anal. Calc. for $C_{100}H_{52}N_{12}Zn$, C, 80.77; H, 3.52; N, 11.30. Found: C, 81.14; H, 3.97; N, 10.82. MALDI-TOF-MS (m/z): 1486 amu; Found: 1490 $[M+4H]^+$. FT-IR [ATR (ν_{max}/cm^{-1})]: 3102 (C-H aromatic), 1737-1635 (C-N imine), 1455 (C=C aromatic). ^{1}H NMR (600 MHz, DMF-d_7): δ ppm: 11.10 (s, 4H, imine-H), 9.72 (d, *J* = 9.3 Hz, 4H, Py-H), 8.86 (d, *J* = 7.9 Hz, 4H, Pc-H), 8.72 – 8.67 (m, 8H, Pc-H), 8.56 (m, 9H, Py-H), 8.41 (dd, *J* = 24.6, 17.0 Hz, 6H, Py-H), 8.55 - 8.54(m, 8H, Py-H), 8.43 - 8.37(m, 9H, Py-H).

2.6.2. Synthesis of cobalt tetra-substituted pyrene phthalocyanine, CoTPyPc (11), Scheme 3.4.

The synthesis and purification process of complex **11** was as outlined for complex **10**, except that cobalt tetraamino phthalocyanine (**CoTAPc**) (0.05g, 0.98 mmol)

was employed. Complex **11** yield: (42%). UV–Vis (DMF): λmax/nm (log ε): 706 (4.25), 641 (2.47), 395 (3.47 360 (5.18). Anal. Calc'd for $C_{100}H_{52}N_{12}Co$, C, 81.13; H, 3.54; N, 11.35. Found: C, 81.90; H, 4.02; N, 11.05. MALDI-TOF-MS (m/z): 1482 amu; Found: 1486 $[M+4H]^+$. FT-IR [ATR (v_{max}/cm^{-1})]: 1728-1626 (C-N imine), 1446(C=C aromatic).

2.6.3. Synthesis of zinc tetramaleimido phthalocyanine, ZnTMPc (12), Scheme 3.5.

The synthesis of complex **12** was achieved by the conversion of the four (4) terminal amino groups ($-NH_2$) on complex **1** (ZnTAPc) to maleimide groups following procedures described previously for the transformation of amino moiety to a maleimide moiety **[200]**, with modifications. Briefly: ZnTAPc (**1**) (0.38 g, 0.6 mmol) in 10 mL of DMF was mixed with maleic anhydride (1 g, 10.12 mmol) in dry benzene (100 mL). The mixture was thoroughly stirred at room temperature for 1 h. The resulting mixture was further refluxed for 4 h, followed by the addition of $ZnBr_2$ (2.28 g, 9.7 mmol) in one portion, and the mixture was further refluxed for 1 h. After this time, the mixture was allowed to cool and a solution of hexamethyldisilazane (HMDS) (2.75 mL, 13.42 mmol) in dry benzene (30 mL) was added slowly over a period of 30 min. Next, the mixture was refluxed for an additional 4h. After cooling to room temperature, the resulting mixture was poured into 1.0 M HCl (140 mL). Liquid-liquid extraction procedure was employed to extract the aqueous phase using ethyl acetate. The organic phase recovered after the extraction was washed successively with 80 mL of saturated $NaHCO_3$ and 120 mL of brine and then

dried over anhydrous $MgSO_4$. The crude product was concentrated using a rotary evaporator and further purification was done over a silica gel column chromatography using a mixture of chloroform and ethyl acetate (10:3) as the eluent solvent system to yield compound **12**.

Complex **12** yield: (20.5%). UV–Vis (DMSO): λ_{max}/nm (log ε): 699 (5.02), 630 (2.74), 358 (3.81). Anal. Calc. for $C_{48}H_{20}N_{12}Zn$, C, 60.17; H, 2.10; N, 17.54. Found: C, 60.73; H, 2.52; N, 18.30. MALDI-TOF-MS (m/z): 956 amu; Found: 957 $[M+H]^+$. ^1H NMR (600 MHz, DMSO-d_6) δ 8.97 – 8.87 (m, 3H), 8.40 (s, 1H), 8.44 (d, 2H), 7.27 – 7.14 (m, 6H), 6.24-6.18 (m, J = 21.9, 12.8 Hz, 8H). FTIR [ATR (v_{max}/cm^{-1})]: 3239, 2916, 2856 (C–H aromatic), 1710 (maleimide carbonyls), 1647, 1488 (C=C aromatic), 1222, 1195 (Pc-Skeleton).

2.7. Conjugation of MPcs to nanomaterials (NPs)

2.7.1. Synthesis of MPc (5)-Au@Ag NPs hybrid, Scheme 3.6.

MPc complex **5** was conjugated to Au@Ag NPs via the interaction between the NPs and the bridging sulfur of complex **5**. Electrostatic interaction is also possible using the quaternized N groups of complex **5** **[201-203]**. Briefly: 2 mg of the as-synthesized Au@Ag NPs and 0.2 mg (0.052 mmol) of complex **5** were dissolved in 5 mL of water and allowed to stir for 96 h at ambient temperature for the adsorption of the MPc onto the surface of Au@Ag NPs. At the end of this time, the obtained product was centrifuged and washed with a mixture of ethanol and water in order to expel the non-conjugated molecules. The obtained product (**5**-Au@Ag) was further air dried and subsequently characterized.

2.7.2. General procedure for π-π conjugation, Scheme 3.7.

The coordination of MPcs to GQDs in this work was largely via the non-covalent (π-π stacking) method **[145]** due to the rich π-electron systems of GQDs and MPcs, respectively. The conjugates were prepared following methods previously described for the non-covalent (adsorption) of MPcs to carbon nanomaterials with some modifications **[145]**. Generally, GQDs (pristine or modified) (2 mg/mL) in 10-50 mM PBS (pH 7.2) were added to **2** (0.1 g, 0.089 mmol) in DMF/PBS (pH 7.2) (4:1); **3** (0.2 g, 0.026 mmol in DMF/PBS (pH 7.2) (4:1); **4-7** (0.2 mg, 0.0512 mmol); **8** (0.2 mg, 0.025 mmol) in DMSO; **9** (0.5 mg, 0.03 mmol); **10** (0.5 mg, 0.003 mmol), **11** (0.5 mg, 0.003 mmol) and **13** (0.5 mg, 0.004 mmol) in dry DMF and **12** (0.5mg, 0.0052 mmol) in DMSO. **5**-Au@Ag conjugate was coordinated to PEI-GQDs via π-π stacking as explained above using PEI-GQDs (5 mg) and **5**-Au@Ag (0.5 mg) in water.

The various mixtures were ultrasonicated for 2-4 h, followed by stirring for 2-4 days. Ethanol, hexane, toluene and water were employed to repeatedly wash the products. The solid products were dried under vacuum overnight at 60 °C or air dried in some cases.

2.7.3. Covalent conjugation, Scheme 3.8.

The method employed here was an adaptation of the procedures described previously with some slight modifications to achieve covalent linkage of complex **1** (ZnTAPc) to GQDs via amide coupling **[148, 197]**. Briefly: chloroacetic acid (0.2 g) and NaOH (0.15 g) were added to GQDs (20 mg) in 10 mL Millipore water, followed by ultrasonication for 3 h to convert the surface –

OH groups of the GQDs to $-OCH_2COO-$. After neutralization by 1 M HCl, the –COOH covered GQDs (carboxylated GQDs) were obtained. This was followed by the incubation of the carboxylated GQDs with EDC (0.025 g, 0.13 mmol) and NHS (0.013 g, 0.11 mmol) in phosphate buffer solution (PBS, 50 mM, pH 9.2) at room temperature for 2 h under gentle stirring to activate the carboxylic groups. After this time, complex **1** (ZnTAPc) (20 mg, 0.26 mmol) in dimethylformamide (DMF)/PBS solution of (4:1) was added and the mixture further stirred for 24 h. The resulting conjugate was precipitated out from solution using ethanol and was repeatedly washed with water followed by DMF to ensure that uncomplexed GQDs and complex **1** were eliminated.

2.8. Procedures for fluorescence detection

2.8.1 Ascorbic acid detection

GQDs-4A-TEMPO, SN-GQDS-4A-TEMPO, gCNQDs-4A-TEMPO (embedded) and gCNQDs-4A-TEMPO (linked) (2 mL, 0.5-2 mg/mL) in PBS (pH 8.0/9.0) were incubated with different concentrations of AA (0.1 to 50 nM) sequentially, followed by the measurement of the fluorescence emission of the resulting mixtures after allowing 1 min of equilibration time. For **8**-GQDs, **8**-SN-GQDs and **8**-gCNQDs, 0.5-1.0 mg of the conjugates were dissolved in DMSO (3 mL) and the above procedure was followed

AA detection in real samples was done using vitamin C tablets. The purchased vitamin C tablets were firstly crushed to give a fine powder and were dissolved in dry DMSO. The resulting solution was filtered through a 0.22 μm membrane. The filtrate was diluted accordingly. Ascorbate is easily oxidized during sample

preparation; hence great precaution was taken so as to achieve quantitative recovery. Human serum albumin and water samples were spiked with known concentrations of AA and further subjected to analysis by the prepared probes following the procedures described above.

2.8.2. Biothiols (Cys, Hcy or GSH) detection

M-GQDs (2 mL, 0.1 mg/mL in PBS, pH 7.0) and **12**-GQDs [0.5 mg/mL in DMSO/PBS (1:4)] were incubated with different concentrations of Cys, Hcy and GSH and fluorescence measurements were done as described above.

Maleimide moieties are known to react specifically with thiols (-SH) groups when the pH of the reaction mixture is between pH 6.5 and 7.5 **[204]**; GQDs PL properties are generally at optimum within pH 7.0-9.0, hence pH 7.0 was employed due to the desired sensing at physiological pH. Also in DMSO (and other polar solvents), thiol-maleimide Michael addition reaction has been described to occur very rapidly **[75]**. Hence, DMSO/PBS (1:4) (pH 7.0) solvent mixture was employed due to the solubility of complex **12** in DMSO and the desired aqueous environment for the test analytes (Cys, Hcy or GSH).

Biothiols detection using PEI-GQDs-Au@Ag blend and PEI-GQDs-**5**-Au@Ag hybrid was done by incubating 0.3 mL (0.5 mg/mL in PBS) of these conjugates with 0.1 mL (2.5 nM) Hg^{2+}, then different concentrations of the biothiols (Cys, Hcy and GSH) were sequentially added and measurements were taken as described above.

2.8.3. Mercury ion (Hg^{2+}) detection

Conjugates of 4-7-GQDs (0.1 mg), 9-GQDs and 9-T-GQDs (5 mg) were dissolved in 1:4 mixture of DMF/PBS (10 mM, pH 7.4 and 7.0) and ultrasonicated for 2 min, followed by the addition of different concentrations of Hg^{2+} aqueous solution. The fluorescence spectra were recorded afterwards.

Procedures for the sensing of Hg^{2+} using T-GQDs alone (2 mL, 0.5 mg/mL) were done strictly in PBS (10 mM, pH 7.0) due to the excellent solubility of T-GQDs in aqueous medium following procedure described above.

2.9. Fluorescence parameters

2.9.1. Fluorescence quantum yields (Φ_F)

Fluorescence quantum yields of the GQDs were determined by the comparative method as described previously [205] according to Eq. 2.1.

$$\Phi_{F(GQDs)} = \Phi_F^{Std} \frac{F\, A^{Std}\, n^2}{F^{Std} A\, (n^{Std})^2} \qquad (2.1)$$

where A and A^{Std} are the absorbances of the sample and the standard, respectively. F and F^{Std} are the areas under the fluorescence curves of the GQDs and the standard, respectively, n and n^{Std} are the refractive indices of the solvents used for the sample and standard. Quinine sulphate in 0.1 M H_2SO_4 (Φ_F = 0.52) [206] was used as standard for the GQDs. ZnPc in DMSO (Φ_F = 0.20, [130]) and ZnTPP in DMF (Φ_F = 0.033 [207]) were used as standards for the MPcs and MP, respectively.

The fluorescence quantum yields of GQDs after conjugation ($\Phi_{F(GQDs)}^{conjugate}$) to the respective MPcs, MP, 4A-TEMPO or maleimide were determined using Eq. **2.2** [208]:

$$\Phi_{F(GQDs)}^{conjugate} = \Phi_{F(GQDs)} \frac{F_{conjugate}}{F_{(GQDs)}} \qquad (2.2)$$

where $\Phi_{F(GQDs)}$ is the fluorescence quantum yield(s) of GQDs alone and was used as the standard, $F_{(GQDs)}$ is the fluorescence intensity of GQDs alone and $F_{\text{conjugate}}$ is the fluorescence intensities of GQDs upon coordination.

2.9.2. Förster resonance energy transfer (FRET)

PhotochemCAD software was used to compute some of the FRET parameters [209].

FRET efficiency (E*ff*) was determined experimentally from the fluorescence quantum yields of the donors (GQDs) in the absence ($\Phi_{F(GQDs)}$) and presence ($\Phi_{F(GQDs)}^{conjugate}$) of the acceptor (MPcs) using Eqn **2.3** [170]:

$$Eff = 1 - \frac{\Phi_{F(GQDs)}^{conjugate}}{\Phi_{F(GQDs)}} \qquad (2.3)$$

RESULTS AND DISCUSSIONS

Chapter 3: Synthesis and characterization of GQDs, gCNQDs, Au@Ag NPs, novel MPcs and their various conjugates (MPcs-GQDs, GQDs-4A-TEMPO, Maleimide-GQDs, GQDs-Au@Ag, MPc-Au@Ag, GQDs-MPc-Au@Ag, MPc-gCNQDs).

Chapter 4: AA detection using TEMPO-functionalized GQDs, gCNQDs and MPcs.

Chapter 5: Biothiols (Cys, Hcy and GSH) detection using maleimide-functionalized GQDs (M-GQDs), MPc conjugates and PEI-GQDs-Au@Ag hybrid.

Chapter 6: Mercury (II) ion detection using thymine-functionalized GQDs (T-GQDs), MPc and MPc-GQDs conjugates.

Chapter 7: Dual detection of mercury (II) ion biothiols and using PEI-GQDs-Au@Ag, PEI-GQDs-MPc-Au@Ag supramolecular hybrid.

PUBLICATIONS

Publications in peer-reviewed journals from the results presented in this thesis are listed below. These articles are not referenced in this thesis.

1. Ojodomo J. Achadu, Imran Uddin, Tebello Nyokong, Fluorescence behavior of nanoconjugates of graphene quantum dots and zinc phthalocyanines. *J. Photochem. Photobiol. A: Chem*, 317 (2016) 12-25.

2. Ojodomo J. Achadu, Tebello Nyokong, Interaction of graphene quantum dots with 4-acetamido-2,2,6,6-tetramethylpiperidine-oxyl free radicals: A spectroscopic and fluorimetric study, *J. Fluoresc*, 26(1) (2016), 283-295.

3. Ojodomo J. Achadu, Imran Uddin, Tebello Nyokong, The interaction between graphene quantum dots grafted with polyethyleneimine and Au@Ag nanoparticles: Application as a fluorescence "turn-on" nanoprobe, *J. Photochem. Photobiol. A: Chem*, 324 (2016) 96-105.

4. Ojodomo J. Achadu, Tebello Nyokong, Application of graphene quantum dots decorated with TEMPO-derivatized zinc phthalocyanine as novel nanoprobes: Probing the sensitive detection of ascorbic acid, *New J. Chem.*, 40 (2016) 8727-8736.

5. Ojodomo J. Achadu, Jonathan Britton, Tebello Nyokong, Graphene quantum dots functionalized with 4-amino-2, 2, 6, 6-tetramethylpiperidine-N-oxide as fluorescence "turn-ON" nanosensors, *J. Fluoresc*, 26(6) (2016) 2199-2212.

6. Ojodomo J. Achadu, Muthumuni Managa, Tebello Nyokong, Fluorescence behaviour of supramolecular hybrids containing graphene

quantum dots and pyrene-derivatized phthalocyanines and porphyrins, *J. Photochem. Photobiol. A*: *Chem*, 333 (2017) 174-185.

7. Ojodomo J. Achadu, Tebello Nyokong, Graphene quantum dots coordinated to mercaptopyridine-substituted phthalocyanines: Characterization and application as fluorescence "turn ON" nanoprobes, *Spectrochim. Acta Part A: Mol. Biomol. Spec.*, 174 (2017) 339-347. (***Front page feature article for the journal***).
8. Ojodomo J. Achadu, Tebello Nyokong, Application of graphene quantum dots functionalized with thymine and thymine-appended zinc phthalocyanine as novel photoluminescent nanoprobes, *New J. Chem*, **41** (2017) 1447-1458. ***(Invited as cover article for the journal issue)***.
9. Ojodomo J. Achadu, Tebello Nyokong, Graphene quantum dots decorated with maleimide and zinc tetramaleimido-phthalocyanine: Application in the design of "OFF-ON" fluorescence sensors for biothiols, *Talanta*, 166 (2017) 15-26.
10. Ojodomo J. Achadu, Tebello Nyokong, Graphene quantum dots anchored onto mercaptopyridine-substituted zinc phthalocyanine-Au@Ag nanoparticle hybrid: Application as dual-modal fluorescence nanosensors for Hg^{2+} and biothiols, *Dyes and Pigments*, 145 (2017) 189-201.
11. Ojodomo J. Achadu, Tebello Nyokong, *In situ* one-pot synthesis of graphitic carbon nitride quantum dots and its 2,2,6,6-tetramethyl(piperidin-1-yl)oxyl) derivatives as fluorescent nanosensors for ascorbic acid, *Analytica Chim. Acta*, 991 (2017) 113-126.

Extra publications not directly related to thesis

1. Owolabi. M. Bankole, Ojodomo J. Achadu, Tebello Nyokong, Nonlinear interactions of zinc phthalocyanine-graphene quantum dots nanocomposites: Investigation of effects of surface functionalization with heteroatoms, *J. Fluoresc*, 27 (2017) 755-766.
2. Sixolile Centane, Ojodomo J. Achadu, Tebello Nyokong, Effects of substituents on the electrocatalytic activity of cobalt phthalocyanines when conjugated to graphene quantum dots, *Electroanalysis*, 29 (2017) 2470-2482.
3. Refilwe Matshitse, Edward K. Sekhosana, Ojodomo J. Achadu, Tebello Nyokong, Characterization and physicochemical studies of the conjugates of graphene quantum dots with differently charged zinc phthalocyanines, *Journal of Coordination Chemistry*, 70 (2017) 3306-3324.
4. Gertrude Fomo, Ojodomo. J. Achadu, Tebello Nyokong, One-pot synthesis of graphene quantum dots-phthalocyanines supramolecular hybrid and the investigation of their photophysical properties, *Journal of Materials Science*, 53 (2018) 538-548.
5. Muthumuni Managa, Ojodomo J. Achadu, Tebello Nyokong, Photophysical studies of graphene quantum dots - pyrene-derivatized porphyrins conjugates when encapsulated within Pluronic F127 micelles, *Dyes and Pigments*, 148 (2018) 405-416.
6. Gugu. Kubheka, Ojodomo J. Achadu, J. Mack, T. Nyokong, Optical limiting properties of 3,5-diphenyldibenzo-aza BODIPY at 532 nm. *New J. Chem.*, 2017, 41, 12319-12325.

3. SYNTHESIS AND CHARACTERIZATION

This chapter outlines the synthesis and characterization of nanomaterials, MPcs and their conjugates employed in this thesis.

3.1. GQDs

3.1.1. Synthesis

The GQDs (doped, co-doped or *in situ* functionalized) employed in this work followed the hydrothermal bottom-up and/or top-down synthetic routes. Pristine GQDs synthesized in this work via the bottom-up route were achieved by the hydrothermal condensation and aromatization of citric acid (CA) in the presence of sodium hydroxide (NaOH) **[12]**. In order to surface functionalize the GQDs by introducing heteroatoms such an nitrogen (N) or sulfur/nitrogen (S/N), urea (N-source) or thiourea (S-N source) were added to citric acid and NaOH precursors, to obtain nitrogen-doped GQDs (N-GQDs) or sulfur-nitrogen co-doped GQDs (SN-GQDs), respectively **[12, 196]**. Pristine GQDs and SN-GQDs were further linked to 4A-TEMPO (as shown in Scheme 3.1), in order to compare with MPc complex **8** with TEMPO substituents for the detection of AA.

Top-down synthetic routes were also used to prepare GQDs functionalized with PEI or thymine (T) via *in situ* one-pot process. The main precursor used was graphene oxide (GO) which possesses multi-layered graphitic sheets **[210, 211]**. The large GO sheets were cut into smaller nanosheets of GQDs hydrothermally and/or via oxidative cutting to derive highly fluorescent graphene-like nanosheets of GQDs with sizes typically within the range of 2-10 nm. PEI-GQDs were linked to maleimide group to derive M-GQDs for biothiol sensing as shown in Scheme 3.2.

Table 3.1 shows GQDs and their conjugates employed in this thesis.

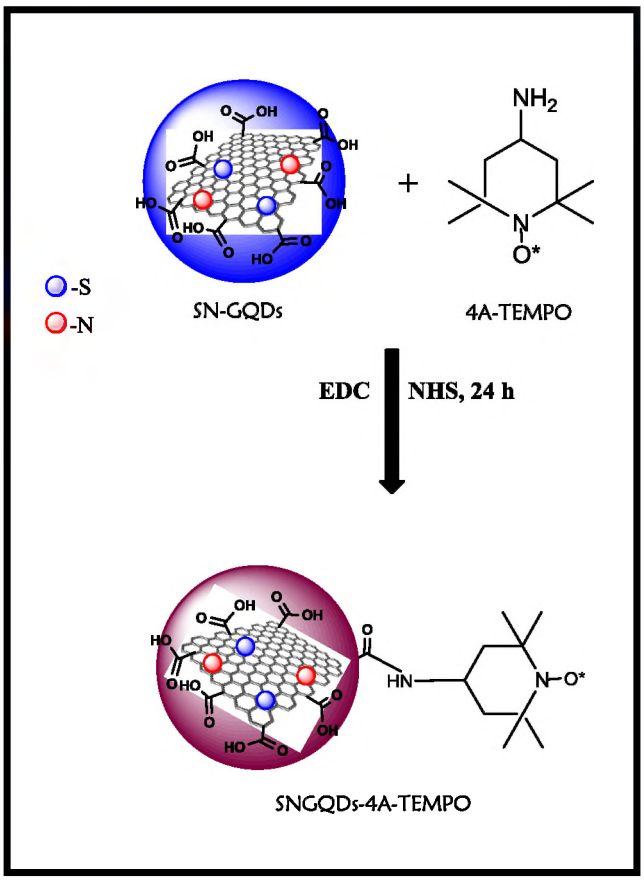

Scheme 3.1. Schematic representation of the covalent linking of SN-GQDs to 4A-TEMPO using EDC/NHS chemistry.

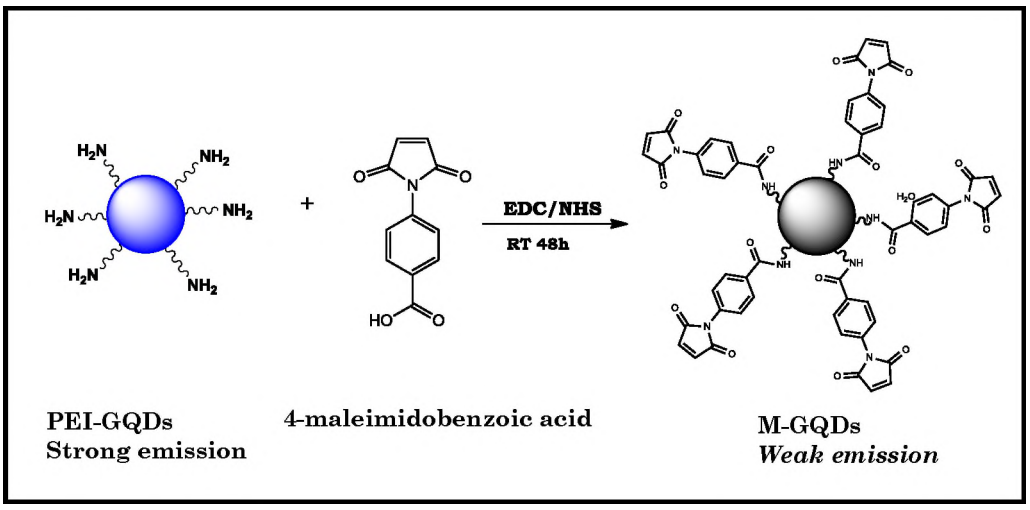

Scheme 3.2. Synthetic route for the preparation of maleimide-derivatized GQDs (M-GQDs) via EDC/NHS chemistry.

Table 3.1. The nanomaterials and MPcs conjugates employed in this thesis

QDs/NPs	Complex linked	Method of linking	Name of conjugate
Pristine GQDs	1 2-13 4A-TEMPO	Covalent Non-covalent (π-π) Covalent	1-GQDs 2-13-GQDs GQDs-4A-TEMPO
SN-GQDs	8 4A-TEMPO	Non-covalent (π-π) Covalent	8-GQDs SNGQDs-4A-TEMPO
T-GQDs	9	Non-covalent (π-π)	9-GQDs
PEI-GQDs	Maleimide Au@Ag NPs 5-Au@Ag	Covalent Electrostatic Non-covalent (π-π)/electrostatic	M-GQDs PEI-GQDs-Au@Ag PEI-GQDs-5-Au@Ag
gCNQDs	8 4A-TEMPO	Non-covalent (π-π) Covalent/*in situ*	8-gCNQDs gCNQDs-4A-TEMPO (linked/embedded)

Note: Complexes 1-3, 10, 11 and 13 were used for photophysical studies only (not used for analytes sensing).

3.1.2. XPS analysis

X-ray photoelectron spectroscopy (XPS) analysis was carried out to probe the structural compositions of the GQDs employed in this work. Full scan XPS spectrum of pristine GQDs shows C1s, Na auger and O1s signals at 284.5, 496 and 530 eV, respectively (Fig. 3.1A). Na auger peak at 496 eV is as a result of

NaOH employed in the synthesis of GQDs. The wide scan survey XPS spectra of N-GQDs and SN-GQDs (Fig. 3.1A) showed peaks at 530, 398 and 284.5 eV corresponding to O1s, N1s and C1s in both N-GQDs and SN-GQDs, respectively. However, the wide scan survey of SN-GQDs showed extra peaks at 227 and 162 eV attributed to S2s and S2p signals, respectively. The appearance of N1s (for N-GQDs) and N1s, S2s and S2p (for SN-GQDs) in the full survey spectra, relative to that of pristine GQDs confirms the successful doping of the GQDs.

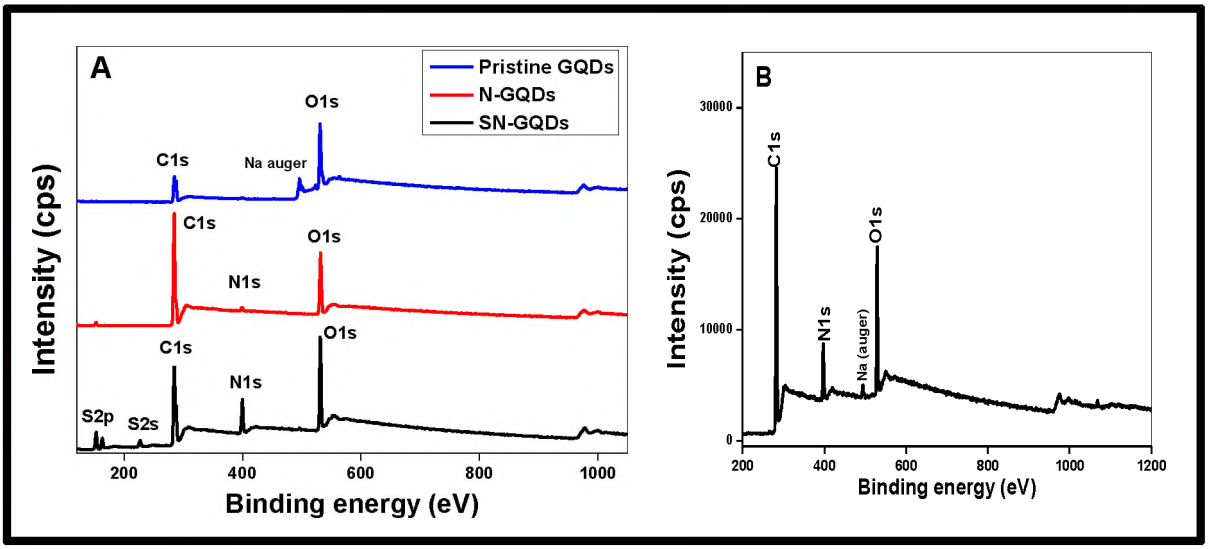

Fig. 3.1. Wide scans survey for (A) pristine GQDs, N-GQDs and SN-GQDs and (B) GQDs-4A-TEMPO (as an example).

The core level high-resolution C1s XPS spectrum of pristine GQDs could be deconvoluted into three chemically distinct carbon species centered at 284.5, 286.2, and 288.4 eV, which are attributed to sp^3 C (C-C, C-O), sp^2 C (C=C) and oxidized C (C=O), respectively, Fig. 3.2A.

The C1s signal of the SN-GQDs, Fig. 3.2B, which shows three distinct carbon species belonging to sp^3 carbons (C-S, C-N and C-O) in graphene at 284.9 eV.

sp^2 hybridized carbons (C=C) were found at 286.2 eV and oxidized carbons (C=O) were found at 288.6 eV.

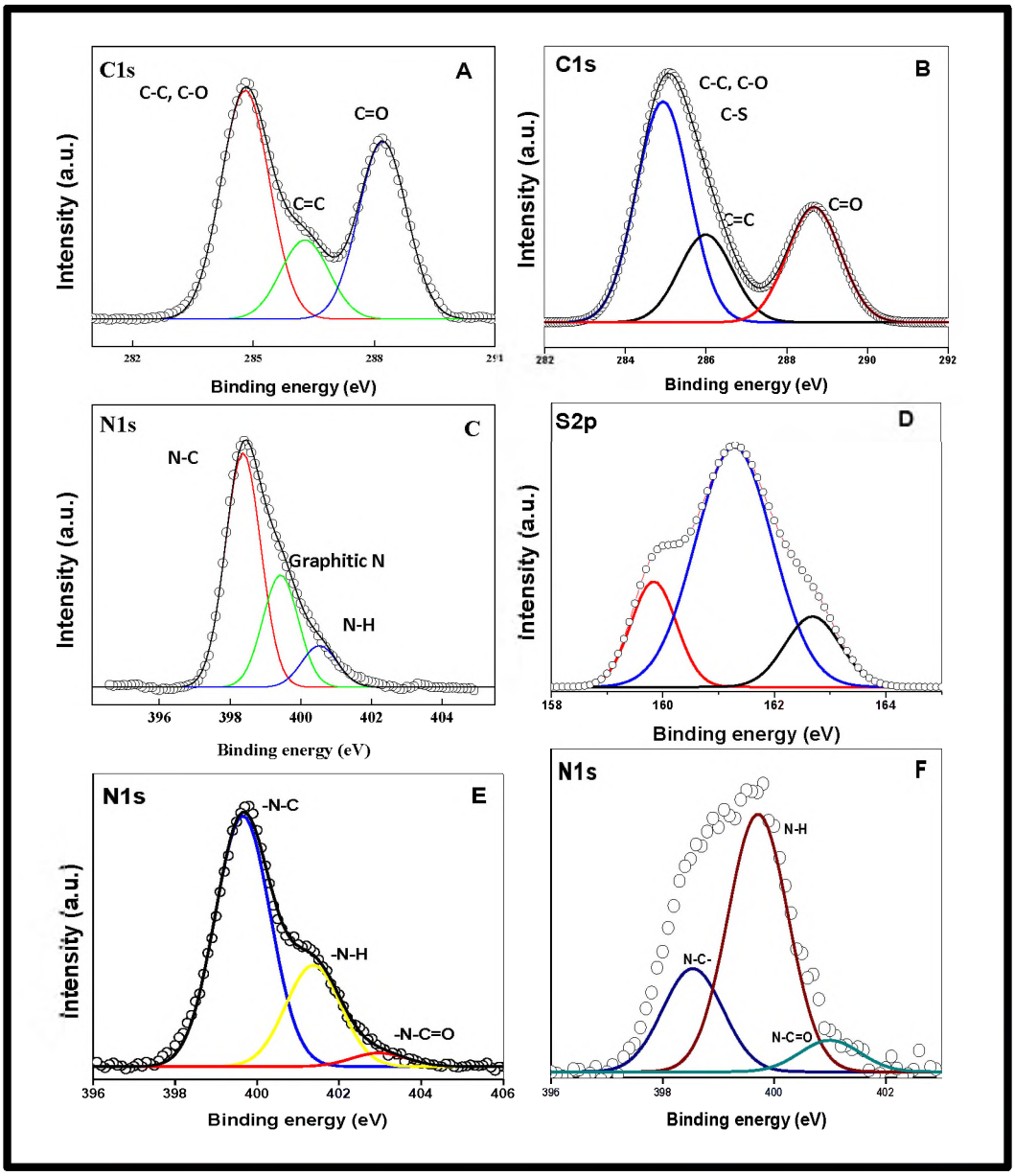

Fig. 3.2. High resolution XPS spectra for (A) C1s of pristine GQDs, (B) C1s of SN-GQDs, (C) N1s of SN-GQDs, (D) S2p of SN-GQDs, (E) N1s of GQDs-4A-TEMPO, and (F) N1s of M-GQDs.

High resolution of N1s of SN-GQDs (shown as a representative) displayed peaks attributed to -C-N-C- at 398.5 eV and graphitic N at 399.7 and N-H peak at 400.5 eV, respectively (Fig. 3.2C). The deconvoluted S2p peak from the full survey scan further shows three distinct peaks at 162.4, 163.8 and 165.1 eV, respectively (Fig. 3.2D). This implies the incorporation of S into the structure of GQDs and the doping was successful. The expected XPS results were obtained for GQDs, N-GQDs and SN-GQDs, PEI-GQDs and T-GQDs employed in this study, and conform closely to results that have been reported in the literature **[12, 64, 196]**.

The XPS wide scans for pristine GQDs-4A-TEMPO conjugate showed the appearance of N1s peak at 400 eV as shown in Fig. 3.1B, which was not present in the full survey spectrum obtained for pristine GQDs alone (Fig. 3.1A). The high-resolution spectrum of N1s signal for GQDs-4A-TEMPO reveals three peaks centred at 399.5, 401.4 and 403.02 eV respectively, which were attributed to N-C, N-H and amide N (-N-C=O) (Fig. 3.2E). The appearance of this peak at higher binding energy (403.02 eV) could be attributed to the successful formation of amide linkage(s) in the nanoconjugates of GQDs-4A-TEMPO **[197]**. The amide bond was observed at 401.2 eV for M-GQDs (Fig. 3.2F).

3.1.3. AFM analysis

Atomic force microscopy (AFM) was employed for the topographic evaluation of the GQDs. The results obtained for all GQDs (Fig. 3.3, pristine GQDs shown as a representative of others) showed average topographic height range of 0.75-1.5

nm. Thus, indicating that the GQDs are composed of single-few layers of graphitic sheets in accordance with literature [12, 64, 196, 212].

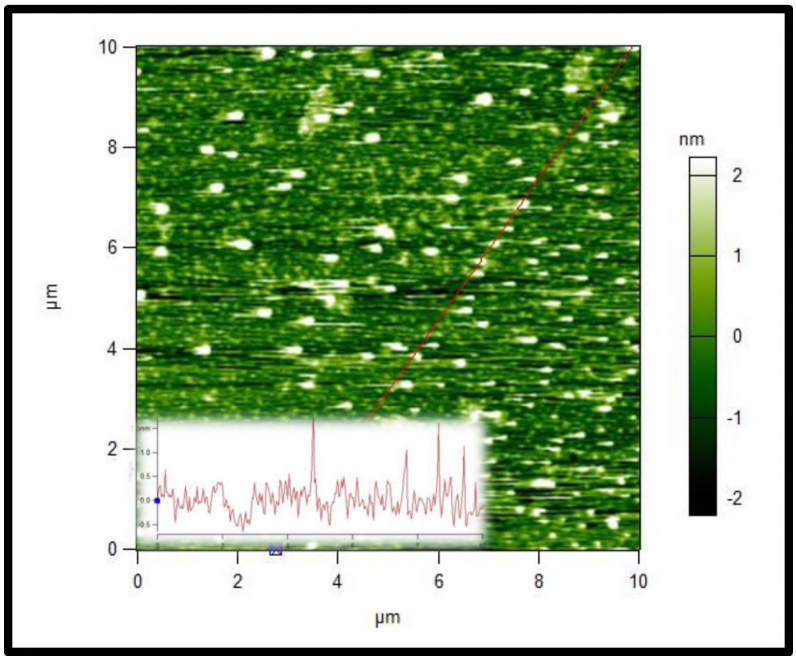

Fig. 3.3. AFM of pristine GQDs. Inset is the height profile.

3.1.4. X-ray diffractometry (XRD)

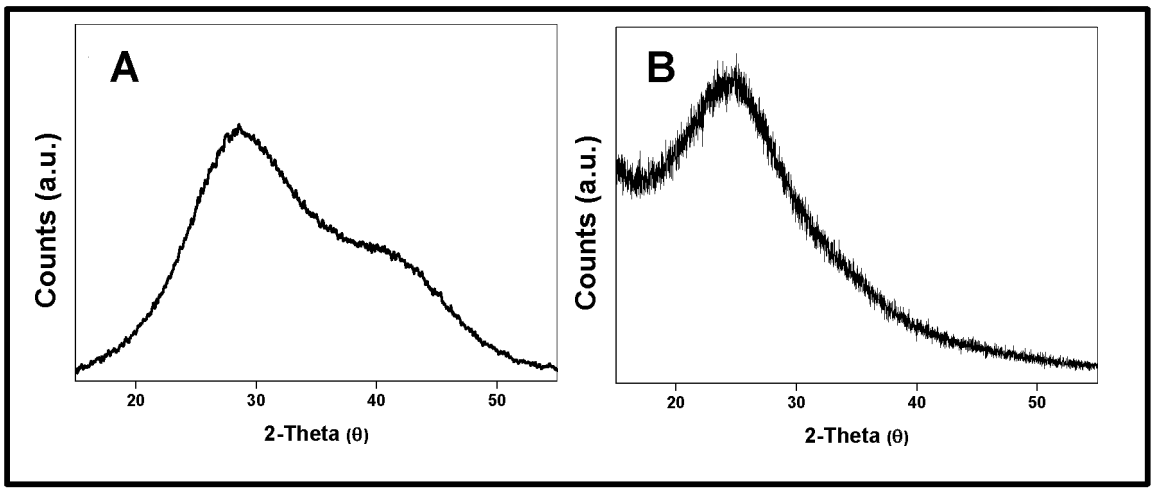

Fig. 3.4. Powder XRD spectra of as-synthesized (A) pristine GQDs and (B) PEI-GQDs.

XRD patterns of pristine GQDs and PEI-GQDs are shown as representatives in Fig. 3.4. The XRD patterns of the GQDs employed in this work generally showed broad peaks centered at 2Θ = 20-30^0 which is consistent with the (002) lattice spacing and Bragg's reflection of the carbon architecture of graphene based nanomaterials [1, 145, 201]. XRD profiles of the doped and functionalized GQDs exhibited similar 002 peaks, thus confirming similar graphitic structural base.

3.1.5. Raman spectroscopic analysis

GQDs are known to exhibit the diagnostic Raman bands termed the G and D bands resulting from the E_{2g} tangential vibrational mode of the sp^2 bonded carbons and the disordered A_{1g} breathing vibrational mode of the aromatic sp^2 carbon rings, respectively [213].

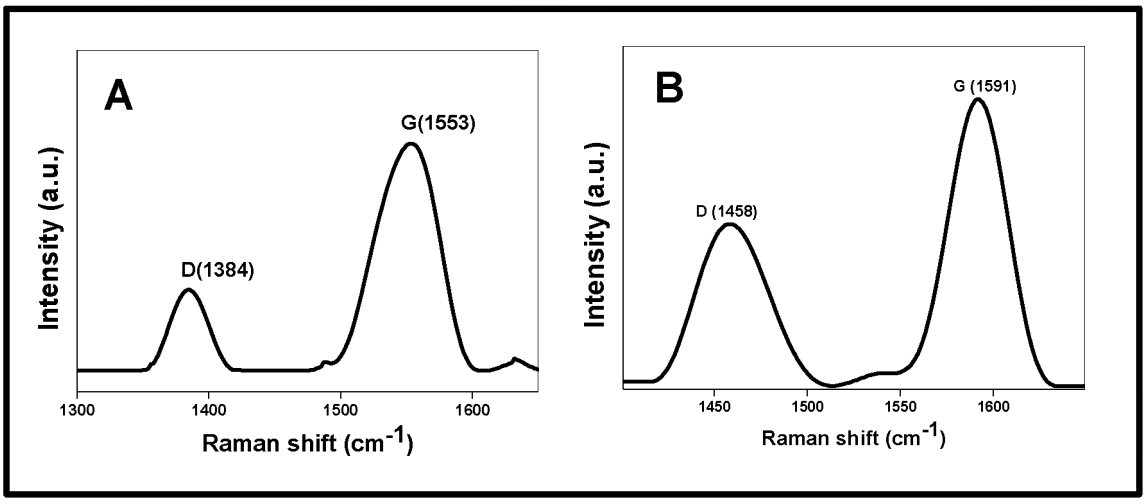

Fig. 3.5. Raman spectra for (A) pristine GQDs and (B) PEI-GQDs.

Raman spectra of pristine GQDs and PEI-GQDs (Fig. 3.5, as representative of the others) showed the distinctive features typical of sp^2 and sp^3 of C in carbon-based nanostructures. D and G bands were observed for pristine GQDs at 1384 and

1553 cm^{-1}, respectively. The values were 1458 and 1591 cm^{-1} for PEI-GQDs as shown in Fig 3.5B (which is similar to other functionalized GQDs) due to the surface defects on the graphitic frame of PEI-GQDs. In the case of SN-GQDs, the D and G bands were found at 1420 and 1579 cm^{-1}, respectively. The observed shifts are due to the cooperative defect (SN-doping) introduced into the lattice structure of the GQDs, thus stretching of the graphitic layers as previously reported in literature **[214]**. The ratio of the intensities (I_D/I_G) of D and G bands has been used to correlate the structural properties of carbon nanomaterials **[213]**. The I_D/I_G ratios for N-GQDs and SN-GQDs were found to be 0.62 and 0.77, respectively, as compared to 0.51 obtained for pristine GQDs. The I_D/I_G ratios for PEI-GQDs and M-GQDs were 0.85 and 0.95, respectively. These values are close to previously reported values for GQDs (N and SN-GQDs) and PEI-GQDs **[12, 64, 196]**.

Thus, the disordered sp^3 C increases with doping and defects increased with the grafting of the GQDs. Similar results were obtained for GQDs functionalized with other molecules via the one-step (*in situ*) synthetic approach.

3.1.6. TEM analysis

TEM analysis was performed in order to determine the sizes and shape of the GQDs. Fig. 3.6 (A-D) shows the TEM images of pristine GQDs, SN-GQDs, PEI-GQDs and T-GQDs, respectively, showing their monodispersed nature with an overall quasi-spherical morphology. PEI-GQDs had particle size ranging from 7-15 nm, with an average of 10.5 ± 1.5 nm, and hence the largest. The size ranges obtained for all GQDs using TEM are shown Table 3.2.

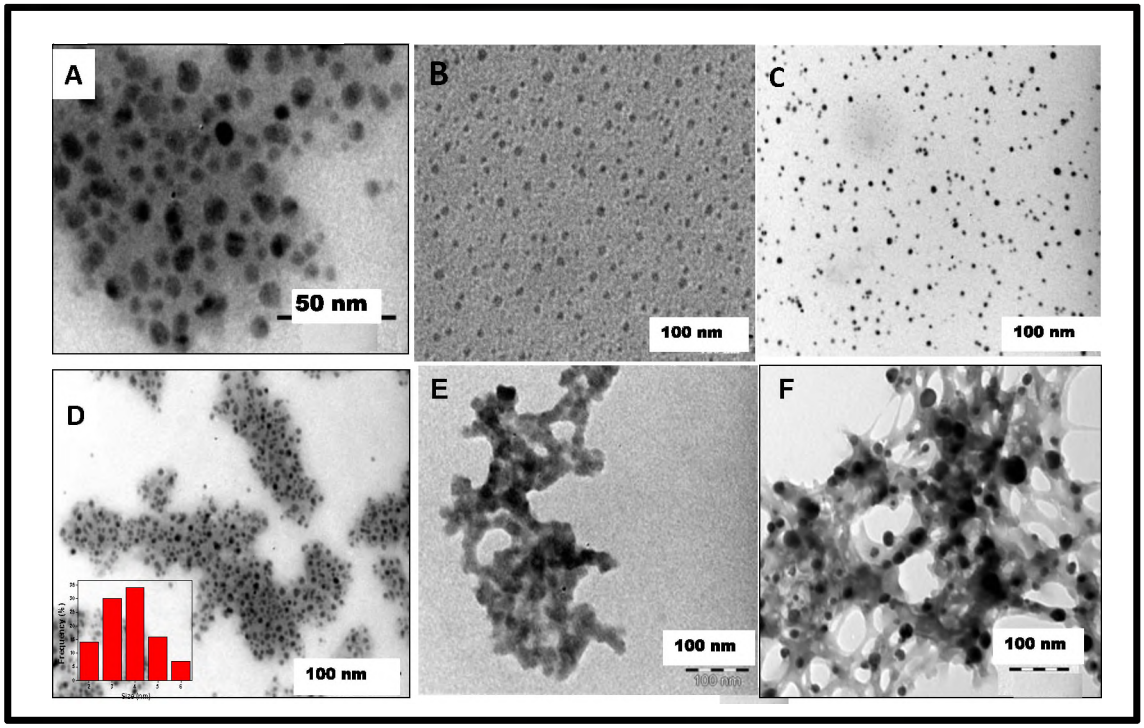

Fig. 3.6. TEM images for (A) pristine GQDs, (B) SN-GQDs, (C) PEI-GQDs, (D) T-GQDs, (E) 1-GQDs, and (F) 9-GQDs.

It is possible that both N–H and/or O–H groups are present in the spectra of the doped GQDs (N-GQDs and SN-GQDs, Fig. 3.7 A(a and b), PEI-GQDs and T-GQDs (the latter two due to the presence of amino groups in the surface capping agents). The bands at 1632 cm^{-1} are attributed to the vibrational band of C=O of carboxyl groups (COOH) for all the GQDs. The peak around 1203 cm^{-1} in SN-GQDs is attributed to the C=S. Weak C–S stretching was observed at 635 cm^{-1}, Fig. 3.7A (a). The appearance of the primary and secondary carbonamide bands at 1656 and 1557 cm^{-1} in GQDs-4A-TEMPO (which was not present in GQDs or 4A-TEMPO alone, Fig. 3.7B) further confirmed the formation of amide linkages between GQDs and 4A-TEMPO. SN-GQDs-4A-TEMPO and M-GQDs gave the expected peaks as well.

3.1.7. FT-IR and EDX analysis

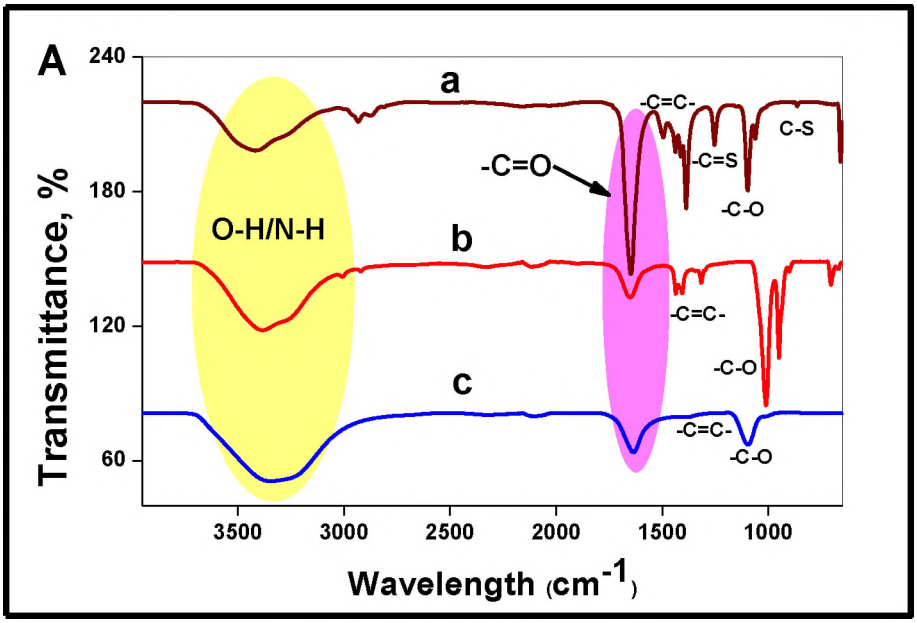

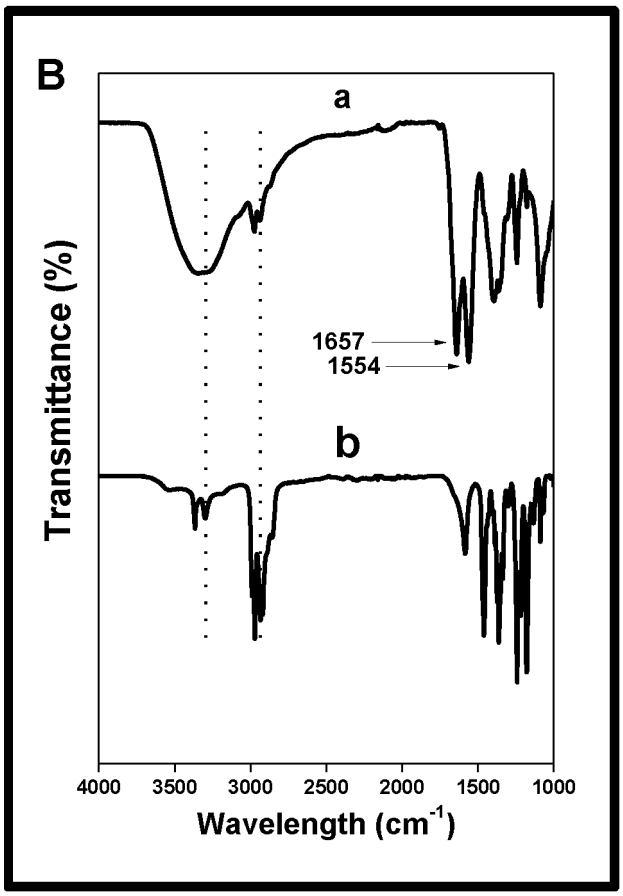

Fig. 3.7. FT-IR spectra of the as-synthesized (A) SN-GQDs (a), N-GQDs (b), pristine GQDs (c), and (B) GQDs-4A-TEMPO (a), and 4A-TEMPO (b).

FT-IR spectra of the GQDs revealed the presence of functional groups usually at the edges or intercalated within the graphitic framework of graphene-based nanomaterials **[5, 6]**. FT-IR analysis was used to characterize and ascertain the surface functional groups present on pristine GQDs, N-GQDs and SN-GQDs. The FT-IR spectra (Fig. 3.7) showed broad absorption bands in all the synthesized GQDs within 3000-3500 cm^{-1} which is characteristic absorption band for O–H stretching vibration. Thus, it can be inferred that hydroxyl groups are present on the surface of the GQDs.

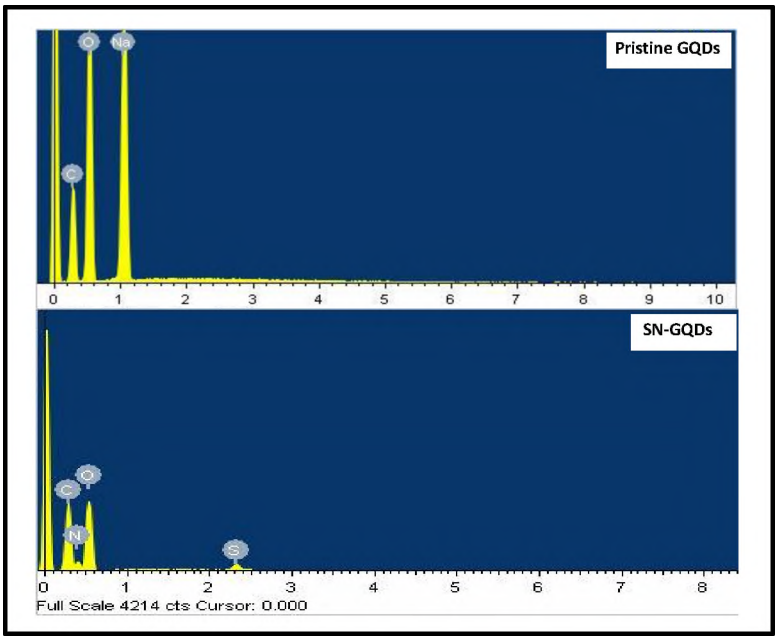

Fig. 3.8. EDX of pristine GQDs, N-GQDs and SN-GQDs showing their various elemental compositions.

Energy dispersive X-ray spectroscopy (EDX) was employed to qualitatively ascertain the elemental compositions of the GQDs. As shown in Fig. 3.8, the results obtained were consistent with the expected elemental compositions of pristine GQDs and SN-GQDs (as an example), respectively, which further confirm

the successful doping of the GQDs. The Na is from the NaOH (as a base) employed in the synthesis and the S, N is from doping using thiourea.

3.1.8. DLS and zeta potential experiments

All the as-synthesized GQDs were further analyzed for average size determination using dynamic light scattering (DLS) technique. The average sizes of all GQDs acquired from DLS experiments are shown in Table 3.2, and are in agreement with size distribution range acquired from TEM analysis.

Typical sizes of GQDs (< 10 nm) were successfully obtained for pristine GQDs and their S, N doped analogues (Fig. 3.9, pristine GQDs and T-GQDs shown as representatives of others). Expectedly, the size of PEI-GQDs increased from ~10 nm (average size) to 19.5 nm to form M-GQDs (Table 3.2). This result for PEI-GQDs is in close.

Zeta potential measurements were further used to determine the surface charge(s) and as such the stability of the GQDs in aqueous media. As shown in Table 3.2, pristine GQDs exhibited the highest negative zeta potential values, which are ascribed to the fact that their surface is covered by oxygen rich groups such as OH and COOH [1, 5, 6, 215]. However, the doped and functionalized GQDs derivatives (N-GQDs, SN-GQDs, PEI-GQDs and T-GQDs) exhibited lower zeta potential values which are due to the surface modification leading to the removal of the OH/COOH groups or replacement of these groups on the GQDs surfaces. For PEI-GQDs, the zeta potential value was found to be positive, hence showing that PEI-GQDs surface is positively charged. This is due to the surface grafting with PEI, a polycationic amino compound. The results obtained from

DLS and zeta potential experiments are in accordance with results well-documented in the literature for GQDs and modified GQDs.

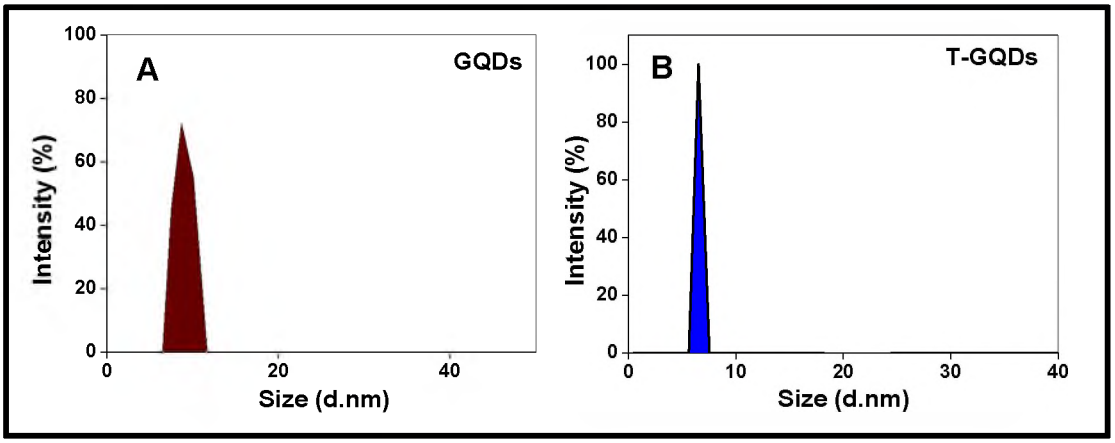

Fig. 3.9. DLS graphs showing the sizes of (A) pristine GQDs and (B) T-GQDs as example of others.

3.1.9. TGA analysis

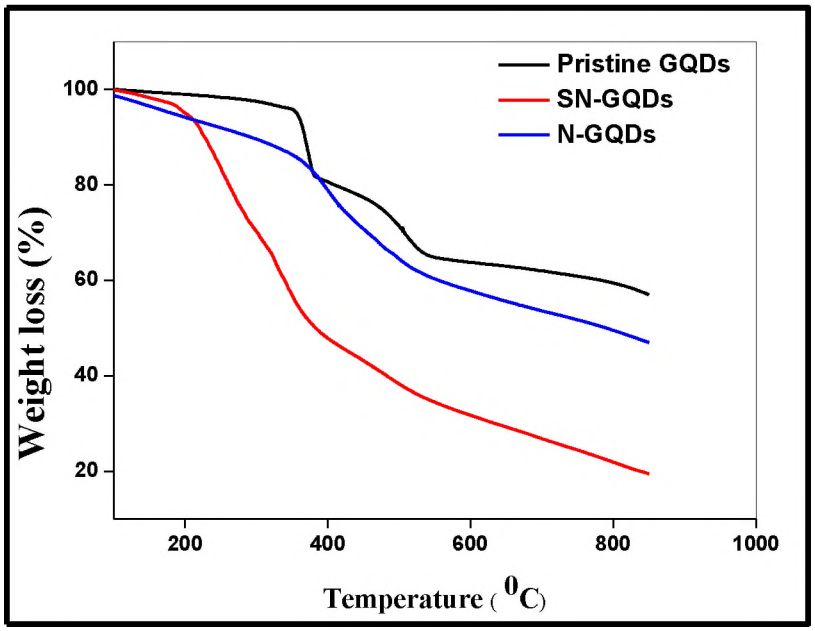

Fig. 3.10. TGA profiles of GQDs and its doped analogues.

Thermal properties of the as synthesized GQDs were investigated. The data obtained showed that the GQDs displayed high degree of stability. Generally, from the TGA curves (Fig. 3.10), pristine GQDs showed the most stability with increasing temperature. N-GQDs were found to be more stable than SN-GQDs.

This can be ascribed to the N and SN dopants elimination processes taking place as the temperature increases. Weight loss processes at higher temperatures (~400-800 ^{0}C) could be due to the relaxation of the graphene structure **[216]**.

3.1.10. Electronic absorption and emission properties of GQDs

The UV-Vis absorptions of the as-synthesized GQDs were observed at 335 nm (for pristine GQDs), 340 nm for N-GQDs and 337, 550 and 598 nm (for SN-GQDs), all dispersed in aqueous medium (Fig. 3.11A, Table 3.2). The red shifting of the peak near 340 nm for N-GQDs and SN-GQDs when compared to pristine GQDs can be ascribed to changes in chemical functionalities and defects as reported previously **[217]**. The appearance of absorption peaks at 550 and 598 nm in SN-GQDs absorption spectrum is due to the doping with sulfur which has been reported previously **[196]**.

The UV-Vis absorption of GQDs-4A-TEMPO shown in Fig. 3.11C (a) indicates that the nitroxide free radical absorption typically around 430 nm (Fig. 3.11C (c)) was clearly retained in the spectra of the nanoconjugates and could mean the preservation of the nitroxide (-N-O*) moiety, since the amino groups (-NH_2) were used for the covalent linkage. Pristine GQDs absorption peak [Fig. 3.11 C (b)] was observed in GQDs-4A-TEMPO conjugate, Fig. 3.11 C (a). The spectral changes further confirmed the formation of new nanocomplexes.

Table 3.2. List of GQDs employed in this work and their optical parameters. Average sizes and size ranges of the GQDs obtained from DLS and TEM are shown. Solvent PBS.

GQDs (nm)[a]	Abs (nm)	Ems (nm)	Φ_F (±0.01)	τ(ns) (±0.1)	Size range (nm)[a]	Size (nm)[b], DLS	Zeta (ζ)
Pristine GQDs	335	445	0.21	5.7	2-7	3.5	-88.5
NGQDs	340	450	0.77	7.8	2-7	4.7	-55.2
SN-GQDs	337, 550, 598	470	0.81	11.6	2-7	5.0	-68.9
PEI-GQDs	360	448	0.88	9.8	7-15	10.5	+13.5
T-GQDs	344	443	0.42	6.5	2-6	6.5	-15.6
GQDs-4A-TEMPO	334, 430	445	0.09	3.5	-	12.5	-24.5
SN-GQDs-4A-TEMPO	430, 596	470	0.05	9.6	-	14.1	-26.0
M-GQDs	344	452	0.06	1.50	-	19.5	+5.2

[a]Size range from TEM. [b]Mean size from DLS.

GQDs may exhibit excitation-wavelength dependent (where there is a change in emission wavelength with changes in excitation wavelength) or independent (where there is no change in emission wavelength, but there may be a change in intensity) photoluminescence (PL) **[1, 5, 6, 7, 64, 196, 217]**. As stated in the introduction, the excitation-dependent PL is proposed to reflect the differences in nanoparticle sizes and also the presence of a mixture of different emissive sites. Conversely, excitation-wavelength independent emissions in GQDs have been ascribed to the uniformity in both size and surface states. In this work, pristine GQDs, N-GQDs and SN-GQDs were excited at wavelengths from 300-400 nm

with emission maxima as shown in Fig. 3.11B and Table 3.2. Since emission wavelength did not change with change in excitation wavelength, the GQDs are excitation wavelength-independent, suggesting a common emissive site. However, excitation-wavelength dependent PL emission was observed as shown in (Fig. 3.12A) for T-GQDs. The aqueous solution of T-GQDs showed a light-yellow, transparent and clear solution under daylight, and exhibited bright blue fluorescence under 365 nm UV light (Fig. 3.12B inset). Maximum emission intensity was recorded for all GQDs and further studies were carried out at the respective PL emission maxima.

The shifts in PL emission wavelength for the doped and functionalized GQDs may be due to lowering of band gaps as a result of increased electron density to the sp^2 clusters of graphene layers **[218]**. SN-GQDs recorded a maximum emission at 470 nm (Fig. 3.11B, Table 3.2) at an excitation wavelength of 390 nm. When compared to the PL emission maximum of pristine GQDs, a red shift of ca 25 nm is observed which can be attributed to an increase in the electron density introduced via the hetero atomic SN-doping **[196, 218]**.

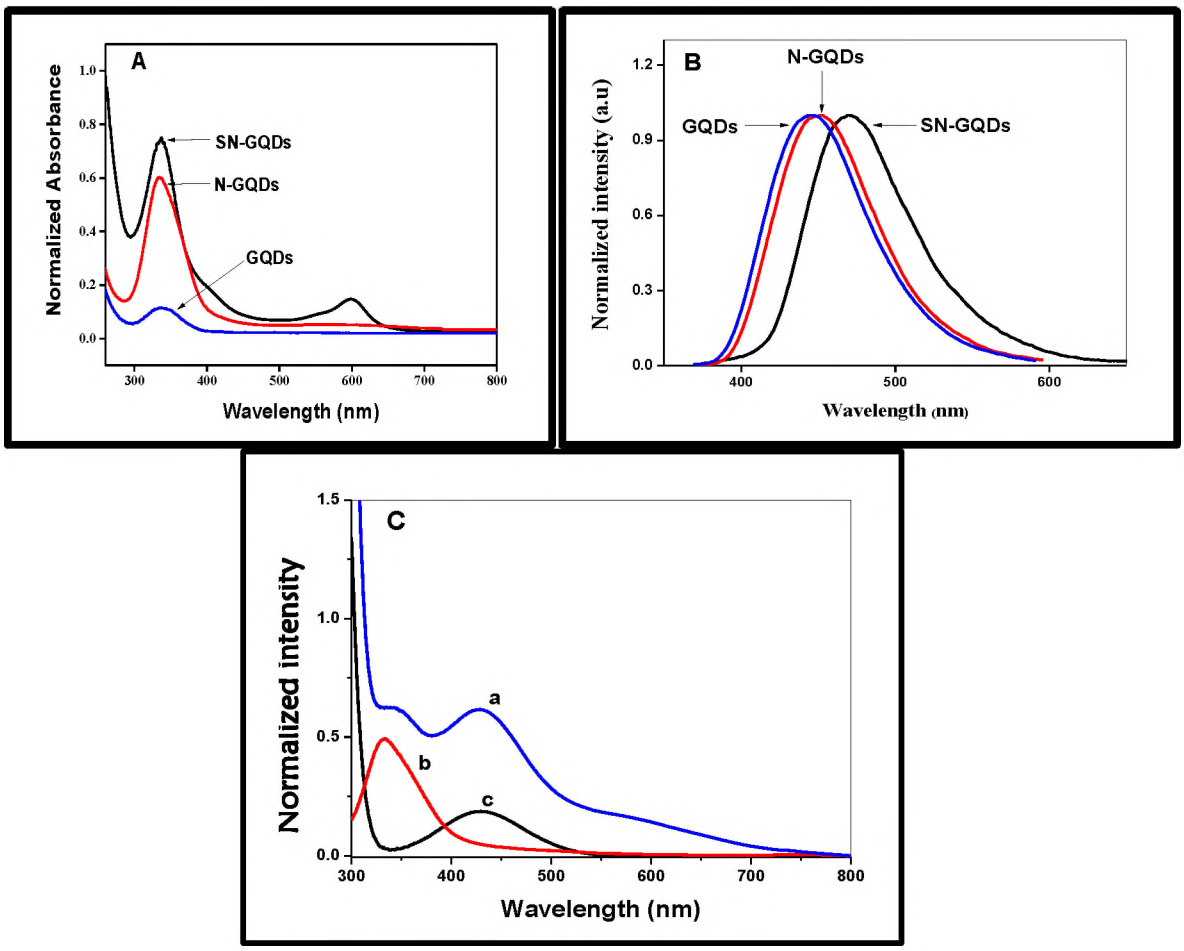

Fig. 3.11. (A) UV-Vis spectra for (A) pristine GQDs, N-GQDs and SN-GQDs, (B) Fluorescence emission spectra of pristine GQDs, N-GQDs and SN-GQDs, excitation wavelengths = 350 , 360 or 390 nm for GQDs, N-GQDs or SN-GQDs, respectively. (C) GQDs-4A-TEMPO (a), pristine GQDs (b), and 4A-TEMPO (c) in PBS.

The PL emission of GQDs can be attributed to the radiative recombination of electrons and holes trapped on the surface of GQDs [5, 6, 219, 220], which may be enhanced by surface functionalization compared to pristine GQDs. It can be observed that the doped analogues have higher Φ_F values (The S, N co-doped GQDs have the highest Φ_F value of 0.81, Table 3.2).

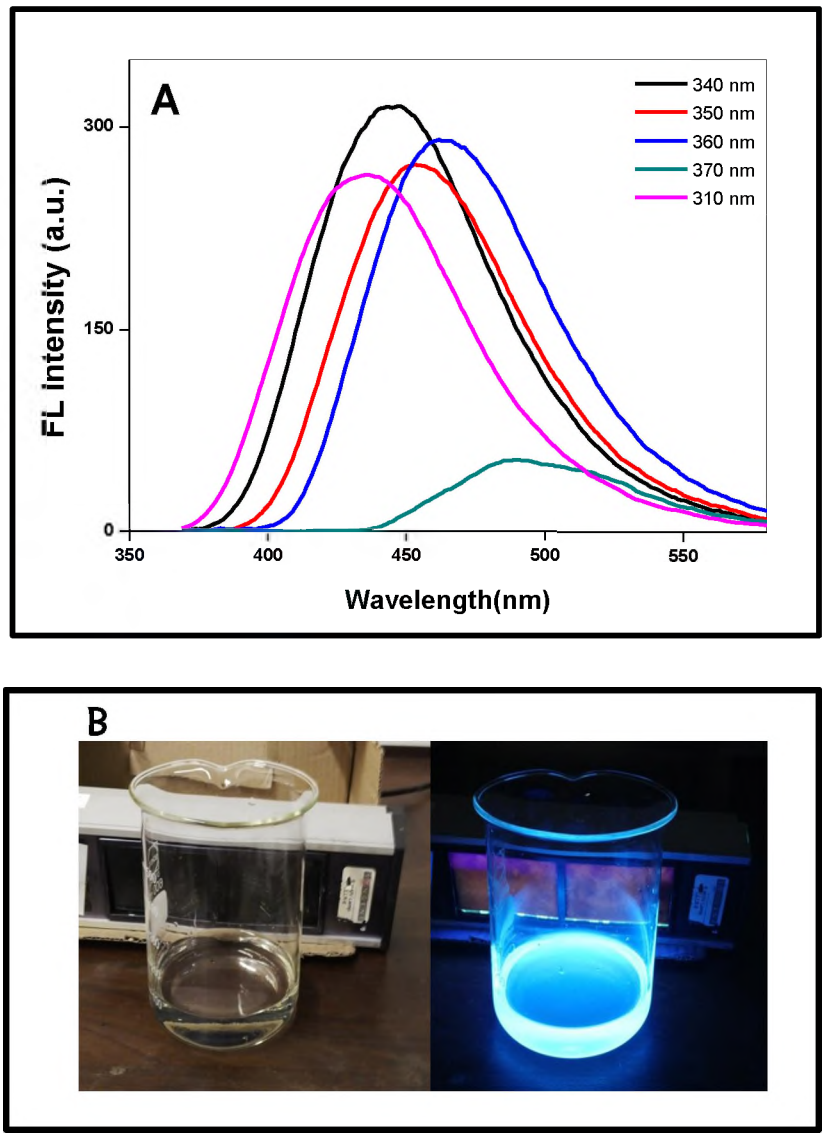

Fig. 3.12. (A) Fluorescence emission at different excitation wavelengths for T-GQDs and (B) T-GQDs viewed under UV 365nm and visible light in PBS (10 mM pH 7.0).

This further relates to the fact that functionalized GQDs could have defect states which are different from pristine GQDs [196]. The Φ_F of PEI-GQDs and T-GQDs were also higher compared to pristine GQDs due to effects of surface grafting/functionalization.

Conversely, the fluorescence of the GQDs was quenched in the presence of TEMPO (quencher molecule) which was further reflected in decreased Φ_F of GQDs upon conjugation to 4A-TEMPO (Table 3.2).

3.1.11. Fluorescence lifetime (τ_F) measurements

In this work, the fluorescence lifetimes (τ_F) were found to be single exponential decay (Fig. 3.13) for all the GQDs synthesized as shown in Table 3.2. The fluorescence lifetimes for the doped N-GQDs and SN-GQDs are longer than that for pristine GQDs corresponding to larger fluorescence quantum yields as discussed above.

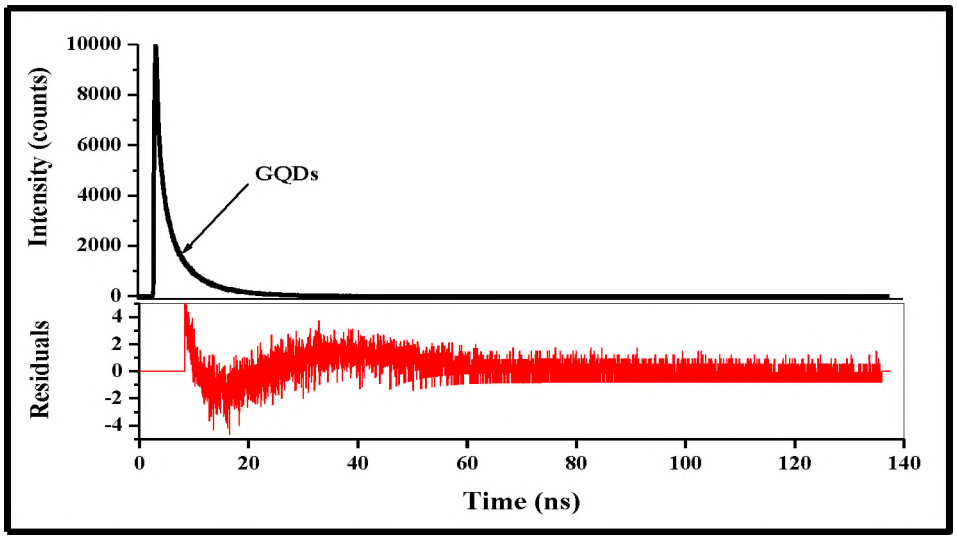

Fig. 3.13. Fluorescence decay curve of pristine GQDs shown as an example.

The fluorescence lifetime of PEI-GQDs was found to be 9.8 ns, which is an increase compared to that recorded for the pristine GQDs (without PEI) (5.7 ns), Table 3.2. T-GQDs also have single exponential lifetime decay value of 6.5 ns

which is longer as compared to the pristine GQDs, hence showing that the functionalization of GQDs affects their fluorescence properties.

Similar to Φ_F above for GQDs and 4A-TEMPO conjugates, τ_F was decreased as well, resulting from the rapid depopulation of the excited states of GQDs due to the energy and/or electron accepting behaviour of 4A-TEMPO.

3.2. gCNQDs

3.2.1. Synthesis

In this work, a novel precursor of diaminomaleonitrile (DAMN) was employed for the synthesis of gCNQDs (due to its higher nitrogen content than most precursors reported in the literature). Novel gCNQDs functionalized with TEMPO [gCNQDs-4A-TEMPO (embedded)] were also prepared via a low temperature *in situ* one-pot process as shown in Scheme 3.3A. The optical emission of the as-synthesized gCNQDs-4A-TEMPO (embedded) was excitation wavelength–dependent as similarly exhibited by the pristine gCNQDs. Table 3.3 summarizes the optical parameters of the as-synthesized gCNQDs and its TEMPO derivatives. Post-synthesis covalent conjugation of gCNQDs to 4A-TEMPO (as opposed to *in situ* functionalization) was performed by linking the amino group (NH_2) of 4A-TEMPO to gCNQDs (the conjugate is represented as gCNQDs-4A-TEMPO (linked) (Scheme 3.3B).

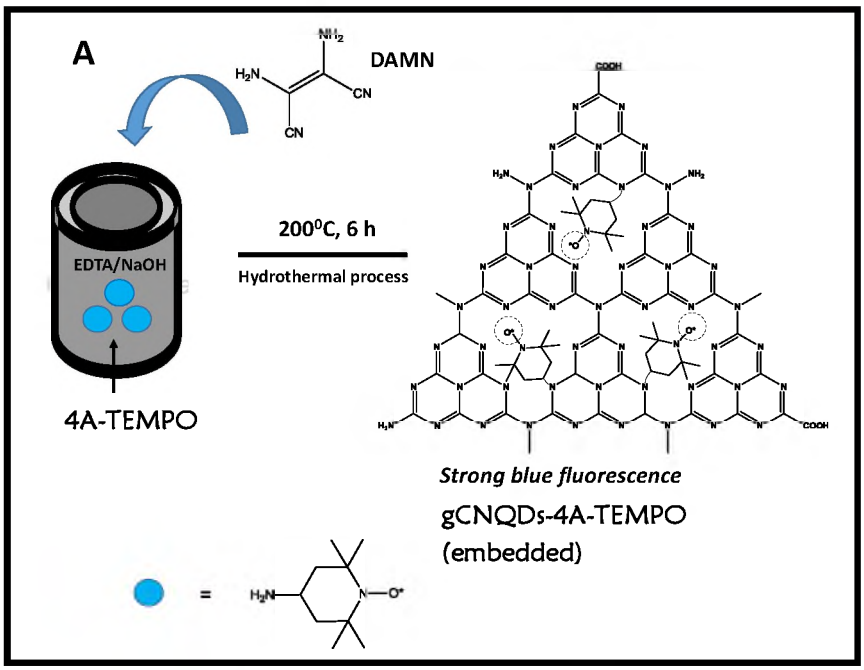

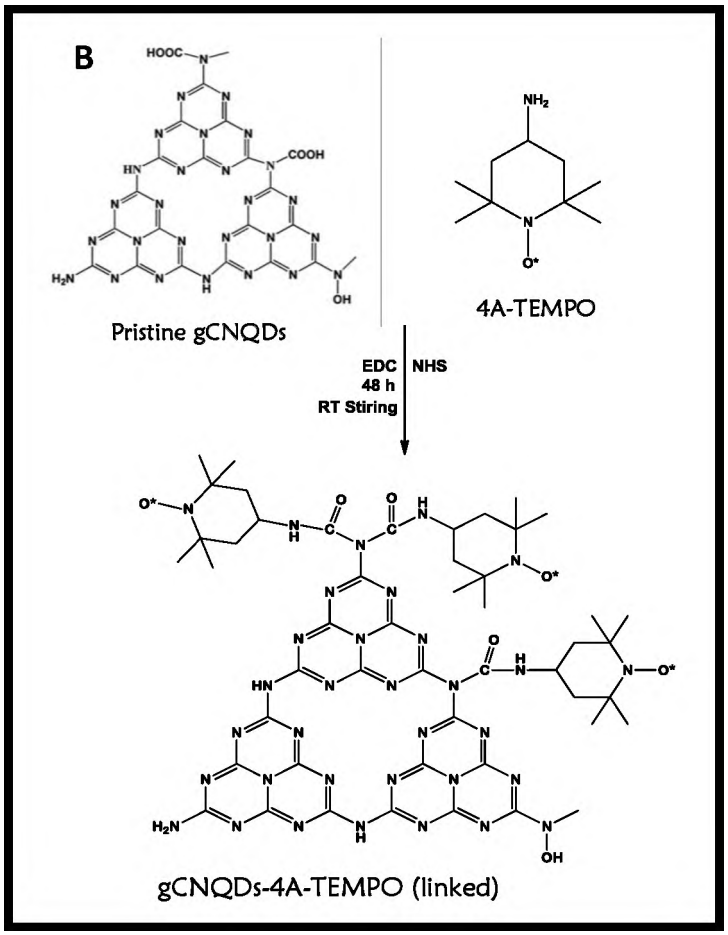

Scheme 3.3. Schematic illustrations of (A) gCNQDs-4A-TEMPO (embedded) preparation, and (B) the covalent attachment of 4A-TEMPO to pristine gCNQDs.

Table 3.3. Optical parameters of gCNQDs and its TEMPO-functionalized derivatives (PBS 10 mM, pH 7.0).

QDs (nm)	$\lambda_{absorption}$ (nm)	$\lambda_{emission}$ (nm)	Φ_F (± 0.01)	τ(ns) (± 0.10)	Size (nm)
Pristine gCNQDs	335	445	0.43	7.40	6.5
gCNQDs-4A-TEMPO (embedded)	340	450	0.51	10.05	7.0
gCNQDs-4A-TEMPO (linked)	332, ~420	445	0.02	1.02	9.8

This conjugate was fabricated so as to assess the optical performance of gCNQDs when it is covalently linked to TEMPO (4A-TEMPO) as opposed to when TEMPO is embedded.

3.2.2. XPS

To characterize the as-synthesized gCNQDs (or gCNQDs-4A-TEMPO (embedded)), X-ray photoemission spectroscopy (XPS) analysis was employed. As shown in Fig. 3.14A using gCNQDs as an example, the elemental survey scans for gCNQDs and gCNQDs-4A-TEMPO (embedded) expectedly showed the elements C, N, O at 284.5, 399.8 and 530.5 eV, respectively. The C1s and N1s peaks were further deconvoluted in order to identify the different bonding states of the C and N species, which are the principal components of gCNQDs. The high resolution XPS spectrum of C1s of gCNQDs revealed the adventitious states of carbon in gCNQDs where three bonding states of carbon were identified at 285.4 eV (C-C, C-N), 287.9 eV (C-N) and 289.0 eV (C=O) as shown in Fig. 3.14B (similar C1s spectrum was obtained for gCNQDs-4A-TEMPO (embedded)

as shown in Fig. 3.14C). The Gaussian peaks of carbon identified in the as-synthesized gCNQDs (or gCNQDs-4A-TEMPO (embedded)) have been previously observed in carbon nitride quantum dots [104, 107].

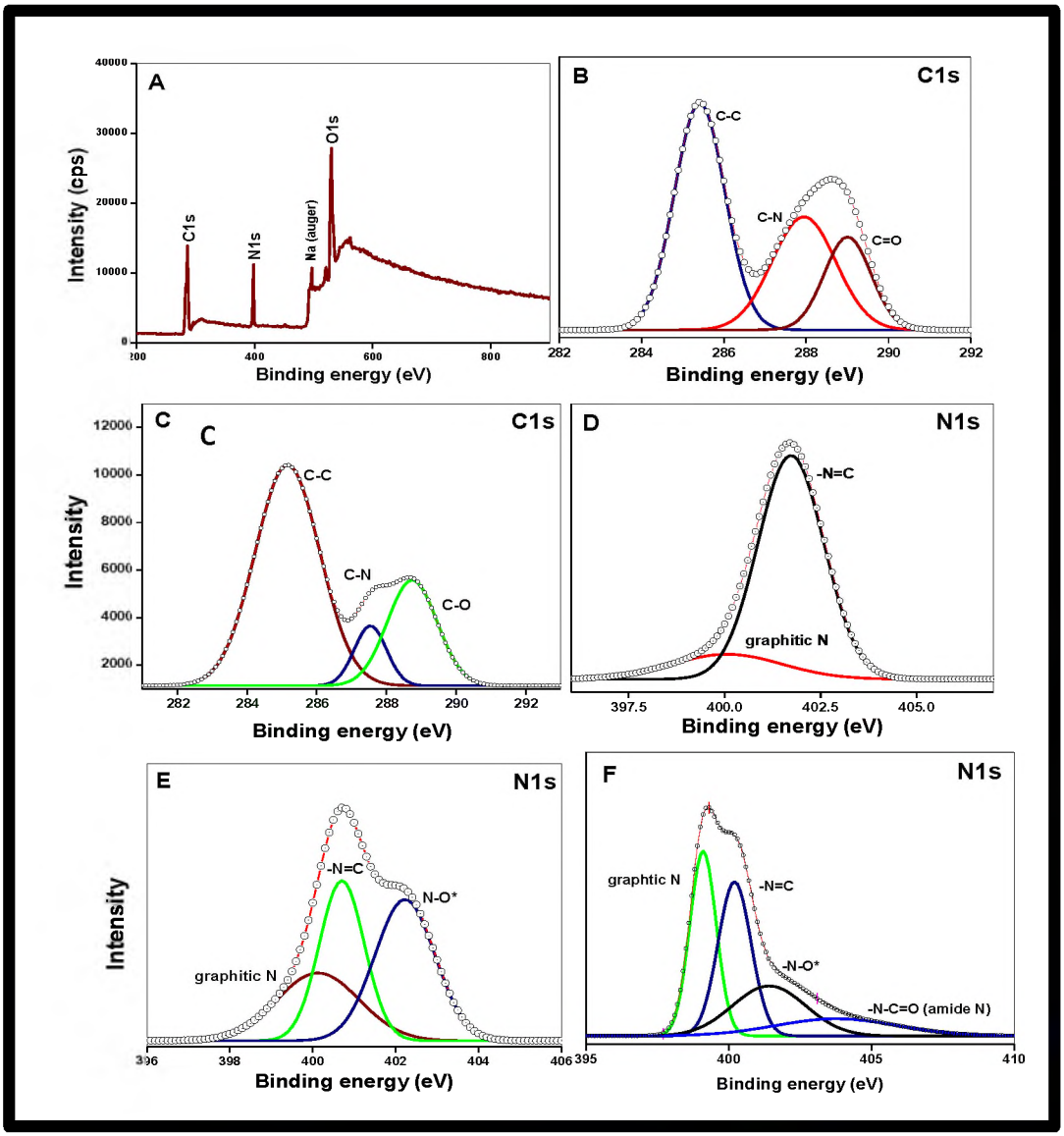

Fig. 3.14. XPS wide scan of gCNQDs (A), high resolution C1s of gCNQDs (B), gCNQDs-4A-TEMPO (embedded) (C), N1s of gCNQDs (D), gCNQDs-4A-TEMPO (embedded) (E) and gCNQDs-4A-TEMPO (linked) (F).

The N1s of pristine gCNQDs was further fitted into two Gaussian peaks with binding energies around 400.1 and 401.2 eV, which corresponds to the intercalated graphitic N atoms(sp^2) and -N=C, respectively (Fig. 3.14D). An evaluation of the N- peaks ratio gave 1.76, which has been previously identified as close to that of the triazine based graphitic carbon nitrides **[104]**. The high resolution XPS spectrum of deconvoluted N1s of gCNQDs-4A-TEMPO (embedded) resulted in three distinct bonding states of N atoms (Fig. 3.14E). The binding energies observed at 400.5 and 401.2 eV are attributed to the graphitic N and -N=C (sp^2), as the same for gCNQDs. However, the additional peak at 402.2 eV is due to the nitroxide (N-O*) of the TEMPO introduced into the graphitic backbone of gCNQDs-4A-TEMPO (embedded), hence showing the successful incorporation of TEMPO functionality into the carbon nitride quantum dots. As shown in Fig. 3.14F, four peaks were observed which conforms to four different bonding states of N atoms present within the conjugate. It is expected that an amide peak with higher binding energy emerges as a result of the coupling between pristine gCNQDs and 4A-TEMPO which was observed at ~404 eV, further showing the successful covalent linkage of the materials.

3.2.3. AFM

Atomic force microscopy (AFM) was employed for the topographic evaluation of gCNQDs (or gCNQDs-4A-TEMPO (embedded)). The acquired images (Fig. 3.15A and B) showed average topographic heights of 1.25 and 1.5 nm for gCNQDs and gCNQDs-4A-TEMPO (embedded), respectively, thus indicating that gCNQDs are composed of few to single layers of graphitic sheets (C-N) in accordance with previous reports **[104, 107, 108]**.

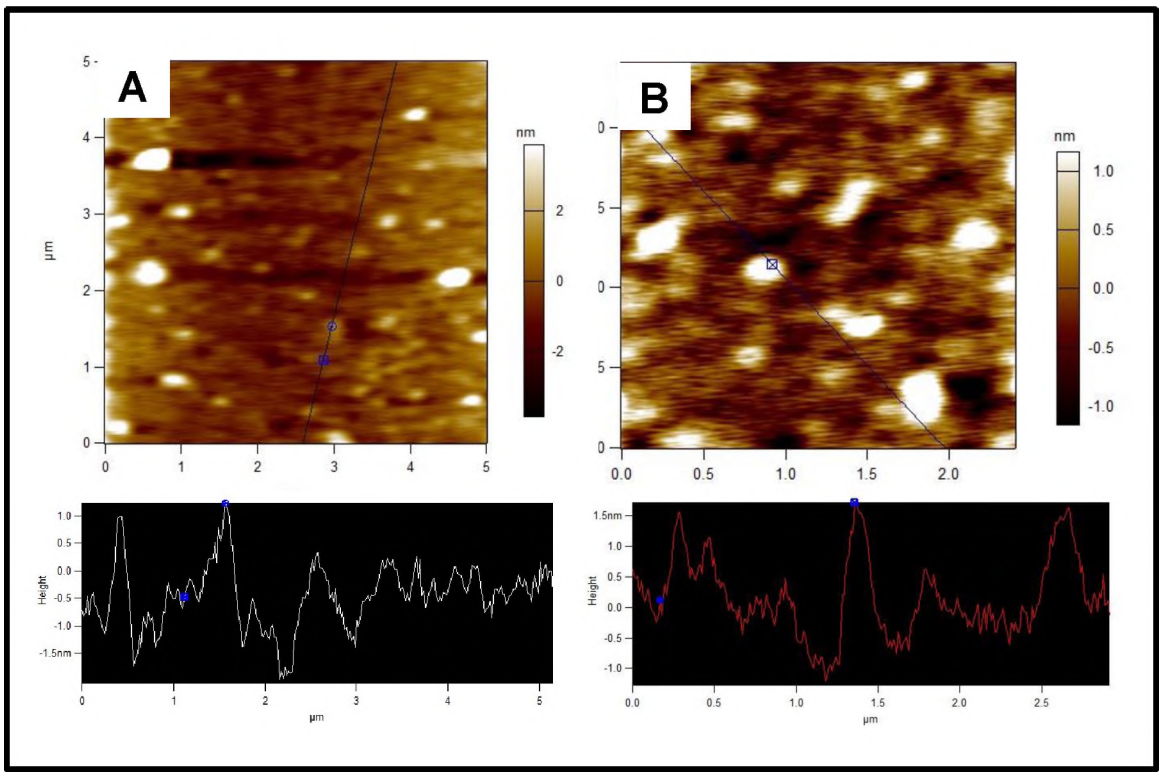

Fig. 3.15. AFM images and corresponding height profiles for (A) gCNQDs and (B) gCNQDs-4A-TEMPO (embedded).

3.2.4. FT-IR

Fourier transform infrared (FT-IR) spectroscopy of the as-synthesized gCNQDs further revealed the base structure of gCNQDs and their TEMPO derivatives. As shown in Fig. 3.16, vibrations at 774 cm^{-1} due to the heptazine units of the gCNQDs were observed. Bands at 1416 cm^{-1} and 1316 cm^{-1} show the characteristic presence of C=N/C-N stretching modes of the graphitic structure. Asymmetric vibrations corresponding to the carboxylic groups introduced by EDTA as surface groups could be observed at 1628 cm^{-1}. Broad peaks typical of the N-H/O-H vibrations were observed around 3715-2985 cm^{-1}. The characteristic bands recorded here are in agreement with well-documented results for carbon nitride QDs presented in the literature **[104, 107-112]**, and confidently showed that

gCNQDs were successfully prepared using the novel precursor material (DAMN). FT-IR was used to confirm the covalent attachment of 4A-TEMPO to gCNQDs as shown in Fig. 3.16 C, It was observed that the vibrational broad band of the –COOH group on the graphitic sheet of gCNQDs depleted upon conjugation which indicates the conversion of the –COOH to amide group upon linking with the NH_2 of 4A-TEMPO. Further, a secondary amide band was observed at 1667 cm^{-1} which was not present in the gCNQDs alone. The primary amide band, however, could not be observed due to the overlap caused by the broad and intense C=O stretching vibration at 1628 cm^{-1} which was still present in the formed conjugate.

3.2.5. XRD, TEM and DLS

The powder X-ray diffraction (XRD) patterns of gCNQDs are similar to those of GQDs shown in Fig. 3.4 with a single peak at $2\theta = 27.9^{0}$, which corresponds to graphitic interplanar 002 (d-spacing structure of graphitic materials). This result conforms to what has been reported before **[104, 107, 108]**, and further indicates the successful formation of gCNQDs.

TEM micrograph of the as-synthesized gCNQDs were monodispersed with particles of gCNQDs possessing sizes typically estimated within the range of 2-7 nm as observed for GQDs in Fig. 3.6.

Dynamic light scattering (DLS) experiments showed that the average size distribution of gCNQDs was 6.5 nm and 7.0 nm for gCNQDs-4A-TEMPO (embedded) (Table 3.3) further indicating sizes typical of carbon-based QDs. An

average size of 9.8 nm was obtained for gCNQDs-4A-TEMPO (linked) was obtained, showing an increase in size upon conjugate formation.

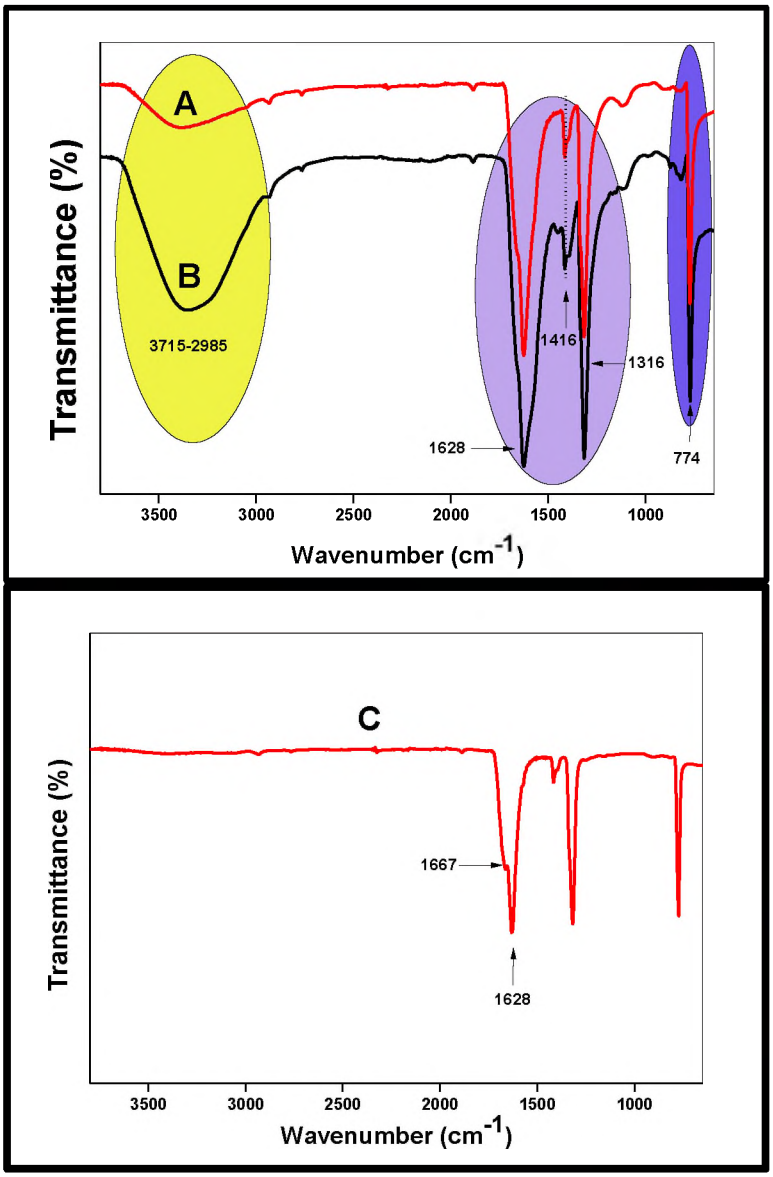

Fig. 3.16. FT-IR spectra for (A) gCNQDs (B) gCNQDs-4A-TEMPO (embedded) and (C) gCNQDs-4A-TEMPO (linked).

3.2.6. Optical and electronic properties

The ground-state absorption behaviour of the as-synthesized gCNQDs and gCNQDs-4A-TEMPO (embedded) are as shown in Fig. 3.17, and they exhibit

typical absorptions at in the region ~400 nm in both cases which has been ascribed to electronic transition (π-π*) of the s-triazine units of the carbon nitride family [104, 107-112]. The n-π* peak at 332 nm is attributed to unsaturated units with lone pairs on the nitrogen or oxygen atoms.

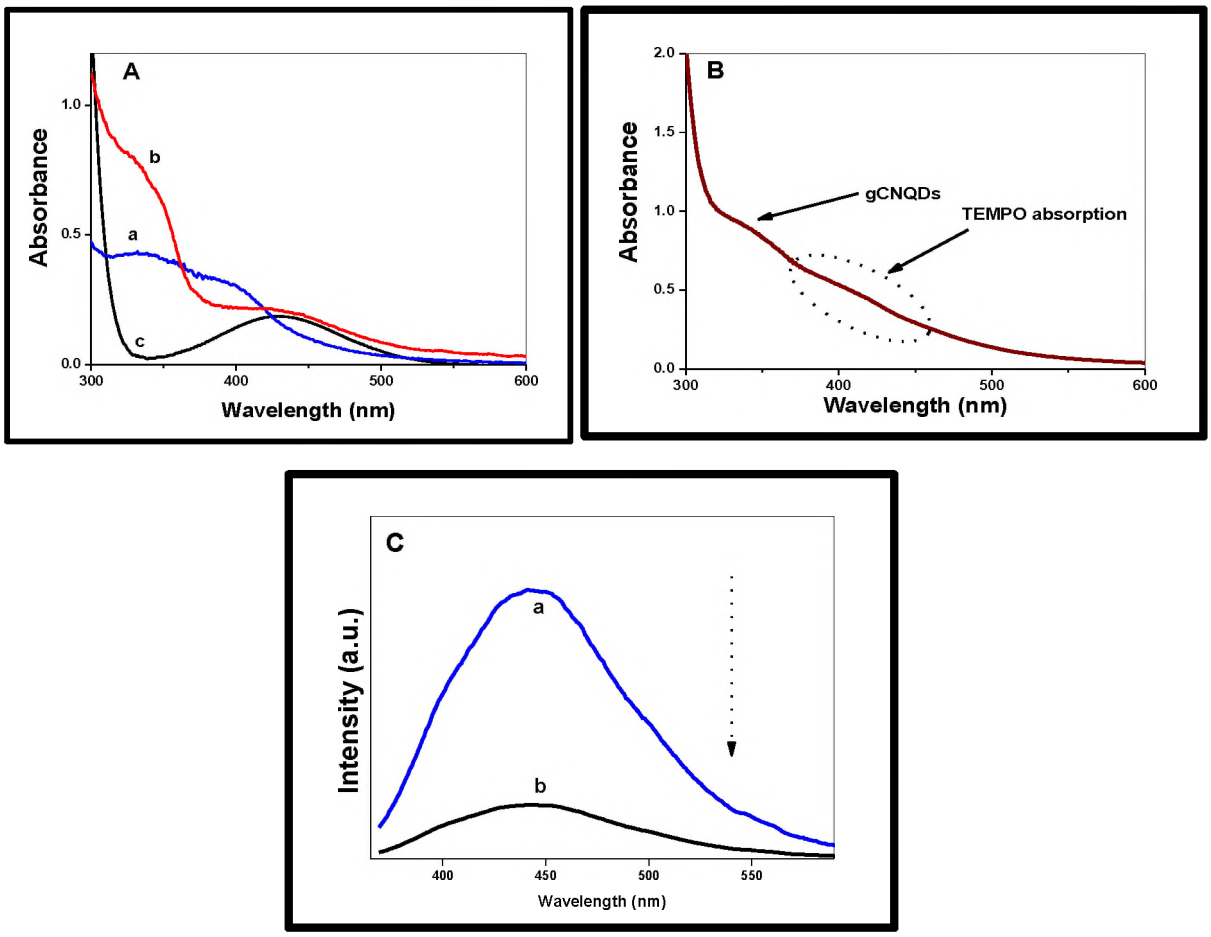

Fig. 3.17. UV-Vis spectra (A) gCNQDs (a), gCNQDs-4A-TEMPO (embedded) (b), and 4A-TEMPO (c), (B) gCNQDs-4A-TEMPO (linked), and (C) Fluorescence spectra of gCNQDs alone (a), and upon conjugation with 4A-TEMPO (b), in PBS (10 mM pH7.0).

In the case of gCNQDs-4A-TEMPO (embedded) [Fig. 3.17 A(b)], the incorporation of TEMPO onto gCNQDs sheets was confirmed by the broad

absorption around 440 nm which is a typical absorption of a TEMPO moiety (Fig. 3.17 A(c), 4A-TEMPO lone). This absorption peak is conspicuously absent in the pristine gCNQDs [Fig. 3.17 A(a)], further indicating the successful functionalization of gCNQDs with 4A-TEMPO. UV-Vis absorption spectrum of gCNQDs-4A-TEMPO (linked) is shown in Fig. 3.17B. The slight deflection around 420 nm in the spectrum is ascribed to the presence of the TEMPO moiety and could mean the preservation of the nitroxide (N-O*), since the amino group (-NH_2) was used for the covalent linkage. This further confirmed the formation of a new nanoconjugate of gCNQDs and 4A-TEMPO.

The fluorescence properties of the as-synthesized gCNQDs were evaluated, and at maximum excitation-wavelength of 360 nm, pristine gCNQDs and gCNQDs functionalized with TEMPO (embedded) exhibit intense blue emission at 456 and 460 nm, respectively, Fig. 3.18A (inset: bright blue emission of gCNQDs under 365 nm UV light). The excitation-wavelength dependent properties of gCNQDs, where the FL intensity varies and wavelength shifts at different excitation wavelengths from 340 to 400 nm are shown in Fig. 3.18B. This FL behavior which is similar to other carbon nitrides QDs reported in the literature **[104, 107-112]**, is a reflection of the different sizes and trap sites on the planar surface of gCNQDs. As shown in Table 3.3, high relative fluorescence quantum yields ($\mathbf{\Phi_F}$) of 43 % and 51 % for gCNQDs and gCNQDs-4A-TEMPO (embedded), respectively, were obtained. The exponential decay kinetics (lifetimes) were found to be 7.40 and 10.05 ns for pristine gCNQDs and gCNQDs-4A-TEMPO (embedded), respectively. In this work, it should be noted that the fluorescence

quantum yields obtained are much higher than carbon nitrides QDs prepared from other sources reported to date **[104, 107-112]**. For TEMPO derivatized gCNQDs, this is ascribed to the introduction of additional defects on the surface states of gCNQDs resulting in possible trapping of the excited state energy, hence increased number of photons emitted and as such a high quantum yield, as it is the case for GQDs. The fluorescence emission of gCNQDs was quenched upon covalent conjugation to 4A-TEMPO via a possible electron transfer process (Fig. 3.17C). This was further reflected by the decrease in the fluorescence quantum yield (Φ_F) and lifetime (τ_F) of gCNQDs within gCNQDs-4A-TEMPO (linked) conjugate (Table 3.3).

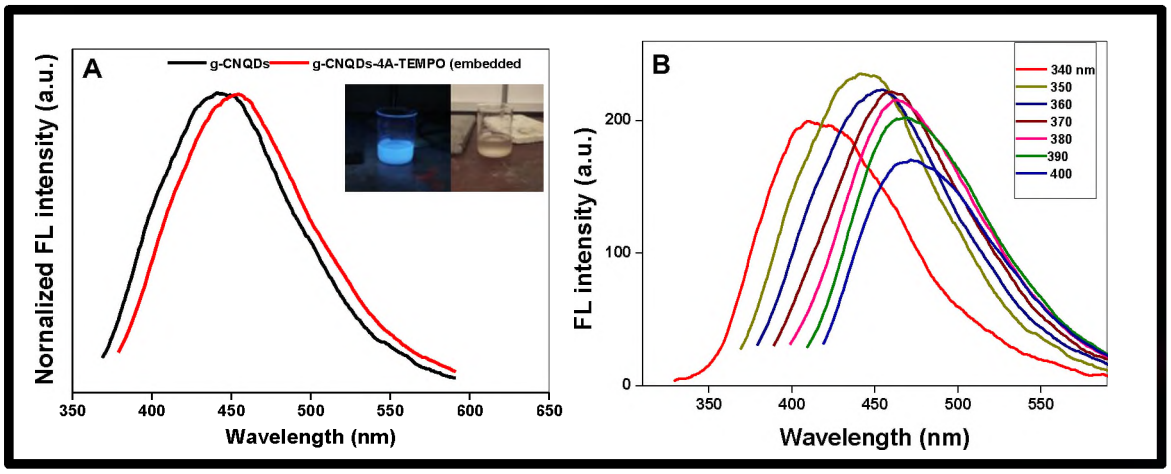

Fig. 3.18. Fluorescence emission spectra of (A) gCNQDs, and gCNQDs-4A-TEMPO (embedded) and (B) Excitation-wavelength dependent behaviour of gCNQDs (as an example). Inset of A: gCNQDs viewed under 365 nm UV and visible light, respectively. Solvent: PBS (10 mM, pH 7.0).

3.3. Au@Ag NPs

Au@Ag NPs synthesized in this work involved the use of tyrosine to cap the Au NPs which aided the reduction of Ag ions into its nanoparticles form and results in the formation of Au@Ag core-shell NPs. The as-synthesized Au@Ag NPs show an SPR peak at 473 nm (Fig. 3.19A) which corresponds to excitonic transition in the core-shell nanocrystallites [221].

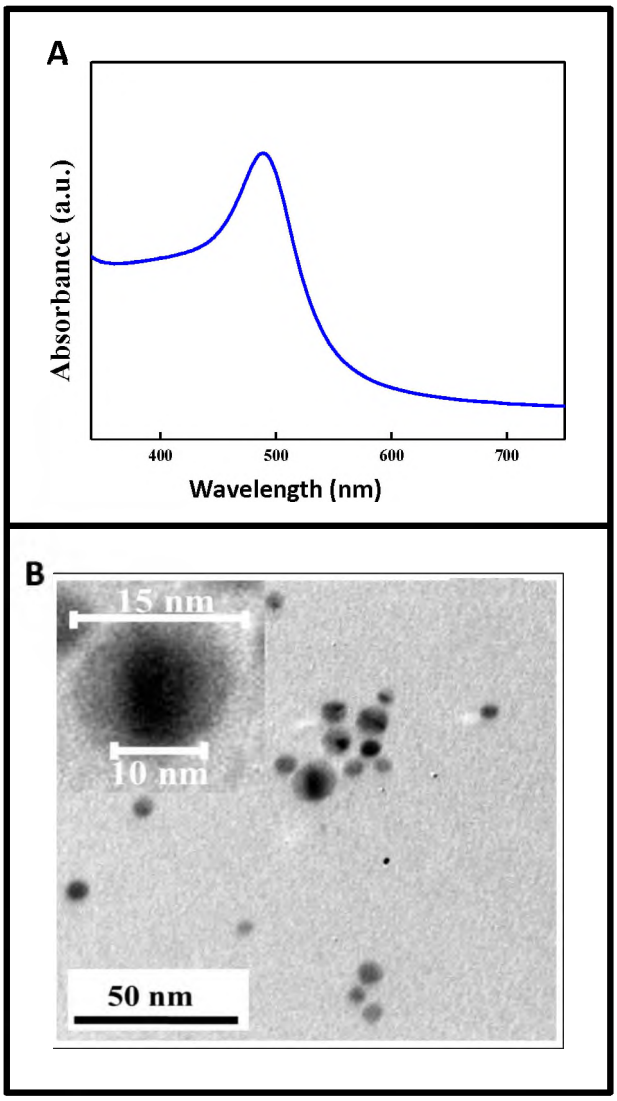

Fig. 3.19. (A) UV-Vis spectra and (B) TEM of Au@Ag NPs.

The TEM image of Au@Ag NPs depicts mainly quasi-spherical morphology (Fig. 3.19B). The average particle size of Au@Ag NPs was determined to be around 15 nm. The nanoparticles show contrast features with a dark centre and a lighter shell, which reveals the core-shell architecture.

3.4. Synthesis and characterization of new MPcs (10-12)

3.4.1. Pyrene-derivatized MPcs (10 and 11)

The synthetic route for the formation of complexes **10** or **11** followed the Schiff base reactions between complex **1** with 1-pyrene-carboxyaldehyde as shown in Scheme 3.4. The absorption spectra of complexes **10** or **11** in DMF (Fig. 3.20) showed the characteristic features of pyrene moiety with typical absorptions at 395 and 360 nm. The Q-band for complex **10** was observed at 723 nm, Fig. 3.20 and Table 3.4. The Q-band for complex **11** in DMF was observed at 716 nm (Fig. 3.20). The Q-band for complex **10** was more red shifted than for complex **11**, which is typical of ZnPc complexes compared to CoPc **[222]**. The B-bands of complexes **10** or **11** were more intense than the Q-bands because of the absorptions by the four pyrene substituents on the MPcs rings in this region. Beer-Lambert's law was obeyed within the concentration range of 1×10^{-7} to 2.5×10^{-5} M (in DMF) for both complexes, further demonstrating the lack of aggregation. Other techniques such as FT-IR, MALDI-TOF, ^{1}H NMR and elemental analysis were employed to characterize the compounds and the results obtained were in agreement with the expected results.

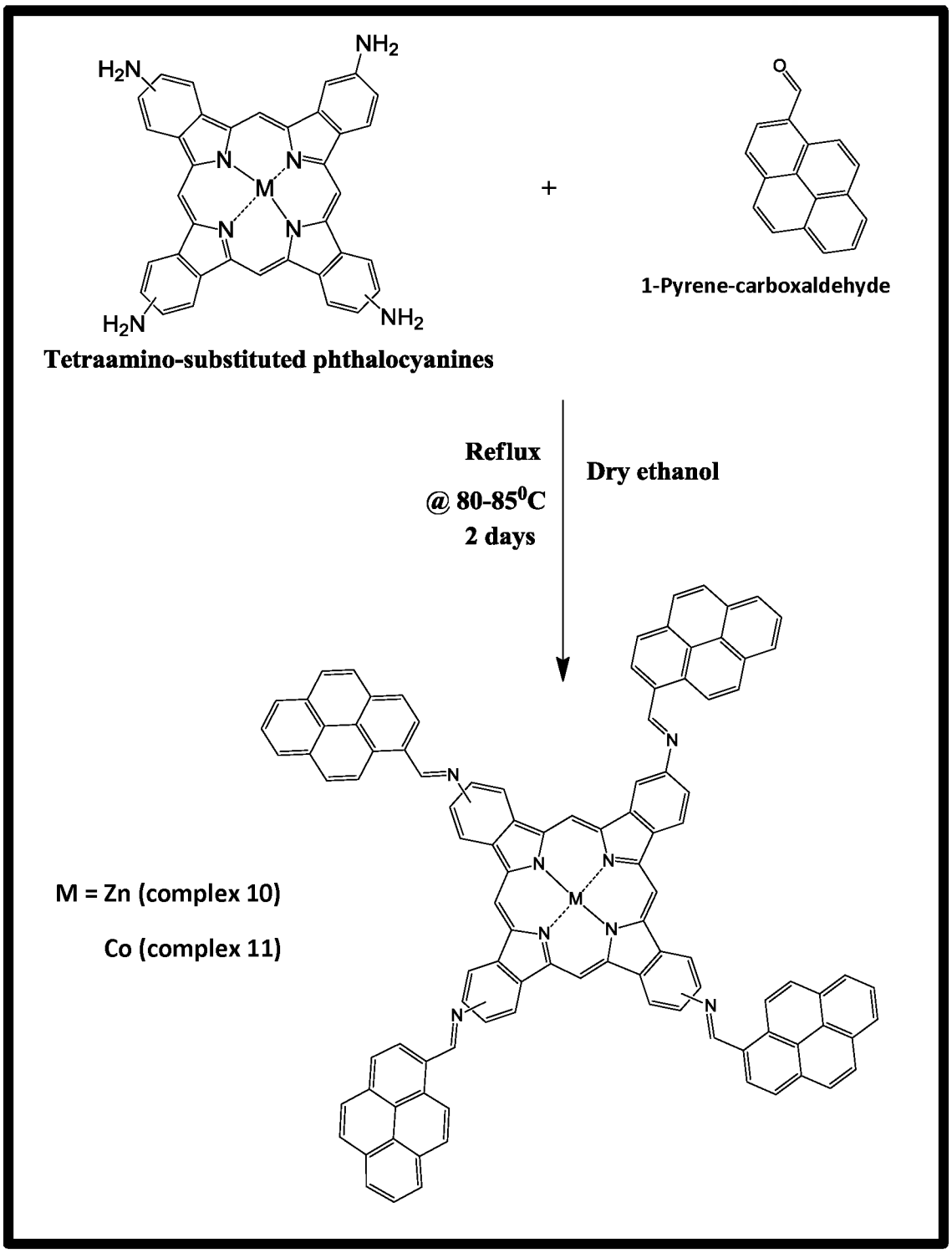

Scheme 3.4. Synthetic routes of pyrene-derivatized MPc complexes 10 and 11.

Table 3.4. Optical and fluorescence parameters, size and FRET efficiency (E*ff*) of the various conjugates of GQDs and MPcs/MP employed in this work.

Complex (nm)[a]	[b]$\lambda_{absorption}$ (nm)	$\Phi_{F(QDs)}$ (± 0.01)	$\tau_{F(QDs)}$(ns) (± 0.10)	E*ff*	Solvent
1-GQDs (21)	718 (715) (720)[c]	0.12	5.65	0.45	DMF:PBS (50 mM) 4:1 (v/v)
2-GQDs (46)	680 (678)	0.19	5.62	0.14	DMF:PBS (50 mM) 4:1 (v/v)
3-GQDs (23)	680 (679)	0.18	5.61	0.18	DMF:PBS (50 mM) 4:1 (v/v)
4-GQDs (14)	688	0.18	5.50	0.20	PBS (10 mM, pH 7.4)
5-GQDs (21)	706	0.16	5.20	0.27	PBS (10 mM, pH 7.4)
6-GQDs (22)	702	0.16	5.33	0.25	PBS (10 mM, pH 7.4)
7-GQDs (27)	719	0.12	4.95	0.48	PBS (10 mM, pH 7.4)
8-GQDs (17)	679	0.09	1.9	0.66	DMSO
8-SNGQDs (18)	679	0.15	0.9	0.92	DMSO
9-GQDs (20)	686	0.09	1.95	0.51	DMF 15% in PBS (pH 7.0)
9-T-GQDs (31)	686	0.03	1.05	0.42	DMF 15% in PBS (pH 7.0)
10-GQDs (28)	711 (723)	0.12	2.10	0.55	DMF
11-GQDs (30)	706 (716)	0.09	1.95	0.62	DMF
12-GQDs (25)	708 (699)	0.10	1.02	0.68	DMSO/PBS (pH 7.0)
MP-GQDs					
13-GQDs (28)	440	0.05 (0.21)[d]	1.53 (10.6)[d]	0.91	DMF

[a]Values in brackets are for DLS sizes, [b]MPcs alone (where not stated, means no shift), [c]value in DMSO/PBS). [d]Values in brackets are for exciting where MP (13) absorbs. PBS = Phosphate buffer solution, $\Phi_{F(GQDs)}$ alone = 0.21, $\tau_{F(QDs)}$ alone = 5.7 ns, $\Phi_{(13)}$ = 0.18, $\tau_{(13)}$ = 3.30 ns. DMF = Dimethyl formamide, DMSO = Dimethyl sulfoxide.

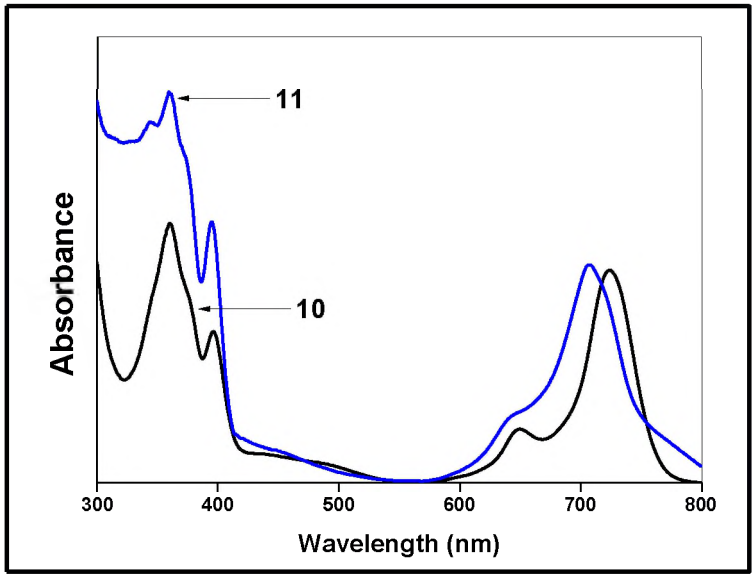

Fig. 3.20. UV-Vis spectra of complexes 10 (ZnTPyPc) or 11 (CoTPyPc). Solvent: DMF.

3.4.2. Maleimido-ZnPc (12)

The synthesis of maleimide-derivatized ZnPc **(12)** was achieved by the conversion of the four (4) terminal amino groups (-NH_2) on complex **1** to maleimide groups following procedures described previously for the transformation of amino moiety to a maleimide moiety **[200]**. Scheme 3.5 shows the synthetic pathways adopted for the preparation of MPc complex **12**. The conversion of complex **1** (with terminal amino groups) to complex **12** (with maleimide groups) was verified and confirmed by the observed changes in the ground-state absorption of the MPc complex (before and after conversion). The ground state absorption Q-band of complex **1** in DMSO/PBS (1:4) occurred at 720 nm which is highly red-shifted compared to complex **12** at 699 nm (DMSO/PBS, 1:4)(Table 3.4), due to the presence of electron donating terminal amino groups (-NH_2) on the MPc ring **[223]**. The same trend was observed when UV-Vis spectra were recorded for

complexes **1** and **12** in DMSO (Fig. 3.21). Consequently, the transformation of the amino groups on the terminal positions of complex **1** to maleimide units resulted in a blue-shifted Q-band as shown in Fig. 3.21, due to the conversion of the electron donating amino groups to the electron withdrawing (deficient) maleimide groups (maleimide moieties are known to be electron deficient due to their low lying n-π^* state [224]). Within the concentration range of ca 1 X 10^{-6} to 1 X 10^{-5} mol/L in DMSO, complex **12** did not show any signs of aggregation as Beer-Lambert's law was obeyed. The novel MPc complex was further characterized by ^{1}H NMR, MALDI-TOF mass spectroscopic technique, FT-IR and elemental analysis and satisfactory results were obtained which further confirmed the formation of the desired MPc.

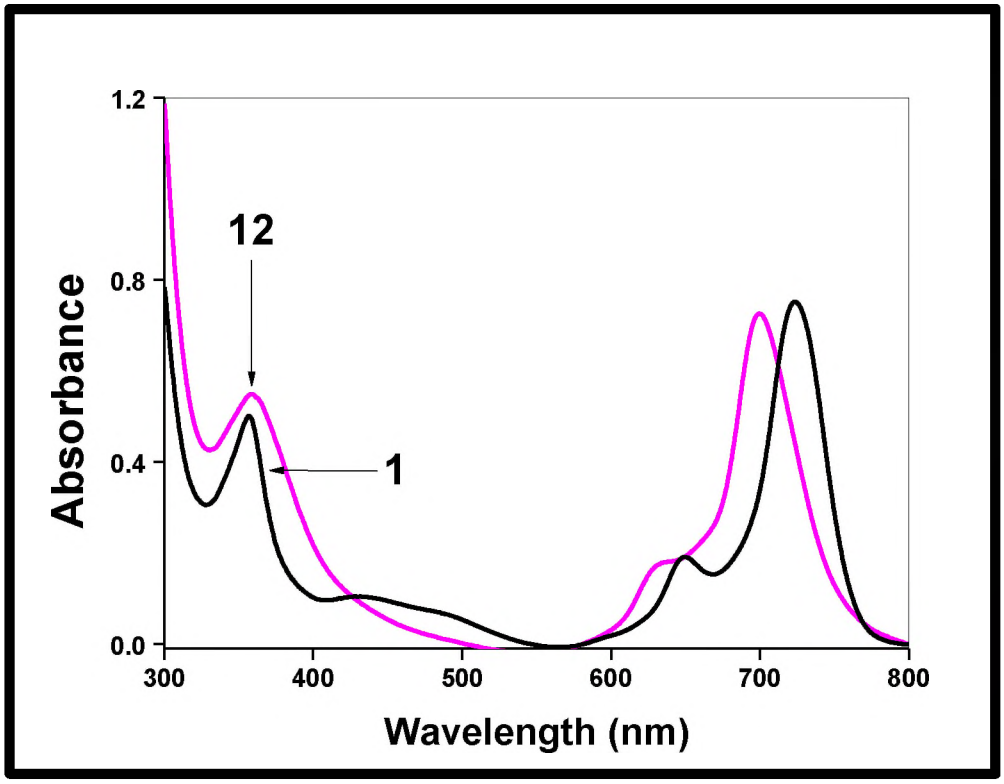

Fig. 3.21. UV-Vis spectra of complexes 1 (ZnTAPc) and 12 (ZnTMPc) in DMSO.

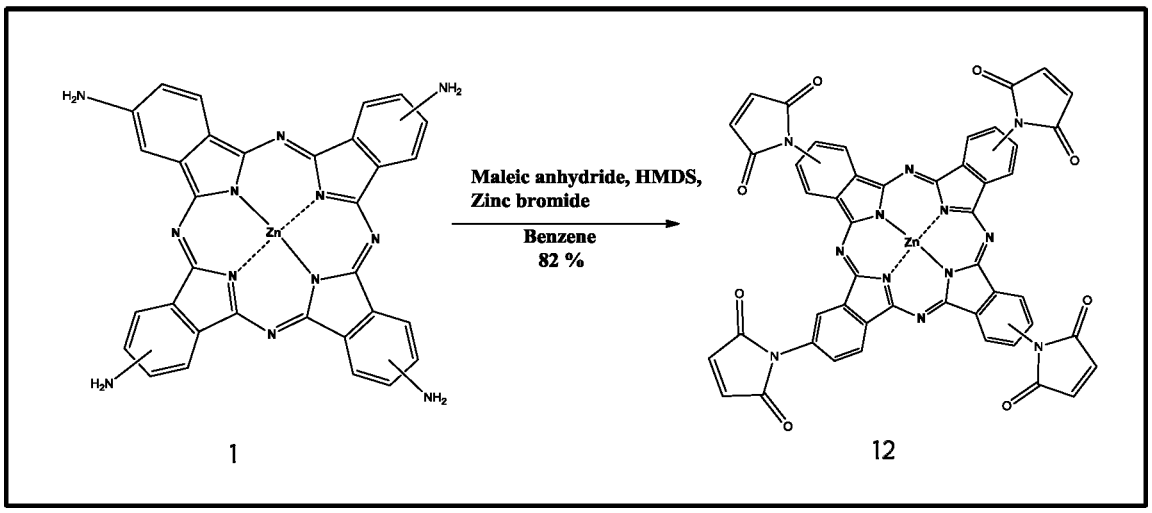

Scheme 3.5. Synthetic route for the preparation of maleimide-derivatized MPc (complex 12, ZnTMPc) from complex 1 (ZnTAPc).

3.5. Conjugation of complex 5 to Au@Ag NPs

In this work, Au@Ag NPs were functionalized with complex **5** to form **5**-Au@Ag conjugate by utilizing the strong binding affinity of Au or Ag NPs for the bridging S and N atoms of complex **5**. Electrostatic interaction between Au@Ag NPs (with negatively charged surface) and the quaternized N groups of the MPc (positively charged) is also possible. A representation of the coordination between Au@Ag NPs and complex **5** (to form **5**-Au@Ag) is shown in Scheme 3.6.

The non-covalent coordination (π-π stacking) of PEI-GQDs to **5**-Au@Ag conjugate resulted in PEI-GQDS-**5**-Au@Ag hybrid. Supramolecular hybrids containing multi-functional materials are quite interesting due to the unique functionality introduced by the constituent materials and the fine tuning of the hybrids for desired applications. Hence, this work also explored the fabrication of supramolecular hybrid containing PEI-GQDs, Au@Ag NPs and complex **5**. The optical parameters of the supramolecular hybrid are shown in Table 3.5.

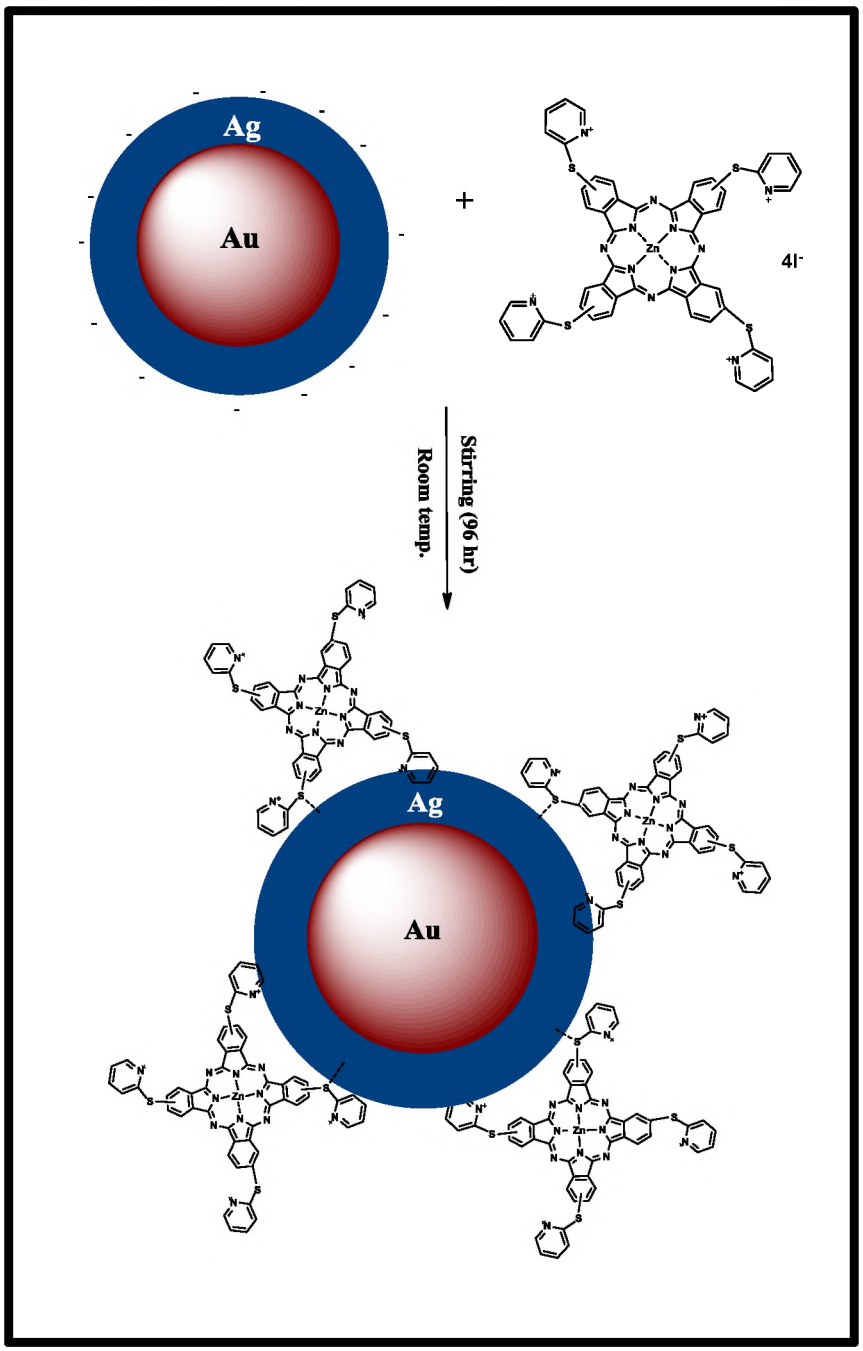

Scheme 3.6. Synthetic route for the preparation of 5-Au@Ag conjugate.

3.5.1. UV-Vis absorption spectra

The ground-state absorption spectra of **5**-Au@Ag conjugate showed red-shifts of both the Q-band of the MPc and the surface plasmonic resonance (SPR) band of Au@Ag NPs as shown in Fig. 3.22A, Table 3.5.

The SPR band of the Au@Ag NPs, which exhibited an intense absorption band at around 473 nm, was observed in the ground-state spectra of the **5**-Au@Ag conjugate at 497 nm, Fig. 3.22A. The changes in the spectral features of complex **5** in the presence of Au or Ag NPs are ascribed to the orientation of the molecular dipole of the NPs with respect to **5**-Au@Ag hybrid complex as described previously [202, 203].

Table 3.5. Optical parameters of PEI-GQDs-5-Au@Ag supramolecular hybrid, 5-Au@Ag derivative. Solvent PBS (10 mM, pH 7.0).

Complex	$\lambda_{absorption}$ (nm)	Φ_F (± 0.01)	τ (ns) (± 0.10)	Mean size DLS (nm)	[a]Zeta potential (ζ)
5-Au@Ag	694 (497)[a]	-	-	29	-5.6
PEI-GQDs-5-Au@Ag	697[b]	0.10	0.19	55	-2.8
5	676	-	-	-	+2.1
Au@Ag	473	-	-	15	-36.1
PEI-GQDs	360	0.68	8.02	10	+13.5

[a] Value in bracket for Au@Ag. [b]Value for complex 5 alone (monomer maxima are listed).

The band shifts in **5**-Au@Ag conjugate could point to the binding of complex **5** to Au@Ag NPs. The observed shift in the SPR band of Au@Ag NPs within the conjugate from 473 to 497 nm could probably be due to some aggregation.

The ground-state absorption spectrum of PEI-GQDs-**5**-Au@Ag hybrid shown in Fig. 3.22B (a) exhibited specific absorptions which correspond to those observed for **5**-Au@Ag conjugate (excluding the SPR peak of Au@Ag NPs, due to the intense absorption of PEI-GQDs) or PEI-GQDs alone (Fig. 3.22 A and B).

Complex **5** showed to be aggregated, where the high energy band is due to the so called "H" aggregate and the low energy band (Q-band) is due to the monomer [225]. As such, the Q-band of complex **5** (within the hybrid) was red-shifted from 694 nm of **5**-Au@Ag to 697 nm, Fig. 3.22, which is an indication of ground state interaction between PEI-GQDs and **5**-Au@Ag.

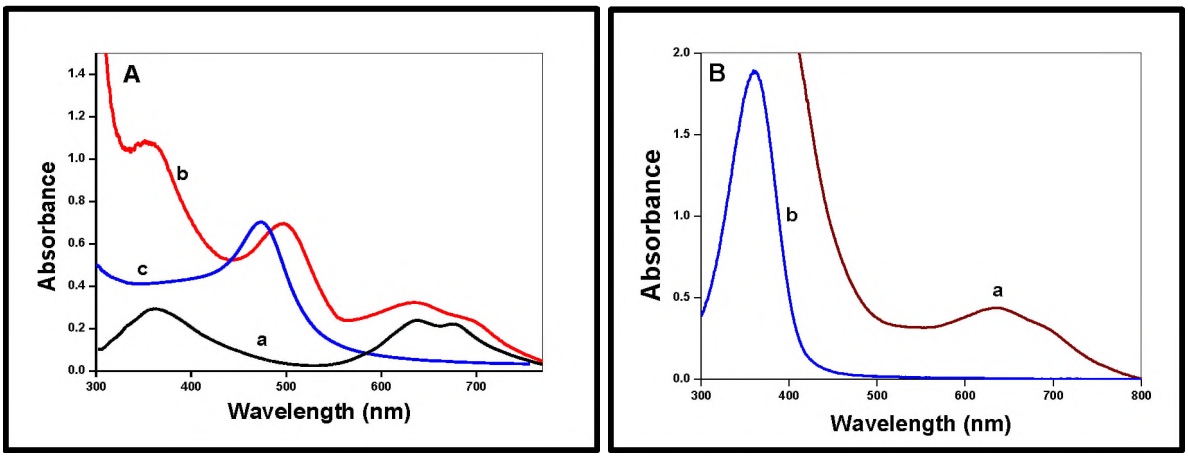

Fig. 3.22. UV/Vis absorption spectra of (A) complex 5 (a), 5-Au@Ag (b), Au@Ag NPs (c), and (B) PEI-GQDs-5-Au@Ag (a), and PEI-GQDs (b). Solvent: PBS (10 mM, pH 7.0).

3.5.2. AFM/DLS

Surface topographical analysis by atomic force microscopy (AFM) was credibly employed to ascertain the size and shape of Au@Ag NPs after conjugation to complex **5**. There was an increase in the diameter of the **5**-Au@Ag conjugate (~25 nm) compared to Au@Ag NPs alone (~13 nm) as shown in Fig. 3.23A and B. The topographic image also shows that **5**-Au@Ag size became larger and uneven in structure, Fig. 3.23B, as compared to the round shaped and core-shell like architecture of Au@Ag NPs alone. This indicates the incorporation of

complex **5** onto Au@Ag NPs surface. Morphological characterization of the supramolecular hybrid containing PEI-GQDs and **5**-Au@Ag was carried out using AFM. As shown in Fig. 3.23 C and D, the interaction between **5**-Au@Ag and PEI-GQDs was confirmed by the observed change in the height profile of PEI-GQDs (1.7 nm, single to few layered GQDs [12]) and 5.1 nm for PEI-GQDs-**5**-Au@Ag hybrid, indicating multi-layered components. The difference in height profile could be a reflection of the structural and topographical difference resulting from PEI-GQDs coordination to **5**-Au@Ag. The topographic image (Fig. 3.23D) also shows that the supramolecular size of PEI-GQDs-**5**-Au@Ag hybrid became larger as compared to the size of PEI-GQDs alone (Fig. 3.23C). This is an indication of the incorporation of PEI-GQDs onto the larger surface of **5**-Au@Ag.

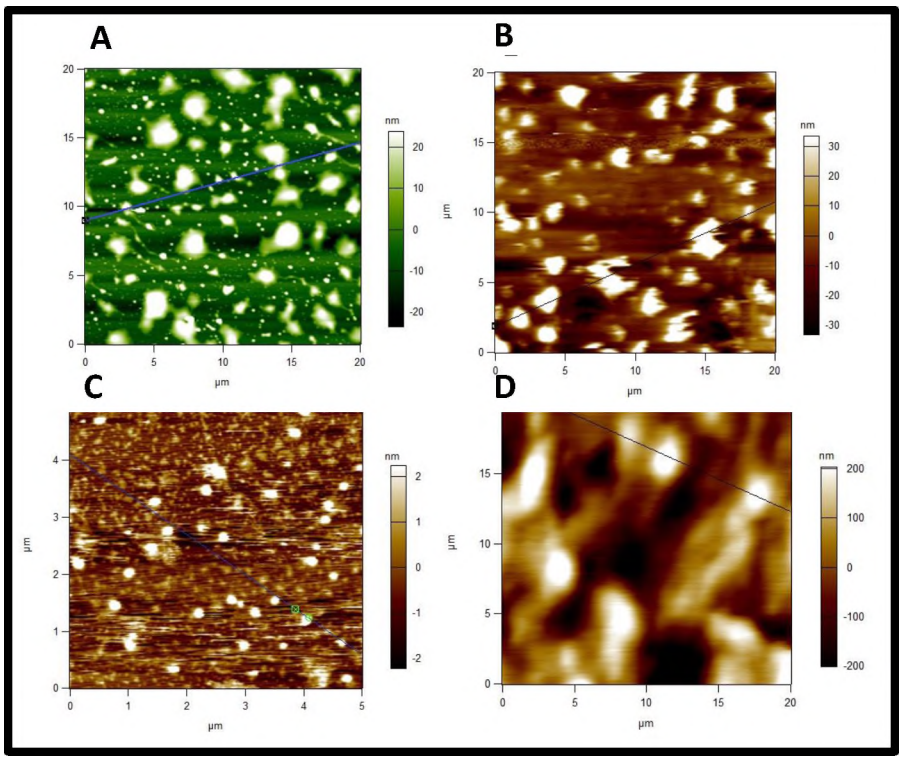

Fig. 3.23. AFM images for (A) Au@Ag NPs, (B) 5-Au@Ag conjugate, (C) PEI-GQDs, and (D) PEI-GQDs-5-Au@Ag.

The average particles size determined using dynamic light scattering (DLS) was found to be ~29 nm for **5**-Au@Ag as compared to the average size of 15 nm of Au@Ag NPs alone (Table 3.5), further showing an increase in the size of Au@Ag NPs due to the formation of **5**-Au@Ag complex. DLS also showed an increase in the size of the hybrid of PEI-GQDs-**5**-Au@Ag (55 nm) as compared PEI-GQDs (with average size of ~10 nm) or **5**-Au@Ag at ~29 nm as shown Table 3.5.

3.5.3. XRD/EDX

The X-ray diffractogram of **5**-Au@Ag conjugate showed a broad peak occurring at 2θ = 14–32° due to the amorphous MPc (**5**) incorporated onto Au@Ag NPs surface. The XRD spectra were closely similar to that of Au@Ag NPs before conjugation to complex **5**, Fig. 3.24. Both XRD patterns showed well-defined crystalline peaks attributed to 111, 200, 220, 311 and 222 planes which are in close agreement with the planes of face centered-cubic of metallic Au and Ag **[226]**. Slight broadening and reduction in the intensity of the Au@Ag NPs signature peaks were observed upon conjugation to form **5**-Au@Ag conjugate as shown in Fig. 3.24.

The elemental constituents of Au@Ag NPs and its complex **5** conjugate were deduced qualitatively via energy dispersive X-ray spectroscopy (EDX) as shown in Fig. 3.25. **5**-Au@Ag conjugate displayed characteristic peaks of Au, Ag, Zn, C, N, and S, which corresponds to the exact elemental compositions of both Au@Ag NPs and complex **5**. EDX spectra of complex **5** and Au@Ag alone are additionally shown in Fig. 3.25 (B and C). Additional peaks resulting from

precursor materials ($HAuCl_4$ used for the synthesis of Au@Ag NPs could also be seen in the spectra.

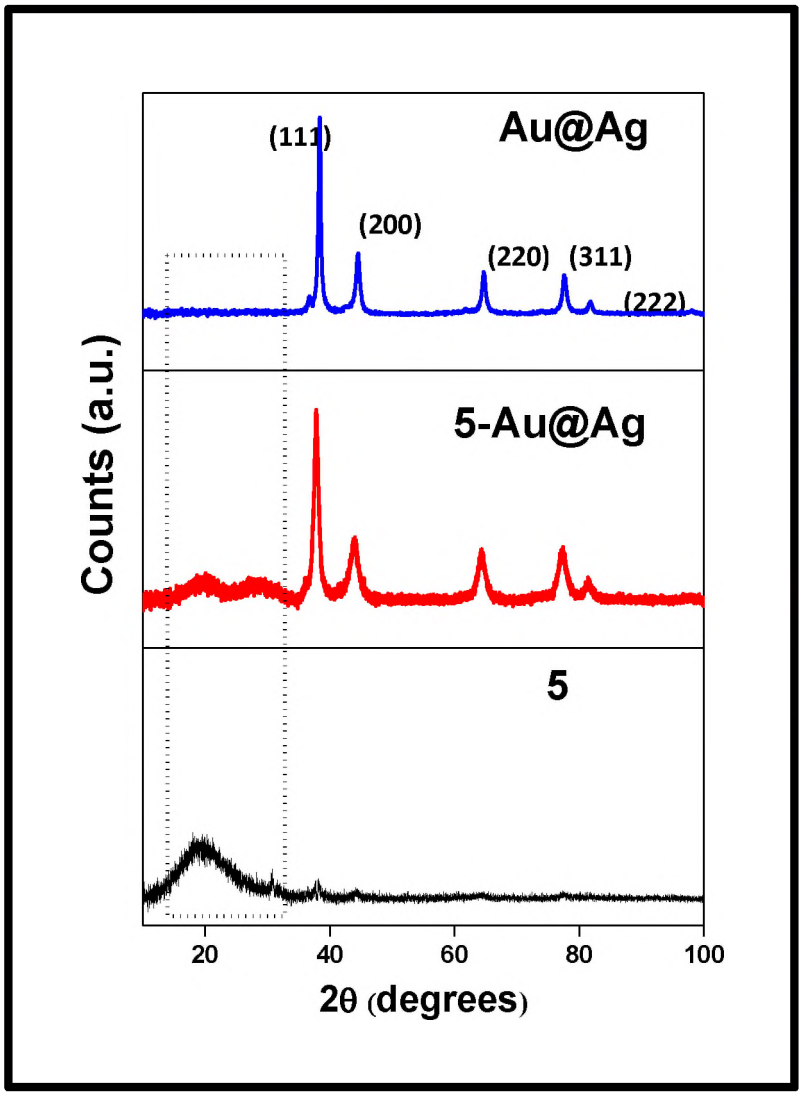

Fig. 3.24. X-ray diffractograms of Au@Ag NPs, 5-Au@Ag conjugate and complex 5.

3.5.4. Fluorescence behaviour

At excitation wavelength of 350 nm, PEI-GQDs-5-Au@Ag supramolecular hybrid displayed almost complete quenching (turn "OFF") of the fluorescence of PEI-GQDs component compared to PEI-GQDs alone (Fig. 3.26).

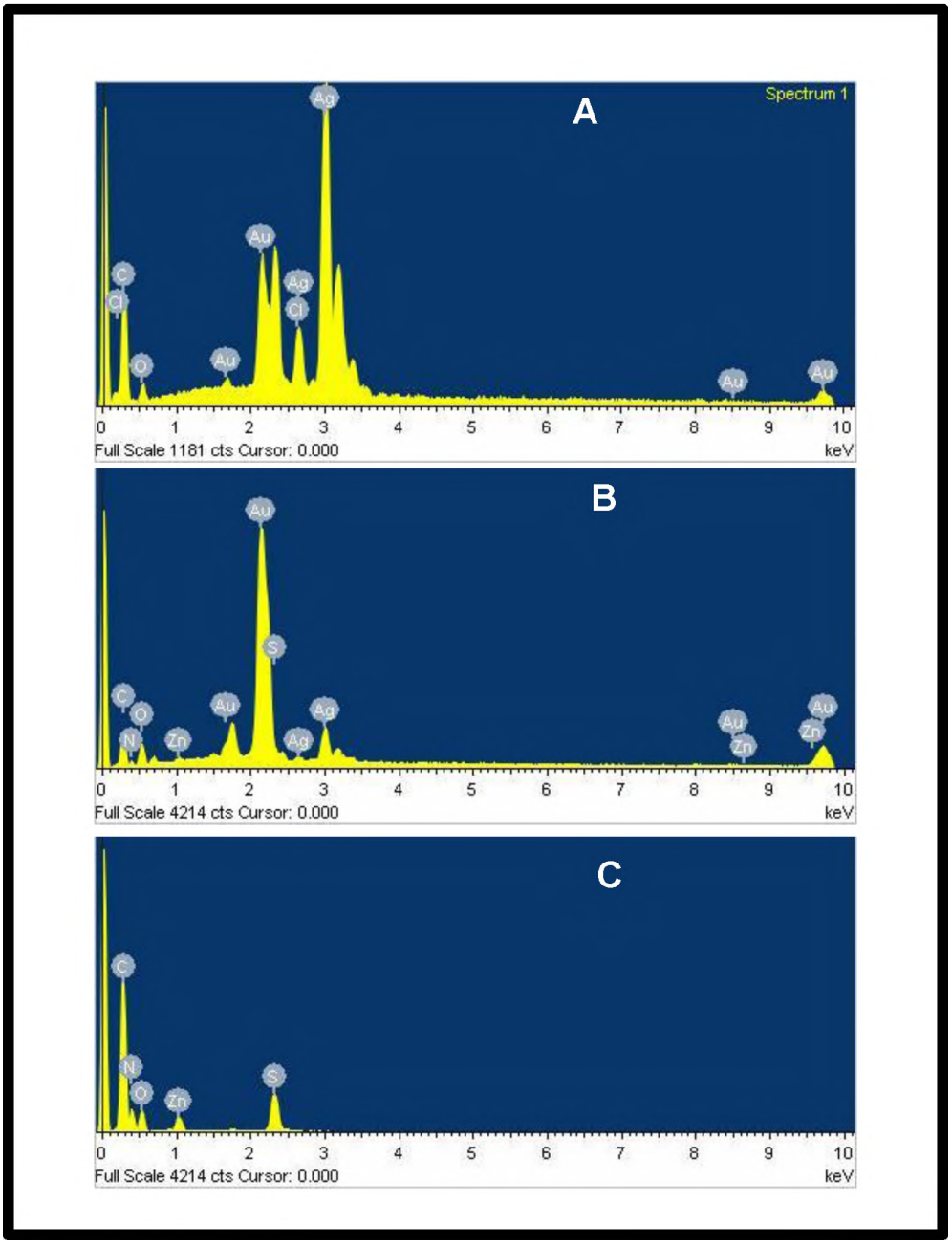

Fig. 3.25. EDX spectra for (A) Au@Ag NPs, (B) 5-Au@Ag, and (C) complex 5.

The quenched fluorescence was estimated to be about 95% within the hybrid. This very high quenching efficiency is presumably due to the dominance of the electrostatic attraction between the positively charged PEI-GQDs and negatively charged **5**-Au@Ag (as indicated by zeta potential in Table 3.5). The formation of

N-metal (Au/Ag) bonds is also possible due to NH_2 group of PEI-GQDs. Fluorescence quantum yield (Φ_F) and lifetime (τ_F) of PEI-GQDs upon coordination to **5**-Au@Ag were investigated in order to elucidate the kind of interaction and possible quenching dynamics of the fluorescence of PEI-GQDs within the supramolecular hybrid. There was a decrease in Φ_F and τ_F of PEI-GQDs upon coordination to **5**-Au@Ag as shown in Table 3.5.

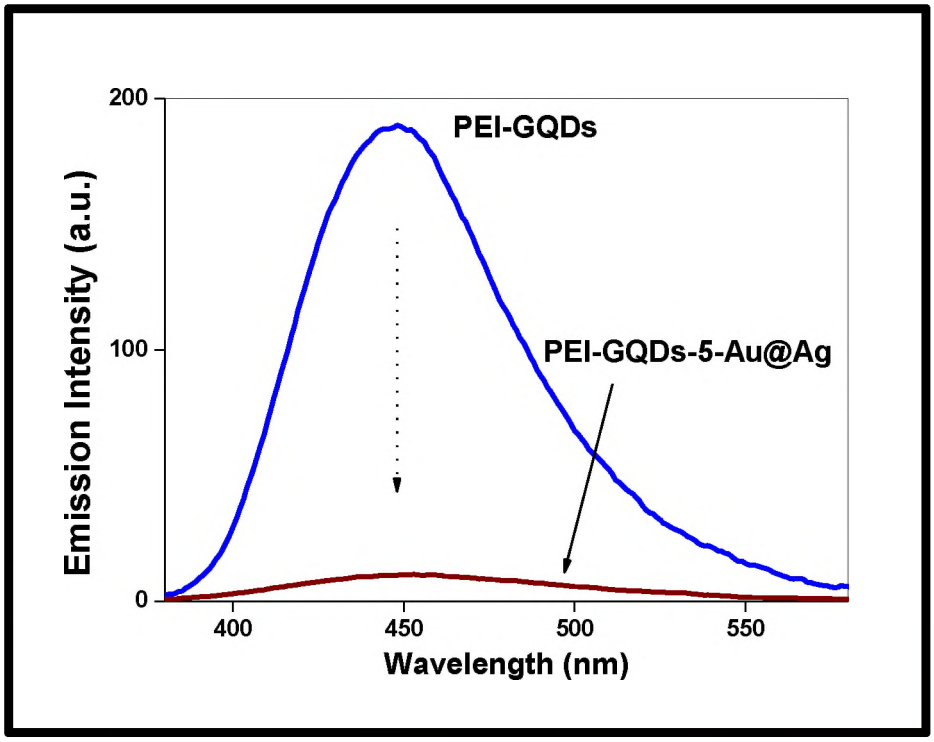

Fig. 3.26. Fluorescence emission spectra of PEI-GQDs alone and upon conjugation to 5-Au@Ag. Excitation wavelength =350 nm. Solvent: PBS (10 mM, pH 7.0).

Excited state interactions of GQDs and MPs (similar in structure to MPcs) are known to result into non-radiative recombination of the excitons of GQDs with a consequent deactivation of the radiative recombination pathways, hence quenching of GQDs fluorescence **[98]**. As such, the observed fluorescence

quenching of PEI-GQDs could potentially mean that energy (or electron) transfer process has taken place upon coordination to **5**-Au@Ag hybrid, as it is the case with other QDs-macrocycles derivatives previously reported **[98, 148]**.

3.6. MPcs/MP and GQDs conjugates

3.6.1. MPcs-GQDs

Scheme 3.7 illustrates the non-covalent (π-π) conjugation of MPcs to GQDs employed in this work. Complexes **2**-**13** were studied. Table 3.4 summarizes the optical and fluorescence results obtained for the various GQDs and MPcs/MP (π-π) conjugates employed in this work. Schematic representation of MPc (**1**) covalently linked to GQDs is shown in Scheme 3.8. The -COOH group of GQDs where coupled to the $-NH_2$ of complex **1** via EDC/NHS chemistry.

3.6.2. XPS analysis (1-GQDs)

The wide scan XPS spectrum for **1**-GQDs (covalent conjugate) displayed the appearance of N1s peak at 398 eV and Zn 2p at 1026 eV, Fig. 3.27A, which is a confirmation of the linking of complex **1** to GQDs (this peak was not present in GQDs alone shown above (Fig. 3.1A). The core level spectrum of N1s of complex **1** alone, Fig. 3.27B, revealed the following peaks: N-H (400.5 eV), N=C (399.4 eV) and N-C (398.3 eV). In the deconvoluted N1s spectrum of **1**-GQDs conjugate; N-C (398.2 eV), N=C (399.2 eV), N-H (400.5 eV) and N-C=O (401.5 eV) were observed as shown in Fig. 3.27C. The appearance of a new peak at higher binding energy (401.5 eV) is as a result of the successful amide linkage in the nanoconjugate of **1**-GQDs. This peak occurred at binding energies

which have been previously reported for amide linkage in MPc nanoconjugates [227].

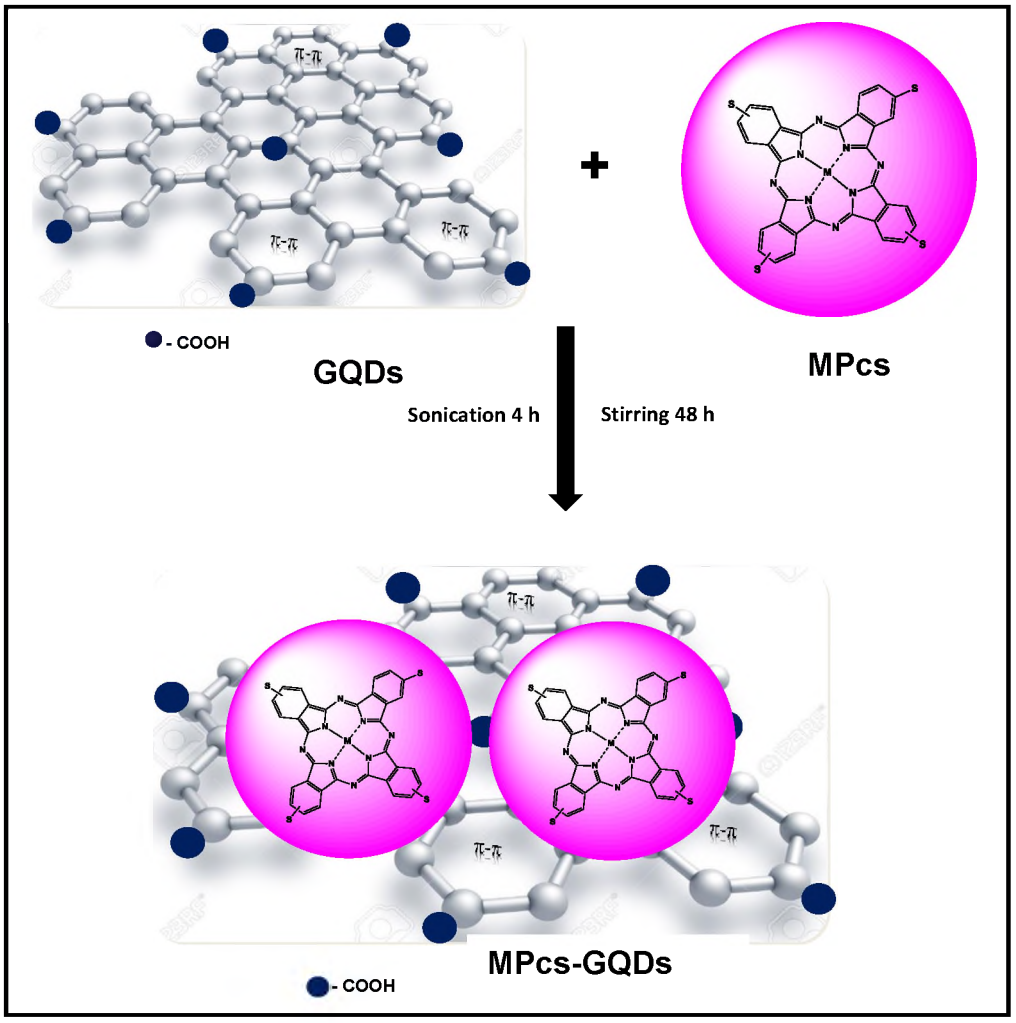

Scheme 3.7. An illustration of the non-covalent (*π-π* stacking) conjugation of GQDs to the variously employed MPcs.

3.6.3. XRD/ Raman spectra

Nanoconjugates of GQDs and the various MPcs were characterized by XRD, the diffraction patterns showed a broad ill-defined peak in the region where the peaks for GQDs and complex **10** were observed in Fig. 3.4 and 3.24, respectively.

Raman spectroscopic technique was employed to ascertain the quality of the MPcs-GQDs nanoconjugates. The 1-GQDs conjugate displayed the characteristic Raman peaks termed the G-band (sp^2) tangential mode and the D-disorder band (breathing mode, sp^3) at 1554 cm^{-1} (G-band) and 1385 cm^{-1} (D-disorder band) similar to Fig. 3.5.

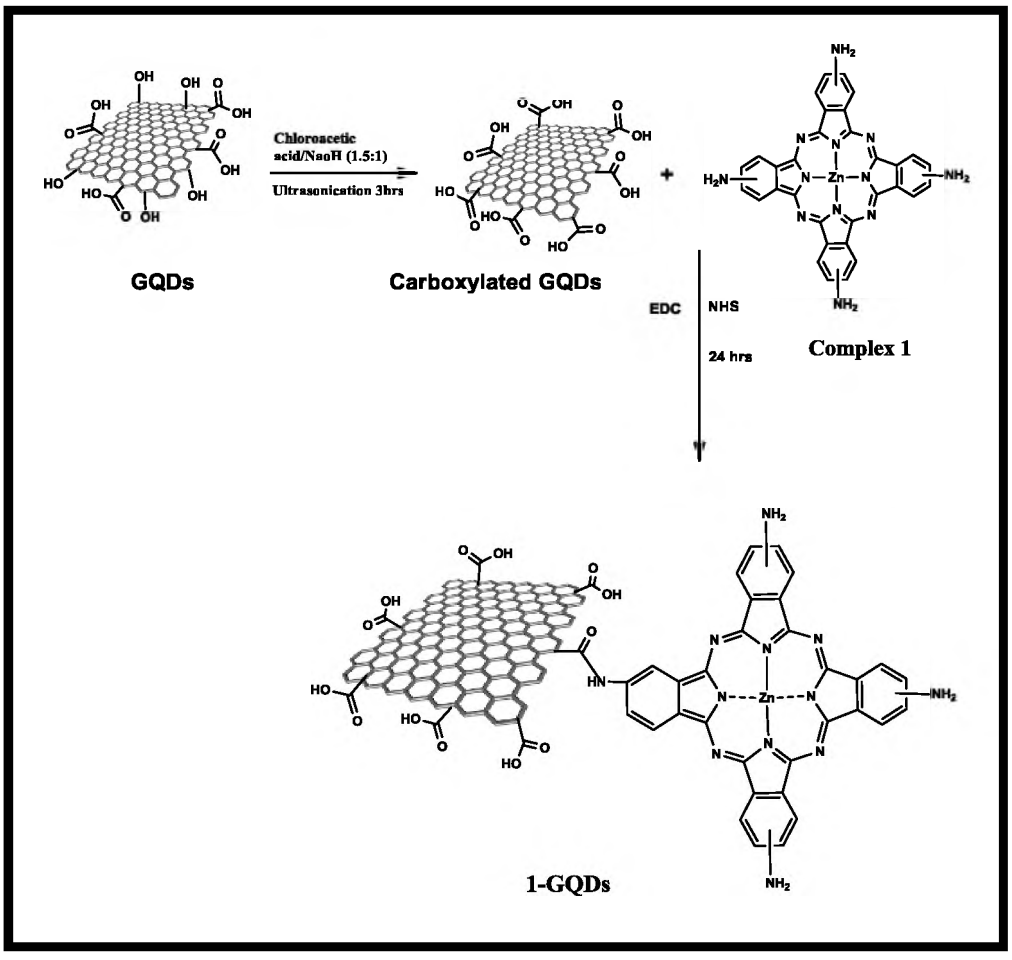

Scheme. 3.8. Illustration of MPc (1)-GQDs nanoconjugate preparation via covalent linkage.

Calculations revealed that the D:G ratio of GQDs is 0.51 (section 3.1.5) and decreases to 0.32 for 1-GQDs, The decrease in the D:G ratio is due to the increase in the intensity of the G band. Increases in G band have been associated with the removal of some amorphous carbons [228]. For the non-covalently

linked conjugates the presence of π-π stacking interaction between GQDs and the MPcs (**2-12**), resulted in a high density of sp^2 bonds vibrations, hence lower D:G ratios were generally observed. Defects of the graphene core structure of GQDs are not expected since the π-π interaction preserves the structural integrity of both interacting molecules.

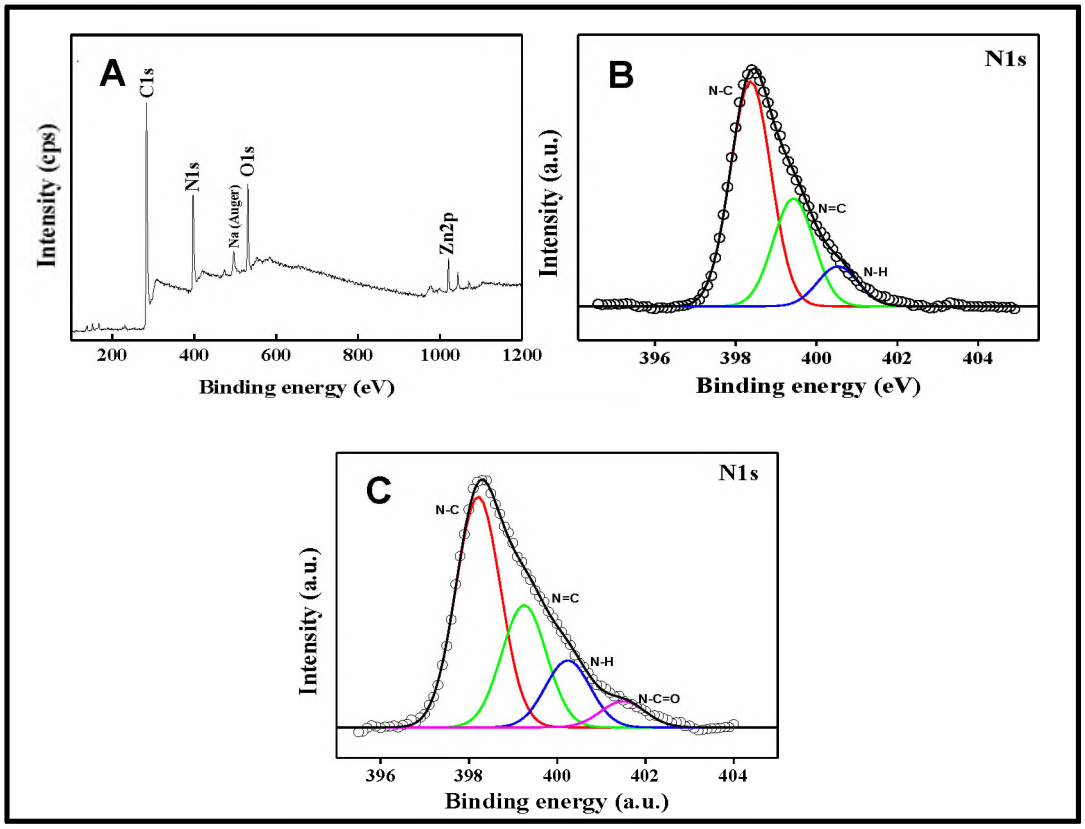

Fig. 3.27. XPS spectra of (A) wide scan for 1-GQDs, high resolution N1s spectra of (B) complex 1, and (C) 1-GQDs conjugate.

3.6.4. TEM analysis

A TEM image of the **1**-GQDs covalent nanoconjugate is shown Fig. 3.6E, which displayed some aggregation. Aggregation in MPcs is well documented **[157, 225]**, and reported to be due to the π-π stacking between the rings of MPcs. For **1**-GQDs, the grafting of more than one MPc to the surface of the GQDs is possible

due to the presence of extra -COOH groups on the surface of GQDs. The interaction between adjacent MPc molecules would result in aggregation as well. Also, since the linking of more than one molecule of GQDs to one molecule of complex **1** is less likely due to the small size of complex **1** (~1 nm) compared to GQDs, it is also possible that complex **1** can act as links between two GQDs forming a chain. This type of arrangement would result in interactions which may be observed as agglomeration in TEM.

TEM images for the non-covalent conjugates of GQDs and MPcs are shown in Fig. 3.6F, using **9**-GQDs as an example of others. As similarly observed in the case of **1**-GQDs nanoconjugate, the nanoconjugates of GQDs and MPc complexes **2-13** appeared to be aggregated. MPcs are known to show aggregation upon non-covalent interactions with carbon based nanomaterials **[157, 201, 228, 229]**. The visible particle-like dispersions of GQDs in the nanoconjugates indicate that the strong π-π interaction between GQDs and the respective MPcs could be ascribed to the excellent immobilizations of the MPcs onto GQDs as a result of the high density of delocalized π-electrons of both materials.

3.6.5. FT-IR

FT-IR analysis was deployed to elucidate the covalent linkage between GQDs and MPc complex **1**. The FT-IR spectrum of the covalently linked **1**-GQDs conjugate, Fig. 3.28 A (ii), shows peaks between 3525-3327 cm^{-1} attributable to N-H (stretching) and also 1665 cm^{-1} (C=O, N-H bend of amide), which shows the presence of an amide bond. The characteristic peak at 1665 cm^{-1} in **1**-GQDs was not observed in the FT-IR spectra of GQDs alone [Fig. 3.28 A(i)] or complex

1 alone [Fig. 3.28 A(iii)]. These results confirm the amide coupling between complex 1 and GQDs to form 1-GQDs nanocomplex.

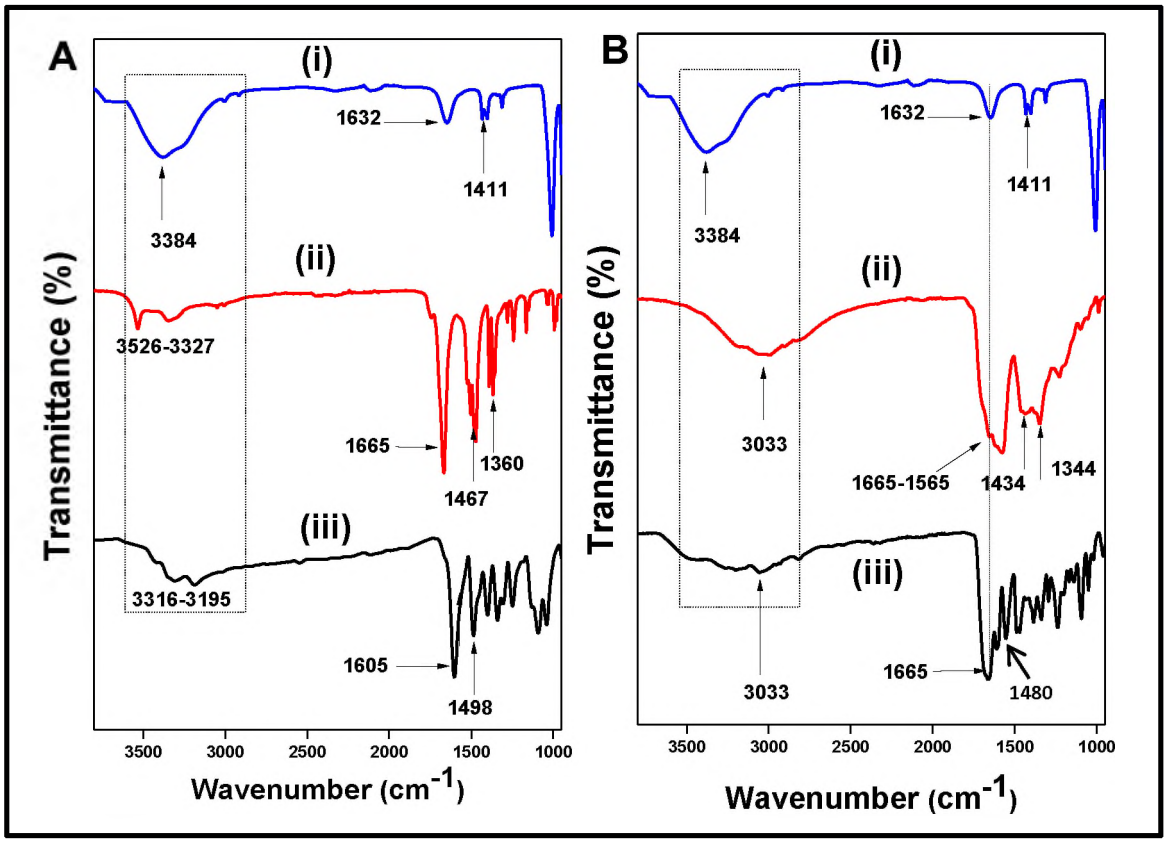

Fig. 3.28. FT-IR spectra for (A) GQDs (i), 1-GQDs (ii), 1 (iii), (B) GQDs (i), 9-GQDs (ii), and 9(iii).

FT-IR analysis was employed to characterize the non-covalently linked nanoconjugates of MPcs-GQDs (Fig. 3.28 B, 9-GQDs shown as an example of others). Vibrations of the hydroxyl group on the GQDs surface or edges were observed at 3384 cm^{-1} for GQDs (Fig. 3.28 B(i)) and appeared at around 3033 cm^{-1} for 9-GQDs. The –C=O stretching vibrations ca 1665-1565 cm^{-1} for 9-GQDs (Fig. 3.28 B (ii)) were more broadened compared to a single peak at 1632 cm^{-1} for GQDs alone. The peak occurring at 1434 cm^{-1} for 9-GQDs is attributed to –C=C- and it is present in GQDs and complex 9 alone [Fig. 3.28 B (iii)], but with

some shifts (1411 and 1480 cm^{-1}, respectively). The shifts in IR bands further confirmed structural changes as a result of new complexes formation [230].

3.6.6. DLS

The increase in the hydrodynamic sizes of the MPcs-GQDs nanoconjugates was confirmed by employing DLS experiments. The DLS results showed that the average sizes ranged from 14 to 46 nm, Table 3.4. The sizes of the nanoconjugates are larger relative to that of GQDs alone with size range of 3.5-19.5 nm (Table 3.2). Hence, the adsorption of the MPcs/MP to the GQDs surface via π-π stacking interaction was confirmed by the observed increase in sizes from the DLS experiments.

3.6.7. UV-Vis absorption spectral studies

The UV-Vis absorption spectra of **1**-GQDs (GQDs and complex **1** alone) are shown in Fig. 3.29 A. Following the covalent attachment of complex **1** to GQDs, the Q-band of complex **1** was slightly red-shifted to 718 nm (from 715 nm in DMF/PBS, this mixture was employed to allowed for the solubility of the MPc and GQDs), Fig 3.29 A (iii) and Table 3.4, with increase in absorption in the blue region due to the effects of the GQDs. The absorption spectrum of GQDs displayed strong absorption at 335 nm. The spectroscopic results obtained further confirmed the successful coupling of complex **1** to GQDs.

Non-covalent (π-π) stacking of MPc complexes (**2-13**) onto GQDs surface was achieved by utilizing the extensive π-electrons systems of MPcs/MP and GQDs. This form of interaction was further verified by the slight change in the UV-Vis absorption of the MPcs-GQDs conjugates as shown in Fig. 3.29 B (**9**-GQDs

shown as an example). MPs UV-Vis absorptions are characterized by intense bands called the Soret bands (mainly between 400-500 nm) with weak Q-band at ~650 nm. The ground state absorptions of **13**-GQDs nanoconjugate exhibit no significant shifts of the Soret band of complex **13** (Fig. 3.29C). The retention of the pyrene substituents absorptions around 322 and 339 nm further indicates the preservation of the structural integrity of complex **13** due to the π-π stacking interaction with GQDs.

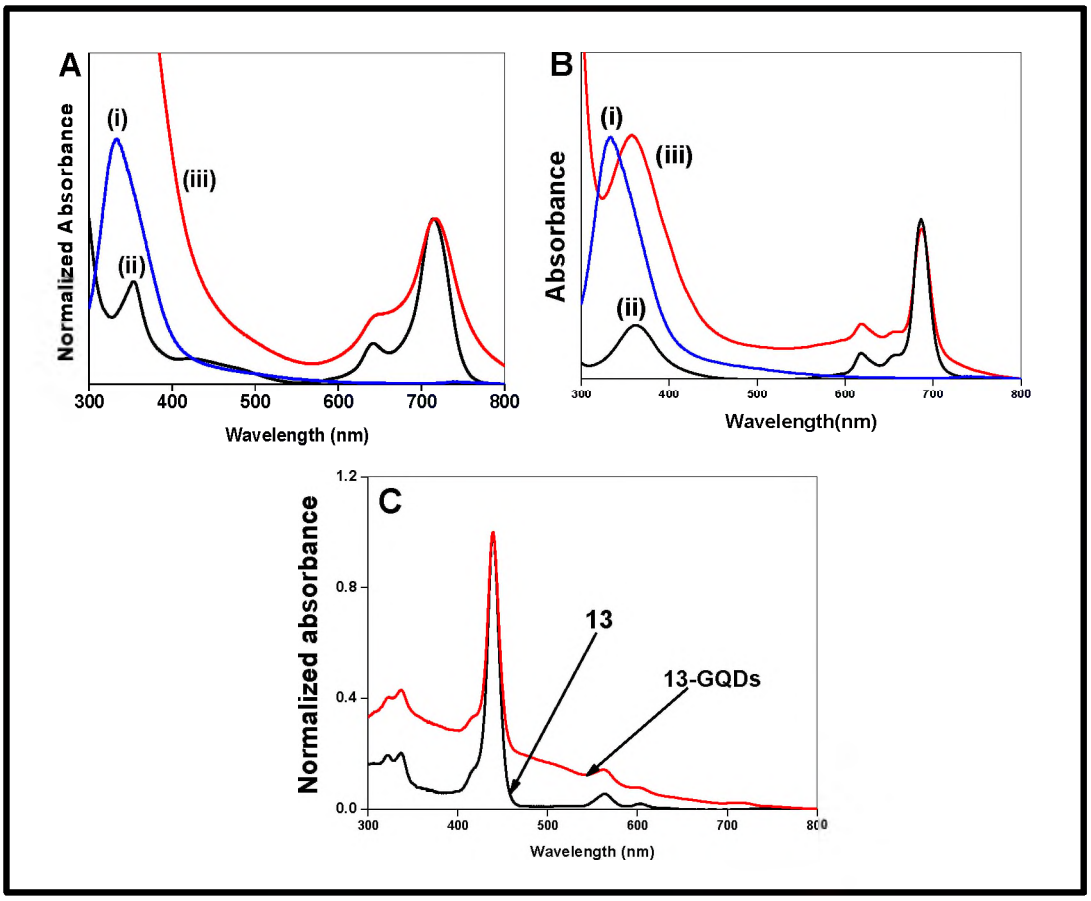

Fig. 3.29. UV-Vis spectra of (A) GQDs (i), complex 1 (ii) and 1-GQDs(iii), (B) GQDs (i), complex 9 (ii), 9-GQDs (iii), and (C) complex 13 and 13-GQDs. Solvent: (A) 4:1 (v/v) DMF: 50 mM PBS, (B) PBS (10 mM)(i) and DMF/PBS (ii-iii) and (C) DMF.

3.6.8. Fluorescence behaviour of MPcs-GQDs conjugates

Fluorescence quantum yields (Φ_F) were determined for GQDs conjugated to the respective MPcs as shown in Table 3.4.

The results showed reduction in the $\Phi_{F(GQDs)}^{Conjugate}$ and $\tau_{F(QDs)}$ of the MPcs-GQDs conjugates compared to GQDs alone at 0.21, due to the fluorescence quenching effects of the MPcs on GQDs, as similarly observed for other QDs (exciting where GQDs absorb) **[148, 231, 232].**

Forster resonance energy transfer (FRET) is the main proposed underlying mechanism for the apparent quenching of the fluorescence of GQDs triggered by their interaction with the MPcs.

For FRET phenomenon to occur there has to be an overlap between the donor (GQDs) emission and acceptor (MPcs derivatives) absorption spectra. Pristine GQDs and MPcs spectra showed to have weak overlaps (but stronger for SN-GQDs due to the red-shifted emission, Fig. 3.30 A shown as an example), hence some FRET is possible. There was a decrease in the fluorescence intensity (upon excitation at 340 nm, where GQDs absorb) within **2**-GQDs conjugate. This was followed by an emergence of an emission peak ~700 nm as shown in Fig. 3.30B due to FRET. Since excitation at 340 nm will also result in the excitation of the MPcs, fluorescence emission was recorded for the respective MPcs complexes (350-800 nm) in the absence of GQDs at 340 nm excitation. There was only a weak emission of the MPcs due to the excitation in the B-band region.

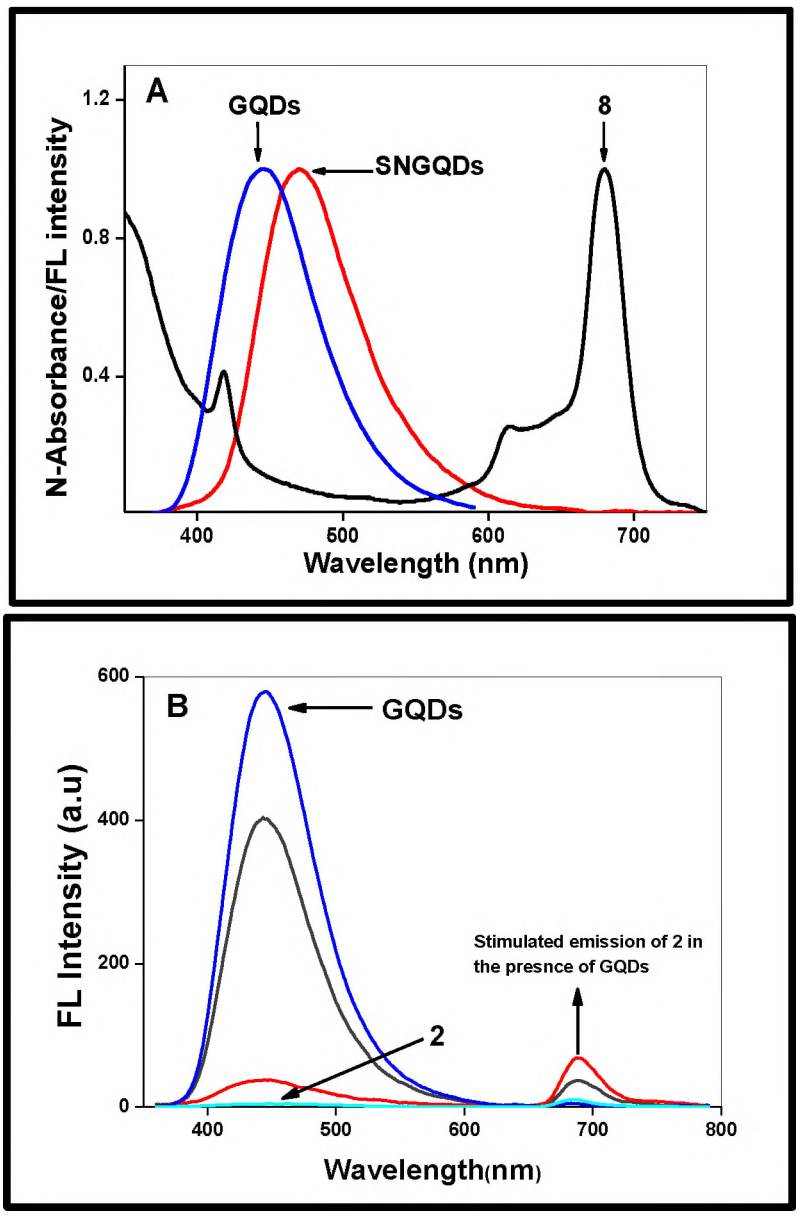

Fig. 3.30. (A) Normalized absorbance/fluorescence intensity showing the overlap between the emission spectra of GQDs or SNGQDs and absorption spectra of complex 8. (B) Stimulated emission of complex 2 (as an example of others) via energy transfer from GQDs within the conjugate. Excitation wavelength = 340 nm. Solvent: DMF/PBS (10 mM, pH 9).

It follows that the enhanced emission of the MPc complexes in the presence of GQDs must be due to fluorescence induced (stimulated emission) by GQDs onto

the MPcs. Similar observations have been reported where there are stimulated emissions in MPcs upon interaction with semiconductor QDs **[148, 231, 232]**, as similarly observed in this work. The E*ff* values for the conjugates listed in Table 3.4 are based on estimates since there might be other factors in addition to FRET which could influence the decrease in the fluorescence of GQDs. The largest E*ff* for MPcs-GQDs conjugates was observed for the **8**-SNGQDs due to better spectral overlap.

Similar to MPcs-GQDs conjugates, **13**-GQDs conjugate displayed weak fluorescence emission upon excitation at 340 nm where GQDs absorb (weaker in the MP conjugate) (Fig. 3.31A). This observation is an indication of the deactivation of GQDs emission resulting from mechanistic pathways involving energy transfer from GQDs to complex **13**. Similar observations have been previously reported in the literature where GQDs PL emission is attenuated upon coordination to MPs **[98, 233]**, possibly due to FRET as a result of the complete overlapping of GQDs emission spectra by complex **13** absorption spectra as shown in Fig. 3.31B. The comparative FRET efficiencies recorded for both class of macrocycles conjugates with GQDs are listed in Table 3.4; the MP-GQDs have higher FRET E*ff* than the MPcs-GQDs conjugates, which is ascribed to the complete spectra overlap in the former. In order to further understand the extent of the mutual interaction between GQDs and complex **13**, fluorescence quantum yield ($\Phi_{F(P)}$) and lifetime ($\tau_{(P)}$) were evaluated (by exciting where complex **13** absorbs) in the presence of GQDs and the results reflected large increase in the fluorescence lifetime ($\tau_{F(P)}$) of the conjugate (Table 3.4).

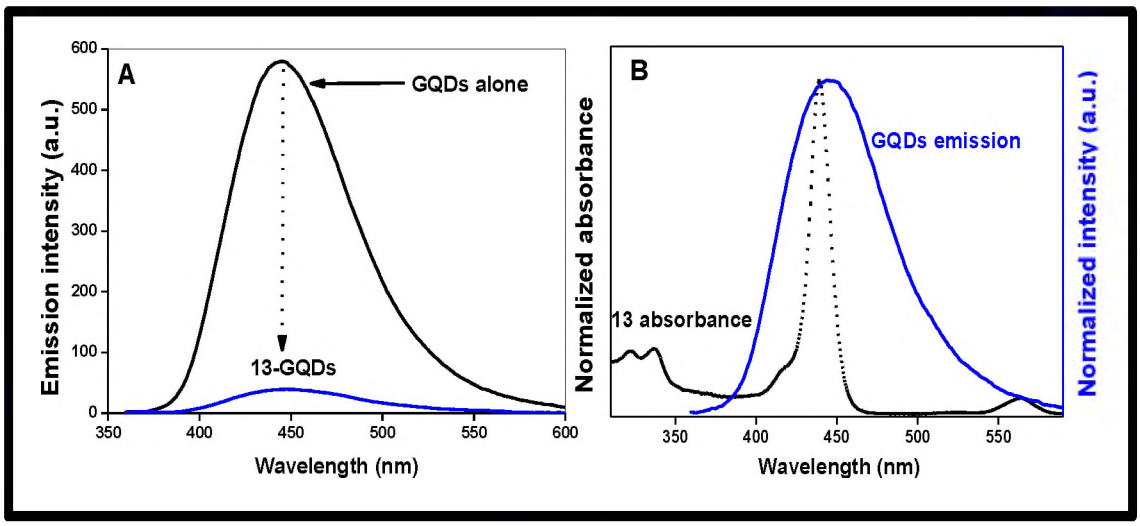

Fig. 3.31. (A) Fluorescence spectra of GQDs alone and upon non-covalent conjugation to 13 as an example. (B) UV-Vis spectrum of 13 and emission spectrum of GQDs showing the complete spectral overlap. Solvent: DMF.

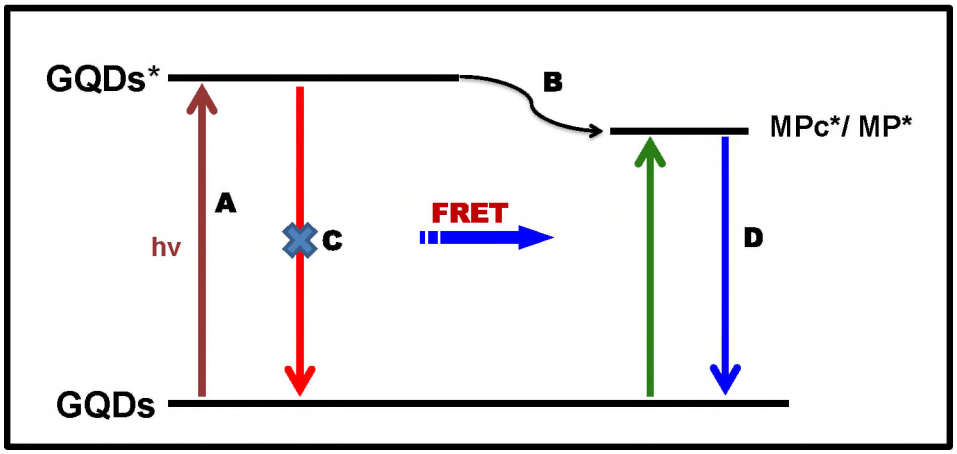

Fig. 3.32. Interaction pathways between GQDs and MPcs or MPs leading to the quenching of the GQDs emission upon coordination. A = excitation, B = energy transfer, C= deactivation of exciton relaxation and D = possible stimulated emission.

The increase in the fluorescence parameters ($\Phi_{F(P)}$ and $\tau_{F(P)}$) of complex **13** upon coordination to GQDs could indicate that energy transfer process must have

occurred between GQDs and complex **13** resulting in the quenching of the fluorescence of GQDs, since GQDs acted as the energy donor to complex **13**. A general possible interaction pathway between GQDs and the MPcs or MP is further illustrated in Fig. 3.32.

The fluorescence intensity of GQDs is substantially reduced in the presence of MPc/MP relative to GQDs alone; this feature may be attributed to the blocking of the radiative recombination pathway (**C**) of GQDs excitons due to the transfer of energy (FRET) to the MPcs/MP (**B**). The energy accepted by the MPcs/MPc could in turn be radiated (lost) where a stimulated emission may be observed in the MPc//MP complexes (**D**).

3.7. Non-covalent (π-π) conjugates of 8-gCNQDs

Non-covalent (π-π) coordination of complex **8** (TEMPO-ZnPc) to pristine gCNQDs was carried out by taking advantage of the planar aromatic structures of both gCNQDs and complex **8**. Table 3.6 shows the optical parameters recorded for the conjugate. Scheme 3.9 shows non-covalent (π-π) stacking of **8** onto gCNQDs.

Table 3.6. Optical parameters of gCNQDs and 8-gCNQDs.

Complex	$\lambda_{absorption}$ (nm)	$\Phi_F \pm 0.01$	τ(ns) ($\pm$ 0.10)	Size (nm)
Pristine gCNQDs	332/334[b]	0.43	7.40	6.5
8	679	(0.19)	(1.59)	-
8-gCNQDs	679	0.05 (0.21)[#]	0.9 (2.2)[#]	19.8
8-GQDs	679	0.15	0.9	20

[#] Values in brackets are for excitation where MPc (8) absorbs.

3.7.1. TEM and DLS

8-gCNQDs non-covalent conjugate was subjected to TEM analysis. The TEM micrograph acquired showed the clustering together of complex **8** and gCNQDs which could be due to the adsorption and/or agglomeration of complex **8** onto the gCNQDs planar surface as observed above (Fig. 3.6) and for previously reported QDs-MPcs conjugates **[148, 150]**. DLS results showed that **8**-gCNQDs conjugate possesses a mean size of 19.8 nm (Table 3.6), which is larger than gCNQDs alone recorded at 6.5 nm, but same as **8**-GQDs at 20 nm. This further shows the adsorption of complex **8** onto gCNQDs to form its hybrid complex of **8**-gCNQDs.

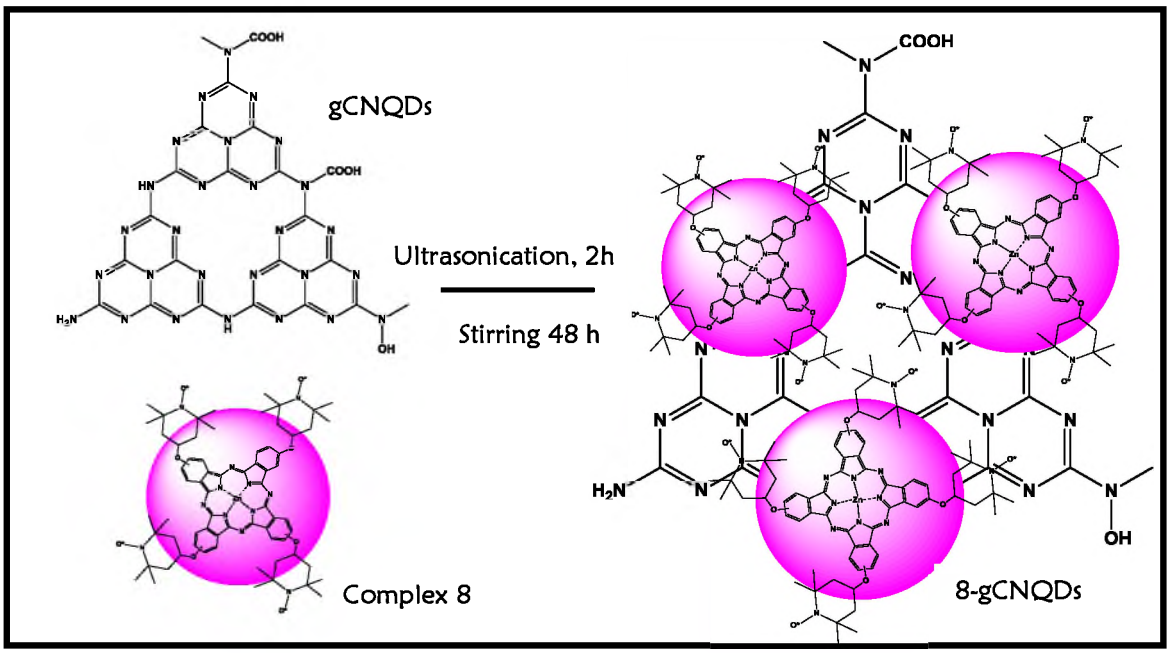

Scheme 3.9. Representation of the non-covalent, **π-π** stacking of gCNQDs with complex 8.

3.7.2. Optical properties

UV-Vis absorption of complex **8** with the characteristic Q-band was observed at ~ 679 nm (in DMSO), Fig. 3.33A (b), Table 3.6. Then, after coordination of complex **8** to gCNQDs to form **8**-gCNQDs conjugate, the obtained hybrid displayed absorptions confirming the presence of complex **8** and gCNQDs in the hybrid, as shown in Fig. 3.33A(c). Due to the predominance of gCNQDs absorption in the blue region of the spectrum, there was a sharp increase in absorbance in this region (below the 600 nm). No shift in the Q-band attributed to complex **8** component of the hybrid was observed as compared to complex **8** alone.

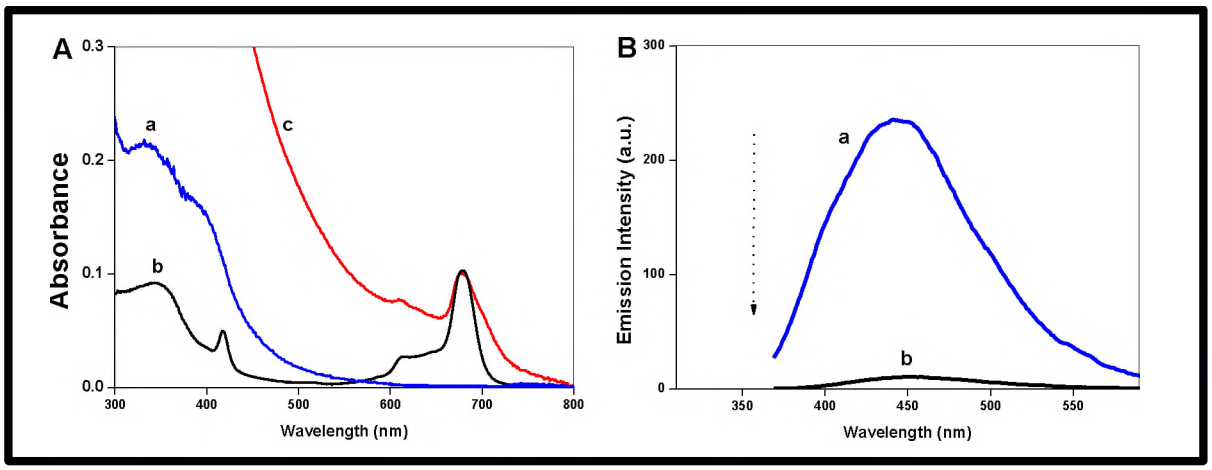

Fig. 3.33. (A) UV-Vis spectra of gCNQDs (a), complex 8 (b), and 8-gCNQDs (c). (B) Emission spectra of gCNQDs (a), and 8-gCNQDs (b) at 360 nm excitation wavelength. Solvent: DMSO.

Negligible changes in the Q-bands of MPcs upon coordination to carbon nanomaterials are known and widely observed **[145]**. The peak at about ~410 nm in the absorption spectrum of complex **8** is due to TEMPO moieties on the complex **8** ring. Fluorescence behaviour of gCNQDs in the presence of complex

8 was also explored. It was observed that at similar excitation wavelength of 360 nm, **8**-gCNQDs (π-π) hybrid displayed suppressed fluorescence of gCNQDs [Fig. 3.33B (b)], as compared to gCNQDs alone, Fig. 3.33B (a), due to the quenching effect of complex **8** on the gCNQDs. Φ_F and τ_F values of gCNQDs decreased upon coordination to complex **8** (Table 3.6). Based on this quenching observation, it is highly plausible to conclude that complex **8** could draw some energy from the gCNQDs via FRET, thereby deactivating the radiative recombination pathways of the gCNQDs, which leads to the quenching of the fluorescence of gCNQDs similar to that of MPcs-GQDs conjugates above.

3.8. Conclusion

Pristine GQDs and their functionalized derivatives were synthesized and characterized. Results obtained demonstrated the successful preparation of the intended GQDs. Further, conjugates of the GQDs with 4A-TEMPO, Au@Ag NPs and MPcs were prepared via covalent and non-covalent conjugation. Various spectroscopic techniques were deployed for their characterization and the results obtained, as presented in this chapter, confirmed that the conjugates were formed. The nature of the interaction between the GQDs and MPcs leading up to the change in fluorescence properties of the GQDs was elucidated.

4. Ascorbic acid detection using TEMPO derivatives

This chapter describes the detection of ascorbic acid (AA) using TEMPO-derivatized GQDs, gCNQDs and TEMPO-ZnPc-GQDs/gCNQDs conjugates.

TEMPO has a specific affinity to interact with AA, hence the various platforms are compared.

Table 4.1, summarizes the target analytes and the corresponding nanoprobes designed for their detection in this thesis.

Table 4.1. List of analytes detected in this work and the fabricated probes employed.

Analyte	Probe
AA	GQDs-4A-TEMPO
	SNGQDs-4A-TEMPO
	gCNQDs-4A-TEMPO (embedded)
	gCNQDs-4A-TEMPO (linked)
	8-GQDs
	8-SNGQDs
	8-gCNQDs
Biothiols (Cys, Hcy and GSH)	PEI-GQDs-Au@Ag
	PEI-GQDs-Au@Ag-Hg
	PEI-GQDs-5-Au@Ag
	PEI-GQDs-5-Au@Ag-Hg
	M-GQDs
	12-GQDs
Hg	T-GQDs
	4-7-GQDs
	9-GQDs
	9-T-GQDs
	PEI-GQDs-5-Au@Ag

Note: Complexes 1-3, 10, 11 and 13 not employed for sensing, only photophysical studies.

4.1. GQDs and TEMPO

4.1.1. Fluorescence quenching of GQDs by 4Acetamido-TEMPO

This section reports on the fluorescence quenching of GQDs emission upon interaction with 4Acetamido-TEMPO (4AC-TEMPO) as a proof-of-concept of the sensing abilities of GQDs. Expectedly, fluorescence of the GQDs (pristine, N-doped or S, N co-doped) were efficiently quenched at different concentration of 4AC-TEMPO upon simple mixing (4AC-TEMPO was employed here due to its availability). It has been widely reported that fluorescence quenching can occur between unbonded GQDs fluorophores and quencher molecules (upon simple mixing) **[234]**. Simple mixing could be important due to the fact that some properties which are important for bio-assays and applications are preserved **[235]**. GQDs may interact with a wide array of molecules through π-π stacking, electrostatic interaction, and chemical bonding resulting in the quenching of their fluorescence **[5, 6, 236]**. Stable free radicals of TEMPO compounds are known fluorescence quenchers and are used in this work to quench the fluorescence of GQDs. For quenching experiments, aqueous buffered solutions of GQDs, N-GQDs and SN-GQDs were titrated with varying concentrations of 4AC-TEMPO.

The quenching studies were investigated by combined steady state and time resolved fluorescence spectroscopic measurements. The tendency to suppress or quench the fluorescence intensity of GQDs upon interaction with metal ions and organic compounds has led to the fabrication of GQDs based nanosensors **[5, 6, 236]**. Studies on the use of GQDs to scavenge reactive oxygen species (ROS) are sparse or non-existent. Hence, it is expected that the results of the work in this

section, presents an understanding of the fluorescence switching of GQDs in the presence of molecules with specific and selective affinity for free radicals.

Fig. 4.1 shows the quenching of the fluorescence of N-GQDs upon addition of various amounts of 4AC-TEMPO. The fluorescence intensity gradually decreased as the concentration of 4AC-TEMPO was increasingly varied. Changes were not observed in the spectral peak width or emission wavelength maxima of the spectra recorded for all the GQDs.

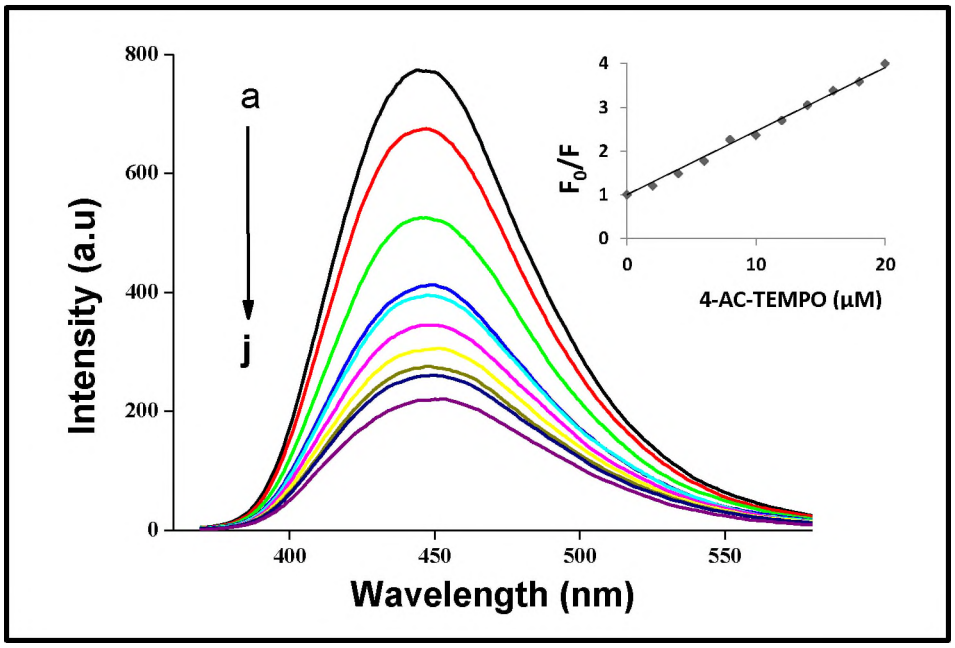

Fig. 4.1. Fluorescence spectra of (A) N-GQDs (as an example) in the presence of increasing concentration of 4AC-TEMPO in PBS (pH 9.2, 50 mM). [4AC-TEMPO] a-j: 2.0, 4.0, 6.0, 8.0, 10.0, 12.0, 14.0, 16.0, 18.0, 20.0 µM. Inset: corresponding Stern-Volmer plot. Starting concentration of GQDs = 2 mL of 1.0 mg/ml.

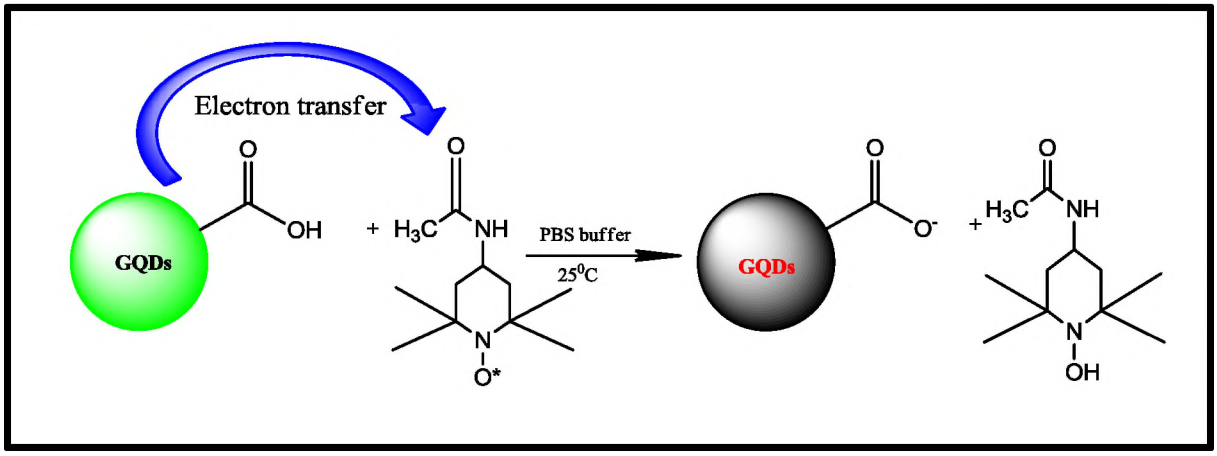

Scheme 4.1. Plausible Interaction mechanism between GQDs and 4acetamido-TEMPO.

Charge/energy transfer leading to the non-radiative relaxation of excitons due to the collision with interacting molecules has been proposed to lead to fluorescence quenching in GQDs **[12, 237]**. It is can be assumed that 4AC-TEMPO and GQDs are in close proximity, resulting in photoinduced electron transfer (PET) from the latter to the former as depicted Scheme 4.1.

The quenching of the fluorescence of GQDs and its doped derivatives by 4AC-TEMPO free radical can be described by the Stern-Volmer equation (Eq. 4.1):

$$\frac{F_0}{F} = 1 + K_{SV}[Q] \qquad (4.1)$$

where F_0 and F are the FL intensities of GQDs in the absence and presence of 4AC-TEMPO, respectively. K_{sv} is the Stern–Volmer quenching rate constant which is related to the quenching efficiency. The K_{sv} values were obtained from the slopes of the Stern-Volmer plots (inset in Fig. 4.1) and the values are listed in Table 4.2.

Table 4.2. Stern Volmer quenching constant (K_{SV}) and bimolecular quenching constant (k_q) obtained for the GQDs in the presence of 4AC-TEMPO. Temperature depend K_{SV} also shown at 25, 32 and 40 ^{o}C.

QDs	K_{SV} (M^{-1})	k_q ($dm^3\ mol^{-1}\ s^{-1}$)	K_{SV}		
			25 (^{o}C)	32 (^{o}C)	40 (^{o}C)
GQDs	1.3×10^4	2.5×10^{13}	1.1×10^4	9.8×10^3	8.9×10^3
N-GQDs	1.5×10^5	2.0×10^{13}	9.6×10^4	8.3×10^4	6.1×10^4
SN-GQDs	1.7×10^5	1.5×10^{13}	1.2×10^5	1.0×10^5	9.2×10^4

The K_{sv} value of SN-GQDs was the highest, suggesting that the fluorescence of SN-GQDs is most efficiently quenched by TEMPO. This might be attributed to the following possible reasons: (i) the disruption of the electrical neutrality of the sp^2-hybridized carbon atoms of SN-GQDs graphene core by the electron rich N and S atoms leading to charged sites within the intrinsic states **[12, 36, 196]** which favour more interaction with TEMPO. (ii) The S and N atoms on SN-GQDs introduces new surface states **[196]**, thus creating emissive traps for electron-hole recombination. The interaction of the new surface states with TEMPO free radicals could prevent the excitons from recombining due to the transfer of the electrons to the free radical molecules of 4AC-TEMPO. To further elucidate the mode of the interaction leading up to the quenching, temperature-dependent quenching studies were carried and as shown in Table 4.2, the Stern-Volmer quenching constants (K_{SV}) obtained were inversely related to

temperature, which indicates that the probable quenching mechanism was initiated by complex formation rather than by dynamic collision [238].

The bimolecular quenching constant k_q was determined using Eq. 4.2.

$$K_{SV} = k_q \tau_F \qquad (4.2)$$

where τ_F is the fluorescence lifetime of the GQDs in the presence of 4AC-TEMPO. The k_q values are higher (being in the order of 10^{13} dm^3 mol^{-1} s^{-1}, Table 4.2) than the proposed value for dynamic quenching (10^{10} dm^3 mol^{-1} s^{-1}) [239], hence indicating that the quenching occurred via static quenching mechanism.

To further understand the nature of the interaction of the GQDs with 4AC-TEMPO, changes in the UV-Vis absorption spectra of 4AC-TEMPO with time in the presence of GQDs, N-GQDs and SN-GQDs (using the latter two as examples) were recorded and shown in Fig. 4.2. The absorption of 4AC-TEMPO at 426 nm gradually decreased with time following the addition of fixed concentrations of the respective GQDs. A new peak was formed near 340 nm. The spectral changes as shown in Fig. 4.2 confirmed the formation of ground-state complexes between the GQDs and 4AC-TEMPO. The likely new product which absorbs near 340 nm was not fluorescent. It is most likely the hydroxylamine derivative of 4AC-TEMPO as shown in Scheme 4.2 [240].

Electron paramagnetic resonance (EPR) analysis was carried out to further elucidate the interaction dynamics between 4AC-TEMPO and the GQDs (N-GQDs and SN-GQDs) as shown in Fig. 4.3. Nitroxides (TEMPO) are well known spin labels for EPR studies due to the stability of the unpaired electrons [241]. Hence, EPR measurements could provide information about the spatial

distribution and behaviour of TEMPO free radicals in the presence of fluorophores [240, 241].

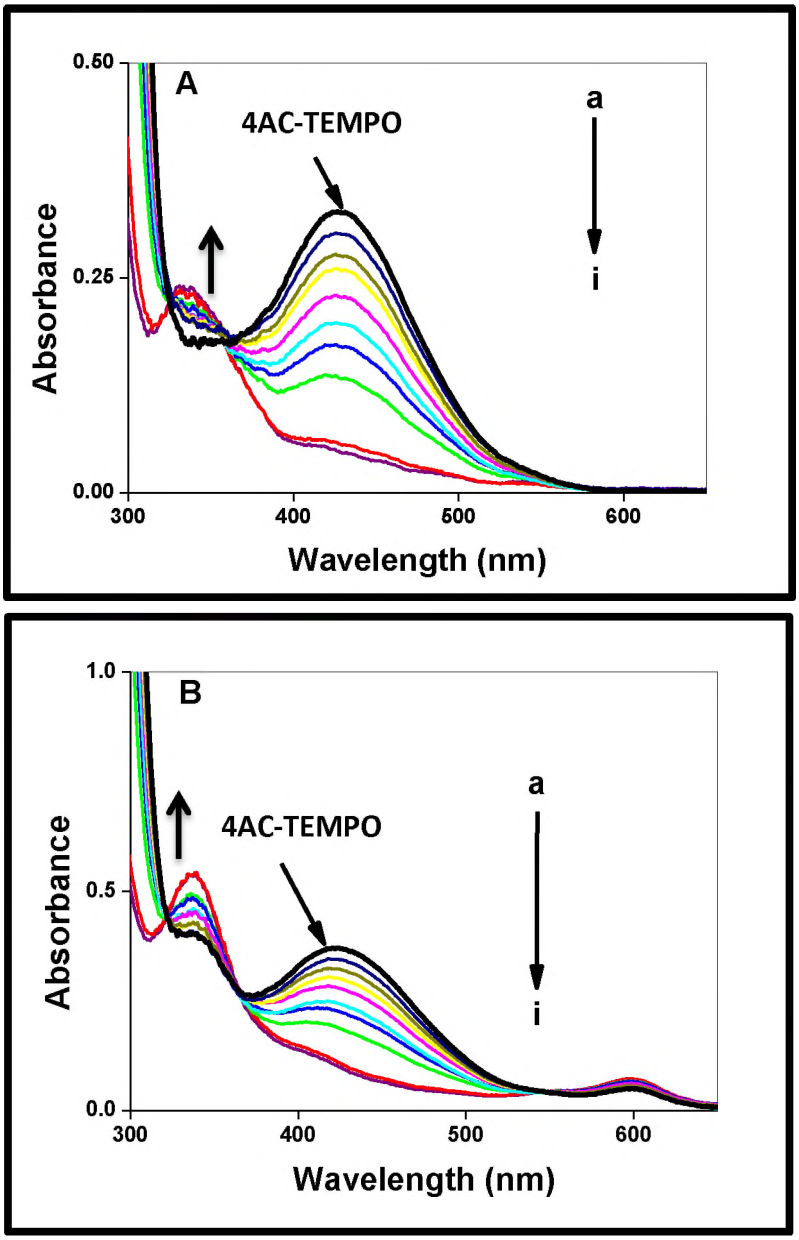

Fig. 4.2. UV-Vis spectra changes of 4AC-TEMPO with time following the addition to 1.0 mg/mL of (A) N-GQDs, and (B) SN-GQDs. a-i: 0, 0.08, 0.17, 0.25, 0.5. 1, 4, 6, 10, 12, 15 h. Solvent: PBS buffer (pH 9.2) solution.

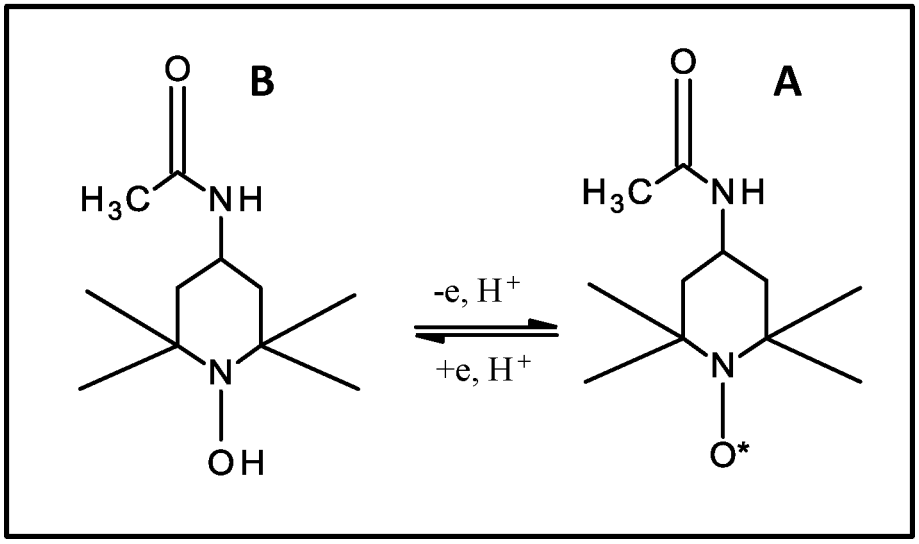

Scheme 4.2. A representation of the transformation of 4AC-TEMPO (A) to diamagnetic hydroxylamine (B) upon electron transfer [240].

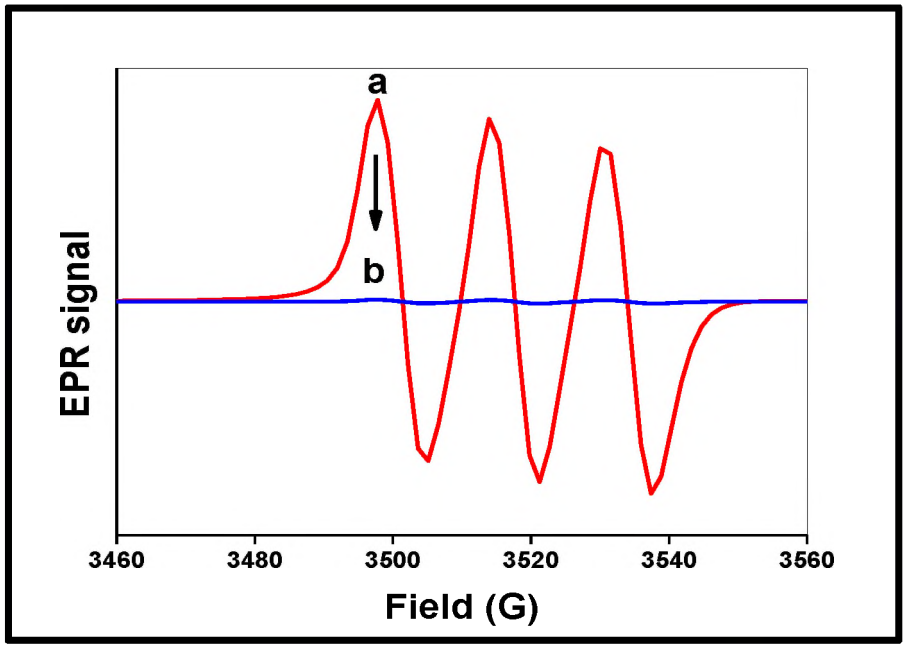

Fig. 4.3. EPR spectra of 4acetamido-TEMPO (a) and in the presence of pristine GQDs (b) shown as an example, recorded in 50 mM PBS of pH 9.2.

As confirmed above, a ground-state complex was formed between 4AC-TEMPO and the GQDs. There was no clear EPR signal of 4AC-TEMPO upon interaction

with the GQDs (Fig. 4.3, pristine GQDs shown as an example). The results confirm that the likely new product is not a radical as stated above.

4.1.2. AA detection using GQDs/SNGQDs-4A-TEMPO

In this section, the sensing of AA as target analyte using GQDs/SNGQDs-4A-TEMPO (4A = 4-Amino) systems is discussed. For this study, pristine GQDs or SN-GQDs were covalently attached to 4A-TEMPO (4A-TEMPO was employed in order to use the NH_2 for linking). GQDs may be used as "turn ON" fluorescence sensors in the presence of analyte (as demonstrated in this work), following the fluorescence "turn OFF" by quenchers such as TEMPO free radicals. The fluorescence may be restored in the presence of suitable molecules which possess a strong and selective affinity to interact with TEMPO such as AA, which has been detected selectively using TEMPO free radical **[242-245]**. Hence, AA is employed in this work as a test analyte.

The design of fluorescence "turn ON" nanoprobes for AA sensing using GQDs and its N or S, N derivative after being functionalized with 4A-TEMPO is reported. The deployment of SN-GQDs-4A-TEMPO nanoconjugate in particular, was an attempt to improve the sensitive detection of the test analyte (AA) due to the better fluorescence properties of SN-GQDs compared to pristine GQDs, Table 3.2. GQDs or SN-GQDs were covalently tethered to 4A-TEMPO via EDC/NHS chemistry as shown in Scheme 4.3. The resulting conjugates exhibited quenching of the fluorescence of GQDs (weak emission) due to the quenching ("turn OFF") effect of 4A-TEMPO (in a manner similar to Fig. 4.1).

4.1.2.1. Fluorescence "turn ON"

The quenched fluorescence of GQDs could be "turned ON" in the presence of AA as judged by the enhancement of the fluorescence upon the addition of AA to aqueous solutions of SN-GQDs-4A-TEMPO as shown in Fig. 4.4A, as an example.

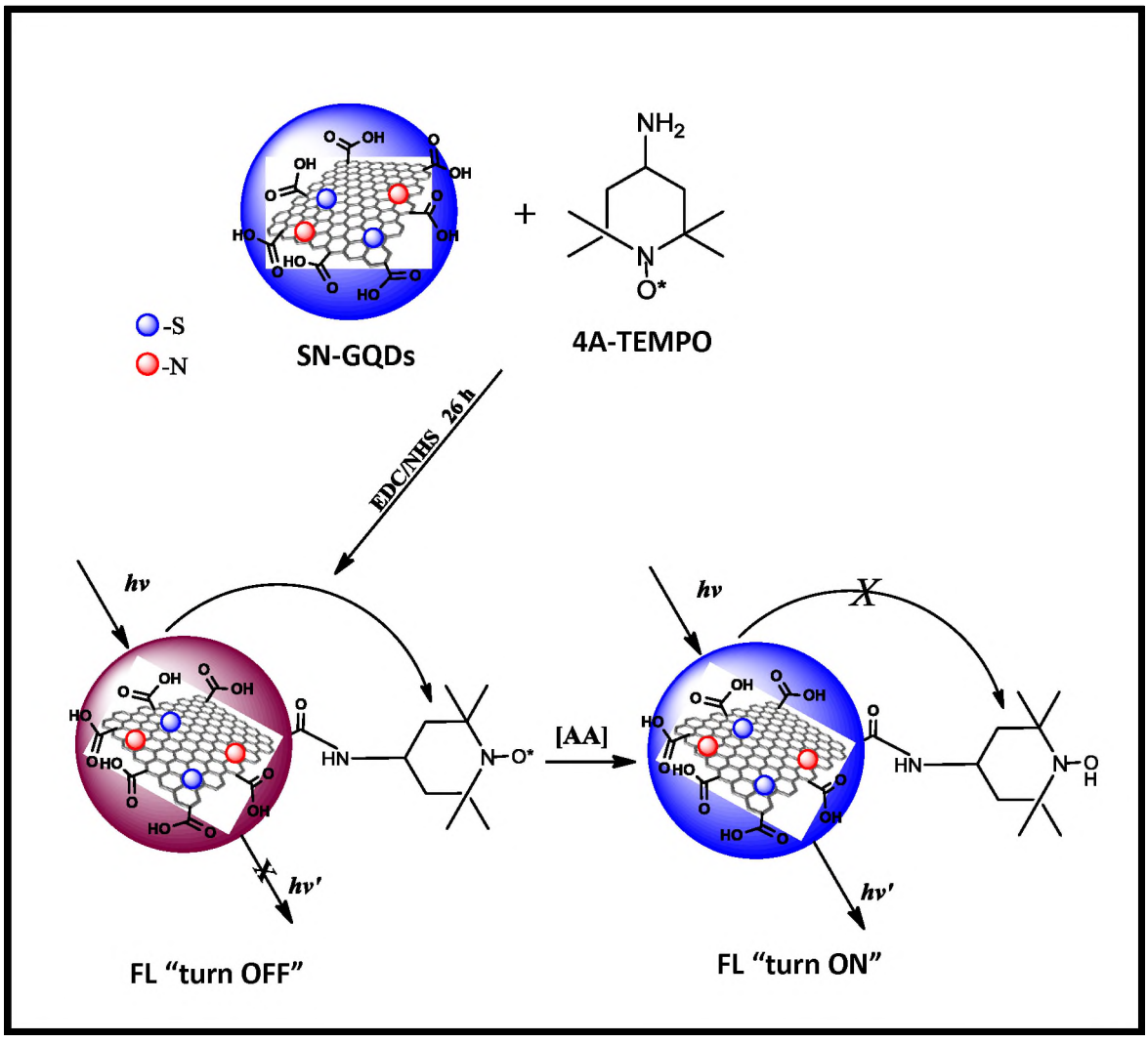

Scheme. 4.3. Covalent linkage of SN-GQDs to 4A-TEMPO and "*off-on*" switching of SN-GQDs fluorescence in the presence of AA.

To ascertain that the fabricated sensor probes could respond to the presence of AA in nanomolar concentrations, calibration curves of the fluorescence intensity as a result of the presence of AA were constructed (shown as inset in Fig. 4.4A) using Eq. **4.3 [246]**.

$$\frac{F-F_0}{F_0} = 1 + K[AA] \qquad (4.3)$$

where F_0 and F are the fluorescence intensities before and after addition of AA, respectively, K is the fluorescence enhancement factor and [AA] is AA concentration. Please note that $F\text{-}F_0/F_0$ was used due to fluorescence enhancement instead of F_0/F (in Eq. 4.1) normally used to indicate a fluorescence quenching process.

The limits of detection (LODs) were evaluated using Eq. **4.4**.

$$LOD = 3\delta/K \qquad (4.4)$$

(where δ is the standard deviation of blank measurement (n=11) and K is the slope of the calibration graphs). In the calibration graphs, $[(F\text{-}F_0)/F_0]$ represents the fluorescence emission recovery as a result of the increasing concentration of AA in Fig. 4.4A (inset). The linear ranges were found to be 0.1-5.5 μM for SN-GQDs-4A-TEMPO and 0.5-5.7 μM for GQDs-4A-TEMPO as shown in Table 4.3. The LODs were 84 nM and 60 nM for GQDs-4A-TEMPO and SN-GQDs-4A-TEMPO, respectively. Thus, it can be concluded that the nanoprobes present improved fluorescence sensing approach for AA quantification in terms of sensitivity, rapidity and simplicity when compared to some detection systems reported, Table 4.3 **[89, 164, 247-252]**.

Table 4.3. Comparison of the sensitivity of all the designed nanoprobes for AA detection in this work with some reported analytical techniques for the detection of AA.

Method	LOD	Linear range	REF.
Chemiluminescence	5 µM	10-100 µM	[247]
Electrochemistry(Ag-Valine GCE)	3.0 µM	0.01-1.0 mM	[248]
Electrochemistry (Complex 8)	1.75 µM	2.5-100 µM	[164]
Fluorescence (CdTe QDs)	74 nM	0.3-10 µM	[249]
Fluorescence (Au NCs)	0.2 µM	1.5-10 mM	[250]
Fluorescence (GQDs-Cu^{2+})	94 nM	0.3-10 µM	[89]
Fluorescence time-gated technique (Eu^{3+} and TEMPO)	9.1 nM	-	[251]
Fluorimetry (CdSe-DPC)	2 nM	60-300 nM	[252]
GQDs-4A-TEMPO	84 nM	0.5-5.7 µM	This work pH 9
SNGQDs-4A-TEMPO	60 nM	0.1-5.5 µM	This work pH 9
8-GQDs	0.8 nM	0.7-15 nM	This work
8-SN GQDs	0.2 nM	2.7-25 nM	This work
gCNQDs-4A-TEMPO (embedded)	0.15 nM	0.5-50 nM	This work pH 7
gCNQDs-4A-TEMPO (linked)	1.25 nM	1-100 nM	This work pH 7
8-gCNQDs	0.55 nM	1-100 nM	This work pH 7

4.1.2.2. Optimization studies

The effect of pH on the detection sensitivity was studied, because it has been reported that the fluorescence of GQDs is affected by pH **[85]**. Different pH were tested and it was observed that GQDs are strongly fluorescent in neutral to alkaline media, whereas the fluorescence is completely quenched in acidic media. Stable fluorescence intensity was observed over a long range of pH 8-10 as shown in Fig. 4.5A. Thus, pH 9.0 was chosen as a suitable pH for the fabrication of the nanoprobes for the sensitive detection of AA.

Also investigated was the concentration of the probes which could result in optimum recovery of the fluorescence intensities. Different concentrations (1.0-2.5 mg/mL) of the probes solution were screened in the presence of fixed concentration of AA (5 μM). SN-GQDs-4A-TEMPO probe showed better restored fluorescence intensity than GQDs-4A-TEMPO at similar concentrations with both peaking at 2.0 mg/mL concentration. Thus, all other investigations were carried out at a concentration of 2.0 mg/mL.

4.1.2.3. Selectivity studies

AA is known to possess the specific affinity for TEMPO free radicals **[192, 197]**; hence fluorophores attached to TEMPO compounds have been specifically deployed as probes to selectively detect AA **[192, 197, 253]**. Biomolecules with properties similar to AA were also evaluated for fluorescence recovery so as to assess the selectivity of the nanoprobes towards AA detection.

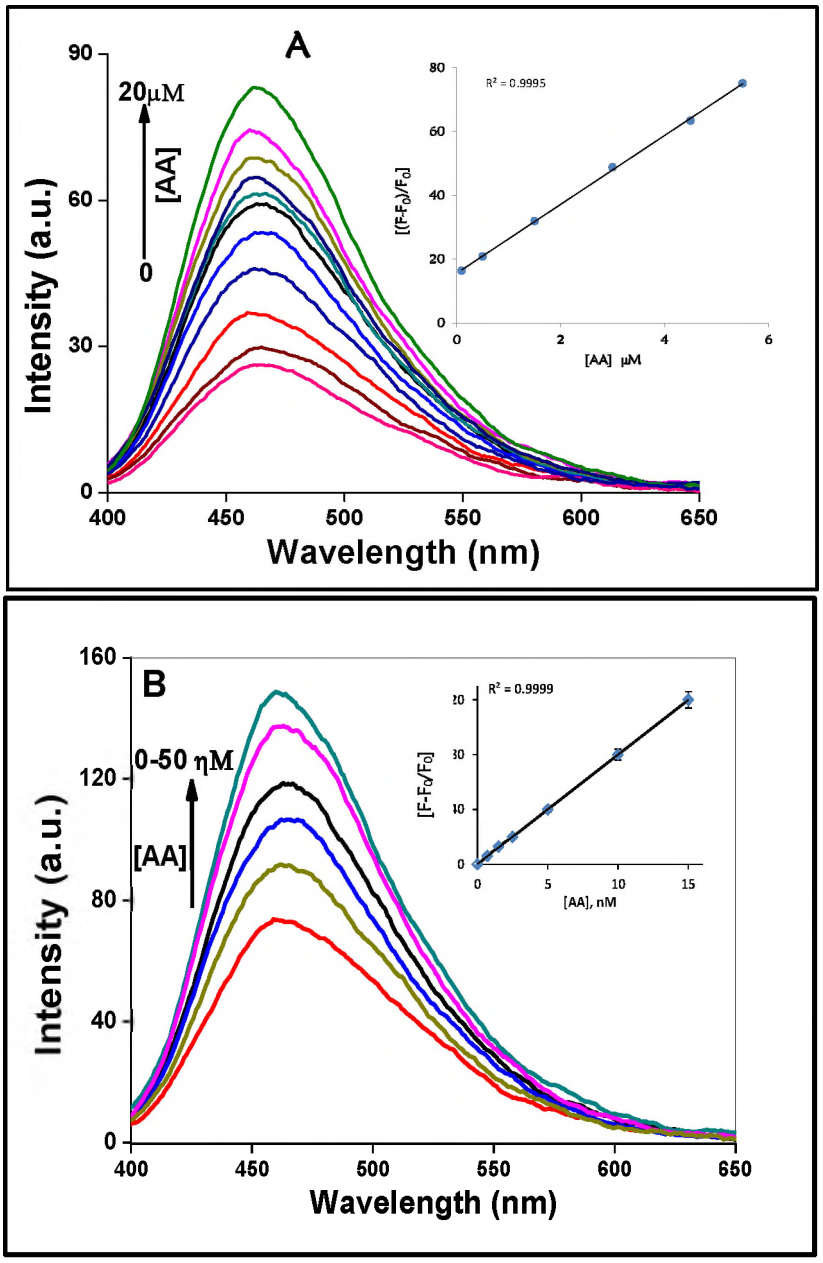

Fig. 4.4. (A) Fluorescence spectra of (A) SN-GQDs-4A-TEMPO (2 mg/mL), and (B) 8-GQDs in the presence of different concentrations of AA (0-20 and 50 μM). Insets: calibration graphs. Solvent: PBS (50 mM, pH 9.0 and DMSO). Excitation wavelength = 380 and 350, respectively.

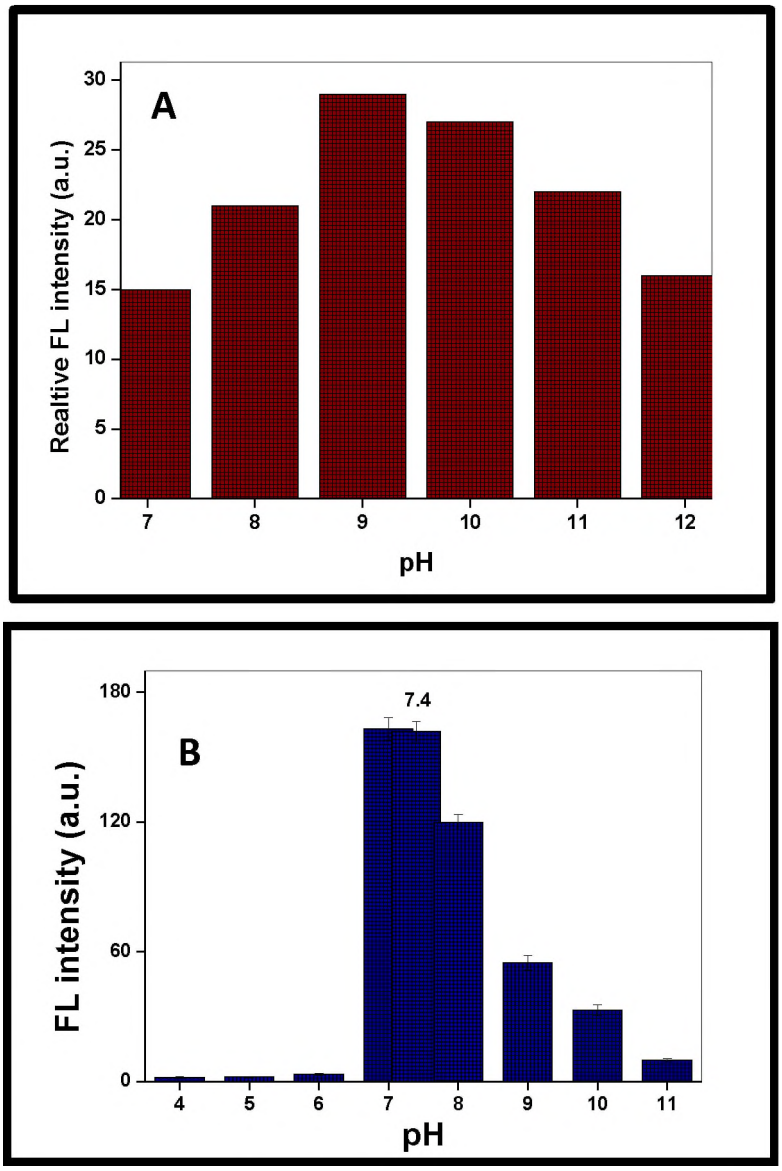

Fig. 4.5. Effect of pH on the fluorescence response of (A) GQDs-4A-TEMPO - 2 mg/mL, and (B) gCNQDs-4A-TEMPO (embedded) nanoprobes towards AA detection. Solvent is PBS [50 mM, pH 9 (A), and 10 mM, pH 7 (B)].

As shown in Fig. 4.6A, glutathione (GSH), L-cysteine (L-Cyst), citric acid (CA), folic acid (FA), oxalic acid and glucose (GLU) were investigated under optimized conditions and at concentrations of 500 μM (which is about 100 fold higher than the upper limit of the linear range for AA).

The relative fluorescence intensities of the tested molecules (after replicate measurements (n=3) and a tolerable error limit of ±5.0% in the fluorescence intensities) were recorded.

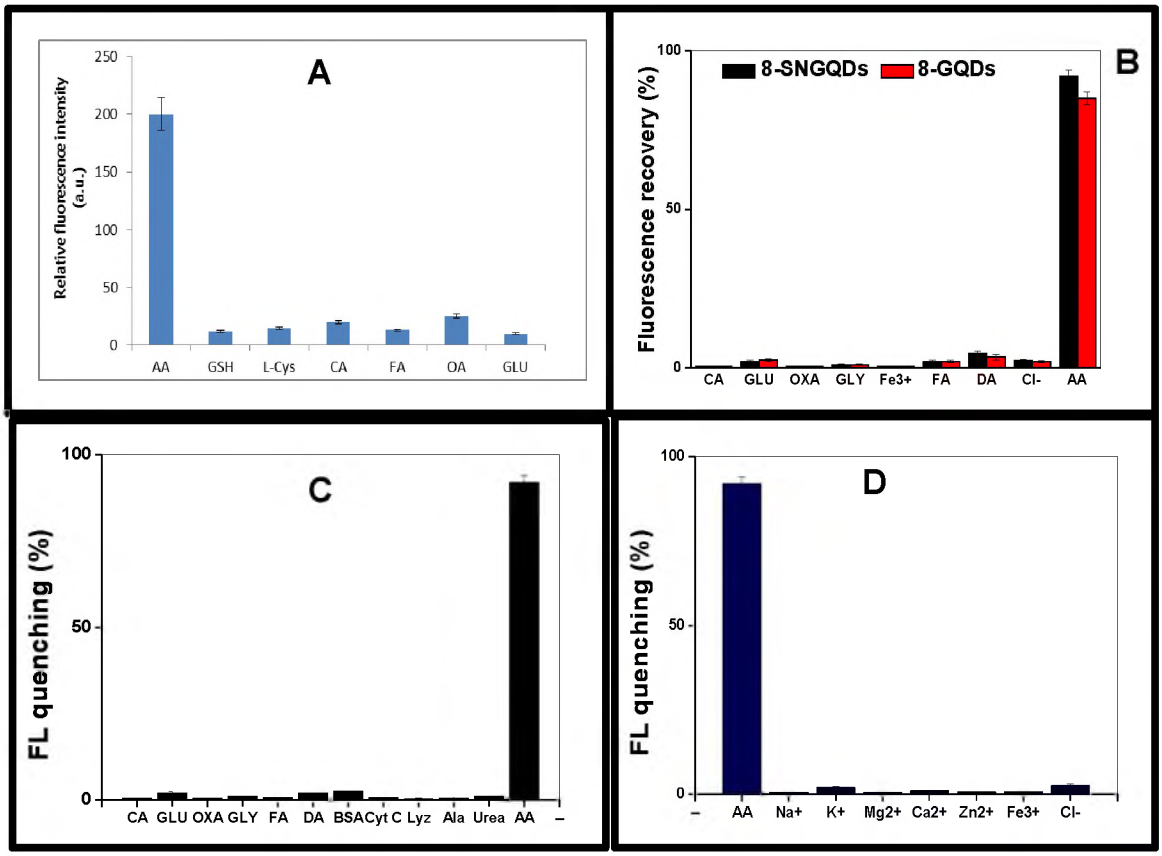

Fig. 4.6. Selectivity studies of (A) GQDs-4A-TEMPO (2 mg/mL) sensing system (as an example) towards AA and other biomolecules (500 μM). Solvent is PBS (50 mM, pH 9.0). (B) 8-GQDs/SNGQDs -0.5 mg/mL, [AA] = 20 nM in DMSO. gCNQDs (0.5 mg/mL) in the presence of (C) biomolecules (250 nM), (D) metal ions (250 nM) in PBS 10 mM, pH 7. Number of replicate measurements, n=3. Tolerable error limits = ±5%. CA = citric acid; GLU = glucose; OXA = oxalic acid, GLY = glycine, DA = dopamine, FA = folic acid, BSA = bovine serum albumin, Cyt c = cytochrome c, Lyz = lysozyme, Ala = alanine, GSH = glutathione.

As clearly depicted in Fig. 4.6A, the observed remarkable differences in the relative fluorescence intensities was quite significant considering that the concentrations of the other molecules were much higher (~100 fold) than that of the test analyte (AA). Thus, this result shows that the nanoprobes are highly selective towards AA and offer a highly sensitive and selective method for the detection of AA.

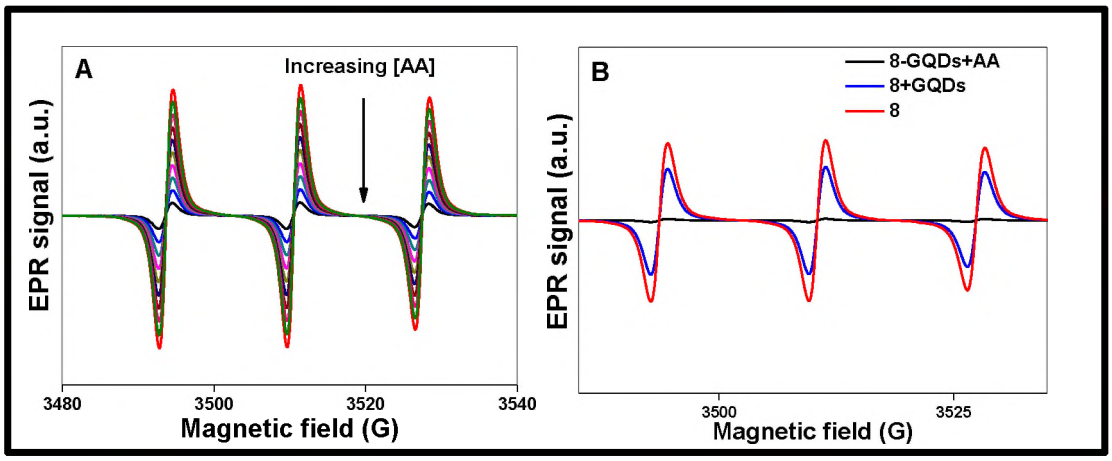

Fig. 4.7. Decrease in the EPR signals (in the presence of AA) for (A) GQDs-4A-TEMPO in 50 mM PBS of pH 9.0 [AA] 0-20 µM. (B) 8-GQDs (as an example) in DMSO.

4.1.2.4. Proposed detection mechanism

Following the good response of the nanoprobes to AA, it could be theorized that the TEMPO free radicals moiety conjugated to the GQDs were converted to their diamagnetic hydroxylamine derivative by AA, resulting in the hindrance of intra-molecular electron(s) and or energy transfer process originally occurring between the GQDs and 4A-TEMPO as shown in Scheme 4.3, thus resulting in the restoration of the quenched fluorescence of the respective GQDs. The conversion

of the paramagnetic TEMPO moieties to non-radical species in the presence of AA was shown by EPR studies (Fig. 4.7A).

4.2. AA sensing using 8-GQDs/SNGQDs (π-π)

Nanoconjugates of MPc complex **8** and GQDs or SN-GQDs were specifically tailored towards the recognition of AA based on a design strategy of non-covalent interaction (π-π stacking) between GQDs and complex **8**. As such, conjugates of GQDs (with excellent PL properties) and TEMPO (N-O*) derivatized π-conjugated structure (such as MPcs) were fabricated. Most studies have been based on covalent linkages and/or mixing of fluorophores with TEMPO compounds **[197, 242, 253]**. Non-covalent interaction (π-π stacking) is advantageous over covalent linkage since the optical and electronic properties of the interacting molecules are preserved within the supramolecular assembles **[68, 201]**.

4.2.1. Fluorescence "turn ON" detection

The fluorescence of the respective GQDs was quenched ("turned OFF") upon non-covalent stacking of complex **8** onto their surfaces (forming **8**-GQDs or **8**-SN-GQDs conjugates) in a similar manner to Fig. 3.26. However, the fluorescence emission was restored upon addition of AA to **8**-GQDs or **8**-SN-GQDs conjugates as presented in Fig. 4.4 B). The fluorescence intensity was modulated by different amounts of AA. The observed phenomenon is an indication that the GQDs components of the probes were switched back to the "ON" mode. The fluorescence recovery was rapid; reaching an optimum within 1 min. Fig. 4.4B (inset) shows that the fluorescence intensity of **8**-GQDs probe

increased linearly with increasing concentration of AA. The fluorescence "turn ON" sensitivities and LODs of the probes were evaluated using Eq. **4.3** and **4.4** above. The linear ranges were 0.7-15 nM (R^2 = 0.9988) for **8**-SN-GQDs and 2.7-25 nM (R^2 = 0.9983) for **8**-GQDs, Table 4.3. The LODs were estimated to be 0.2 nM and 0.8 nM for SN-GQDs and GQDs conjugates, respectively. The LODs are lower (better) than some reported LODs (for AA detection) in literature (Table 4.3) and the LODs obtained using GQDs-4A-TEMPO systems discussed earlier in this thesis, hence showing the advantage of MPcs. The observed high sensitivity for AA detection obtained in this work using MPcs-GQDs hybrid, may be due to the non-covalent (π-π) interaction between GQDs and complex **8**, which preserves the electronic and optical properties of the π-conjugated molecules.

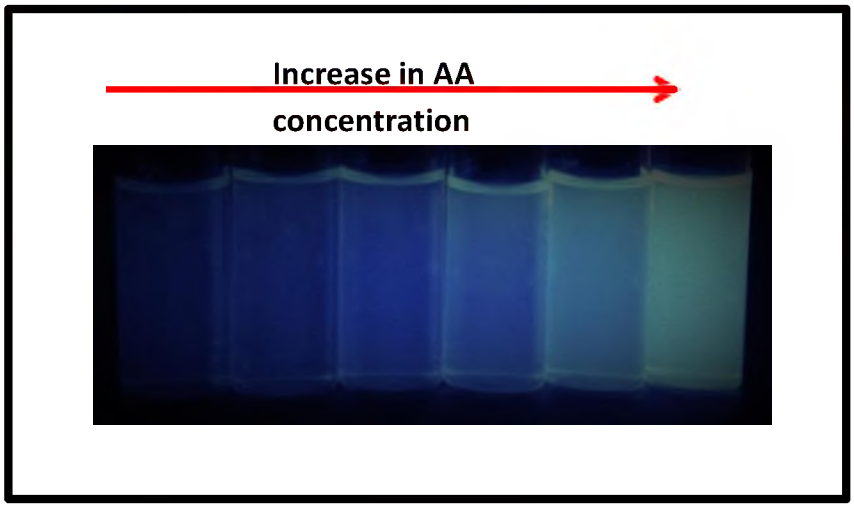

Fig. 4.8. Fluorescence "turn ON" of 8-GQDs (as an example) upon the addition of increasing concentration of AA (0-50 nM) to the probe solution viewed under UV light of 365 nm.

The non-covalent attachment of complex **8** to GQDs/SN-GQDs also allows for the ease of interaction of AA with the TEMPO-bearing complex **8**, which could potentially result in the incorporation of AA molecules as spacers between the GQDs and complex **8** thus releasing GQDs from their electronic and optical relationships with the MPc, and the consequent "switch ON" of the fluorescence of GQDs. The sensing systems for AA quantification could be visualized under UV light of 365 nm as shown in Fig. 4.8 using **8**-GQDs as an example.

4.2.2. Selective screening of various biomolecules

Various biomolecules and ions were screened as potential interferences in the detection of AA. The compounds screened and the results are shown in Fig. 4.6B. Dopamine (a common interference) which contains hydroxyl groups similar to AA was also tested and did not interfere within the concentration range of 0-50 nM of AA investigated and even up to 5 μM dopamine concentration. This indicates that the nanoprobes could respond to the presence of AA in nanomolar concentrations without false positive signals from other analytes, hence demonstrating the selectivity and specificity of the nanoprobes for AA detection, which is based mainly on its radical scavenging ability hence strong interaction with TEMPO moiety on complex **8** compared to the other molecules or ions tested.

4.2.3. Proposed mechanism

The sensing of AA by the prepared nanoprobes (**8**-GQDs/SN-GQDs) is due to the electronic interaction between AA and the TEMPO moieties on complex **8** ring, leading to their conversion to the diamagnetic hydroxylamine derivative as

depicted in Scheme 4.4. Spectroscopic evidence from EPR experiments, UV-Vis absorption and time-resolved steady state measurements clearly showed that the interaction resulting into the recognition of AA was strictly between TEMPO substituents of complex **8** and AA. When complex **8** was not coordinated to GQDs, EPR signal was observed due to the paramagnetic nature of TEMPO, Fig. 4.7B. Upon the non-covalent coordination of complex **8** to GQDs/SN-GQDs, the EPR signals were still observed as expected since the interaction does not affect the TEMPO moiety on the ring of complex **8**. However, on addition of AA to **8**-GQDs or **8**-SN-GQDs conjugates, there were no clear EPR signals of TEMPO, thus confirming that the TEMPO moieties on complex **8** ring have been converted into a non-radical complex by AA.

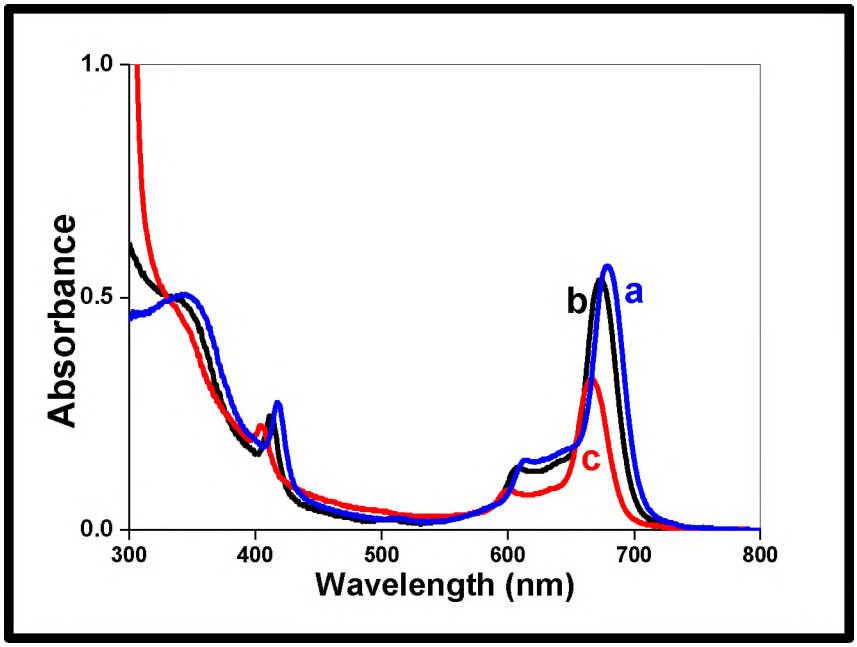

Fig. 4.9. UV-Vis absorption of 8 (a) and in the presence of 20 nM (b) and 50 nM (c) of AA. Solvent: DMSO.

Table 4.4. Fluorescence lifetime values of 8-GQDs and 8-gCNQDs nanoprobes with different concentration of AA in DMSO/PBS (1:4).

Probe	[AA](μM)	τ_F(ns)	Probe	[AA] (μM)	τ_F(ns)(± 0.10)
8-GQDs (π-π)	0	1.90	8-gCNQDs (π-π)	0	0.90
	10	2.30		1	2.90
	25	3.70		5	3.50
	50	4.90		10	4.80
8-SNGQDs (π-π)	0	0.92		20	5.50
	10	3.30		50	6.02
	25	6.25		100	6.34
	50	9.33	gCNQDs	-	7.40

τ_F (ns) of GQDs = 5.7 and SN-GQDs = 11.6.

Further, the absorption and fluorescence spectra of SN-GQDs or GQDs alone did not change in the presence of AA. However, there were noticeable changes in the ground state absorption of complex **8** in the presence of AA (Fig. 4.9). The Q-band of complex **8** blue-shifted as AA was added and the shift further increased with increase in AA concentration. The observation confirmed that there is interaction between complex **8** and AA thereby disrupting the interaction of complex **8** and GQDs, leading to the turn "ON" of the fluorescence signals of the GQDs. Fluorescence lifetime measurements were further used to evaluate this observation. Fluorescence lifetimes sequentially increased as the concentration of AA added to the nanoprobes was increased (Table 4.4 and Fig. 4.10). This

observation which is similar to the spectrofluorimetric measurements depicts the turn "ON" of the fluorescence of GQDs.

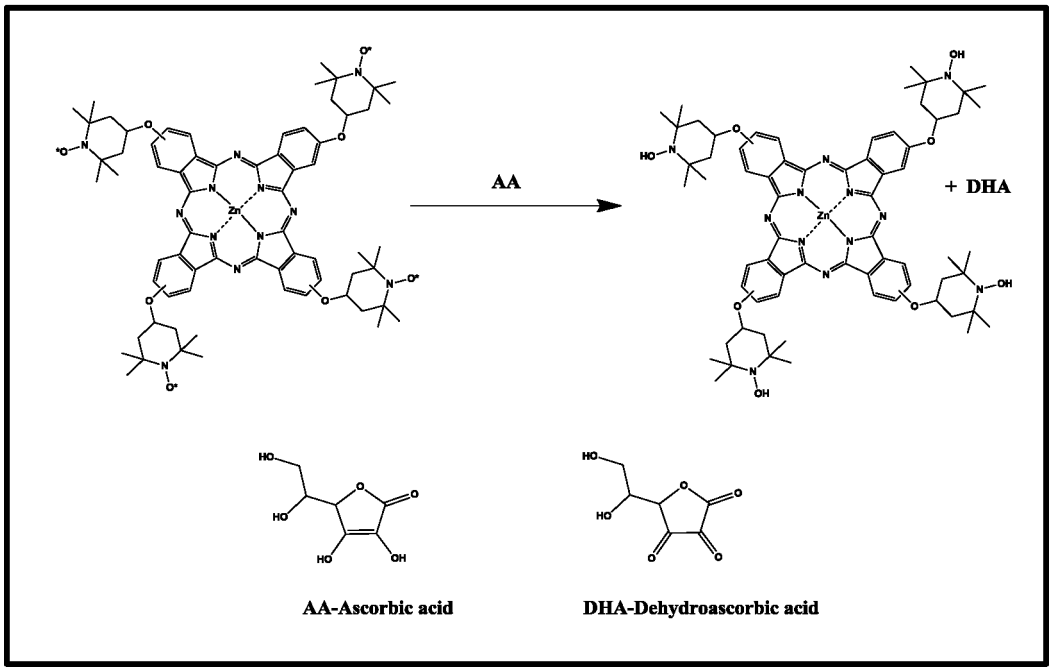

Scheme 4.4. Molecular structure of complex 8 and the proposed interaction mechanism with ascorbic acid (AA).

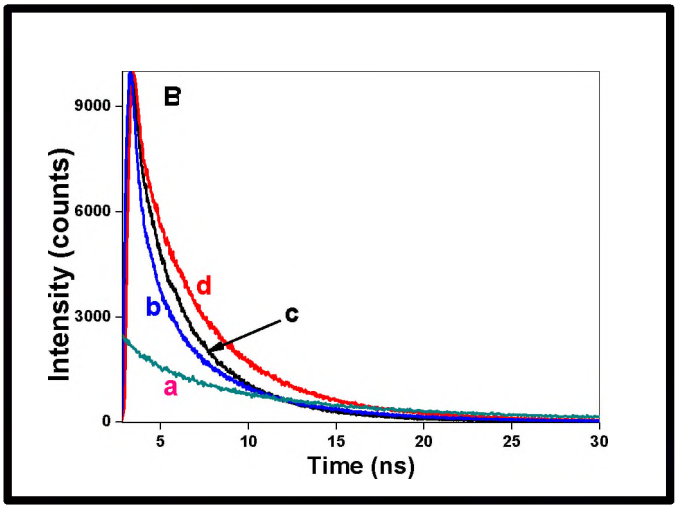

Fig. 4.10. Fluorescence decay curves showing lifetime profiles of 8-GQDs (π-π) (as example) in the absence (a), and presence of (b), 10 nM, (c) 25 nM, and (d) 50 nM of AA. Solvent: DMSO:PBS (1:4).

Lifetimes remained unchanged when AA was titrated against GQDs/SN-GQDs solution and this potentially indicates that the fluorescence modulation of GQDs (within the nanoconjugates) was largely as a result of the interaction between complex **8** components of the probes and AA.

It is plausible to propose that the interaction between AA and the respective conjugates resulted into the disruption of the GQDs/complex **8** energy transfer process due to the following proposed reasons: Firstly, AA is a radical scavenger and it would react with TEMPO on complex **8** as shown in Scheme 4.4, forming a non-radical derivative of complex **8**. Secondly, AA molecules could have acted as spacers between the GQDs and complex **8** which potentially trigger the fluorescence "turn ON" mode of the GQDs as shown in Scheme 4.5.

4.2.4. Real samples analysis (validation studies)

Real sample (vitamin C tablets) and spiked water samples with known concentration of AA were further subjected to analysis, so as to demonstrate the applicability of the fabricated nanoprobes. Table 4.5 shows the quantification of AA (%) and the relative standard deviation (RSD) evaluated from three replicate measurements.

AA recoveries from vitamin C and the spiked water sample were 97.5 % (RSD: 2.9) and 102.2 % (RSD: 2.1) for **8**-GQDs. 99.2 % (RSD: 1.0) and 101.1 % (RSD: 1.5) were obtained for **8**-SN-GQDs probe. The recoveries were close to the concentration of AA in the samples as shown in Table 4.5, and show that **8**-SN-GQDs nanoprobe could function as a more sensitive probe due to the better

fluorescence properties of SN-GQDs (Table 3.2). Nonetheless, the feasibility of AA quantification by the nanoprobes in real samples was demonstrated.

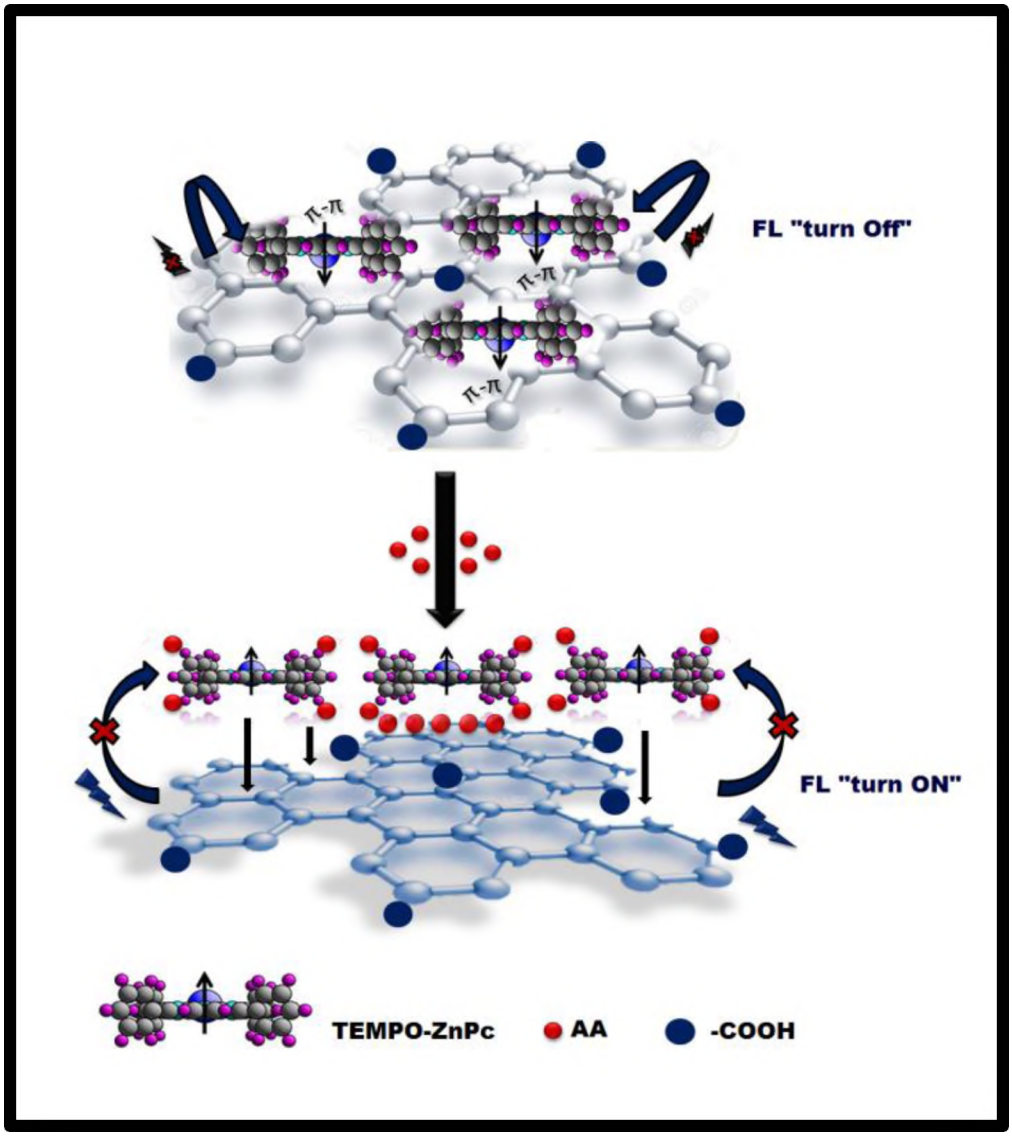

Scheme 4.5. Schematic illustration of the non-covalent coordination (*π-π* stacking) between GQDs and complex 8 to form 8-GQDs supramolecular assemble and interaction with AA. "*Off-On*" sensing process of AA is also illustrated.

Table 4.5. Analytical application of 8-GQDs/SN-GQDs nanoprobes for AA estimation in commercial and spiked samples.

Probe	Sample	% Recovery	RSD (n=3)
8-GQDs (π-π)	Vitamin C	97.5	2.9
	Spiked sample	102.2	2.1
8-SN-GQDs (π-π)	Vitamin C	99.2	1.02
	Spiked sample	101.1	1.5

4.3. gCNQDs-4A-TEMPO (embedded), gCNQDs-4A-TEMPO (linked) and 8-gCNQDs (π-π) conjugate.

This section of the thesis discusses the fluorescence detection of AA using conjugates of gCNQDs with TEMPO molecules (4A-TEMPO) or TEMPO-derivatized MPc (complex **8**). The results and LODs obtained herein are compared with those of GQDs. This work was aimed at establishing that other carbon-based QDs (such as gCNQDs) could be deployed for AA sensing following similar principles and phenomenon observed for GQDs and also to establish the superior sensing potentials of the carbon-based QDs.

4.3.1. Fluorescence "turn OFF/ON"

It was observed that the fluorescence of the *in situ* functionalized gCNQDs (as-synthesized gCNQDs-4A-TEMPO (embedded)) could be quenched in the presence of AA due to the specific interaction between the embedded TEMPO moiety of gCNQDs-4A-TEMPO (embedded) and AA via a "turn OFF" process

(Scheme 4.6). The quenching increased as the concentration of AA was increasingly varied (Fig. 4.11), hence showing the ability of gCNQDs-4A-TEMPO (embedded) to respond to the presence of AA.

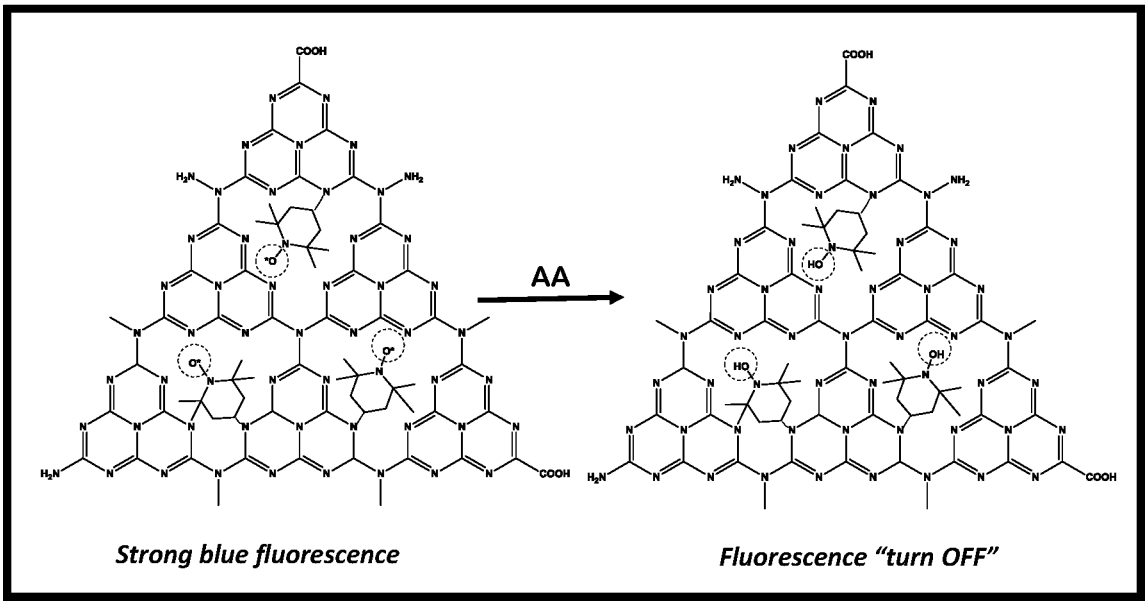

Scheme 4.6. The plausible interaction mechanism between gCNQDs-4A-TEMPO (embedded) and the target analyte (AA) for its sensitive detection.

On the other hand, upon covalent linking of gCNQDs to 4A-TEMPO to form gCNQDs-4A-TEMPO (linked), the fluorescence of gCNQDs is quenched ("turned OFF") and recovered ("turned ON") in the presence of AA with spectra similar to Fig. 4.4, thus, the efficiency of AA detection by "turn ON" (using gCNQDs-4A-TEMPO (linked)) and "turn OFF" (using gCNQDs-4A-TEMPO (embedded)) was compared. Complex **8** was adsorbed via non-covalent π-π stacking onto gCNQDs to form **8**-gCNQDs (π-π stacking interaction). The conjugate was then used as a "turn-ON" probe for AA detection. The fluorescence of gCNQDs was quenched by complex **8** via a possible energy transfer from gCNQDs to complex **8** (similar to GQDs), which was then restored in the presence of AA.

The fluorescence quenching dynamics of gCNQDs-4A-TEMPO (embedded) by AA was followed by the construction of a calibration curve, a linear plot was obtained using the fluorescence quenching ratio $(F-F_0)/F_0$ versus AA concentration (Fig. 4.11 inset). The LODs were determined using Eq. **4.3** and **4.4** described above. The linear concentration range within which the fluorescence of the probe was quenched was in the nanomolar range (0.5-50 nM, R^2 = 0.9988). On the other hand, It was observed that gCNQDs-4A-TEMPO (linked)) could respond to the presence of AA within the linear concentration range of 1-100 nM with an R^2 value of 0.9922. The LOD was calculated to be 1.25 nM for gCNQDs-4A-TEMPO (linked) for AA detection (Table 4.3). This further indicates the ability of the probes to sensitively detect AA in the nanomolar concentration. Thus, gCNQDs-4A-TEMPO (linked) which detects AA by "turn ON" process shows a higher detection limit than gCNQDs-4A-TEMPO (embedded)) which detects AA by "turn OFF" process. Generally, fluorescence "turn ON" detection methods are preferred over "turn OFF" methods, since there could be other processes which could decrease fluorescence signals of fluorophores in addition to the analyte of interest.

Similar to gCNQDs-4A-TEMPO (linked) probe, **8**-gCNQDs (π-π) hybrid detected AA via a fluorescence "turn ON" process. The design strategy was firstly based on the efficient quenching of gCNQDs fluorescence upon non-covalent (*π-π* stacking) interaction with complex **8**. Then in the presence of AA, the TEMPO groups on the MPc complex **8** could specifically and selectively interact with AA, thus disrupting the existing interaction between gCNQDs and complex **8** within the hybrid and the fluorescence of gCNQDs can be restored. The quenched

fluorescence of gCNQDs within the hybrid was recovered and the enhancement was directly proportional to AA concentration in the nanomolar range. The linear detection range was found to be 1.0-100 nM (R^2 = 0.9821) with an LOD estimated to be 0.55 nM as shown Table 4.3. This value is an improvement compared to gCNQDs-4A-TEMPO (linked) "turn ON" sensor at 1.25 nM, showing the importance of using MPc complexes in conjunction with QDs for sensing (similar to the observation in the case of GQDs). The LODs obtained using the carbon nitride-based probes are better or comparable to values reported in literature (Table 4.3).

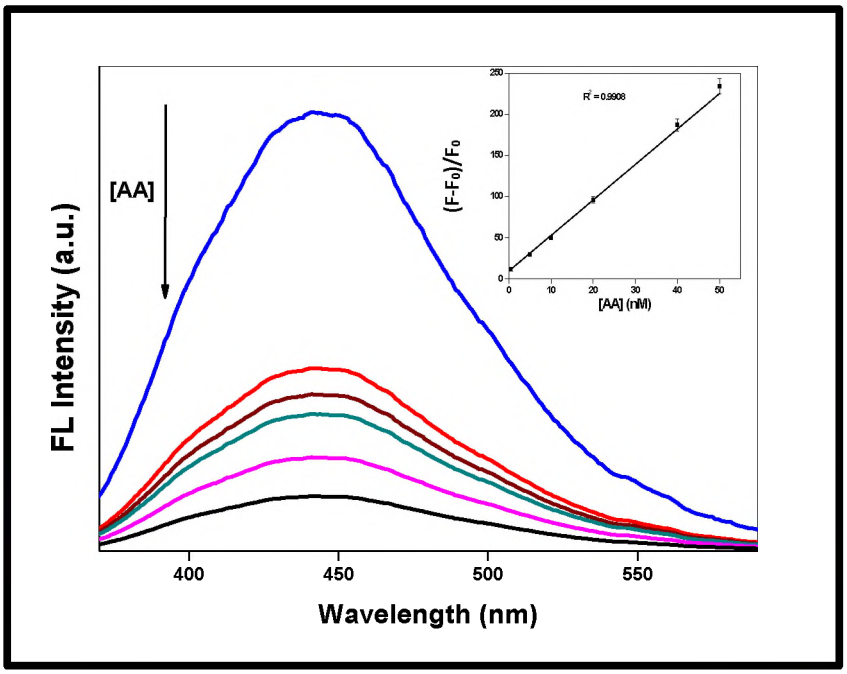

Fig. 4.11. Fluorescence spectra of gCNQDs-4A-TEMPO (embedded) in the presence of different amounts of AA (inset: calibration plot) in PBS (10 mM, pH 7.0).

The detection of AA using all the gCNQDs based probes discussed in this work when compared with graphene QDs functionalized with TEMPO (GQDs-4A-

TEMPO) via "turn ON" with an LOD of 84 nM, Table 4.3, shows the superiority of gCNQDs. The tendency of gCNQDs to function as a better fluorescence probe material when compared to GQDs could be ascribed to the defect rich nature of gCNQDs due to the N-bridged poly(tri-s-triazine) layers, thus making them to exhibit excellent medium-band gap and indirect semiconductor electronic properties [102]. The probes designed in this work are capable of responding to nanomolar concentration of AA, hence ideal for AA detection.

4.3.2. Optimization of AA detection

Experimental optimization was carried out following the confirmation of the effectiveness of the gCNQDs-based probes to sharply respond towards AA recognition even at nanomolar concentration. The effect of pH was evaluated by using phosphate buffers of pH 4.0-11.0, respectively. The probe solutions were prepared at various pH, and incubated with the variously modified gCNQDs, after which fluorescence measurements were carried out. Fig. 4.5B shows the fluorescence response of gCNQDs-4A-TEMPO (embedded) at the respective pH as an example. From the results obtained, it was found that acidic pH (4.0, 5.0 and 6.0) was not favorable for fluorescence detection using gCNQDs; the fluorescence is quenched at this pH compared to other pH media (7.0 and 7.4), pH 7 was employed.

This result follows from the fact that carbon-based nanomaterials (GQDs and carbon dots) are known to be non-fluorescent at acidic pH [85], which was similarly observed in this study.

4.3.3. Selectivity studies

Under the optimized conditions, the specificity and selectivity of the gCNQDs-based probes were tested in the presence of compounds with properties close to that of AA. The compounds screened are shown in Fig 4.6 C and D. The detection scheme in the presence of the compounds was within tolerable error levels of 5% (with up to 1 μM concentration of the tested compounds) and three replicate measurements (n=3). The investigated compounds had no effects on the fluorescence properties of the probes except for AA as observed for GQDs-4A-TEMPO and **8**-GQDs. This result is indicative of the fact that the TEMPO-functionalized gCNQDs could respond to the presence of AA (even at nanomolar concentrations) without false positive signals from other analytes, hence demonstrating the selectivity and specificity of the probes for AA sensing.

4.3.4. Proposed mechanism

Considering that gCNQDs functionalized with TEMPO moieties could detect AA sensitively, whereas the gCNQDs alone are unresponsive to the presence of AA, it is plausible to conclude that the electronic interactions between AA and the TEMPO moieties of gCNQDs-4A-TEMPO (embedded), gCNQDs-4A-TEMPO (linked) and **8**-gCNQDs (π-π) probes provided the mechanistic avenue for AA sensing. It is known that AA molecules can effectively interact with TEMPO compounds and result in their conversion to the diamagnetic hydroxylamine derivatives, Scheme 4.3, as also observed for GQDs **[197, 244]**. Fluorescence lifetimes were also employed to elucidate AA sensing mechanism by the designed probes.

Table 4.6. Recovery studies of AA in commercially obtained vitamin C tablets and spiked samples (water and human serum albumin) as demonstration of analytical applicability and reproducibility of gCNQDs-based probes.

Probe	Added AA (nM)	Found AA (nM)	Recovery (%, n = 3)	RSD (%)
(gCNQDs-4A-TEMPO (embedded))	Vitamin C tablet (50 nM)	45.50	91.0±0.32	3.12
	Spiked water sample			
	25 50	25.90 50.05	103.6±1.88 100.1±0.55	1.56 0.98
	Spiked HSA (in PBS) 10 20 50	9.72 20.12 49.80	97.23 100.60 99.60	2.10 1.25 0.92
8-gCNQDs (π-π)	Vitamin C tablet (50 nM)	50.20	100.4±1.01	077
	Spiked water sample			
	25 50	23.92 49.80	95.7±1.20 99.6±2.34	2.95 3.45
	Spiked HSA 10 20 50	9.40 19.86 50.5	94.00 99.30 101.00	2.30 0.78 1.30

HSA = human serum albumin, RSD = relative standard deviation.

Table 4.4 shows the various changes recorded during the fluorescence "turn ON" of gCNQDs within 8-gCNQDs (π-π) hybrid in the presence of different amounts of AA. The fluorescence lifetime increased gradually close to the fluorescence

lifetime value recorded for the uncoordinated gCNQDs, therefore showing that the interaction of AA with the complex **8** perturbed the interaction between gCNQDs and complex **8**, leading to the "turn ON" of the fluorescence of gCNQDs. The same trend in fluorescence lifetime recovery was observed for gCNQDs-4A-TEMPO (linked) in the presence of AA, hence showing the signal "turn ON" of gCNQDs in the presence of AA.

4.3.5. Analytical applicability (recovery studies)

Based on the AA detection ability demonstrated by the TEMPO-functionalized gCNQDs, the applicability of the probes was demonstrated by the analytical recovery studies of real samples. Commercially available vitamin C tablets containing declared amount of AA concentration and spiked samples were employed. As shown in Table 4.6, the obtained results gave good percentage recovery of AA in the real samples, respectively. Recovery studies are usually employed as a tool to ascertaining the accuracy of a proposed assay. Precision and reproducibility were also assessed by batch to batch analysis and expressed in terms of the relative standard deviation (RSD) (also known as percent coefficient of variation, % CV). As shown in Table 4.6, the quantified AA amounts (against known amounts in the samples) and the relative standard deviations (RSD, replicate measurements, n=3) further demonstrates the precision and reproducibility of the assays. Satisfactory recoveries obtained are indications of the practical usability of the designed probes.

4.4. Conclusion

In summary, TEMPO derivatized MPc and carbon nanomaterials of GQDs and gCNQDs were fabricated and were successfully deployed in the sensitive detection of AA. The TEMPO functionality introduced onto the materials resulted in their sensitive and selective interaction with AA, hence the analytical detection of AA. TEMPO derivatized MPc (**8**) was non-covalently conjugated to GQDs/gCNQDs via π-π stacking and its performance as probes for the detection of AA was compared with GQDs/gCNQDs directly functionalized with TEMPO (without MPc (**8**)). For all the probes, nanomolar range LODs were obtained, hence showing the sensitive nature of the fabricated probes. However, the LODs obtained when GQDs (but not for gCNQDs) were functionalized with MPc (**8**) were better than when directly functionalized with TEMPO molecules (without MPc), hence showing the important of MPc complex **8** as a component of the nanoprobes. Also, gCNQDs TEMPO derivatives showed better performance in terms of sensitivity towards AA detection as compared to their GQDs counterparts, hence showing the superiority of gCNQDs as better probes materials. However, **8**-SNGQDs exhibited a slightly better sensitivity of 0.2 nM for AA detection as compared to 0.55 nM of **8**-gCNQDs further showing that doped or functionalized GQDs could offer a better performance. The probes showed to be highly selective towards AA detection in the presence of other molecules with properties close to that of AA, hence showing the robust nature of the probes. The nanoprobes were used to quantify AA in real samples with good recoveries, hence showing the analytical applicability of the probes.

5. Biothiols detection

This chapter describes the detection of biothiols such as cysteine, homocysteine and glutathione. GQDs are employed with Au@Ag NPs, MPc (5)-Au@Ag, maleimide and maleimide-derivatized MPc (12) owing to the affinity of biothiols binding to Au@Ag NPs and maleimide, respectively.

5.1. PEI-GQDs-Au@Ag

The detection of Cys, Hcy or GSH using graphene quantum dots grafted with polyethyleneimine (PEI-GQDs) and Au@Ag NPs blend as a nanoprobe is presented. PEI-GQDs are employed due to their positively charged surface which could electrostatically interact with negatively charged Au@Ag NPs. The fluorescence of PEI-GQDs was quenched efficiently upon interaction with Au@Ag NPs, but was restored in the presence of biothiols. Also, PEI-GQDs could be converted to M-GQDs (see Scheme 3.2, the latter are specific for biothiols. Au@Ag NPs are employed due to their affinity for biothiols.

5.1.1. Fluorescence quenching

From preliminary runs, it was discovered that the fluorescence of PEI-GQDs was quenched by Au@Ag NPs. However, this was not the case for pristine GQDs (without PEI). This can be ascribed to the weak or non-interaction between pristine GQDs and Au@Ag NPs, since they both possess similar surface charges (both negatively charged surface). Hence, further studies were carried out using PEI-GQDs having established its superior characteristics to function as a better signal reporter compared to pristine GQDs for this particular study.

The emission spectra of PEI-GQDs were recorded upon titration of a fixed concentration of PEI-GQDs (500 µL, 0.5 mg/L) with varying concentrations of Au@Ag NPs. As shown in Fig. 5.1A, the fluorescence intensity gradually decreased ("turned OFF") as Au@Ag NPs concentration was sequentially increased.

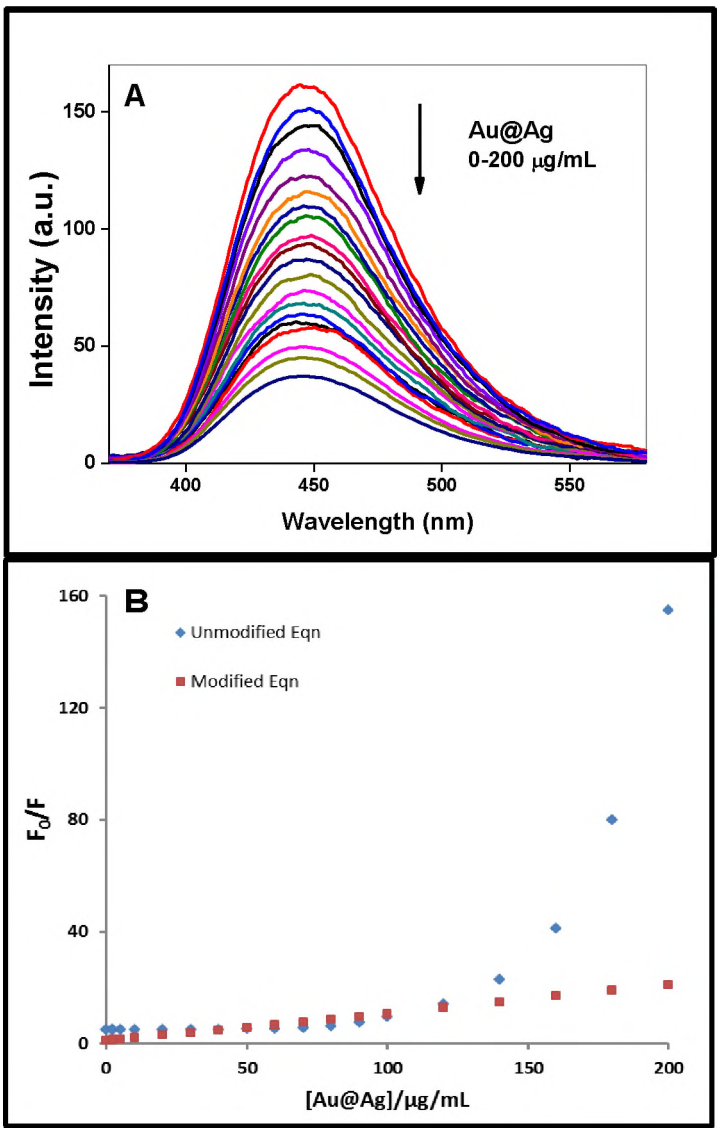

Fig. 5.1. (A) Fluorescence quenching of PEI-GQDs by increasing concentration of Au@Ag NPs and (B) Stern-Volmer plots showing the modified and unmodified quenching mechanisms. Solvent: 50 mM PBS (pH 8.0), GQDs (0.5 mg/mL), Au@Ag NPs (0-200 µg/mL). Excitation wavelength = 350 nm.

Stern-Volmer relationship was used to assess the nature of the quenching mechanism and a non-linear trend was observed with a positive deviation from linearity (Fig. 5.1B). Deviations of this kind could mean that both static and dynamic quenching could be occurring simultaneously [197, 235].

The Stern-Volmer (S-V) plot showed positive deviation from the S-V relationship (Fig. 5.1B) by showing upward curvature in the plot. The positive deviation (upward curvature) of the plot of F_0/F versus concentration [Au@Ag] is an indication of the coexistence of both static and dynamic quenching mechanisms. The linear S-V plot was obtained by calculating the apparent values of K_{app} using Eq. 5.1.

$$K_{app} = \left(\frac{F_0}{F} - 1\right)\frac{1}{[Au@Ag]} \qquad (5.1)$$

Apparent quenching constant (K_{app}) values were calculated and then plotted against [Au@Ag] and extrapolated to [Au@Ag] = 0 to obtain K_{SV}, the Stern-Volmer constant. A straight line from $F_0/F = 1$ represents the expected S-V plot, Fig. 5.1B. The deviation from linearity in the S-V plots (Fig. 5.1B) was accommodated by treating the data based on a modified Stern-Volmer equation (Eq. 5.2) to accommodate both dynamic and static quenching mechanisms [197].

$$F_0/F = (1+K_{SV}\,[Au@Ag])\,(1+ e^{K\,[Au@Ag]}) \qquad (5.2)$$

The first term in Eq. 5.2 is the original Stern-Volmer equation which represents the dynamic component and the second term is the static component. K_{SV} and K were evaluated to be 1.6 X 10^3 M^{-1} and 2.5 X 10^4 M^{-1}, respectively.

The quenching of PEI-GQDs fluorescence by Au@Ag NPs via static and dynamic mechanisms as observed in this study is ascribed to both collisional (diffusion controlled) and electrostatic (static) interactions between PEI-GQDs and Au@Ag NPs. Electrostatic interactions is a plausible reason for the observed static fluorescence quenching of PEI-GQDs by Au@Ag NPs [234]. Dynamic quenching

would normally occur due to collisional interaction between fluorophores and quenchers in a diffusion-controlled surface absorption or interaction. The value of the static quenching constant (K) is larger than the dynamic quenching constant (K_{sv}) of PEI-GQDs and Au@Ag NPs interaction. It can be concluded that static quenching dominates hence a larger value. This is also in agreement with the fact that electrostatic interaction would largely result in static quenching and since PEI-GQDs and Au@Ag NPs possess oppositely charged surfaces, static quenching is more favoured. Similar observations have been reported in fluorescence quenching involving both static and dynamic quenching mechanisms where the interaction between fluorophores and quenchers would have larger values of static quenching constants (K) in systems involving electrostatic interaction with the possibility of surface diffusion or collision also leading to dynamic quenching [197, 235].

5.1.2. Optimization of experimental parameters

Prior to the 'turn ON' experiments, a couple of factors which might affect the interaction of PEI-GQDs-Au@Ag blend with the biothiols were optimized. The concentration of PEI-GQDs suitable for biothiols detection was determined (using 0.5, 1.0, 2.0 mg/L) in the presence of 100 µg/mL Au@Ag NPs. It was established that 0.5 mg/mL is most suitable for interaction with Au@Ag NPs since the fluorescence of PEI-GQDs was most efficiently quenched at this concentration. Also from the quenching experiments, it was observed that at Au@Ag NPs concentration above 100 µg/mL, there was a positive deviation from linearity in the Stern-Volmer plot (Fig. 5.1B). The best signal was also observed at 100 µg/mL

of Au@Ag NPs. Hence, 0.5 mg/mL of PEI-GQDs and 100 µg/mL Au@Ag NPs were employed.

The pH of PBS employed was also optimized. The mercapto group (SH) of biothiols has been reported to get oxidized at pH>9.0 to generate the disulphide bond [254], hence biothiols detection in the pH range of 7-10 was carried out. As shown in Fig. 5.2, there were no significant difference in the recovered fluorescence emission (F/F_0) at pH 7.0 and 8.0; hence pH 8.0 was selected for the detection procedures.

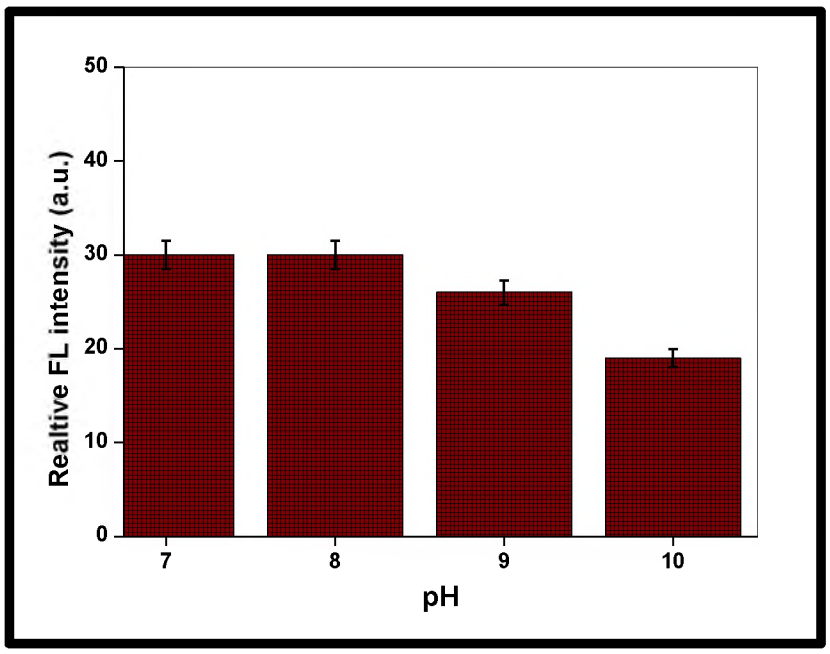

Fig. 5.2. Optimization of pH for the fluorescence recovery (turn-ON) procedure for biothiols detection. Solvent: PBS (50 mM, pH 8.0).

The effect of the Incubation time on the detection sensitivity was also assessed; the recovered fluorescence (F/F_0) increased rapidly within 2 min and remained constant over time. This implies that the 'turn-ON' procedure for biothiols

quantitation could be carried out in a very short time (within 2 min) which is also an added advantage of the designed nanoprobe.

5.1.3. Fluorescence "turn-ON" detection of biothiols.

The results obtained under optimized conditions revealed the rapid and increasing recovery of the fluorescence of PEI-GQDs (initially quenched by Au@Ag NPs) upon the addition of increasing concentration of Cys, Hcy or GSH, respectively, Fig. 5.3 (Hcy shown as an example).

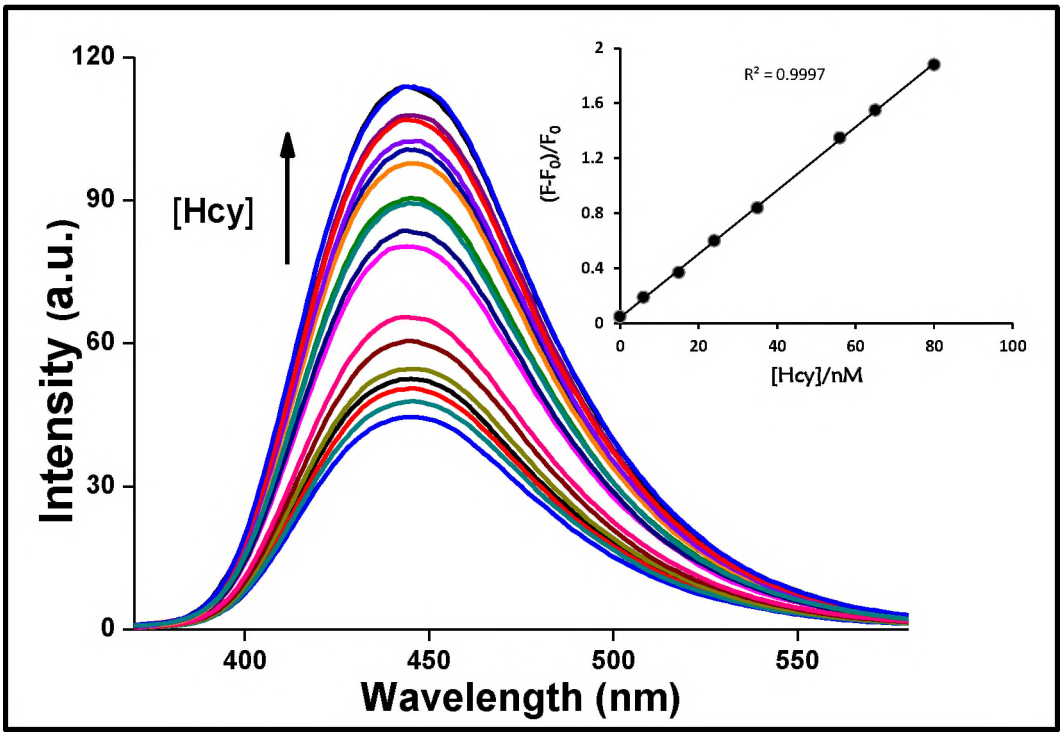

Fig. 5.3. Fluorescence "turn-ON" spectra of PEI-GQDs-Au@Ag blend in the presence of Hcy (as an example) in 50 mM PBS solution (pH 8.0). Excitation wavelength = 350 nm. Inset: Calibration curve.

Table 5.1. Comparison of the sensitivity of the nanoprobes in this thesis with some reported analytical techniques for the detection of biothiols.

Method	FL ON/OFF	LOD (nM)			REF.
		Cys	Hcy	GSH	
BSA-Ag nanoclusters	OFF	0.81 µM	1.0 µM	1.1 µM	[254]
Au nanoclusters	OFF	8.3	14.9	9.4	[255]
Carbon dots	OFF	4.9	6.1	8.5	[256]
GO and Ru-complex	OFF	2.34	4.60	6.20	[257]
GQDs	OFF	6.2	4.5	4.1	[53]
GQDs-Hg^{2+}	ON	2.5	5	5	[84]
PEI-GQDs/Au@Ag	ON	1.5	3.0	4.5	This work
M-GQDs	ON	0.30	0.45	0.86	This work
12-GQDs	ON	0.85	1.42	3.2	This work

BSA= bovine serum albumin, GO = graphene oxide, Ru = Ruthenium.

The detection pathway is depicted in Scheme 5.1. In addition to the recovered fluorescence of PEI-GQDs, there were no changes in the emission maximum wavelength or distortions of the emission spectra, which points to the fact that the restored fluorescence originates from PEI-GQDs rather than any likely new products. In order to establish the sensitive nature of the probe, the LODs for the

biothiols were evaluated using Eq. **4.3** and **4.4**. The $[(F-F_0)/F_0]$ values were plotted against the biothiols concentrations (Fig. 5.3 inset). Interestingly, the LODs were as low as 1.5 nM, 3.0 nM and 4.5 nM for Cys, Hcy or GSH, respectively (Table 5.1).

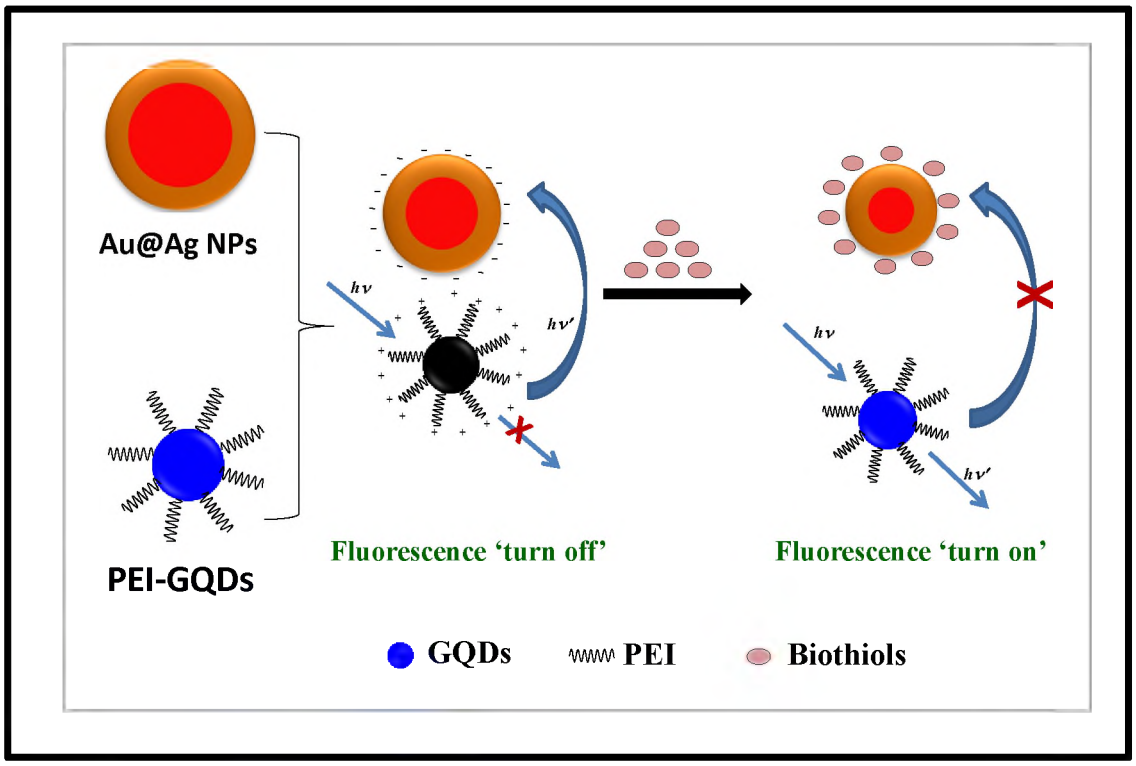

Scheme. 5.1. Graphical illustration of the interaction between PEI-GQDs and Au@Ag NPs and the pathway for biothiols detection.

The results show that the detection sensitivity is in the order of Cys>Hcy>GSH. GSH showed the least sensitivity (LOD) among the biothiols detected and this could be attributed to steric hindrance due to the bulky nature of GSH (compared to Cys and Hcy) and the presence of more functional groups **[255, 256]**. As such, the effective binding of GSH to Au@Ag NPs could be sterically restrained. The LODs obtained which are better than some reported probes in literature (Table 5.1) **[53, 84, 254-257]**, indicates that PEI-GQDs-Au@Ag system

for biothiols detection can be achieved in biological media coupled with a rapid detection time.

5.1.4. Selectivity studies

To test the selectivity of the probe with respect to biothiols sensing without interferences from other molecules, the relative fluorescence intensity of PEI-GQDs was assessed in the presence of five common α-amino acids (glysine, lysine, histidine, tryptophan and DL-lactic acid) and three proteins (bovine serum albumin (BSA), lysozyme, and cytochrome c) under similarly optimized conditions as shown in Fig. 5.4A. It was interesting to observe remarkable differences in the relative fluorescence intensities between that recorded for the respective biothiols and other α-amino acids and proteins. The difference is the presence of thiol group (SH) in Cys, Hcy or GSH. Au and Ag have a stronger affinity for thiols than NH_2 groups present in the other α-amino acids and proteins. This further adds to the analytical figures of merits of the nanoprobe for biothiols detection with a high degree of selectivity.

5.1.5. Proposed detection mechanism

The detection mechanism for the fluorescence "turn ON" detection of biothiols using PEI-GQDs-Au@Ag blend is premised on some theoretical insights that the addition of the respective biothiols to PEI-GQDs-Au@Ag blend could disrupt the interaction between PEI-GQDs and Au@Ag NPs.

This is ascribed to the known strong affinity of Au and Ag for thiol group and their tendencies to preferentially bind with biothiols to form the very strong Ag-S and/or Au-S bonds **[255, 258]**.

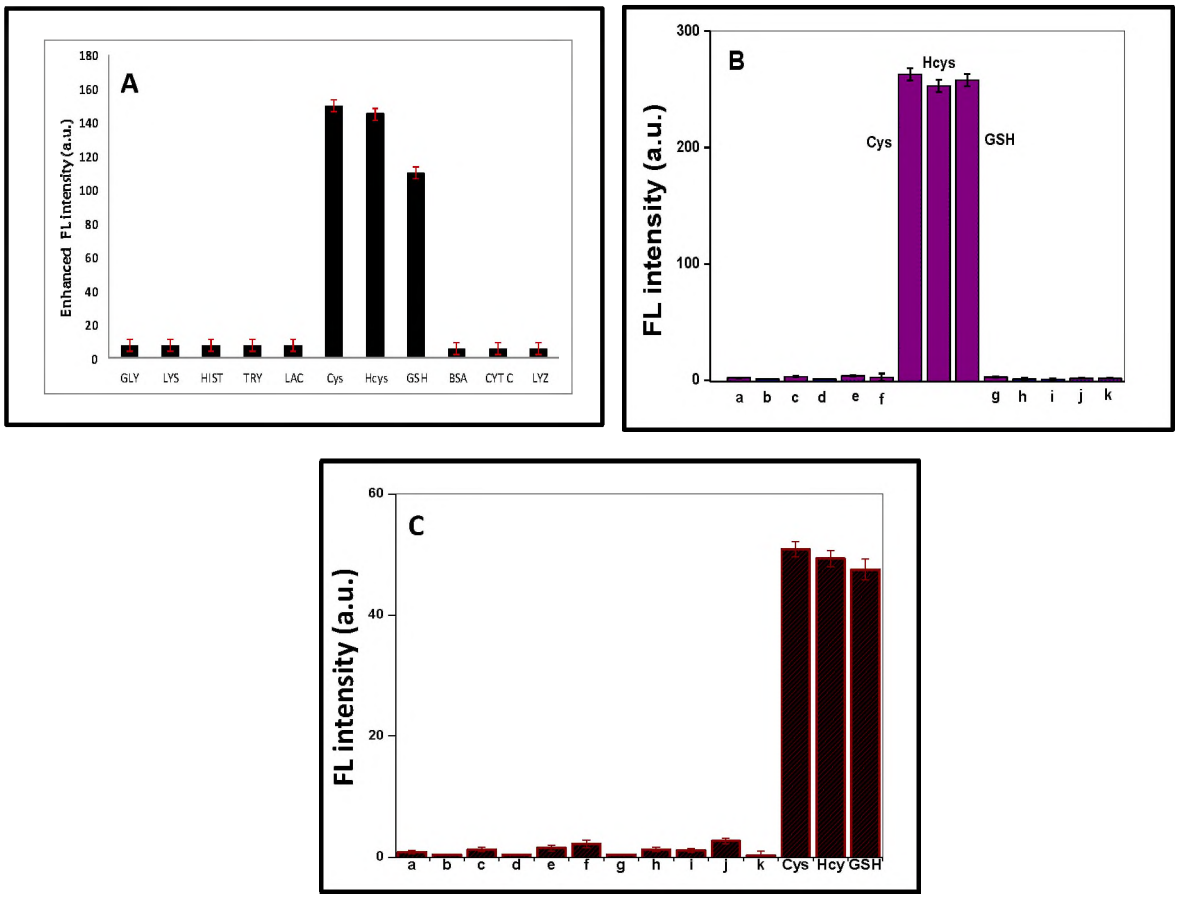

Fig. 5.4. Fluorescence intensity of (A) PEI-GQDs-Au@Ag, (B) M-GQDs, and (C) 12-GQDs for biothiols (50-120 nM) detection in the presence of other α-amino acids (1.0 μM) and proteins (1.0 mg/mL) (at tolerable error level of 5% and three replicate measurements, n=3). a-k : Glycine (GLY), lysine (LYS), histidine (HIST), tryptophan (TRY), trypsin, cystine, alanine, lactic acid (LAC), bovine serum albumin (BSA), cytochrome c (CYT C) and lysozyme (LYZ), respectively.

The binding of biothiols (via -SH group) to the surfaces of the Au and Ag NPs through covalent bonding is known [259, 260]. Thus, PEI-GQDs could be possibly released from its electrostatic interaction and/or surface adsorption with Au@Ag NPs due to the stronger binding interaction between Au@Ag NPs and the biothiols, leading to the restoration of the fluorescence of PEI-GQDs.

To prove that no interactions occurred between PEI-GQDs and the target analytes, the biothiols were added to the aqueous solution of PEI-GQDs (in the absence of Au@Ag NPs). The fluorescence intensity of PEI-GQDs remained unchanged (under similar experimental conditions, figure not shown), thus proving that the restored fluorescence was significantly due to the preferential binding of Au@Ag NPs to the biothiols with a consequent recovery of the quenched fluorescence of PEI-GQDs.

5.2. Biothiols detection using M-GQDs and 12-GQDs

In this section, the detection of biothiols (Cys, Hcy or GSH) using maleimide-derivatized-GQDs (M-GQDs) and MPc (**12**) (in the presence of GQDs) is discussed. Analyte detection schemes based on Michael addition mechanism are quite attractive due to the specificity and selectivity of the addition reaction **[75]**. In this work, it was envisaged that by anchoring Michael acceptors such as maleimides to the terminals of MPcs, it could result in the derivation of complexe(s) which can be employed for specific interaction with biothiols via the Michael addition reaction. Maleimide units (Michael acceptor) were attached to GQDs for biothiols detection (in aqueous solution and at physiological pH) via the Michael addition mechanism. It was envisaged that the linking of maleimide to GQDs will result in the quenching ("turn OFF"), which will then be restored ("turn ON") in the presence of biothiols resulting in the selective detection of the latter.

Maleimide-derivatized MPc (**12**) was synthesized by incorporating maleimide groups on the terminals of MPc ring to derive complex **12**. MPc with maleimide

as ring substituents is reported in this thesis for the first time. Complex **12** was designed to specifically interact with biothiols. This work shows the sensing ability of complex **12** towards biothiols when it is non-covalently (*π-π* stacking) conjugated to simple (pristine) GQDs as shown in Scheme 5.2A.

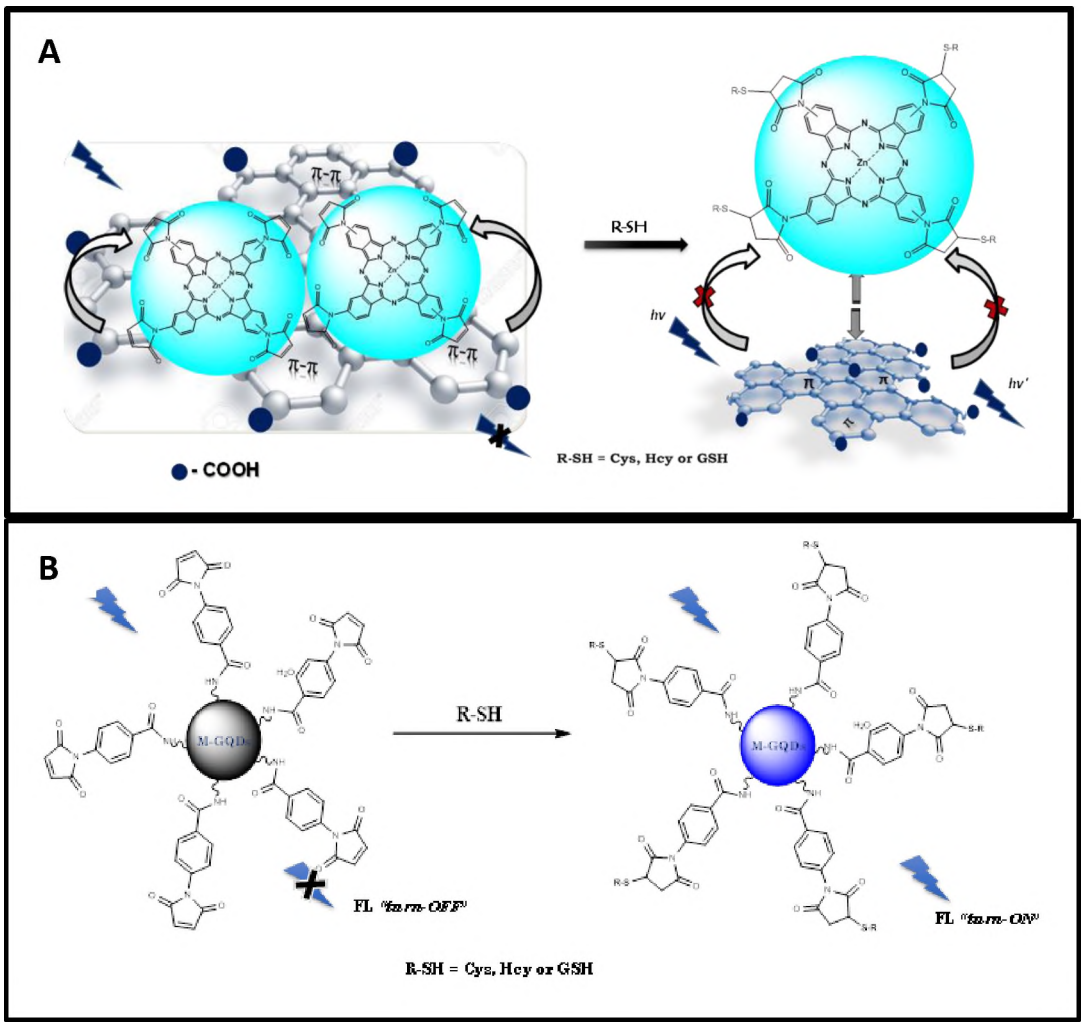

Scheme. 5.2. (A) Schematic illustration of the *π-π* stacking of GQDs and complex 12 and the "turn ON" of GQDs fluorescence in the presence of biothiols. (B) Mechanistic pathways for "*off-on*" switching of M-GQDs fluorescence by biothiols.

5.2.1. Fluorescence "turn ON" process

The studies were carried out in DMSO, since polar solvents have been described to make thiol-maleimide Michael addition reaction occur very rapidly **[75]**, and also due to the solubility of complex **12** in DMSO [a mixture of DMSO:PBS (1:4)] was used for **12**-GQDs. The fluorescence of PEI-GQDs was quenched (similar to Fig. 3.26) upon conjugation to the maleimide units via a fluorescence "turn OFF" process usually occasioned by the attachments of maleimide units to fluorophores **[261-263]**. Conversely, the fluorescence was gradually restored upon the addition of different concentrations of Cys, Hcy or GSH, respectively, in a manner similar to Fig. 5.3. The same applies to **12**-GQDs.

In order to evaluate the fluorescence "turn ON" sensitivity and LODs of M-GQDs and **12**-GQDs probes, the recovered fluorescence intensities in the absence (F_0) and presence (F) of Cys, Hcy or GSH were evaluated using Eq. **4.3** and **4.4**. The linear ranges obtained were 0.5-120 nM for Cys; 0.5-150 nM for Hcy and 1.0-200 nM for GSH, respectively. The LODs (Table 5.1) were evaluated to be as low as 0.30 nM, 0.45 nM and 0.86 nM for Cys, Hcy and GSH, respectively. The LODs for **12**-GQDs probe are 0.85, 1.42 and 3.2 nM for Cys, Hcy and GSH, respectively, Table 5.1. Comparing the results obtained for **12**-GQDs as biothiols sensing probe, it appears to be better than other GQDs and non-GQDs based nanoprobes reported to date as shown in Table 5.1. The LODs for biothiols detection using M-GQDs was better than **12**-GQDs which could be ascribed to the direct attachment of maleimide to GQDs resulting in an effective "*off-on*" compared to that of the bulky ring of complex **12**. However, the LODs of **12**-

GQDs were better than those involving PEI-GQDs-Au@Ag blend discussed above (Table 5.1), showing the advantage of using maleimide as a specific group for biothiols recognition (with or without MPc). Direct detection of biothiols using complex **12** alone was attempted in this work. However, when different concentrations of Cys, Hcy or GSH were added to complex **12** alone, there was no significant increase in the fluorescence of complex **12** (exciting where complex **12** absorbs). This could be due to the low fluorescence of MPcs derivatives such as complex **12**. Hence complex **12** alone cannot be used to sense biothiols even though the maleimide units on complex **12** interact with biothiols.

5.2.2. Selectivity studies

The selective ability of M-GQDs and **12**-GQDs to preferentially recognize biothiols (Cys, Hcy or GSH) without interferences from other molecules was studied. The restored fluorescence emission intensities relative to that acquired in the presence of some proteins (1.0 μM) such as glycine, lysine, histidine, tryptophan, trypsin, cystine, alanine, lactic acid, bovine serum albumin (BSA), cytochrome c and lysozyme, respectively, under optimized conditions are remarkably different as shown in Fig. 5.4 B and C for M-GQDs and **12**-GQDs, respectively. The difference in the recovered fluorescence intensities for the respective biothiols and other α-amino acids and proteins is a demonstration of the high specificity and selectivity for biothiols (Cys, Hcy or GSH) recognition by M-GQDs and **12**-GQDs probes. It is noteworthy to consider that the excellent selectivity results obtained herein originates from the rapid and specific Michael addition reactions propensity of the maleimide bearing M-GQDs and **12**-GQDs

which expediently ensures their specific and selective interaction with thiols **[224, 261-263]**.

5.2.3. Detection mechanism

Maleimide groups are known to react specifically with thiol groups (–SH) which exist in the side-chains of biothiols (Cys, Hcy or GSH) residues **[261-263]** via Michael addition reaction. As discussed earlier, the attachment of maleimide units (which are known electron accepting groups) to the electron donating GQDs resulted in the "turn-OFF" state of M-GQDs. This could be due to either intramolecular charge transfer (ICT) or photo-induced electron transfer (PET) process(es) from the GQDs core to the maleimide domains **[224, 263]**. During the sensing process, the interaction of maleimide-functionalized GQDs (M-GQDs) probe with the respective biothiols (Cys, Hcy or GSH) resulted in the conversion of the double bond of the maleimide ring to a saturated maleimide ring via Michael addition reaction (Scheme 5.2B), hence destroying the quenching ability of the maleimide domains attached to the GQDs by the deactivation of the ICT and/or PET process (es), further leading to the fluorescence "turn-ON" state of M-GQDs. Thus, biothiols addition to maleimide moieties (which occurs rapidly due to the maleimide ring strain) removes the π-electrons **[75, 224]**, and the n-π^* transition is destroyed or affected leading to the passivation of the quenching ability of maleimide. Fluorescence lifetime experiments are highly sensitive and insightful during fluorescence processes, hence were further employed to verify the "*off-on*" process of the probe (M-GQDs) in the presence of biothiols. As shown in Table 5.2, the fluorescence lifetimes increased upon the addition of

increasing concentrations of Cys to M-GQDs probe. Similar changes in the fluorescence lifetimes were observed when Hcy and GSH were separately titrated with M-GQDs probe. The results gave a definite rationalization of the observed "turn-ON" process which is largely ascribed to the blocking of the ICT or PET pathways due to the conjugation of biothiols to the maleimide units attached to GQDs.

On the other hand, the specific mechanism of the recovery of the fluorescence of GQDs coordinated to complex **12** in the presence of biothiols may be based on two rational theories. Firstly, the interaction of complex **12** with pristine GQDs resulted in the quenching of the fluorescence of GQDs, which could be based on either energy or electron transfer from GQDs to the electron deficient complex **12** (due to the low lying n-π^* transition of the maleimide ring attached directly to the MPc ring of complex **12**). Consequently, the Michael addition of biothiols to the probe (which occurs rapidly and selectively with complex **12** as a component of the probe) results in the saturation (removal of π bonds) of the maleimide rings (similar to M-GQDs) Scheme 5.2A. The UV-Vis spectra recorded for complex **12** in the presence of Cys (50 and 100 nM) showed a modified ground-state absorption of complex **12** with a blue-shift of the Q-band, which confirmed the specific interaction between complex **12** and the biothiols (Fig 5.5A). This interaction could disrupt the electronic or energy interaction between GQDs and complex **12**, thus leading to the enhancement of the fluorescence of GQDs within the conjugate. Secondly, the introduced biothiols could be incorporated as spacers between GQDs and complex **12** since both are non-covalently coordinated, hence the attachment of the biothiols to complex **12** to

form the thioether-MPc adduct as depicted in Scheme 5.2A, which could largely result in the dissociation of **12**-GQDs conjugate leading to disrupted interaction and consequent fluorescence "turn ON" process.

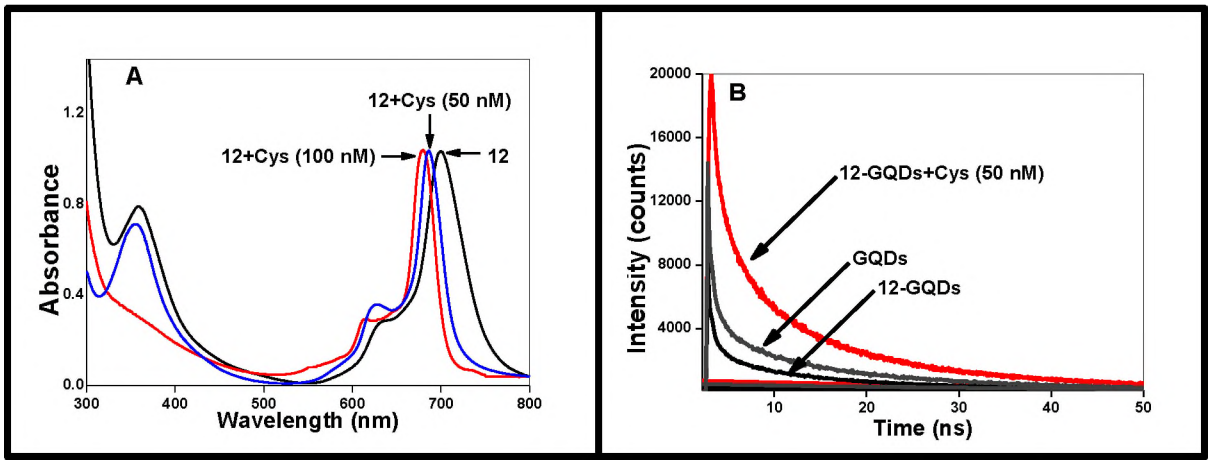

Fig. 5.5. (A) UV-Vis spectra modification of 12 alone and in the presence of different amounts of Cys (50 and 100 nM), and (B) Fluorescence decay curves showing changes in lifetimes of GQDs component of 12-GQDs probe (0.5 mg/mL) before and after addition of Cys. Solvent is DMSO/PBS (1:4) (PBS 10 mM, pH 7.0).

This "turn ON" phenomenon was further confirmed by changes in the lifetime of GQDs before coordination to complex **12** to form **12**-GQDs conjugate, and then upon coordination and further addition of biothiols as shown in Fig. 5.5B and Table 5.2.

5.2.4. Analytical detection in spiked samples

Simulated (spiked) samples with known concentrations of Cys, Hcy or GSH were subjected to analysis by M-GQDs and **12**-GQDs following the devised procedures. The recovery results obtained further demonstrates the usability of

M-GQDs and 12-GQDs for biothiols quantification in real samples. As shown in Table 5.3, the quantified Cys, Hcy or GSH (recovery percent (%) against known amount in the spiked samples) and the relative standard deviation (RSD) evaluated from three replicate measurements (n=3), demonstrates the precision and reproducibility of M-GQDs and 12-GQDs as probe for biothiol assays.

Table 5.2. Fluorescence "turn-ON" dynamics of M-GQDs monitored by changes in the best fit fluorescence lifetimes values upon addition of different concentrations of Cys, Hcy and GHS, respectively. Solvent: PBS (10 mM, pH 7.0).

Probe	Cys		Hcy	GSH
M-GQDs	Conc.(nM)	τ_F(ns)	τ_F(ns)	τ_F(ns)
	5	2.27	1.91	1.56
	20	3.15	2.89	2.52
	50	3.93	3.01	3.64
	100	5.04	4.8	4.02

M-GQDs probe has better recovery (hence sensitivity) (compared to 12-GQDs) towards biothiols, which could be ascribed to the combined advantage of excellent aqueous dispersibility and the direct attachment of the maleimide unit to GQDs surface. Also, thiol-maleimide reaction is rapid and stable in aqueous environments [75].

Table 5.3. Recovery studies of biothiols (Cys shown as an example) in simulated samples demonstrating analytical applicability, reproducibility and stability of the nanoprobes.

Probe	Cys added (nM)	Cys recovered (nM)	Recovery (%, n = 3)	RSD (%)
M-GQDs (in PBS)	50	50.5	101.1±0.55	1.22
	80	78.9	98.6±0.40	3.12
	120	119.9	99.9±1.50	2.25
12-GQDs in DMSO/PBS (1:4)	50	48.5	97.0±0.20	2.30
	80	77.3	96.6±0.13	3.40
	120	118.2	98.5±0.45	1.09

5.3. Conclusion

In summary, PEI-GQDs-Au@Ag blend, M-GQDs and **12**-GQDs were successfully fabricated for the rapid, sensitive and selective fluorescence "*off-on*" detection of biothiols. The nanoprobe contains Au@Ag NPs and maleimide units (M-GQDs and complex **12**) which are highly selective and reactive towards biothiols via the well-known Michael addition reaction (in M-GQDs and **12**-GQDs) and the strong affinity of Au/Ag for thiols compounds. All nanoprobes for biothiols demonstrated nanomolar range detection sensitivity with M-GQDs showing better performance which could be due to the direct attachment of the maleimide units to GQDs surface and the aqueous medium interaction with

biothiols, thus resulting in an effective "*off-on*" compared to that of the bulky ring of complex **12** and the weak electrostatic interaction between Au@Ag NPs and PEI-GQDs. However, the LODs for **12**-GQDs were better than those involving PEI-GQDs-Au@Ag blend, showing the advantage of using maleimide as a specific group for biothiols recognition (with or without MPc). Interference studies showed that several α-amino acids and proteins did not affect the detection sensitivities of the nanoprobes. The excellent recovery studies results obtained when samples with known concentration of biothiols were analysed, demonstrate the applicability of the nanoprobes for biothiols detection.

6. Mercury ion detection

This chapter discusses the detection of mercury ion (Hg^{2+}) using T-GQDs, MPc-GQDs(4-7-GQDs), 9-GQDs, 9-T-GQDs as nanoprobes by taking advantage of the affinity of Hg^{2+} for thymine and the thiol group of complexes 4-7.

6.1. Thymine-functionalized GQDs (T-GQDs)

This section reports on the sensitive detection of Hg^{2+} using thymine functionalized GQDs (T-GQDs). Thymine exhibits specific affinity to bind selectively and strongly with Hg^{2+}. Hence, a novel strategy where GQDs are functionalized with thymine was adopted in order to fabricate nanoprobes for Hg^{2+} detection.

Table 6.1. The comparison of the LODs (in this work and other reported methods) on GQDs-based nanoprobes for the detection of Hg^{2+}.

Probe	Dynamic range	LOD (nM)	REF
4-GQDs	0.5-50 nM	1.50	This work
5-GQDs	0.5-50 nM	0.52	This work
6-GQDs	0.5-50 nM	0.60	This work
7-GQDs	0.5-50 nM	0.12	This work
9-GQDs	0.1-20 nM	0.05	This work
9-T-GQDs	5-50 nM	24.65	This work
T-GQDs	0.5-50 nM	0.15	This work
GQDs	1-50 nM	0.439	[264]
GQDs	0.8-9μM	100	[265]
GQDs	0-60 μM	3360	[236]
GQDs	0.001-10 μM	0.25	[266]
GQDs-AuNPs	0.02-1.5 nM	2.47	[267]

6.1.1. Fluorescence "turn OFF" detection of Hg^{2+}

The detection of Hg^{2+} using T-GQDs alone as a novel nanoprobe followed the fluorescence "turn OFF" mechanism in which the fluorescence of T-GQDs decreased ("turn OFF") upon titration with varied concentrations of aqueous solution of Hg^{2+} under optimized conditions as shown in Fig. 6.1A. The "turn OFF" process is represented in Scheme 6.1. The decreased fluorescence is due to the aggregation of T-GQDs following the formation of T-Hg^{2+}-T base pair (where T represents thymine), which results in the quenching of the fluorescence of T-GQDs. The fluorescence quenching was accompanied by the decrease in the Φ_F of T-GQDs from 0.42 to 0.10 in the presence of Hg^{2+}.

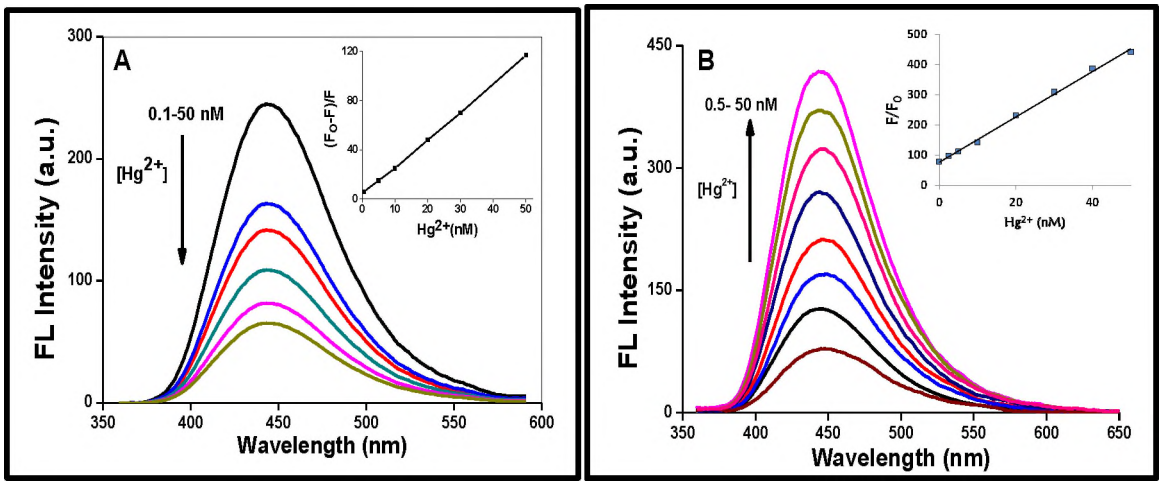

Fig. 6.1. Fluorescence intensity of (A) T-GQDs and (B) 5-GQDs (as an example) upon addition of different Hg^{2+} concentrations (0.1-50 nM) in PBS (10mM, pH 7.0/7.4). Insets: calibration curve. Excitation wavelength = 340 nm.

A linear calibration plot was generated, using the fluorescence quenching ratio, $(F_0\text{-}F)/F_0$ versus Hg^{2+} concentrations within the range of 0-50 nM (Fig. 6.1A inset). The slope (K) of the linear plot was then used to calculate the LOD using Eq. **4.4**.

The obtained LOD was 0.15 nM, Table 6.1, which is better than reported values [236, 264-267].

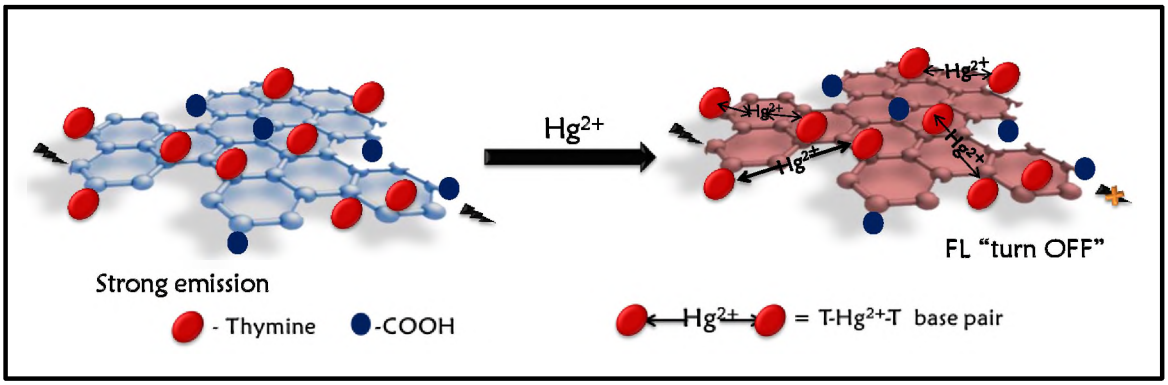

Scheme 6.1. Schematic illustration of the interaction between thymine-functionalized GQDs (T-GQDs) and Hg^{2+} leading to fluorescence quenching.

Since thymine could readily bind with Hg^{2+} to form the T-Hg^{2+}-T base pair complexes on T-GQDs surface, it is plausible to consider that the excellent PL properties of T-GQDs and aqueous medium interaction with Hg^{2+} favored the binding of Hg^{2+} to thymine component of T-GQDs resulting in the efficient and responsive quenching of T-GQDs fluorescence even at very low concentrations (nanomolar) of Hg^{2+}.

6.1.2. Selectivity studies

To evaluate whether T-GQDs probe could detect Hg^{2+} selectively, fluorescence quenching experiment was carried out with different metal ions (2.0 μM) such as Fe^{3+}, Ni^{2+}, Cu^{2+}, Fe^{2+}, Co^{2+}, Mn^{2+}, Pb^{2+}, Al^{3+}, Na^{+} , K^{+} and Ag^{+}, Fig. 6.2A. All the metal ions showed very low fluorescence quenching efficiency compared to Hg^{2+} at concentrations up to 100 folds than that of Hg^{2+} (20 nM), Fig. 6.2A.

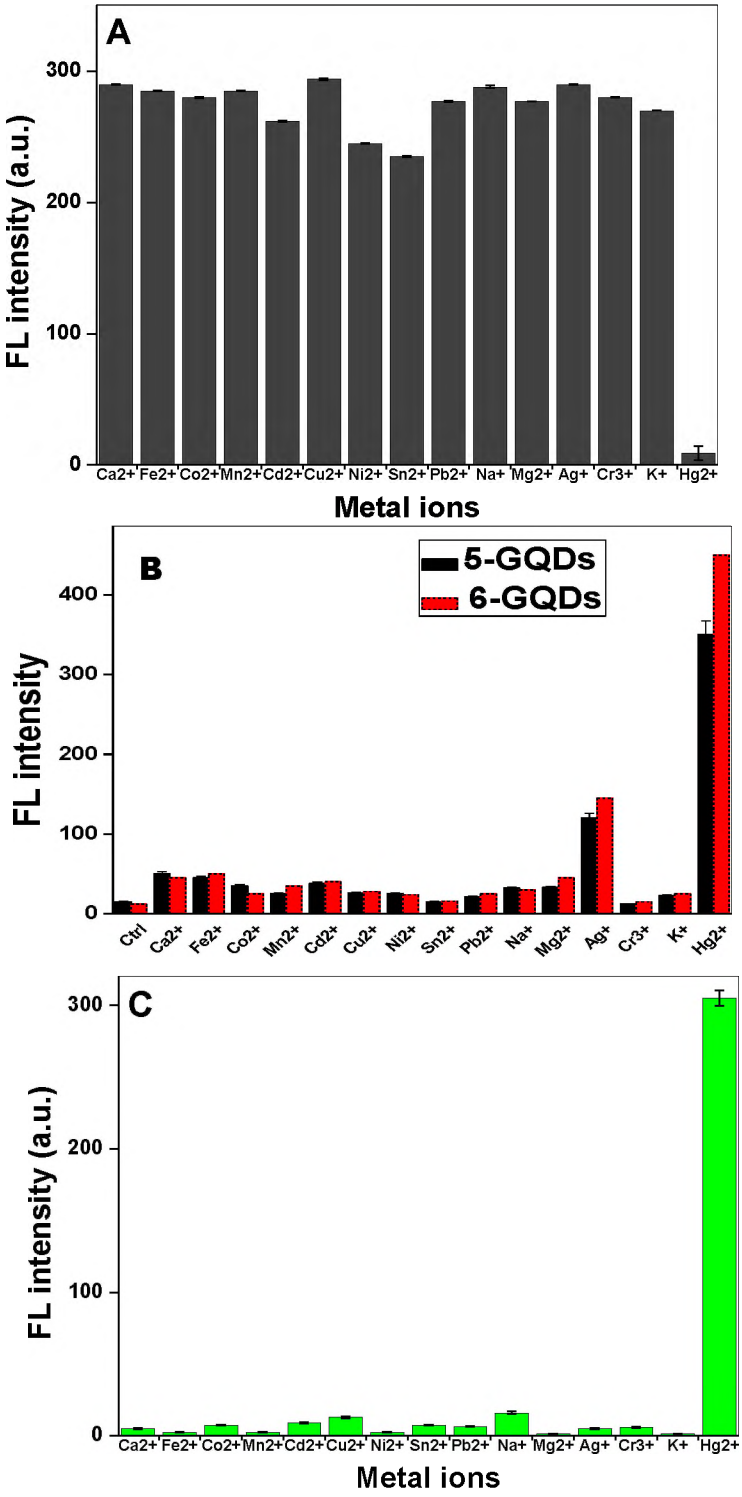

Fig. 6.2. (A) Fluorescence quenching rate of T-GQDs (1.0 mg/mL). Fluorescence intensity of (B) 5-GQDs/6-GQDs and (C) 9-GQDs in PBS (10 mM, pH 7.0 and DMF/PBS (1:4)) in the presence of different metal ions. $[Hg^{2+}]$ = 20 nM, and the concentrations of metal ions = 2.0 μM.

The results obtained upon the screening of the various metal ions reflect the strong selectivity of T-GQDs, hence the quantitative detection of Hg^{2+}.

6.1.3. Detection mechanism

T-GQDs probe acted as an electron donating entity in a typical photoinduced electron transfer (PET) process involving T-GQDs and Hg^{2+}, which have been reported as the major pathways by which the fluorescence of GQDs is quenched by metal ions **[236, 265, 266]**. The binding of Hg^{2+} ions to thymine (T) forming T-Hg^{2+}-T base pairs, could aid the transfer of electrons from the electron-rich fluorophore (T-GQDs) to the electron accepting Hg^{2+} ions following PET mechanism with a consequent quenching of the fluorescence of T-GQDs. To verify this hypothesis, further experiments were conducted such as fluorescence lifetimes which are highly sensitive during quenching processes. Fluorescence lifetimes remained relatively unchanged upon the addition of various concentration of Hg^{2+} to T-GQDs probe (Table 6.2). This result is an indication of the formation of a non-radiative ground state complex between T-GQDs and Hg^{2+} and this supports the fact that the strong binding ability of Hg^{2+} to the thymine (on T-GQDs surface or edges) ensued a tremendous quenching of the T-GQDs fluorescence.

6.1.4. Detection of Hg^{2+} in spiked samples

Analytical validation of T-GQDs as a probe was assessed by subjecting a series of quantitatively prepared spiked samples (with known Hg^{2+} concentrations) to test. Recovery results obtained further demonstrates the applicability of the

nanoprobe for Hg^{2+} quantification in real samples. Table 6.3 shows the quantification of Hg^{2+} (recovered Hg^{2+} (%) against known amounts in the spiked samples) and the relative standard deviation (RSD) evaluated from three replicate measurements, n =3. Replicate runs on the spiked samples (with Hg^{2+}) were done and as shown in Table 6.3, the average recoveries (%) and relative standard deviations (RSD) obtained for T-GQDs probe indicate good precision and reproducibility of the detection scheme. T-GQDs assay for Hg^{2+} combines the advantage of aqueous dispersibility and rapid detection.

Table 6.2. Comparison of the best fit fluorescence lifetime values of T-GQDs and 9-GQDs in the absence and presence of an equivalent of [Hg^{2+}] in 10 mM PBS, pH 7.0 and DMF/PBS (1:4).

Probe	[Hg^{2+}](nM)	τ_F(ns)±0.10, n=3
T-GQDs	0	6.50
	0.1	6.52
	10	6.55
	20	6.45
	50	6.48
9-GQDs	0	1.95
	5	2.52
	10	2.98
	20	3.45
	50	4.02

Table 6.3. Recovery studies (analytical application) of T-GQDs, 9-GQDs and 9-T-GQDs for Hg^{2+} estimation in simulated spiked samples.

Probe	Added (nM)	Found (nM)	Recovery (%, n = 3)	RSD (%)
T-GQDs	20	18.5	91.0±0.75	7.5
	30	26.8	90.0±0.40	4.3
	50	46.9	94.0±3.50	3.9
9-GQDs	20	20.5	102.5±0.60	6.2
	30	30.3	101.0±0.35	3.9
	50	51.2	102.4±0.25	2.7
9-T-GQDs	20	19.02	95.10±0.85	8.0
	30	27.95	93.53±0.46	4.5
	50	45.20	90.40±0.55	5.5

RSD = relative standard deviation

6.2. MPc (9)-GQDs/T-GQDs conjugates

In this work, thymine was appended to MPc ring to form thymine-substituted MPc (complex **9**). The incorporation of thymine onto MPc ring as substituents is aimed at creating functional materials for the selective and specific recognition of Hg^{2+} owing to the known specific interaction between thymine and Hg^{2+} to form the T-Hg^{2+}-T pairs **[139, 140, 268, 269]** as discussed for T-GQDs. Thymine-functionalized MPc and MP have been reportedly employed for the sensing of Hg^{2+} in the literature via fluorescence "turn OFF" process **[139, 140]**, which is less efficient than the "turn ON" employed in this work using same complex **9** when coordinated to GQDs for the first time.

For "turn ON" sensing strategy, pristine (un-functionalized) GQDs and T-GQDs were separately non-covalently coordinated to complex **9** through the π-π stacking method to form **9**-GQDs or **9**-T-GQDs conjugates, respectively.

6.2.1. Fluorescence "turn ON" detection of Hg^{2+}

The fluorescence of GQDs upon conjugation to complex **9** resulted in a fluorescence "turn OFF" process as it is the case with other MPcs coordination to GQDs in this work. However, the fluorescence was restored upon interaction with Hg^{2+} as a test analyte in a similar manner to Fig. 6.1B and illustrated in Schemes 6.2 and 6.3.

For **9**-GQDs conjugate, the fluorescence enhancement was accompanied by an increase in Φ_F value of **9**-GQDs from 0.09 in the absence of Hg^{2+} to 0.26 in the presence of Hg^{2+} (Table 6.4). The same applies to the fluorescence lifetimes which increased from 1.95 ns to 4.02 ns. For **9**-T-GQDs, an increase in the Φ_F value was from 0.03 (without Hg^{2+}) to 0.1 (with Hg^{2+}), with a significant change in fluorescence lifetime observed (Table 6.4).

Using the method described above, the LODs obtained for **9**-GQDs system was 0.05 nM which is much lower than the LOD value of 24.7 nM (within a linear range of 5-50 nM of Hg^{2+}) obtained for **9**-T-GQDs system for Hg^{2+} quantification (Table 6.1). Hence, **9**-GQDs conjugate is more sensitive for the detection of Hg^{2+}. This observation could be ascribed to the fact that Hg^{2+} was bound to T-GQDs as well as complex **9** components of **9**-T-GQDs probe since they both contain thymine functionality (as depicted in Scheme 6.3). It is also possible that the higher LOD for **9**-T-GQDs might be due to competing fluorescence "turn ON"

and "turn OFF" processes occurring simultaneously due to the intra and inter-molecular multiple binding of Hg^{2+} to form T-Hg^{2+}-T base pair complexes with both T-GQDs and complex **9**, hence suppressing the FL "turn ON" signal of T-GQDs within the conjugate.

Table 6.4. Photophysical data obtained for T-GQDs/pristine GQDs and their conjugates with complex 9. Solvent: DMF and PBS (10 mM, pH 7.0).

Complex	Q-band maxima (nm)/$\lambda_{absorption}$	Φ_F (± 0.01)	τ_F(ns) (± 0.01)
GQDs	-	0.31	5.70
T-GQDs	-	0.42	6.50
9-GQDs	686	0.09	1.95
9-T-GQDs	686	0.03	1.05
9-GQDs + Hg^{2+} (50 nM)	682	0.26	4.02
9-T-GQDs + Hg^{2+} (50 nM)	681	0.1	2.01

Thus, the combination of pristine GQDs with complex **9** is better for Hg^{2+} quantification than when T-GQDs are employed with complex **9**. To further confirm this observation, Hg^{2+} was titrated against pristine GQDs solution and the fluorescence of pristine GQDs (alone) remained relatively unchanged (figure not shown) at the investigated concentration range (0.1-50 nM) of the test analyte which points to the fact that the "turn ON" signals are as a result of the binding of Hg^{2+} to the thymine moieties on the MPc (**9**) ring.

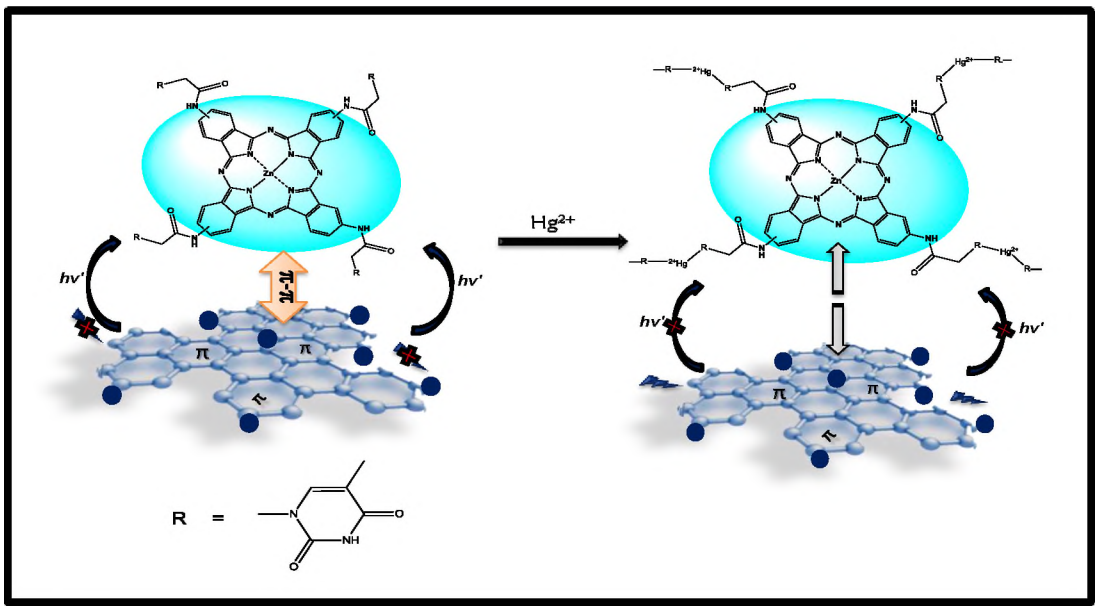

Scheme 6.2. Illustration of non-covalent interaction between pristine GQDs and thymine-appended MPc (9) resulting in the quenching of the fluorescence of GQDs followed by "turn ON" in the presence of Hg^{2+}.

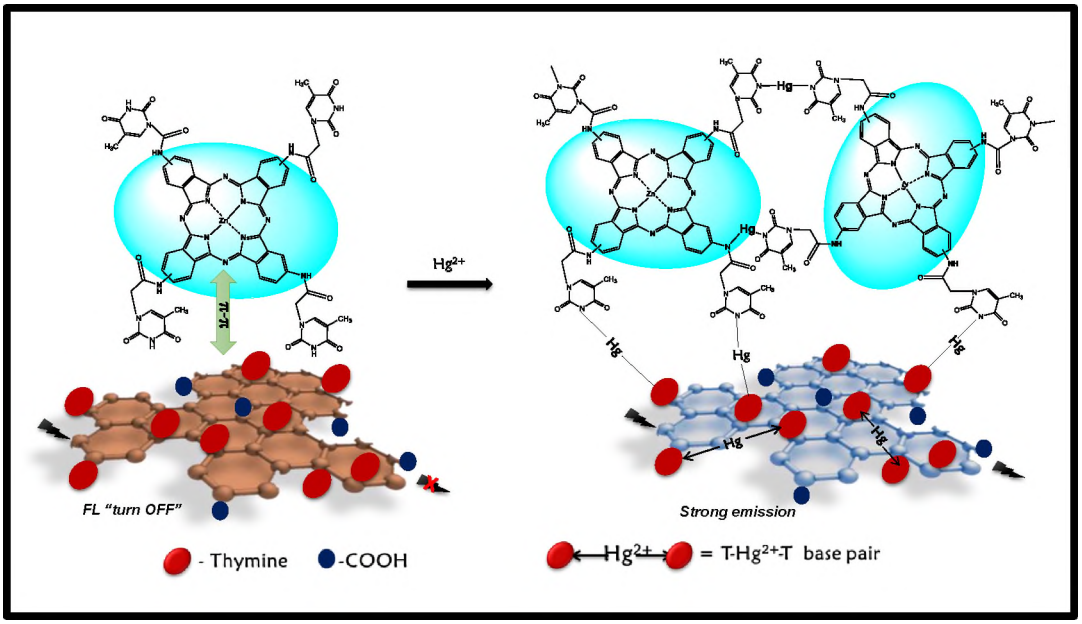

Scheme 6.3. Schematic illustration of the binding interactions between Hg^{2+} to T-GQDs, complex 9 and the possible formation of T-Hg^{2+}-T base pairs between T-GQDs, 9-T-GQDs and 9-9 in the presence of Hg^{2+}.

6.2.2. Selectivity and recovery studies

The selective nature of the thymine derivatized MPc complex **9**-GQDs/T-GQDs probes was verified by carrying out interference studies for the detection of Hg^{2+} in the presence of other metal ions delineated in Fig. 6.2C. To the probe solutions, 2.0 μM aqueous solutions of different metal ions were added to evaluate their effects on the fluorescence behaviour of the GQDs within the conjugates (at tolerable error level of 5% and three replicate measurements, n=3). Clear selectivity for Hg^{2+} by the probes over other metal ions was observed as shown in Fig. 6.2C (as an example). To understand the effects of counter ions (anions) on the selectivity of the probes, Hg^{2+} was screened in the presence of anions such as Cl^-, NO_3^-, CO_3^{2-} and SO_4^{2-}. The results obtained showed no interference of the anions on the quantitative detection of Hg^{2+} by the fabricated nanoprobes.

6.2.3. Proposed mechanism

The observed fluorescence *"off-on"* of complex **9**-GQDs/T-GQDs probes in the presence of Hg^{2+} could be ascribed to the specific binding of Hg^{2+} to thymine molecules appended to the MPc (**9**) ring as similarly discussed for other target analyte specific substituents on MPcs rings in this thesis. For pristine GQDs conjugate with complex **9**, the recovery of the quenched fluorescence could be based on two reasons. Firstly, induced aggregation of complex **9** (non-covalently bound to pristine GQDs) due to the formation of T-Hg^{2+}-T complex upon addition of Hg^{2+}, which could result in the disruption of the energy transfer process occurring between the GQDs and complex **9**, hence the restoration of

the quenched fluorescence. Secondly, in the presence of Hg^{2+}, thymine preferentially binds strongly to Hg^{2+} resulting in the incorporation of Hg^{2+} molecules as spacers between the GQDs and complex **9** which could disrupt the π-π stacking interaction between both materials. The quenching of the fluorescence of GQDs by complex **9** is attenuated, resulting in the enhancement of the fluorescence ("turn ON" sensing). In the case of **9**-T-GQDs system, Hg^{2+} could be bound to both T-GQDs and complex **9**, resulting in the suppression of the "turn ON" fluorescence as stated above.

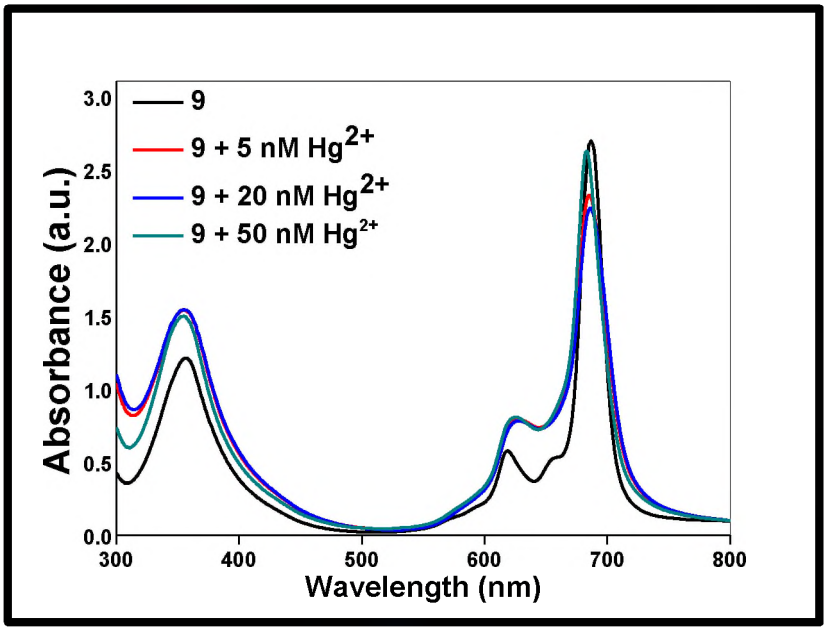

Fig. 6.3. UV-Vis spectral changes of complex 9 alone in the presence of different amounts of Hg^{2+} (5, 20 and 50 nM).

To prove that the interaction between complex **9** and Hg^{2+} specifically led to the observed fluorescence "turn-ON" mode of pristine GQDs, various amounts of Hg^{2+} were titrated against complex **9**. Fig. 6.3 shows the changes in the ground state absorption of complex **9** in the presence of different concentrations of Hg^{2+}. There were blue shifts in the Q-band and an increase in absorbance near 620 nm

due to aggregation. Aggregation in MPcs is judged by splitting or broadening of the Q-band, with the high energy band being due to the aggregate formation [228]. The aggregation is an indication of the formation of T-Hg^{2+}-T complex where a single Hg^{2+} molecule could bind to adjacent complex **9** molecules.

Fluorescence lifetime measurements were further collected and as shown in Table 6.2, the fluorescence lifetime values of pristine GQDs when conjugated to complex **9** increased in the presence of different concentrations of Hg^{2+}, confirming the "turn ON" process.

6.2.4. Recovery studies

Recovery studies were done so as to evaluate the analytical applicability of the nanoprobes. Table 6.3 shows the obtained recovery in a series of spiked samples with known amounts of the target analyte. This result further confirmed that the probes fabricated in this work could be applied in the detection of the target analyte (Hg^{2+}) with good recoveries in real samples.

6.3. MPcs (4-7)-GQDs conjugates

The fluorescence of GQDs was quenched upon coordination to the respective MPcs (complexes **4-7**). However, the fluorescence was "turned ON" in the presence of Hg^{2+} employed as a test analyte. The mechanism of the "turn ON" of the fluorescence of GQDs in the nanoconjugates is ascribed to the strong affinity of Hg^{2+} to bind with the bridging sulfur on the MPcs periphery, thereby disrupting the π-π stacking interaction between GQDs and the MPc complexes with a consequent "turn ON" as depicted in Scheme 6.4.

6.3.1. Fluorescence "turn ON" detection of Hg^{2+}

The fluorescence of GQDs upon coordination to the MPcs (complexes **4-7**) resulted in a "turn OFF" process. Then the fluorescence was "turned ON" by Hg^{2+}. Thus, the fabricated nanoprobes of **4**-GQDs, **5**-GQDs, **6**-GQDs and **7**-GQDs were deployed for the fluorimetric sensing of Hg^{2+} since only this analyte reasonably modulated GQDs fluorescence within the nanoconjugates.

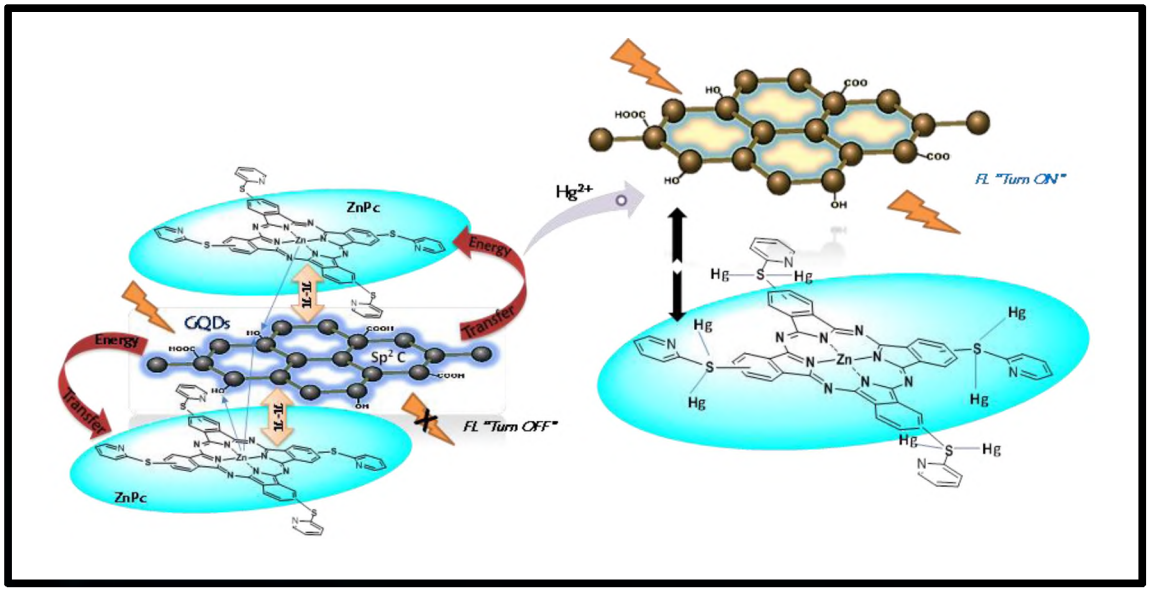

Scheme 6.4. Schematics of the mechanism for Hg^{2+} detection using GQDs and MPcs (4-7) conjugates.

The enhancement ("turn ON") of GQDs fluorescence upon increasing the concentration of Hg^{2+} is shown in Fig. 6.1B (using **5**-GQDs as an example of the others). The fluorescence signals increased linearly with the concentrations of Hg^{2+} in the range of 0.5-50 nM (Fig. 6.1B). The fluorescence emission wavelength maximum of GQDs (alone) remained unchanged at the investigated concentration range of the test analyte which points to the fact that the "turn ON" signals are as a result of the binding of Hg^{2+} to the coordinated MPcs (**4-7**).

This work which is based on GQDs coupled with MPcs (**4-7**) for Hg^{2+} detection via fluorescence "turn ON" mechanism with nanomolar range LODs was compared with some sensing systems from the literature as shown in Table 6.1. The nanoprobes showed LOD values within the nanomolar range with **7**-GQDs showing better values than those reported in literature. Moreover, most methods reported in literature involving the use of GQDs alone as nanosensors are mostly based on "turn OFF" designs, whereas the probes herein are based on fluorescence "turn ON" process which is more reliable than the "turn OFF" process (since "turn OFF" may not be only due to the effects of the test analytes). Thus, this work presents more reliable sensing materials for Hg^{2+} detection and quantification utilizing GQDs conjugates with MPc complexes **4-7**. The nanoprobes responsiveness to the presence of Hg^{2+} remained relatively unchanged after several months of fabrication which attests to the stability of the probes.

6.3.2. Selective screening of various cations

The selectivity of the MPcs-GQDs nanoprobes was evaluated by screening different cations (mostly divalent) of Ca^{2+}, Fe^{2+}, Co^{2+}, Mn^{2+}, Cd^{2+}, Cu^{2+}, Ni^{2+}, Sn^{2+}, Pb^{2+}, Na^{+}, Mg^{2+}, Ag^{+}, Cr^{3+} and K^{+} at concentrations about 10 fold higher than the highest concentration within the linear range of Hg^{2+} detection. Hg^{2+} remarkably gave the highest recovered fluorescence intensity as shown in Fig. 6.2B. Conversely, there were no competing fluorescence "turn ON" signals from other relevant metal ions screened except for Ag^{+} which gave a fluorescence enhancement that was however very much weaker compared to that of Hg^{2+} as shown in Fig. 6.2B. Since mercapto (S) groups bind more strongly to Hg^{2+} **[255]**,

the "turn ON" of the fluorescence of GQDs could be ascribed to the stronger ability of Hg^{2+} to coordinate with the S atom bearing substituents on the periphery of the MPcs (**4-7**). The nanoprobes strike a mutual balance between high sensitivity and selectivity towards Hg^{2+} detection with nanomolar range detection limits typically required for various environmental applications.

6.3.3. Proposed detection mechanism

In order to elucidate the underlying mechanisms for the fluorescence "turn ON" of GQDs in the presence of the test analyte, fluorescence lifetime measurements were carried out. As shown in Fig. 6.4A, the fluorescence decay curve of **5**-GQDs exhibited an increase in the fluorescence decay lifetime in the presence of Hg^{2+} to a value closer to that of GQDs alone. Similar concentration of Hg^{2+} was added to GQDs solution and there were no changes in the fluorescence lifetime of GQDs. Since the fluorescence of GQDs was restored upon interaction of the nanoconjugates with Hg^{2+}, the fluorescence principle of "*off-on*" mode is deemed to have taken place. As such, the quenching of the fluorescence of GQDs resulted when energy transfer occurred between GQDs and the MPcs (**4-7**) leading to the deactivation of the radiative recombination pathways and the depopulation of the excited states of GQDs. Conversely, in the presence of Hg^{2+}, the energy transfer process could have been disrupted due to the binding of Hg^{2+} to thiols (SH) group of the MPcs (**4-7**) and the fluorescence of GQDs is "turned ON" as illustrated in Scheme 6.4.

The disruption of the energy transfer process between GQDs and the MPcs nanoconjugates by Hg^{2+} could be predicated on two reasons. Firstly, the

coordinated MPcs possess sulfur bearing substituents which have specific and strong affinity to preferentially bind Hg^{2+}. Thus, Hg^{2+} could bind specifically to the mercapto groups of the MPc complexes coordinated to GQDs and potentially result in the fluorescence "turn ON" mode of the GQDs.

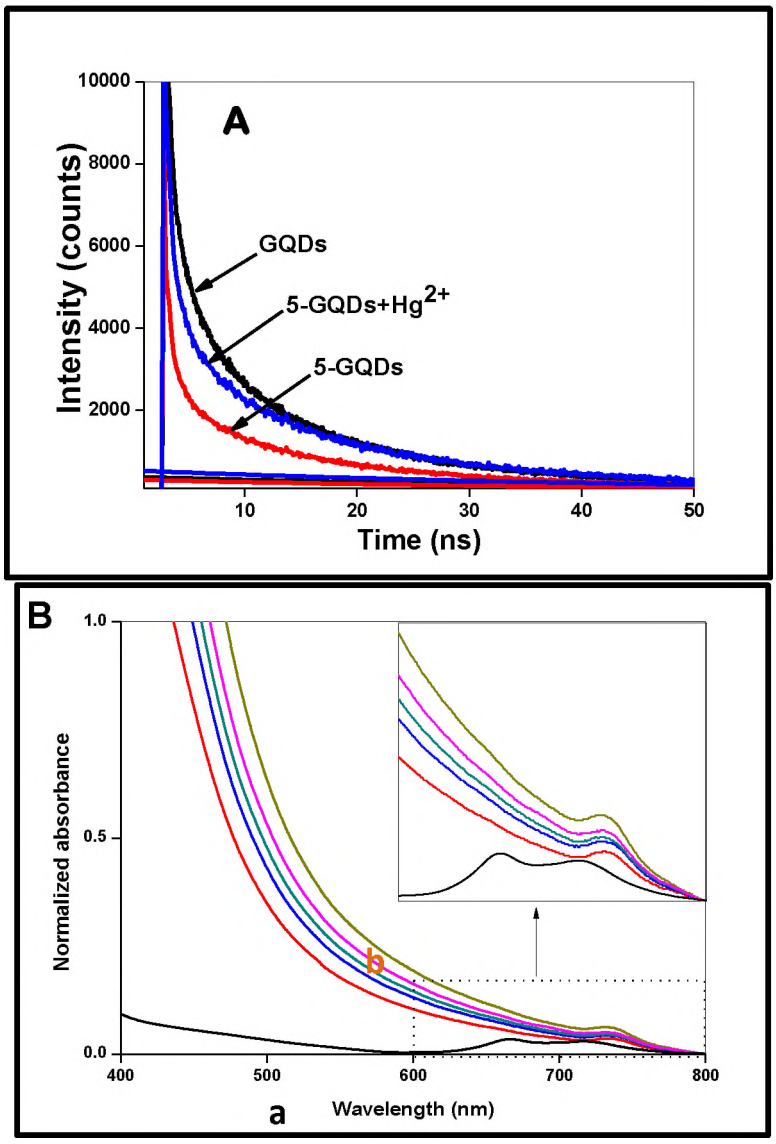

Fig. 6.4. (A) Fluorescence decay profile of GQDs in the presence of complex 5 and upon addition of Hg^{2+}, and (B) UV-Vis absorption of 5-GQDs nanoprobe (as an example) in the presence of different concentrations of Hg^{2+} ion (2.5-50 nM). Solvent: PBS 10 mM, pH 7.4. (a) Start (b) End.

Secondly, Hg^{2+} could act as a spacer between GQDs and the MPcs resulting in the disruption of the π-π interaction and the 'donor-acceptor' relationship between GQDs and the MPcs, hence GQDs fluorescence is "turned ON". Further evaluation was done where the ground state absorption spectra of the MPcs-GQDs conjugates were recorded in the presence of different concentrations of Hg^{2+}. Marked changes in the absorption spectra of **5**-GQDs (shown in Fig. 6.4B as an example of others) were observed as there was a red shift of the monomer component of the Q-band from 718 to 732 nm in the absence and presence of Hg^{2+}, respectively, which is an indication of binding interaction between the MPcs and Hg^{2+} ions, hence the spectra shift. Red shifting is associated with the formation of the rare J aggregates (edge-to-edge as opposed to face-to-face H aggregates) in MPcs **[270]**, hence it is plausible to conclude that the red shift observed in Fig. 6.3B is a result of the formation of these aggregates following coordination of Hg^{2+}.

6.4. Conclusion

When thymine is used to functionalize GQDs or appended to the periphery of MPc (complex **9**), the sensitive detection of Hg^{2+} could be achieved. Complex **9** was coordinated to pristine GQDs and T-GQDs separately via non-covalent π-π stacking to form supramolecular assemblies (**9**-GQDs and **9**-T-GQDs). In a similar manner, the conjugation of MPc complexes **4-7** (possessing a sulfur bridge on their rings) to GQDs could be used for the sensitive recognition of Hg^{2+}. The sensing mechanism is based on the strong affinity of Hg^{2+} for thymine (of T-GQDs or complex **9**) or the thiol group of complexes **4-7**, respectively. The

direct detection of Hg^{2+} was achieved by a "turn OFF" mechanism using T-GQDs. Conversely, nanoconjugates of GQDs and complexes **4-7** and **9** could detect Hg^{2+} via a fluorescence "turn ON" process. The recovered fluorescence intensity was dependent on varied concentrations of Hg^{2+}, hence allowing for the analytical quantification of Hg^{2+}.

Nanomolar LODs were obtained all nanoprobes employed for Hg^{2+} detection. However, better LODs were obtained for **9**-GQDs (0.05 nM), T-GQDs (0.15) and **7**-GQDs (0.12), showing higher sensitivity in the thymine-based probes. All nanoprobes were highly selective and specific for Hg^{2+} in the presence of other metal ions screened. The nanoprobes were used to quantify Hg^{2+} in real samples (spiked) and satisfactory recoveries were obtained which further demonstrated the applicability of these novel sensing systems for Hg^{2+} detection and quantification in real samples.

7. Sequential detection of mercury (II) ion and biothiols

This chapter discusses the sequential approach towards the dual detection of mercury ion (Hg^{2+}) and biothiols, respectively, using PEI-GQDs-Au@Ag and PEI-GQDs-5-Au@Ag hybrid systems.

7.1. PEI-GQDs-Au@Ag

In this chapter, the application of PEI-GQDs-Au@Ag hybrid for the specific recognition of Hg^{2+} is presented. As stated above, Au@Ag NPs and PEI-GQDs could form electrostatic conjugate; hence PEI-GQDs-Au@Ag hybrid exhibited a weak emission of PEI-GQDs within the hybrid as discussed in chapter five. However, there was observed gradual increase ("turn ON") of the fluorescence of PEI-GQDs in the presence of different concentrations of Hg^{2+} (Fig. 7.1A). The LOD for Hg^{2+} detection was evaluated to be 2.45 nM (Table 7.1).

Table 7.1. Limits of detection (LODs) obtained for the sequential detection of Hg^{2+} and biothiols using PEI-GQDs in the presence of Au@Ag NPs or 5-Au@Ag hybrid.

Method Biothiols detection (in water)	FL ON/OFF	LOD (nM)			REF.
		Cys	Hcys	GSH	
PEI-GQDs/Au@Ag+Hg^{2+}	OFF	0.95	2.05	3.56	This work
PEI-GQDs-5-Au@Ag+Hg	OFF	0.72	0.87	1.05	This work
Hg^{2+} detection		Solvent	Linearity	LOD	
PEI-GQDs-Au@Ag	ON	water	0.1-25 nM	2.45	This work
PEI-GQDs-5-Au@Ag	ON	water	0.5-50	0.25	This work

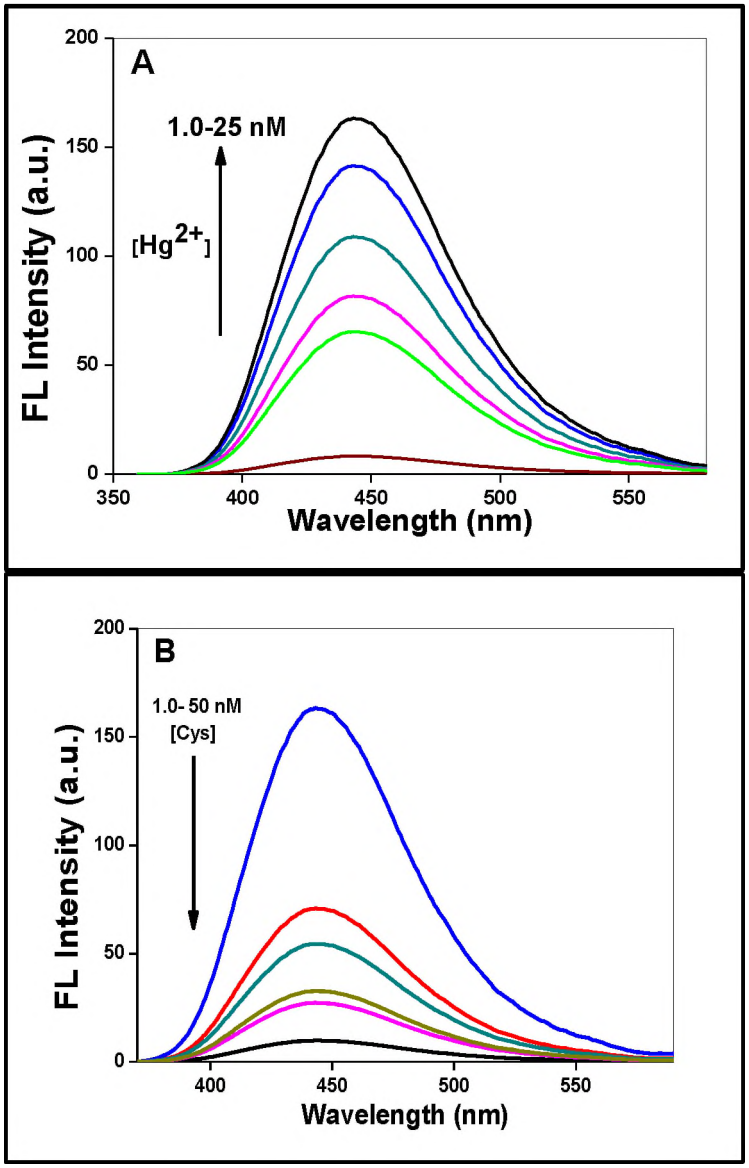

Fig. 7.1. Fluorescence spectra of PEI-GQDs (in PEI-GQDs-Au@Ag hybrid) (A) "turn ON" signal in the presence of Hg^{2+} and (B) induced "turn OFF" signal in the presence of Cys. Solvent: 50 mM PBS solution (pH 8.0). Excitation wavelength = 350 nm.

The detection of biothiols using this hybrid system is based on a mechanism of selective and competitive binding of Hg^{2+} between Au@Ag NPs and biothiols. Biothiols are known mercury capturing molecules due to the very strong binding affinity of their S atom to bind Hg^{2+} ions to form the robust Hg-S bonds with

biothiols [255]. Thus, biothiols can effectively abstract Hg^{2+}, thereby disrupting the metaphilic attraction between Hg^{2+} and Au@Ag NPs.

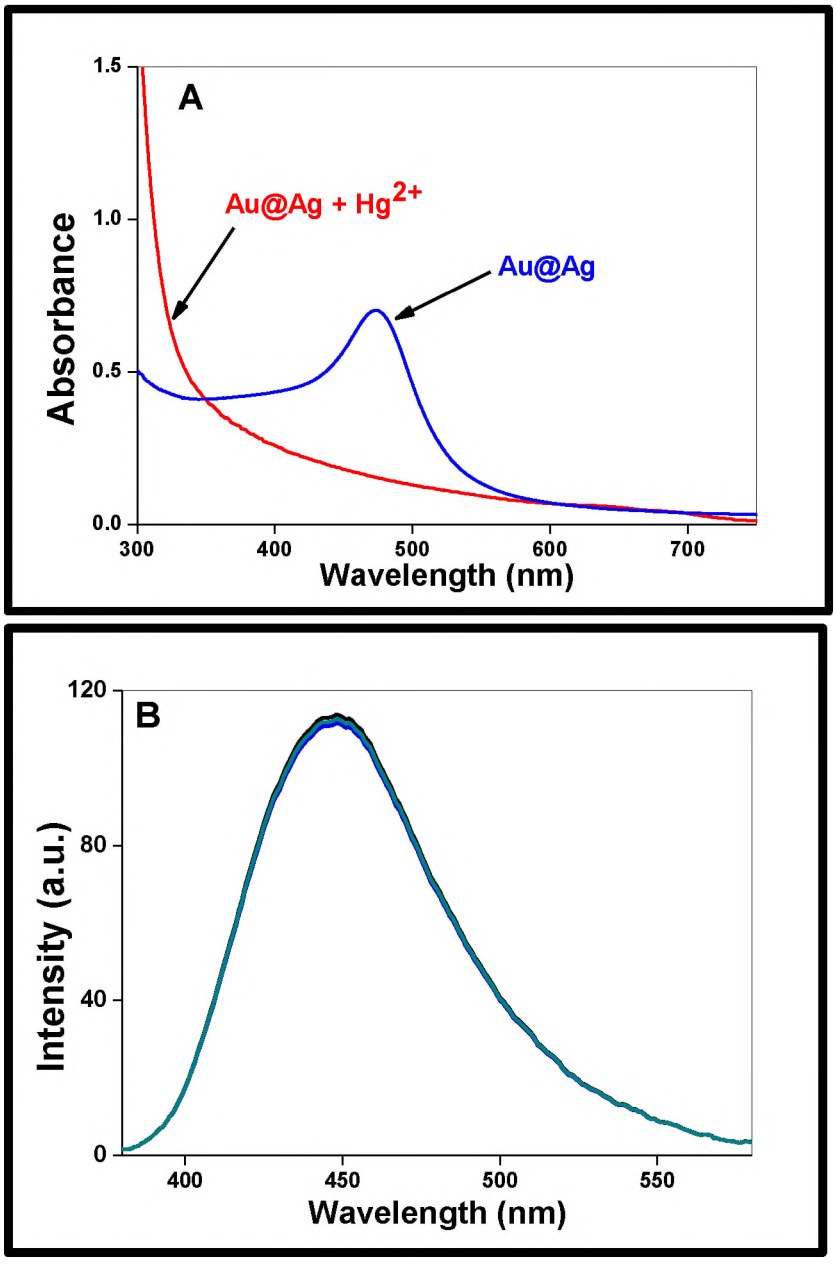

Fig. 7.2. (A) UV-Vis spectra of Au@Ag NPs alone and in the presence of Hg^{2+} and (B) Fluorescence spectra of PEI-GQDs in the presence of Hg^{2+}. Solvent: PBS (10 mM, pH 7.0).

As shown in Fig. 7.1B (using Cys as an example), the gradual increase in the concentration of Cys was accompanied by the fluorescence of PEI-GQDs being "switched OFF" again with a steady decrease in intensity. Therefore, PEI-GQDs/Au@Ag-Hg^{2+} could function as sensitive probe for Cys, Hcy or GSH detection via indirect "switch OFF" of the fluorescence of PEI-GQDs. The LODs for the biothiols were 0.95, 2.05 and 3.56 nM for Cys, Hcy and GSH, respectively (Table 7.1). It can be observed from the obtained LODs that the probe system is quite sensitive with nanomolar LODs for biothiols assays, and are comparable to some other GQDs and non-GQDs based nanoprobes documented in the literature.

The sensing mechanism is based on the induced aggregation of Au@Ag NPs attached to PEI-GQDs upon addition of Hg^{2+}. The induced aggregation of Au or Ag NPs was proved by the addition of Hg^{2+} to Au@Ag NPs alone and the SPR band of Au@Ag NPs completely disappeared (Fig. 7.2A) as a result of aggregation and precipitation. Similar observation has been widely reported in the literature **[271, 272]**.

In addition, there were no spectral changes when Hg^{2+} was added to PEI-GQDs alone as shown in Fig. 7.2B, thus showing no direct interaction between the two materials. To further explain the fluorescence switching of PEI-GQDs, exponential decay kinetics (fluorescence lifetimes) of PEI-GQDs were measured. Table 7.2 shows the recorded lifetimes of PEI-GQDs in PEI-GQDs-Au@Ag system after the addition of various amounts of Hg^{2+} and biothiols. The lifetimes of PEI-GQDs increased close to its original value (up to 85%) upon the addition of Hg^{2+} (15

nM) due to fluorescence "*off-on*" process as explained above, but suffered a sequential decline upon addition of the respective biothiols, which indicates that the fluorescence "*on-off*" process (in the presence of biothiols) is attributable to the re-assembly of PEI-GQDs onto Au@Ag NPs surface and the fluorescence is quenched again. The results further confirmed the influence of Hg^{2+} and biothiols on the fluorescence "*off-on/on-off*" of PEI-GQDs when bound to Au@Ag NPs.

Table 7.2. Fluorescence switching dynamics of PEI-GQDs monitored by changes in the best fit fluorescence lifetimes upon addition of different concentrations of Hg^{2+} or Cys, respectively. Solvent: PBS (10mM, pH 7.0).

Probe	$[Hg^{2+}]$ (nM)	τ_F(ns)±0.13, n=3	Probe	Cys (nM)	τ_F(ns)±0.13, n=3
PEI-GQDs-Au@Ag	0	0.10	PEI-GQDs/Au@Ag-Hg^{2+}	0	7.18
	1	1.20		5	6.55
	5	2.56		10	2.66
	10	4.01		20	1.80
	15	7.18			
PEI-GQDs	-	8.02		25	1.05

7.2. PEI-GQDs-MPc (5)-Au@Ag

PEI-GQDs-**5**-Au@Ag hybrid (similar to above probe, but now with MPc complex **5**) was employed for Hg^{2+} detection using PEI-GQDs as the fluorescence switching signal as discussed above. Hg^{2+} detection was based on the quenching

("turn OFF") of the fluorescence of PEI-GQDs upon π-π interaction or electrostatic attraction with **5**-Au@Ag conjugate. The quenched fluorescence was switched back to the "ON" mode in the presence of Hg^{2+} (in a similar manner to Fig. 7.1A). The ***"off-on"*** process was modulated by different amounts of Hg^{2+}. The detection scheme is as shown in Scheme 7.1.

The LOD for Hg^{2+} was evaluated to be 0.25 nM as shown in Table 7.1. The LOD is indicative of the high sensitivity of the probe towards Hg^{2+} detection at nanomolar range concentrations and better than the above without MPc complex **5**, hence showing the contribution of MPc complex **5** to the sensitive detection of the target analyte. It can be presumed that the different forms of attachment of PEI-GQDs to **5**-Au@Ag which includes electrostatic, NH_2-metal or π-π stacking interactions resulted in the maximum fluorescence quenching, but also allowed for a high "turn ON" process induced by Hg^{2+} upon coordination to **5**-Au@Ag surface. Hg^{2+} could coordinate to Au and Ag metals and the S containing MPc complex **5**.

The detection mechanism is proposed to be based on the induced aggregation of the Au@Ag components of PEI-GQDs-**5**-Au@Ag and/or **5**-Au@Ag as a result of the metaphilic interaction between Hg^{2+} and Au@Ag NPs and/or Hg^{2+} coordination to the S-bridge of MPc complex **5** within PEI-GQDs-**5**-Au@Ag hybrid. The formation of Au-Hg or Ag-Hg bonds within PEI-GQDs-**5**-Au@Ag systems was proved by the addition of Hg^{2+} to Au@Ag NPs as shown Fig. 7.2A.

Also, upon the addition of Hg^{2+} to **5**-Au@Ag solution (Fig. 7.3A (a)), the spectrum was modified with a significant attenuation of the SPR absorbance of

the Au@Ag NPs component of **5**-Au@Ag complex, Fig. 7.3A (b). This could be as a result of the formation of aggregated Au@Ag NPs, leading to changes in the surface states of **5**-Au@Ag hybrid.

The addition of Hg^{2+} to complex **5** alone resulted in increased aggregation of the latter as judged by the increase in the lower energy band due to aggregation, Fig. 7.3B. Hg^{2+} is known to coordinate to the S-bridge on the periphery of sulphur containing phthalocyanines, resulting in the formation of the aggregates with decrease in the intensity of the Q-band of the monomeric species followed by an increase in the aggregate peak [273].

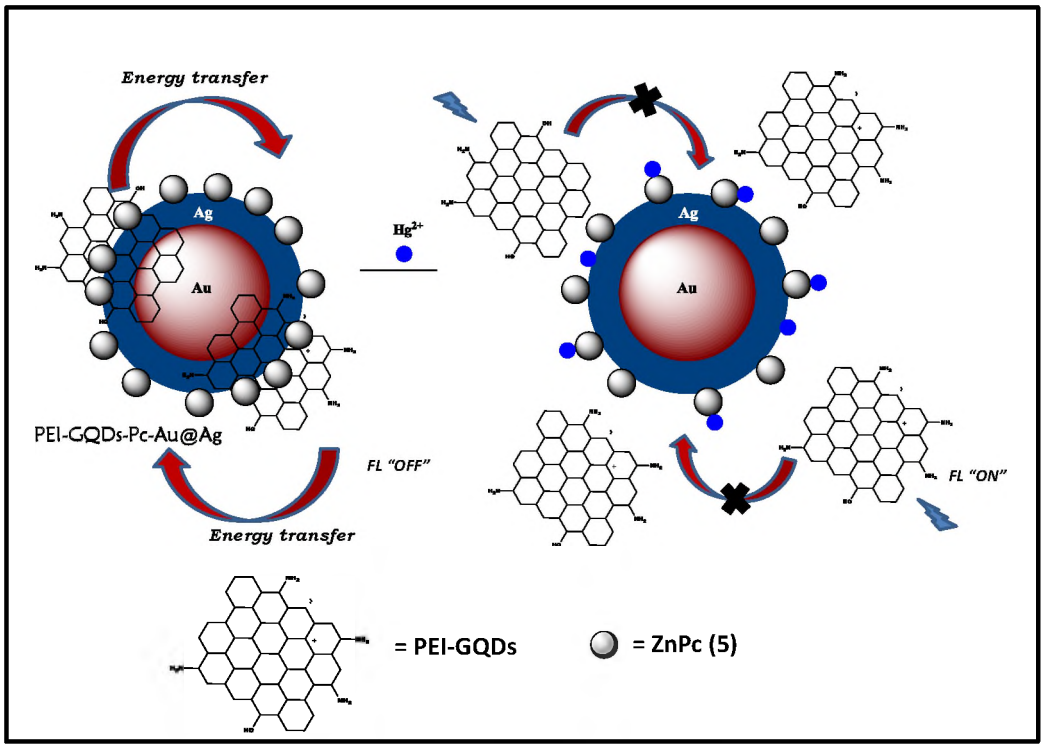

Scheme 7.1. Representative illustration of the fluorescence switching mechanism of PEI-GQDs upon non-covalent interaction with 5-Au@Ag hybrid for Hg^{2+} detection.

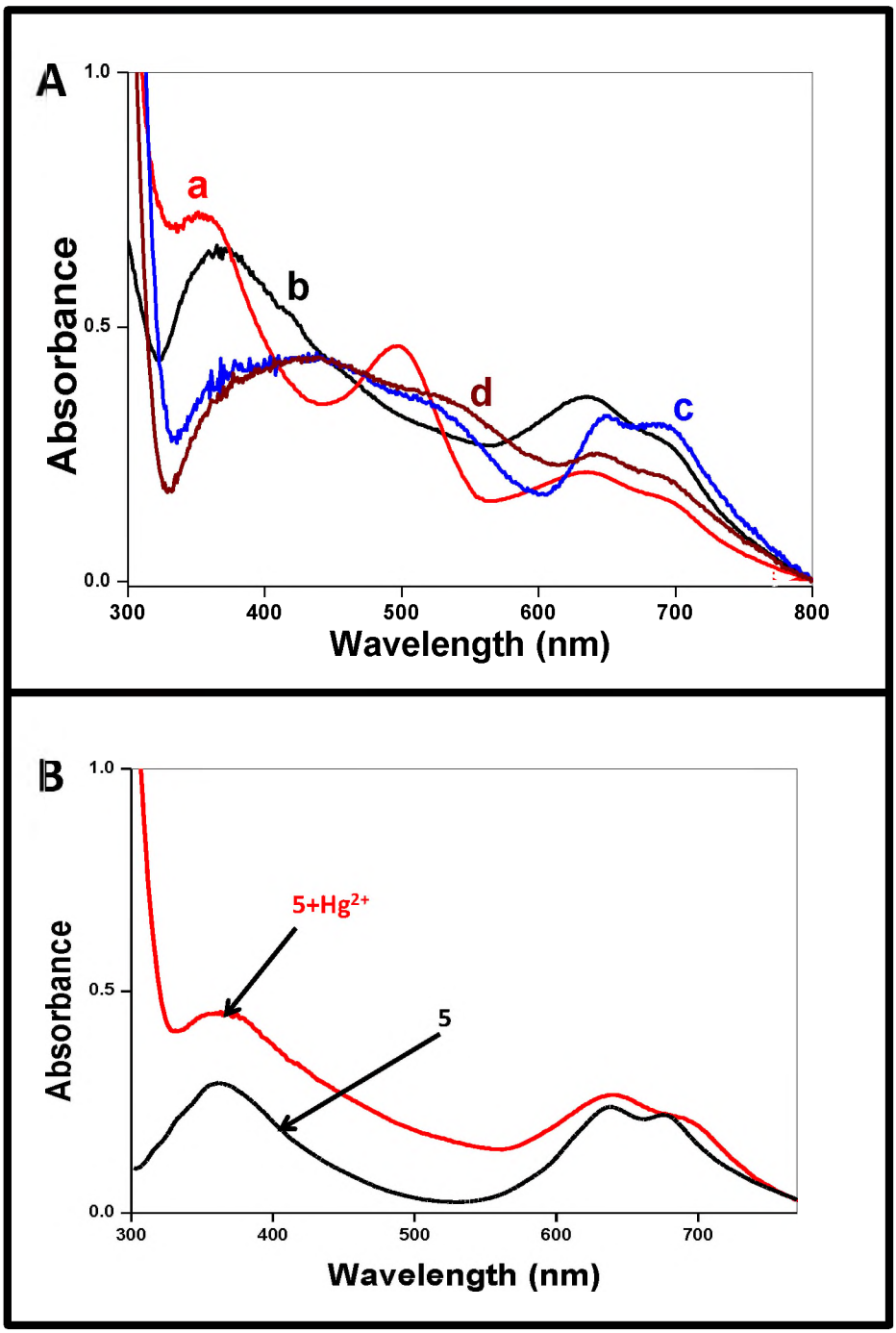

Fig. 7.3. UV-Vis spectra (A) showing changes in the ground-state absorptions of PEI-GQDs-5-Au@Ag alone (a), or in the presence of Hg^{2+} (b), and Cys (50 nM (c), 100 nM (d)). (B) Complex 5 alone and in the presence of Hg^{2+}. Solvent: PBS (10 mM, pH 7.0).

Thus, it can be concluded that Hg^{2+} coordinated with Au@Ag NPs within PEI-GQDs-**5**-Au@Ag system to form Au-Hg or Ag-Hg metaphilic bonds and also bound with complex **5** within PEI-GQDs-**5**-Au@Ag to form S-Hg bonds. Thus, two binding modes (S-Hg and metal-Hg) could be at play upon addition of Hg^{2+} to PEI-GQDs-**5**-Au@Ag hybrid creating a higher chance of PEI-GQDs disassembly from the **5**-Au@Ag surface, resulting in probably more enhanced sensing.

The effects of relevant metals ions that could competitively interfere in Hg^{2+} detection such as Fe^{2+}, Co^{2+}, Mn^{2+}, Cd^{2+}, Cu^{2+}, Ni^{2+}, Pb^{2+}, Mg^{2+}, Ag^{2+} and Zn^{2+} were studied. It was interesting to note that metals ions such as Cu^{2+} and Ag^{2+} which usually interfere in the assay of Hg^{2+} by some reported methods **[265]** did not interfere in the assay for Hg^{2+} using the designed probe (Fig. 7.4A), making it highly selective. Moreover, at tolerable error limits of 5%, experimental results showed that the co-existence of these metals as sample matrix may not influence the detection and quantification of Hg^{2+}, which is a desired advantage of the designed probe.

It could be that the ability of Hg^{2+} to interact with the probe's components (**5** and or Au@Ag) as compared to other metal ions is responsible for the stronger response and thus Hg^{2+} is selectively preferred over other metals ions.

The practical applicability and analytical precision of PEI-GQDs-**5**-Au@Ag probe was evaluated following analytical recoveries studies of spiked samples containing known concentrations of Hg^{2+}. The results shown in Table 7.3 show that the recovered Hg^{2+} was within the range of 98-106% (with RSD less than 5%) using the PEI-GQDs-**5**-Au@Ag system.

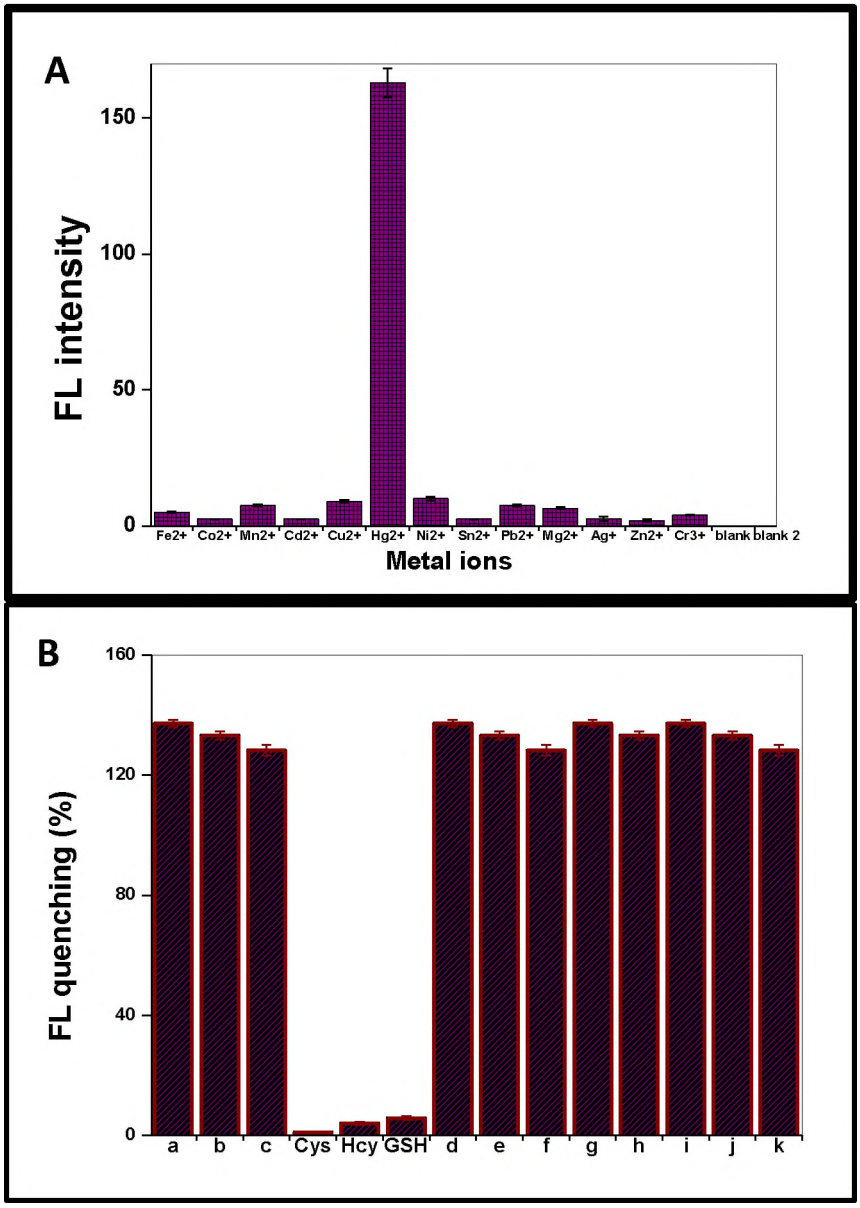

Fig. 7.4. Selectivity studies /fluorescence switching of PEI-GQDs-5-Au@Ag in (A) for Hg^{2+} detection in the presence of metal ions and (B) for Cys, Hcy and GSH (50 nM) premixed with some selected amino acids and proteins (500 μM). Solvent: PBS (10 mM, pH 7.0). a-k = lysine, alanine, cystine, cytochrome c, histidine, lactic acid, bovine serum albumin (BSA), lysozyme, trypsin, tryptophan and glycine.

The results indicate that the PEI-GQDs-**5**-Au@Ag hybrid system could be devised as a potential probe for the analytical sensing of Hg^{2+} commercially with good sensitivity comparable to some methods documented in the literature (Table 6.1).

Table 7.3. Analytical application of PEI-GQDs-5-Au@Ag hybrid for Hg^{2+} and PEI-GQDs/5-Au@Ag-Hg^{2+} for biothiols estimation in simulated spiked samples.

Probe	Added (nM)	Found (nM)	Recovery (%, n = 3)	RSD (%)
PEI-GQDs-5-Au@Ag (Hg^{2+})	5	5.5	101.2±0.32	4.12
	10	9.8	98.0±0.21	5.06
	15	15.9	106.0±1.22	2.08
PEI-GQDs/5-Au@Ag-Hg^{2+} (Biothiols)	10	9.51	9.51±04.35	5.89
	15	14.3	95.33±0.55	5.92
	25	24.2	96.80±0.72	4.32

RSD = relative standard deviation.

Biothiols probe using **5**-Au@Ag hybrid and PEI-GQDs in the presence of Hg^{2+} (PEI-GQDs/**5**-Au@Ag-Hg^{2+}) could be detected in a fluorescence "*off-on-off*" process similar to PEI-GQDs-Au@Ag discussed above. The restored fluorescence of PEI-GQDs from the above interaction with Hg^{2+} could be "turned OFF" again by biothiols; hence the sensor is referred to as "*off-on-off*" system. A schematic representation of the process is as shown in Scheme 7.2.

Upon using PEI-GQDs-**5**-Au@Ag for Hg^{2+} detection, the resulting complex PEI-GQDs/**5**-Au@Ag-Hg could further be deployed for the detection of biothiols

sequentially. As explained earlier, the mechanism of selective and competitive binding of Hg^{2+} between **5**-Au@Ag and biothiols is responsible for this smart sensing platform. The LODs calculated for biothiols are as listed in Table 7.1, which again shows the importance of MPc complex **5** compared to the probe above without complex **5**.

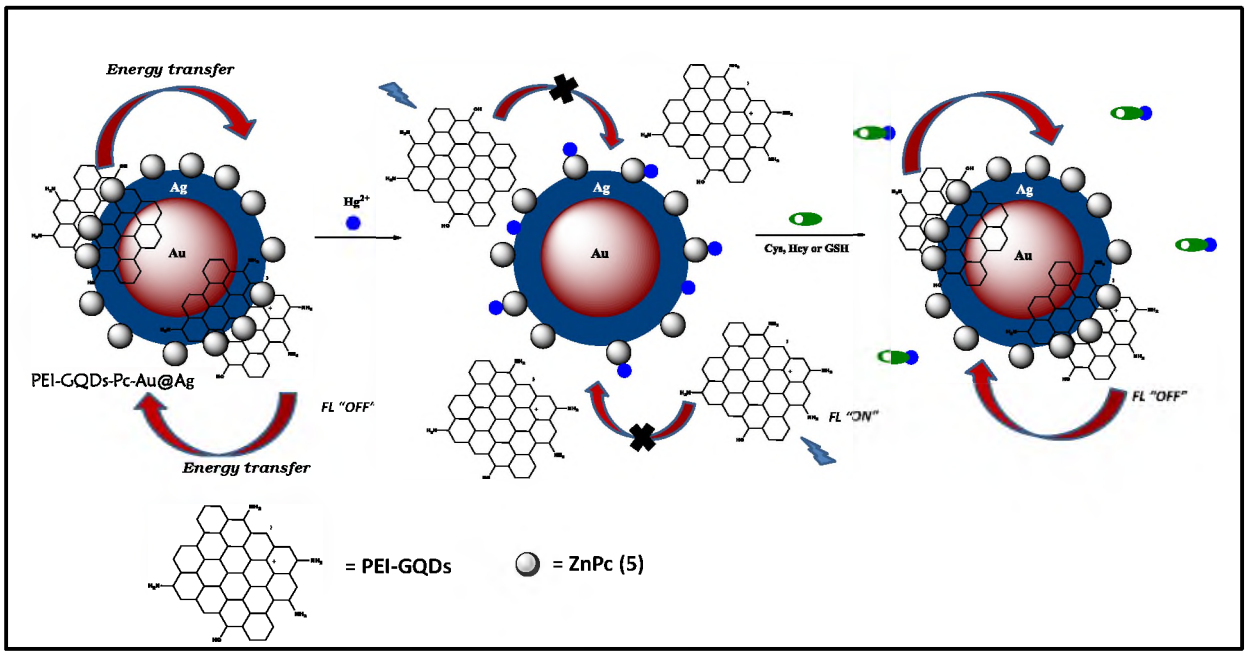

Scheme 7.2. Illustrative description of fluorescence switching mechanism of PEI-GQDs upon non-covalent interaction with 5-Au@Ag hybrid for biothiols detection in the presence of Hg^{2+}.

The mechanism for biothiols detection was in a similar manner described for PEI-GQDs/Au@Ag-Hg probe, where the biothiols exhibit the superior affinity to binding more strongly to Hg^{2+} thereby capturing it from the within the hybrid and also induce some aggregation of Au@Ag component of the probe.

Some tested α-amino acids (glycine, lysine, histidine, tryptophan and DL-lactic acid) without thiol groups did not interfere in the quantitative assay of the

biothiols as shown in Fig. 7.4B. The results demonstrate that PEI-GQDs/**5**-Au@Ag-Hg^{2+} system is specifically selective for the detection of biothiols.

The percentage recovery (%) of Cys, Hcy or GSH (Cys shown as an example in Table 7.3) against known amounts in spiked samples and the RSD evaluated from three replicate measurements, n=3 (Table 7.3), further demonstrates the precision and reproducibility of the probe for biothiols detection in aqueous solution at physiological pH.

7.3. Conclusion

The supramolecular hybrids of PEI-GQDs-Au@Ag NPs and PEI-GQDs-**5**-Au@Ag were deployed as dual sensors for the sequential detection of Hg^{2+} and biothiols. The probes which are capable of detecting Hg^{2+} could also move on to detect biothiols successively in a fluorescence "***off-on-off***" process. The strategy was based on the fluorescence switching of PEI-GQDs occasioned by the disassembly and re-assembly of PEI-GQDs on the surface of Au@Ag NPs or MPc **(5)** grafted Au@Ag NPs, triggered by the target analyte's affinity to bind with Au@Ag NPs/**5**-Au@Ag. A stronger binding affinity between Hg^{2+} and biothiols which is greater than that between Hg^{2+} and Au@Ag NPs/**5**-Au@Ag complex resulted in the disruption of the metaphilic attraction between Hg^{2+} and Au@Ag NPs/**5**-Au@Ag components of the probes. The LODs obtained using PEI-GQDs-Au@Ag NPs or PEI-GQDs-**5**-Au@Ag system showed that the incorporation of MPc complex **5** enhanced the sensing performance of the latter, hence showing the importance of MPcs. Real samples (spiked water) were analyzed and the probes showed good analytical recoveries of the analytes.

8. GENERAL CONCLUSIONS AND FUTURE PROSPECTS

This chapter gives a general summary of the work detailed in this thesis, future prospects and direction.

8.1. Overview of the thesis

The design of nanosensors using graphene quantum dots (GQDs) and graphitic carbon nitrides quantum dots (gCNQDs) when functionalized with molecules and nanoparticles or co-ordinated to macrocyclic compounds such as metallophthalocyanines (MPcs) have been discussed and presented as the focus of this thesis.

As a proof of concept of the sensing ability of GQDs, fluorescence quenching and modulation studies were carried out using known quenchers such as TEMPO (4A-TEMPO and 4AC-TEMPO). The functionalization of GQDs with molecules or nanoparticles with specific affinities for target analytes was the novel insights introduced in this thesis. For example, thymine-functionalized GQDs were synthesized for the first time and deployed for the sensitive recognition of Hg^{2+}. Also, maleimide-functionalized GQDs were employed as ultrasensitive probes for biothiols sensing in aqueous medium and at physiological pH for the first time. Hence, a sensitive "turn ON probe for biothiols was fabricated.

Furthermore, the interaction and modulation of the fluorescence of GQDs by 4A-TEMPO and Au@Ag NPs proved to be useful for the sensitive detection of AA and biothiols, respectively. These analytes detection was based on their abilities to specifically interact with the functionalized GQDs, thereby resulting in the disruption of the GQDs interaction (with 4A-TEMPO and Au@Ag NPs) and the fluorescence is "turned ON" leading to the sensitive detection of the target analytes.

This work further largely explored the possibility of fabricating nanosensors based on MPcs-GQDs non-covalent (π-π) conjugates. The planar structures of both materials

and the presence of π-π conjugation in the respective structures were key advantages to achieving novel supramolecular hybrid nanomaterials containing GQDs (and their functionalized derivatives) and MPcs or MP. The hybrid materials are reported for the first time in this work as well as nanosensors based on the supramolecular hybrid complexes. The fluorescence behaviours of GQDs when coupled with MPcs and MP were fully elucidated and as presented in this thesis, the fluorescence emission of GQDs was quenched in the presence of MPcs or MP. Forster resonance energy transfer (FRET) process where energy is transferred from the GQDs (as donors) to the MPcs/MPs (acceptors) was the underlying mechanism ascribed to be responsible for the observed quenching phenomenon.

Results obtained (sensitivity and LODs) from the sensing application showed that GQDs functionalized with MPcs could act as better "turn ON" nanosensors compared to the functionalized GQDs or GQDs conjugated to 4A-TEMPO or Au@Ag NPs. This could be due to the excellent optical properties of MPcs and their ability to effectively quench the fluorescence of GQDs via FRET mechanism. In addition to the above mentioned point, the fact that the MPcs employed in work contain groups and moieties on their macrocyclic rings which have specific affinities to selectively interact with the target analytes further increased the performance of the hybrid materials as sensing probes.

Lastly, the versatility and the applicability of the sensing concepts of the fabricated functionalized-GQDs or MPcs-GQDs-based probes in this work were further evaluated and demonstrated by using another carbon-based QDs with similar planar graphitic structure such as graphitic carbon nitride QDs (gCNQDs). gCNQDs are however

different from GQDs based on structural composition or building blocks. The gCNQDs were further tethered to 4A-TEMPO (linked and embedded) or MPc complex **8** (TEMPO-ZnPc). As was the case for GQDs, the fluorescence of gCNQDs was quenched in the presence of 4A-TEMPO (when covalently linked) or complex **8** which were switched back "ON" in the presence of AA. The results obtained (LODs and sensitivity) indicated a superior sensing performance for gCNQDs as compared to GQDs which could be ascribed (in this case) to be due to the defect rich nature of gCNQDs.

To demonstrate the sensing performances/analytical applicability of the nanoprobes fabricated in this work, real samples with spiked or known concentrations of the target analytes (AA, biothiols and Hg^{2+}) were analyzed. The recovery results obtained showed that the nanoprobes can be applied for real samples analysis even with complex matrices.

8.2. Future Prospects

For future works and direction, it would be interesting to study the sensing performances of MPcs-GQDs hybrid materials when the MPcs possess central metals that can be axially ligated (such as silicon and indium).

Dual analytes sensing platforms can be designed using MPcs-GQDs hybrids by attaching substituents or groups (which can interact reversibly with target analytes) to MPcs rings.

In situ one-pot synthesis approach can be adopted as a facile route for the preparation of functionalized-GQDs/gCNQDs with desired moieties.

REFERENCES

1. H. Sun, L. Wu, W. Wei, X. Qu, *Mater Today* **11** (2013) 433.
2. L. Li, G. Wu, G. Yang, J. Peng, J. Zhao, J.J. Zhu, *Nanoscale* **5** (2013) 4015.
3. L. Lin, M. Rong. F. Luo, D. Chen, Y. Wang, X. Chen, *Trends Anal. Chem.* **54** (2014) 83.
4. X. Yan, X. Cui, L.S. Li, *J. Am. Chem. Soc*, **132** (2010) 5944.
5. S. Benítez-Martínez, M. Valcárcel, *Trends Anal. Chem.* **72** (2015) 93.
6. Z. Fan, S. Li, F. Yuan, L. Fan, *RSC Adv.* **5** (2015) 19773.
7. J.H. Shen, Y. Zhu, X.Yang, C.Li, *Chem. Commun*, **48** (2012)3686.
8. S.J. Zhu, S. Tang, J. Zhang, B. Yang, *Chem. Commun*, **48** (2012) 4527.
9. Z.F. Wang, H. Zeng, L. Sun, *J. Mater. Chem. C*, **3** (2015) 1157.
10. S. Chen, X. Chen, T. Xia, Q. Ma, *Biosens. Bioelectron.* **85** (2016) 903.
11. H. Razmi, R. Mohammad-Rezaei, *Biosens. Bioelectron.* **41** (2013) 498.
12. D. Qu, M. Zheng, P. Du, Y. Zhou, L. Zhang, D. Li, H. Tan, Z. Zhao, Z. Xied, Z.Sun, *Nanoscale* **5** (2013) 12272.
13. J. Shen, Y. Zhu, X. Yang, J. Zong, J. Zhang, C. Li, *New J. Chem* **36** (2012) 97.
14. Y. Li, Y. Hu, Y. Zhao, G. Shi, L. Deng, Y. Hou, L. Qu, *Adv. Mater* **23** (2011) 776.
15. X. Yan, X. Cui, B. S. Li, L.S. Li, *Nano Lett.* **10** (2010) 1869.
16. H. Chen, Z. Wang, S. Zong, P. Chen, D. Zhu, L. Wu, Y. Cui, *Nanoscale* **7** (2015) 15477.

17. J. Qiu, R. Zhang, J. Li, Y. Sang, W. Tang, P. R. Gil, H. Liu, *Int. J.Nanomedicine*. **10** (2015) 6709.

18. S. Zhu, J. Zhang, C. Qiao, S. Tang, Y. Li, W. Yuan, B. Li, L. Tian, F. Liu, R. Hu, H. Gao, H. Wei, H. Zhang, H. Sun, B. Yang, *Chem. Commun.*, **47** (2011) 6858.

19. M. Zhang, L. Bai, W. Shang, W. Xie, H. Ma, Y. Fu, D. Fang, H. Sun, L. Fan, M. Han, C. Liu, S. Yang, *J. Mater. Chem.* **22** (2012) 7461.

20. J. Ge, M. Lan, B. Zhou, W. Liu, L. Guo, H. Wang, Q. Jia, G. Niu, X. Huang, H. Zhou, X. Meng, P. Wang, C. S. Lee, W. Zhang, X. Han, *Nat. Commun.*, **5** (2014) 4596.

21. C.M. Luk, L.B. Tang, W.F. Zhang, S.F. Yu, K.S. Teng, S.P. Lau, *J Mater Chem,* **22** (2012) 22378.

22. L. Tang, R. Ji, X. Li, G. Bai, C.P. Liu, J. Hao, J. Lin , H. Jiang, K.S. Teng, Z. Yang, S.P. Lau, *ACS Nano* **8** (2014) 6312.

23. W. Gao, J. Shu, C. Qiu, Q. Xu, *ACS Nano* **6** (2012) 7806.

24. J. Lu, P. S. E. Yeo, C. K. Gan, P. Wu, K. P. Loh, *Nat. Nanotechnol.*, **6** (2011) 247.

25. A. Ananthanarayanan, X. Wang, P. Routh, B. Sana, S. Lim, D. Kim, K.H. Lim, J. Li, P. Chen, *Adv. Funct. Mater.* **24** (2014) 3021.

26. Y. Zhang, H. Gao, J. Niu, B. Liu, *New J. Chem*, **38** (2014) 4970.

27. Q. Liu, B. D. Guo, Z. Y. Rao, B. H. Zhang, J. R. Gong, *Nano Lett.*, **13** (2013) 2436.

28. S. Chen, J. W. Liu, M. L. Chen, X. W. Chen, J. H. Wang, *Chem. Commun.*, **48** (2012) 7637.

29. L. L. Li, J. Ji, R. Fei, C. Z. Wang, Q. Lu, J. R. Zhang, L. P. Jiang, J. J. Zhu, *Adv. Funct. Mater.*, **22** (2012) 2971.

30. Y. Dong, H. Pang, S. Ren, C. Chen, Y. Chi, T. Yu, *Carbon*, **64** (2013) 245.

31. D. B. Shinde, V. K. Pillai, *Chem. Eur. J.*, **18** (2012) 12522.

32. F. Liu, M. H. Jang, H. D. Ha, J. H. Kim, Y.H. Cho, T. S. Seo, *Adv. Mater.*, **25** (2013) 3657.

33. J. Peng, W. Gao, B. Kumar Gupta, Z. Liu, R. Romero-Aburto, L. Ge, *et al. Nano Lett*, **12** (2012) 844.

34. R. Ye, C. Xiang, J. Lin, Z. Peng, K. Huang, Z. Yan, et al, *Nat. Commun*, **4** (2013) 2943.

35. Y. Dong, C. Chen, X. Zheng, L. Gao, Z. Cui, H. Yang, et al, *J. Mater. Chem*, **22** (2012) 8764.

36. J. Lee, K. Kim, W.I. Park, B.H. Kim, J.H. Park, T.H. Kim, S. Bong, C.H. Kim, G. Chae, M. Jun, Y. Hwang, Y.S. Jung, S. Jeon, *Nano Lett.*, **12** (2012) 6078.

37. H. Xu, S. Zhou, L. Xiao, H. Wang, S. Li, Q. Yuan, *J. Mater. Chem. C*, **3** (2015) 291.

38. Y. Dong, J. Shao, C. Chen, H. Li, R. Wang, Y. Chi, X. Lin, G. Chen, *Carbon*, **50** (2012) 4738.

39. L. Wang, Y. Wang, T. Xu, H. Liao, C. Yao, Y. Liu, Z. Li, Z. Chen, D. Pan, L. Sun, M. Wu, *Nat. Commun.*, **5** (2014) 5357.

40. Z. Huang, Y. Shen, Y. Li, W. Zheng, Y. Xue, C. Qin, B. Zhang, J. Hao and W. Feng, *Nanoscale*, **6** (2014) 13043.

41. X. Wu, F. Tian, W. Wang, J. Chen, M. Wu, J. X. Zhao, *J. Mater. Chem. C*, **1** (2013) 4676.

42. L. Tang, R. Ji, X. Cao, J. Lin, H. Jiang, X. Li, K. S. Teng, C. M. Luk, S. Zeng, J. Hao and S. P. Lau, *ACS Nano,* **6** (2012) 5102.

43. R. Liu, D. Wu, X. Feng, K. Mullen, *J. Am Chem. Soc.* **133** (2011) 15221.

44. P. Atienzar, A. Primo, C. Lavorato, R. Molinari, H. Garcia, *Langmuir*, **29** (2013) 6141.

45. R. Liu, R. Yang, C. Qu, H. Mao, Y. Hu, J. Li, L. Qu, *Sensors and Actuators B* **241** (2017) 644.

46. A. Suryawanshi, M. Biswal, D. Mhamane, R. Gokhale, S. Patil, D. Guin, S. Ogale, *Nanoscale*, **6** (2014) 11664.

47. S. Kim, S.W. Hwang, M.K. Kim, D.Y. Shin, D.H. Shin, C.O. Kim, S.B. Yang, .J.H. Park, E. Hwang, S.H. Choi, G. Ko, S. Sim , C. Sone, H.J. Choi, S. Bae, B.H. Hong, *ACS Nano.* **6** (2012) 8203.

48. H. Tetsuka, R. Asahi, A. Nagoya, *Adv. Mater.* **24** (2012) 5333.

49. S. Zhu, Y. Song, X. Zhao, J. Shao, J. Zhang, B. Yang, *Nano Res.* **8** (2015) 355.

50. Y. Dong, J. Lin, Y. Chen, F. Fu, Y. Chi, G. Chen, *Nanoscale* ***6*** (2014) 7410.

51. L. Zhang, Z. Zhang, R. Liang, Y. Li, J. Qiu, *Anal. Chem,* **86** (2014) 4423.

52. Q. Feng, Q. Cao, M. Li, F. Liu, N. Tang, Y. Du, *Appl. Phys. Lett*, **102** (2013) 13111.

53. X. Ran, H.J. Sun, F. Pu, J.S. Ren, X.G. Qu, *Chem. Commun.*, **49** (2013) 1079.

54. A. Ananthanarayanan, Y. Wang, P. Routh, M. A. Sk, A. Than, M. Lin, J. Zhang, J. Chen, H. D. Sun, P. Chen, *Nanoscale* **7** (2015) 8159.

55. J. Zhao, L. Tang, J. Xiang, R. Ji, J. Yuan, *Appl. Phys. Lett.* **105** (2014) 111116.

56. J. Liu, X. Zhang, Z. Cong, Z. Chen, H. Yang, G. Chen, *Nanoscale*. **5** (2013) 1810.

57. H. Yuezhen, X. Wang, J. Sun, S. Jiao, H. Chen, F. Gao, L. Wang, *Analytica Chimica Acta*, **810** (2014) 71.

58. X. Li, S. Zhu, B. Xu, K. Ma, J. Zhang, B. Yang, W. Tian, *Nanoscale* **5** (2013) 7776.

59. A. Muthurasu, V. Ganesh, *Appl Biochem Biotechnol.*, **174** (2014) 945.

60. B. Sapkota, M. Mustata, J. Zhang, G. Grigoryan, M. Wanunu, *Biophysical J*, **108** (2015) 393.

61. R. Guo, S. Zhou, Y. Li, X. Li, L. Fan, N.H. Voelcker, *ACS Appl. Mater Interfaces*, **7** (2015) 23958.

62. C.A. Dutta, R.A. Doong, *ACS Appl Mater Interfaces*, **8** (2016) 21002.

63. Z. Qian, J. Ma, X. Shan, L. Shao, J. Zhou, J. Chen, H. Feng, *RSC Adv*, **3** (2013) 14571.

64. X. Liu, L. Hua-Ji, F. Cheng, Y. Chen, *Nanoscale* **6** (2014) 7453.

65. A. Valipour, M. Roushani, Biosens. Bioelectron., **89** (2016) 946.

66. X. Sun, Y. Qian, Y. Jiao, J. Liu, F. Xi, X. Dong, *Talanta*, **165** (2017) 429.

67. P. Luo, Z. Ji, C. Li, G. Shi, *Nanoscale*, **5** (2013) 7361.

68. S. Wang, L. Zachary, S. C. Ivan and Q. Li, *RSC Adv.*, **5** (2015) 41248.

69. D. Dinda, B.K. Shaw, S.K. Saha, ACS Appl. Mater. Interfaces, **7** (2015) 14743.

70. A. Kowalczyk, A. M. Nowicka, Sens. Actuators B: Chemical, **237** (2016) 810.

71. D. Li, A. Wieckowska, I. Willner, Angew. Chem., Int.Ed., **47** (2008) 3927.

72. C.W. Liu, Y.T. Hsieh, C.C. Huang, Z.H. Lin, H.T. Chang, Chem. Commun. **19** (2008) 2242.

73. W. Dou, X. Su, Luminescence, **24** (2009) 45.

74. K.S. Park, M.I. Kim, M.A. Woo, H.G. Park, Biosens. Bioelectron., **45** (2013) 65.

75. D. P. Nair, M. Podgorski, S. Chatani, T. Gong, W. Xi, C. Fenoli, C. Bowman, Chem. Mater, **26** (2014) 724.

76. N. Nwahara, J. Britton, T. Nyokong, *J. Coord. Chem.*, **70** (2017) 1601.

77. A. Ritter, J.W. Lyding, *Nat. Mater.*, **8** (2009) 235.

78. D.Y. Pan, J.C. Zhang, Z. Li, M.H. Wu, *Adv. Mater.*, **22** (2010) 734.

79. S. Zhu, J. Zhang, X. Liu, B. Li, X. Wang, S. Tang, Q. Meng, Y. Li, C. Shi, R. Hu, B. Yang, *RSC Adv.*, **2** (2012) 2717.

80. Y. Sun, S. Wang, C. Li, P. Luo, L. Tao, Y. Wei, G. Shi, *Phys. Chem. Chem. Phys.*, **15** (2013) 9907.

81. M. Nurunnabi, Z. Khatun, G.R. Reeck, D.Y. Lee, Y.K. Lee, *Chem. Commun.*, **49** (2013) 5079.

82. J. Wang, S. Cao, Y. Ding, F. Ma, W. Lu, M. Sun, *Sci. Reps,* **6** (2016) 24850.

83. Y. Feng, G. Zhao, X. Yan, F. Tang, Q. Xue, *Carbon* **66** (2014) 334.

84. Z. L. Wu, M. X. Gao, T. T. Wang, X. Y. Wan, L. L. Zheng, C. Z. Huang, *Nanoscale*, **6** (2014) 3868.

85. F. Yuan, L. Ding, Y. Li, X. Li, L. Fan, S. Zhou, D. Fang, S. Yang, *Nanoscale*, **7** (2015) 11727.

86. S. Zhu, J. Zhang, S. Tang, C. Qiao, L. Wang, H. Wang et al, *Adv. Funct. Mater.*, **22** (2012) 4732.

87. M. Röding, S. J. Bradley, M. Nydén and T. Nann, *J. Phys. Chem. C*, **118** (2014) 30282.

88. Z. Wu, W. Li, J. Chen, C. Yu, *Talanta,* **119** (2014) 538.

89. J. J. Liu, Z.T. Chen, D.S. Tang, Y.B. Wang, L.T. Kang, J.N. Yao, *Sens. Actuators B: Chem.*, **212** (2015) 214.

90. J. Bai, L. Zhang, R. Liang, J. Qiu, *Chem. Eur. J.*, **19** (2013) 3822.

91. H. Pei, S. Zhu, M. Yang, R. Kong, Y. Zheng, F. Qu, *Biosens. Bioelectron.*, **74** (2015) 909.

92. Y. Li, L. Zhang, J. Huang, R. Liang, J. Qiu, Chem. Comm., **45** (2013) 5180.

93. Z. Fan, Y. Li, X. Li, L. Fan, S. Zhou, D. Fang, et al, *Carbon* **70** (2014) 149.

94. Z.S. Qian, X.Y. Shan, L.J. Chai, J.R. Chen, H. Feng, Biosens. Bioelectron., **68** (2015) 225.

95. Z. S. Qian, X. Y. Shan, L. J. Chai, J. J. Ma, J. R. Chen, H. Feng, Nanoscale, **6** (2014) 5671.

96. Q. Zhang, C. Song, T. Zhao, H. Fu, H. Wang, Y. Wang, et al, Biosens. Bioelectron, **65** (2015) 204.

97. L.P. Lin, X.H. Song, Y.Y. Chen, M.C. Rong, Y.R. Wang, L. Zhao, T.T. Zhao, X. Chen, Anal Chim Acta, **891** (2015) 268.

98. L. Zhang, D. Peng, R.P. Liang, J.D. Qiu, Chem. Eur. J. **21** (2015) 9343.

99. L. Zhang, D. Peng, R.P. Liang, J.D. Qiu, Anal. Chem., **87** (2015) 10894.

100. Y. Dong, Q. Wang, H. Wu, Y. Chen, C.H. Lu, Chi, H. H. Yang, *Small*, **12** (2016) 5376.

101. Z. Zhao, Y. Sun, F. Dong, *Nanoscale*, **7** (2015) 15.

102. J. Liu, H. Wang, M. Antonietti, *Chem. Soc. Rev.*, **45** (2016) 2308.

103. C. Li, X. Yang, B. Yang, Y. Yan, Y. Qian, *Materials chemistry and physics*, **103** (2007) 427.

104. S. Barman and M. Sadhukhan, *J. Mater. Chem.*, **22** (2012) 21832.

105. M. Groenewolt and M. Antonietti, *Adv. Mater.*, **17** (2005) 1789.

106. S. Zhang, J. Li, M. Zeng, J. Xu, X. Wang and W. Hu, *Nanoscale*, **6** (2014) 4157.

107. J. Zhou, Y. Yang and C. Y. Zhang, *Chem. Commun.*, **49** (2013) 8605.

108. S. Liu, L. Wang, J. Tian, J. Zhai, Y. Luo, W. Lu, X. Sun, RSC Adv., **1** (2011) 951.

109. Q. Zhuang, L. Sun, Y. Ni, Talanta **164** (2017) 458.

110. Y. Tang, Y. Su, N. Yang, L. Zhang, L. Yi, Anal. Chem., **86** (2014) 4528.

111.S. Chen, N. Hao, D. Jiang, X. Zhang, Z. Zhou, Y. Zhang, K. Wang, J. Electroanal. Chem., **787** (2017) 66.

112. J. Xu, Y. Chen, D. Ma, J. K. Shang, Y. X. Li, Catal. Commun., **95** (2017) 72.

113. S. Liu, J. Tain, L. Wang, Y. Luo, X. Sun, RSC Adv. **2** (2012) 411.

114. M.H. Xiang, J.W. Liu, N. Li, H. Tang, R.Q. Yu, J.H. Jiang, Nanoscale, **8** (2016) 4727.

115. E. Z. Lee, S. U. Lee and N. Heo, G. D. Stucky, Y. S. Jun, W. H. Hong, *Chem. Commun.*, **48** (2012) 3942.

116. Q. Lu, H. Wang, Y. Liu, Y. Hou, H. Li, Y. Zhang, Biosens. Bioelectrons, **89** (2017) 411.

117. M. Rong, L. Lin, X. Song, Y. Wang, Y. Zhong, J. Yan, Y. Feng, X. Zeng, X. Chen, Biosens. Bioelectron, **68** (2015), 210.

118. X.L. Zhang, C. Zheng, S.S. Guo, J. Li, H.H. Yang, G.N. Chen, Anal. Chem., **86** (2014) 3426.

119. H. Z. Gok, H. Kantekin, Y. Gok, G. Herman, Dyes Pigm. **75** (2007) 606.

120. G. Bottari, G. delaTorre, T. Torres, Acc. Chem. Res. **4** (2015) 900.

121. G. Bottari, O. Truhkina, M. Ince, T. Torres, Coord. Chem. Rev. **256** (2012) 2453.

122. J. Bartelme, D.M. Guldi, in: T. Torres, G. Bottari (Eds.), Organic Nanomaterials: Synthesis, Characterization, and Device Applications. Hoboken, NJ, USA; John Wiley and Sons, Inc. (2013).

123. G. de la Torre, C. G. Claessens, T. Torres, Chem. Commun., **0** (2007) 2000.

124. S.K. Das, N.K. Subbaiyan, F. D'souza, A.S. Sandanayaka, T. Wakahara, O. Ito, J. Porphyrins and Phthalocyanines **15** (2011) 1033.

125. G. Bottai, J.A. Suanzes, O. Trukhina, T. Torres, Phys. Chem. Lett. **2** (2011) 905.

126.G. Bottari, G. de la Torre, D. M. Guldi, T. Torres, Chem. Rev., **110** (2010), 6768.

127. M. Gouterman, In The Porphyrins, (Ed. D. Dolphin), Part A. Physical Chemistry. New York; Academic Press (1978).

128. J. McHugh, M. Gouterman, C. Weiss, Theoret. Chim. Acta, **24** (1987) 246.

129. A. M. Schaffer, M. Gouterman, E.R. Davidson, Theoret. Chim. Acta **30** (1973) 9.

130. A. Ogunsipe, J.Y. Chen, T. Nyokong, New J. Chem. **28** (2004) 822.

131. V. M. Vlasov, Russ. Chem. Rev. **72** (2003) 681.

132. A.M. Paoletti, G. Pennesi, G. Rossi, A. Generosi, B. Paci, V.R. Albertini, *Sensors*, **9** (2009) 5277.

133. F.I. Bohrer, A. Sharoni, C. Colesniuc, J. Park, I. Schuller, A. Kummel, W. Trogler, J. Am. Chem. Soc., **129** (2007) 5640.

134. Y. Amao, K. Asai, I. Okura, Anal. Chim. Acta **407** (2000) 41.

135. Z. Dong, X. Kong, Y.L. Wu, J. F. Zhang, Y.L. Chen, Inorg. Chem. Commun., **77** (2017) 18.

136. A. Hassan, T. Basova, S. Tuncel, F. Yuksel, A.G. Gürek, V. Ahsen, Procedia

Engr. **25** (2011) 272.

137. H. Banimuslem, A. Hassan, T. Basova, M. Durmus, S. Tuncel, A.A. Esenpınar, A.G. Gürek, V. Ahsen, J. Nanosci. Nanotechnol., **15** (2015) 2157.

138. A. Gülmez, M. Polyakov, V. Volchek, S. Kostakoglu, A. Esenpinar, T. Durmus, A. Hassan, Sens Actuators B: Chemical, **241** (2017) 364.

139. X. Liu, C. Qi, T. Bing, X. Cheng, D. Shangguan, Anal. Chem. **81** (2009) 3699.

140. X. He, D. Yang, H. Chen, W. Zheng, H. Li, J. Mol. Recognit. **28** (2015) 293.

141. J. Spadavecchia, G. Ciccarella, L. Valli, R. Rella, Sens Actuators B: Chemical, **113** (2006) 516.

142. A.B. El-Bosaty, T.A. El-Brolossy, S. Abdalla, S. Negm, R.A. Abdella, H. Talaat, Egypt. J. Solids **29** (2006) 121.

143. J. Spadavecchia, G. Ciccarella, L. Valli, R. Rella, Sens Actuators B: Chemical, **100** (2004) 88.

144. M. Bacon, S. J. Bradley, T. Nann, *Part. Part. Syst. Charact.* **31** (2014) 415.

145. W. Chidawanyika, T. Nyokong, *Carbon* **48** (2010) 2831.

146. M.E. El-Khouly, O. Ito, P.M. Smith, F. D'Souza, *J. Photochem. Photobiol. C* **5** (2004) 79.

147. M. Ragoussi, G. Katsukis, A. Roth, J. Malig, G. de la Torre, D.M. Guldi, T. Torres, *J. Am. Chem. Soc.* **12** (2014) 4593.

148. O. Adegoke, S. Khene, T. Nyokong, J. Fluoresc. **23** (2013) 963.

149. O. Adegoke, T. Nyokong, *J. Lumin.* **146** (2014) 275-283.

150. O. Adegoke, T. Nyokong, *J. Photochem. Photobiol. A: Chem.* **265** (2013) 58.

151. O. Adegoke, T. Nyokong, *J. Photochem. Photobiol. A: Chem.* **257** (2013) 11.

152. O. Adegoke, T. Nyokong, *Synthetic Metals* **188** (2014) 35.

153. O. Adegoke, T. Nyokong, *J Fluoresc* **24** (2014) 481.

154. M.F. Frasco, V. Vamvakaki, N. Chaniotakis, *J. Nanopart. Res.* **12** (2010) 1449.

155. A. Ivanisevic, A.B. Ellis Langmuir **16** (2000) 7852.

156. C. M. Lemon, E. Karnas, M. G. Bawendi, D. G. Nocera, *Inorg. Chem.*, **52** (2013) 10394.

157. X.F. Zhang, X. Shao, J. Photochem. Photobiol. A: Chemistry, **278** (2014) 69.

158. X.F. Zhang, H. Xu, *Chem. Res. Chin. Univ.*, **15** (1994) 917.

159. M.D.K. Nazeeruddin, R. Humphry-Baker, M. Gratzel, D. Wohrle, G. Schnurpfeil, G. Schneider, A. Hirth, N. Trombach, *J. Porphyrins Phthalocyanines*, **3** (1999) 230.

160. I. Scalise, E.N. Durantini, *Bioorg. Med. Chem.*, **13** (2005) 3037.

161. M. Durmus, H. Yaman, C. Göl, V. Ahsen, T. Nyokong, Dyes Pigments, **91** (2011) 153.

162. Y. Arslanoğlu, M. Idowu, T. Nyokong, *Spectrochim Acta* A: *Mol. Biomol. Spectrosc.* **95** (2012) 407.

163. M. Idowu, Y. Arslanoğlu, T. Nyokong, *Cent. Eur. J. Chem.*, **12** (2014) 403.

164. S. E. Korkut, D. Akyüz, K. Özdoğan, Y. Yerli, A. Koca, M. K, Şener, Dalton Trans., **45** (2016) 3086.

165. T. Zoltan, F. Vargas, C. Rivas, V. Lopez, J. Perez, A. Biasutto, Sci. Pharm., **78** (2010) 767.

166. E. Antunes, C. Litwinski, T. Nyokong, in Intelligent Nanomaterials: Processes, Properties, and Applications (eds A. Tiwari, A. K. Mishra, H. Kobayashi and A. P.F. Turner). Hoboken, NJ, USA; John Wiley & Sons, Inc. (2012).

167. T. Nyokong, E. Antunes, Coord. Chem. Rev., **257** (2013) 2401.

168. S. Dayal, Y. Lou, A.C.S. Samia, J.C. Berlin, M.E. Kenney, C. Burda, J. Am. Chem. Soc., **128** (2006) 13974.

169. O. M. Bankole, T. Nyokong, New J. Chem., **40** (2016) 10016.

170. C. Berney, G. Danuser, Biophysical J., **84** (2003) 3992.

171. D. Guo, G. Xie and J. Luo, J. Phys. D: Appl. Phys. **47** (2014) 013001.

172. V. V. Mody, R. Siwale, A. Singh, H. R. Mody, J Pharm Bioallied Sci., **2** (2010) 282.

173. D. V. Goia, E. Matijevic, New J. Chem. **22** (1998) 1203.

174. C. Templeton, W. P. Wuelfing, R. W. Murray, Acc. Chem. Res., **33** (2000) 27.

175. Y. Li, Y. Wu and Beng S. Ong, J. Am. Chem. Soc. **127** (2005) 3266.

176. L. Cui, J. Wu, J, Li, Y.Q. Ge, H.X. Ju, Biosens. Bioelectron., **55** (2014) 272.

177. Z.Y. Zhang, Z.P. Chen, C.L. Qu, L.G. Chen, Langmuir, **30** (2014) 3625.

178. S. Link, M. A. El-Sayed, J. Phy. Chem. B, **103** (1999) 4212.

179. X. Huang, I. H. El-Sayed, W. Qian, M. A. El-Sayed M. A, J. Am Chem Soc., **128** (2006) 2115.

180. B. G. Rezanejade, Z. Hooshyar, M. Khanjari, M, J.Photochem. Photobiol., A: Chemistry, **276** (2014) 113.

181. N. N. Horimoto, K. Imura, H. Okamoto, Chem. Phys. Lett., **467** (2008) 105.

182. J. H. Hodak, A. Henglein, M. Giersig, G. V. Hartland, J. Phys. Chem. B, **104** (2000) 11708.

183. M. Liu, P. Guyot-Sionnest, J. Phys. Chem. B, **108** (2004) 5882.

184. Y. Lu, Y. Mei, M. Drechsler,M. Ballauff, Angew. Chem., Int. Ed., **45** (2006) 813.

185. L. Shang, S.J. Dong, G.U. Nienhaus, Nano Today **6** (2011) 401.

186. G. Samit, R. Subhasish, B. Arindam, Langmuir **27** (2011) 13198.

187. F. D'Souza, O. Ito, Chem. Commun., **33** (2009) 4913.

188. C. Wang, Z. Xu, C. Zhang, ChemNanoMat, **1** (2015) 122.

189. P. J. Connell PJ, C. Gormally, M. Pravda, G. G. Guilbault, Anal Chim Acta, **431** (2001) 239.

190. E. Cameron, A. Campbell, Chem Biol Interact., **9** (1974) 285.

191. M. Matsuoka, M. Yamato, K. Yamada, J. Clin. Biochem. Nutr., **58** (2016) 6.

192. L. Maurel, M. Laferrière, P. Billone, R. Godin, J. C. Scaiano, J. Phys. Chem. B, **110** (2006) 16353.

193. D.M. Townsend, K.D Tew, H. Tapiero, Biomed. Pharmacother. **57** (2003) 145.

194. H.R. Griffiths, D. Gao, C. Pararasa, Redox Biol., **12** (2017) 50.

195. J.P. Chen, Decontamination of Heavy Metals: Processes, Mechanisms, and Applications. Florida; CRC Press (2012).

196. D. Qu, M. Zheng, L. Zhang, H. Zhao, Z. Xie, X. Jing, E. H. Raid, H. Fan, Z. Sun, Sci. Rep., **4** (2014) 1.

197. F. Lin, D. Pei, W. He, Z. Huang, Y. Huang, X. Guo, J. Mater. Chem., **22** (2012) 1180.

198. P.R. Selvakannan, A. Swami, D. Srisathiyanarayanan, P.S. Shirude, R. Pasricha, A.B. Mandale, M. Sastry, Langmuir, **20** (2004)7825.

199. I. Özcesmeci, A. Gelir, A. Gül, Dyes Pigments, **92** (2012) 954.

200. O. Tall, Y. El; Hou, E. Abou-hamad, I.U. Raja, M.N. Hedhili, W. Peng, O.M. Bakr, P. M. Beaujuge, Chem. Mater., **26** (2014) 2766.

201. X. Zhang, Y. Feng, S. Tang, W. Feng, Carbon, **48** (2010) 211.

202. Y. Noda, S. Noro, T. Akutagawa, T. Nakamura, Sci. Rep., **4** (2014) 3758.

203. N. Masilela, E. Antunes, T. Nyokong, J. Porphyrins Phthalocyanines, **17** (2013) 417.

204. D.J. Bigelow, G. Inesi, G, Biochem., **30** (1991) 2113.

205. S. Fery-Forges, D. Lavabre, J.Chem Ed. **76** (1999) 12660.

206. J. Deng, Q. Lu, H. Li, Y. Zhang, S, RSC Adv., **5** (2015) 29704.

207. H. Brookfield, A. Ellul, J. Chem. SOC. Faraday Trans, **82** (1986) 219.

208. M. Idowu, J.Y. Chen, T. Nyokong, New J. Chem., **32** (2008) 290.

209. H. Du, R.C.A. Fuh, J.Z. Li, L.A. Corkan, J.S. Lindsey, Photochem. Photobiol., **68** (1998) 141.

210. W.S. Hummers, R.E. Offeman, Preparation of graphite oxide, J. Am. Chem. Soc. **80** (1958) 1339.

211. Y.X. Xu, H. Bai, G.W. Lu, C. Li, G.Q. Shi, J. Am. Chem. Soc., **130** (2008) 5856.

212. H. Sun, H. Ji, E. Ju, Y. Guan, J. Ren, X. Qu, Chem. Eur J. **29** (2015)3791.

213. S. Kim, D. H. Shin, C. O. Kim, S. S. Kang, S. S. Joo, S. H. Choi, S. W. Hwang C. Sone, Appl. Phys. Lett. **102** (2013) 53108.

214. C. K. Chua CK, Sofer Z, Šimek P, Jankovský O, KlÍmová K, Bakardjieva S, Kučková SH, Pumera M, ACS Nano **9** (2015) 2548.

215. W. Shi, H. Fan, S. Ai and L. Zhu, New J. Chem., **39** (2015) 7054.

216. M. Nurunnabi, K. Zehedina, M. Nafiujjaman, L. Dong, L. Yong-kyu, ACS Appl. Mater. Interfaces. **5** (2013) 8246.

217. X. T. Zheng, K. Q. Ananthanarayanan, P. Luo, P. Chen P, Small **11** (2015) 1620.

218. S.H. Jin, D.H. Kim, G. H. Jun, S. H. Hong, S. Jeon, ACS Nano **7** (2013) 1239.

219. D. Wei, Z. Wei, S. Chen, X. Qi, T. Yang, J. Hu, D. Wang, W. Li-Jun, F. Shahnaz, L. Li, Angew Chem Int Ed **52** (2013) 11755.

220. K. A. Ritter, J. W. Lyding, Nature Mater. **8** (2009) 235.

221. K. Mallik, M. Mandal, N. Pradhan, T. Pal, Nano Lett. **1** (2001) 319.

222. H. Koçan, A.K. Burat, Monatshefte für Chemie **144** (2013) 171.

223. T. Basova, V. Plyashkevich, A. Hassan, A. G. Gürekc, G. Gümüş, V. Ahsen, Sensors Actuators B **139** (2009) 557.

224. A. B. Mabire, M. P. Robin, W.D. Quan, H. Willcock, V. G. Stavros and R. K. O'Reilly, Chem. Commun. **51** (2015) 9733.

225. M.J. Stillman, T. Nyokong, in Phthalocyanines-Properties and Applications, eds. C. C. Leznoff and A. B. P. Lever, VCH, New York, (1989).

226. T. Morris, H. Copeland, E. McLinden, S. Wilson, G. Szulczewski, Langmuir **18** (2002) 7261.

227. Fashina, E. Antunes, T. Nyokong, Polyhedron **53** (2013) 278.

228. T. Chunder, T. Pal, S.I. Khondaker, L. Zhai, J. Phys. Chem. C **114** (2010) 15129.

229. Y. Wang, A. Zhou, Y. Jiang, X. Chen, J. He, RSC Adv. **5** (2015) 37823.

230. J.H Yang, Y. Gao, W. Zhang, P. Tang, J. Tan, A. H. Lu, D. Ma, J. Phys. Chem. C, **117** (2013), 3785.

231. X. Cai, Y. Zhang, X. Zhang, J. Jiang, J. Mol. Struct: THEOCHEM, **801** (2006) 71.

232. M. Idowu, T. Nyokong, J. Lumin. **129** (2009) 356.

233. M. Mahyaria, Y. Bideb, J.N. Gavgani, Applied Catalysis A: General, **517** (2016) 100.

234. Yi Liu, W. QuanLoh, A. Ananthanarayanan, C. Yang, C. Peng, C. Xu, RSC Adv., **4** (2014) 35673.

235. C.P. Liu, T.H. Wu, C.Y. Liu, H.J. Cheng, S.Y. Lin, J. Mater. Chem. B **3** (2015) 191.

236. H. S. Chakraborti, Sinha, S. Ghosh, S. K. Pal, Materials letters **97** (2013) 78.

237. W. F. Xiang, G. Zhenyan, L. Wu, W. Wenjan, X. Xifeng, H. Qingli, Sensors and Actuators B **190** (2014) 516.

238. E. H. Liu, L. W. Qi, P. Li, Molecules **15** (2010) 9092.

239. S. L. Murov, I. Carmichael, G.L. Hug in: "Handbook of Photochemistry"2nd edition, New York, Decker M. (1993).

240. V. D. Sen, V. A. Golubev, J. Phys. Org. Chem. **22** (2009) 138.

241. G. R. Buettner, Free Radic. Biol. Med. **3** (1987) 259.

242. B.J. Morrow, D.J. Keddie, N. Gueven, M.F. Lavin, S.E. Bottle, Free Radic. Biol. Med., **49** (2010) 67.

243. T. Yang, B. Zheng, H. Liang, Y. Wan, J. Du and D. Xiao, Talanta, **132** (2015) 191.

244. K. Ishii, K. Kubo, T. Sakurada, K. Komori and Y. Sakai, Chem. Commun., **47** (2011) 4932.

245. F. Yu, P. Song, P. Li, B. Wang and K. Han, Chem. Commun., **48** (2012) 7735.

246. J.R. Lakowicz, Principles of fluorescence spectroscopy, third ed., New York; Springer (2009).

247. A. F. Danet, M. Badea, H. Y. Aboul-Enein, Luminescence **15** (2000) 305.

248. W. N. Hu, D.M. Sun, W. Ma, Electroanalysis, **22** (2010) 584.

249. Y. J. Chen, X. P. Yan, Small **5** (2009) 2012.

250. X.X. Wang, P. Wu, X. D. Hou, Y. Lv, Analyst **138** (2013) 229.

251. B. Song, Y. Zhiqing, Y. Yajie, M. Hua, Z. Xianlin, J. Dayong, J. Yuan, Sci. Rep., **5** (2015) 14194.

252. M. Ganiga, J. Cyriac, Michrochim. Acta **408** (2016) 3699.

253. Y. Matsouka et al, RSC Adv., **6** (2016) 60907.

254. C. Zhen, L. Dongtao, C. Zongwei, D. Chuan, S. Shaomin, Luminescence **29** (2014) 722.

255. K.S. Park, M.I. Kim, M.A. Woo, H.G. Park, Biosens. Bioelectron., **45** (2013) 65.

256. L. Zhou,Y.H. Lin, Z.Z. Huang,J.S. Ren, X.G. Qu, Chem. Commun., **48** (2012) 1147.

257. L.L. Wang, T.M. Yao, S. Shi, Y.L. Cao, W.L. Sun, Sci. Rep., **4** (2014) 5320.

258. R.M. Bright, D.G. Walter, M.D. Musick, M.A. Jackson, K.J. Allison, M.J. Natan, Langmuir **12** (1996) 810.

259. P. Alivisatos, Nat. Biotechnol. **22** (2003) 47.

260. D.H. Tsai, M.P. Shelton, F.W. Del Rio, S. Elzey, S. Guha, M.R. Zachariah, V.A. Hackley, Anal. Bioanal. Chem. **10** (2012) 3015.

261. L.J. Qu, C.X. Yin, F.J. Huo, J.F. Li, J.B. Chao, Y.B. Zhang, Sens. Actuator B-Chem., **195** (2014) 246.

262. T. Liu, F.J Huo, J.F. Li, J.B. Chao, Y.B. Zhang, C. Yin, Sens. Actuator B-Chem., **237** (2016) 127.

263. Y.B. Zhang, F.J. Huo, C.X. Yin, Y.K. Yue, J.S. Hao, J.B. Chao, D.S. Liu, Sens. Actuator B-Chem., **207** (2015) 59.

264. L. Zhou, W. Yong, K. Serge, Sensors Actuators B: Chem., **207** (2015) 490.

265. B. J. Wang, S.J. Zhuo, L.Y. Chen, Y.J. Zhang, Spectrochim. Acta: A **131** (2014) 384.

266. X. Zhao, J. Gao, X. He, L. Cong, H. Zhao, X. Li, F. Tan, RSC Adv. **5** (2015) 39587

267. S.L. Ting, J.E. Shu, A. Ananthanarayanan, K.C. Leong, P. Chen. Electrochim. Acta **172** (2015) 7.

268. D. Li, A. Wieckowska , I. Willner, Angew. Chem., Int. Ed., **48** (2008) 3927.

269. C. W. Liu, Y.-T. Hsieh, C.-C. Huang, Z.-H. Lin, H. T. Chang, Chem. Commun., **21** (2008) 2242.

270. A. Henglein, C. Brancewicz, Chem Mater., **9** (1997) 2164.

271. M. S. Frost, M. J. Dempsey, D. E. Whitehead, Colloids and Surfaces A: Physicochem Eng Aspects **518** (2017) 15.

272. L. Li, D. Feng, X. Fang, X. Han, Y. Zhang, J. Nanostruct. Chem., **4** (2014) 177.

273. A. T. Bilgiçli, A. Günsel, M. Kandaz, A. R. Özkaya, Dalton Trans., **41** (2012) 7047.